Title

Catalytic Consequences of Acid Strength and Site Proximity for Acid Chemistry on Solid Brønsted Acid Catalysts

Permalink

https://escholarship.org/uc/item/0gk4z9q9

Author

Knaeble, William John

Publication Date

2015

Peer reviewed|Thesis/dissertation

Catalytic Consequences of Acid Strength and Site Proximity

for Acid Chemistry on Solid Brønsted Acid Catalysts

By

William John Knaeble

A dissertation submitted in partial satisfaction of the

requirements for the degree of

Doctor of Philosophy

in

Chemical Engineering

in the

Graduate Division

of the

University of California, Berkeley

Committee in charge:

Professor Enrique Iglesia, Chair
Professor Jeffrey A. Reimer
Professor T. Don Tilley

Fall 2015

Catalytic Consequences of Acid Strength and Site Proximity for Acid
Chemistry on Solid Brønsted Acid Catalysts

© 2015

by

William John Knaeble

Abstract

Catalytic Consequences of Acid Strength and Site Proximity
for Acid Chemistry on Solid Brønsted Acid Catalysts

by

William John Knaeble

Doctor of Philosophy in Chemical Engineering

University of California, Berkeley

Professor Enrique Iglesia, Chair

The development of reliable, unambiguous, and useful relationships between the properties of solid Brønsted acids (composition, acid strength, structure, site proximity, etc.) and their catalytic function is a critical step for the improvement of solid Brønsted acid catalysts. Structure-function relations for solid Brønsted acid catalysis are developed here using Brønsted acids of known structure and a broad range of acid strengths (Keggin polyoxometalate (POM) clusters) and a set of prototypical, but industrially important, Brønsted acid catalyzed reactions (alkane hydroisomerizations and alcohol dehydrations) that are accessible to detailed mechanistic studies and theoretical calculations. Keggin POM clusters exhibit well-defined atomic structures amenable to reliable theoretical estimates of deprotonation energies (DPE) as rigorous descriptors of acid strength, diverse chemical compositions that provide a wide range of acid strengths, and relatively high stability. These properties make them ideally suited for elucidating reaction mechanisms, developing structure-function relationships, and comparing experiments with theoretical estimates of chemical dynamics and thermodynamics. The identity of central atoms (X) are systematically varied in Keggin POM ($H_{8-n}X^{n+}W_{12}O_{40}$) clusters (X = P^{5+}, Si^{4+}, Al^{3+}, or Co^{2+}) to examine their effects on the reactivity of these clusters for hydroisomerizations reactions of C_6 aliphatic alkanes and methylcyclohexane and dehydration reactions of ethanol (EtOH). Kinetic and thermodynamic constants for kinetically-relevant steps and surface intermediates in these reactions are obtained from mechanism-based interpretations of experimentally measured turnover rates or from free energies derived from density functional theory (DFT) calculations. Active sites are counted by *in operando* titrations with 2,6-di-*tert*-butyl pyridine during catalysis. Experimental constants are compared with ones from DFT-derived free energies and correlated with catalyst DPE values through structure-function relations.

Isomerization reactions and dehydration reactions occur more rapidly on stronger Brønsted acids (with lower DPE values) because the ion-pair transition states (TS) that mediate kinetically relevant steps in these reactions benefit from their more stable conjugate anions. Electrostatic interactions between the cationic moieties and POM anions

1

at such TS offset the large energetic costs for separating charge and attenuate differences in conjugate anion stabilities on activation barriers. The amount and distribution of charge at cationic moieties determines the extent of charge separation, which dictates the fraction of the additional energy required to deprotonate weaker acids that is recovered by the TS through the electrostatic interaction of the ion-pair. Cationic moieties with either larger amounts of or more delocalized charge result in ion-pair TS with greater extents of charge separation. Reactions mediated by TS structures with either small partial charges or localized proton-like charges are thus least sensitive to acid strength, because they recover a large fraction of the ionic and covalent components of DPE. Intrinsic selectivities in alkene isomerization, ring contraction, and EtOH dehydration reactions are independent of acid strength because the TS mediating the kinetically relevant steps for forming each product in these reactions have cationic moieties with similar amounts and localization of charge, which benefit similarly from electrostatic interactions with the conjugate anion.

Although intrinsic selectivities among isomerization or ring contraction products are independent of acid strength, selective product formation may be obtained by exploiting the effects of diffusion-enhanced secondary reactions. Alkane hydroisomerizations reactions are carried out on bifunctional catalysts containing both acid and metal functions. Metal functions serve to equilibrate alkanes with their alkenes and H_2; this provides a low and known concentration of alkenes at acid sites where they undergo rapid isomerization reactions, which limits the build of product alkenes due to the thermodynamic preference for alkanes at the conditions of these reactions. The size and diffusion properties of the acid domains in bifunctional catalysts, and the concomitant metal-acid site proximity, influence rates and selectivities by changing the Thiele moduli for primary and secondary isomerization reactions within acid domains. Measured product selectivities do not rigorously reflect the intrinsic formation rates of each isomer, because subsequent isomerization events of product alkenes occur at rates comparable to their diffusion out of acid domains. Such secondary reactions are more consequential for measured selectivities on stronger acids because their larger rate constants amplify the effects of acid site density on Thiele moduli.

Alcohols can eliminate water on Brønsted acid sites via the formation of monomolecular or bimolecular products (alkenes and ethers, respectively). EtOH is the simplest alcohol to probe both pathways, as it forms both ethylene (EY) and diethyl ether (DEE) on Brønsted acids at conditions relevant to the practice of dehydration catalysis. Measured product formation rate ratios were inconsistent with conventional dehydration mechanisms that propose only monomolecular elementary steps for EY formation and bimolecular steps for DEE formation, because such mechanism overlook low energy bimolecular pathways for EY formation which become relevant at the high EtOH pressures of practical applications. Experiments and theory combine to indicate that both direct and sequential (ethoxide-mediated) routes contribute to DEE formation on Brønsted acids and that EY predominately forms through sequential routes. The kinetically-relevant steps for routes leading to DEE and ethoxide formation are mediated by S_N2-type substitution TS and those for EY formation are mediated by monomolecular and bimolecular syn-E2-type elimination TS; all of these TS benefit similarly from the more stable conjugate anions in stronger acids making the relative rates of their associated steps independent of acid strength.

Through these studies, it is shown how fundamental properties of solid acid catalysts, such as their acid strengths or site proximities, influence reactivities and selectivities in acid-catalyzed reactions. The former affects the stabilities of relevant intermediates and ion-pair transition states according to the amount and locale of their charge, and the latter dictates how diffusion-enhanced-secondary reactions influence measured rates and selectivities.

This dissertation is dedicated to my wife,
Stephanie, for her constant support through
the good and the bad, the late and long
hours, and the unforeseen adventures.

Table of Contents

List of Tables

List of Figures

Chapter 1

ix

List of Schemes

Chapter 3

Acknowledgments

This work would not have been possible without the help, support, guidance, and belief in me from my family and friends. I would first like to thank my parents, Peter and Robin, for allowing me to be the person I am today and for always pushing me to reach my goals. Thank you also to my brother, David, and sister, Claire, for giving me a set of ideal role models to always look up to, and to the rest of my family, whose constant encouragement kept me motivated during this journey. And I would like to thank my wife, Stephanie, to whom this dissertation is dedicated.

A special thank you to my dissertation advisor, Enrique Iglesia, for giving me the opportunity to work in his lab. His strive for rigor and understanding has made me a more thoughtful and critical thinker and a better researcher. I am also indebted to the talented scientists who have helped me along the way. Thank you to Robert Carr for guiding my passage into the world of catalysis research, and to the rest of the LSAC members, especially, Andrew Jones, Dave Flaherty, Raj Gounder, Brett Loveless, David Hibbitts, Prashant Deshlahra, Neelay Phadke, Shuai Wang, Elif Gurbuz, Jianwei Liu, Stanley Herrmann, Allie Landry, Gina Noh, Michele Sarazen, Edwin Yik, and Sarika Goel. I would also like to thank Dr. Cindy Yin and Dr. Stuart Soled for their assistance with the synthesis of samples.

Chapter 1.

Mechanistic Interpretation of the Effects of Acid Strength on Alkane Isomerization Turnover Rates and Selectivity

Abstract

Acid strength effects on alkane isomerization turnover rates and selectivities are probed using hexene isomers as reactants on bifunctional catalysts containing tungsten Keggin polyoxometalates (POM) with different central atoms and exhibiting well-defined structures amenable to reliable estimates of deprotonation energies (DPE) as rigorous descriptors of acid strength. Titrations of protons with hindered bases during catalysis and mechanistic interpretations of rate data on POM acids in terms of a common sequence of elementary steps give isomerization rate constants that decrease exponentially with increasing DPE. The sensitivity to acid strength is the same for all interconversions among isomeric hexenes because their respective transition states are similar in the amount and localized character of their cationic charges, which determine, in turn, the extent to which the ionic and covalent interactions that determine DPE are recovered upon formation of ion-pairs at transition states. The ratios of rate constants for such interconversions, and thus selectivities, are independent of acid strength and their magnitude merely reflects the stability of the gaseous analogs of their respective transition states on all acids.

1.1. Introduction

Catalysis by solid Brønsted acids is ubiquitous in the synthesis and upgrading of fuels and petrochemicals [1]. Rigorous connections between the structure and strength of acid sites and their specific consequences for reactivity and selectivity remain imprecise and often contradictory. Prevailing uncertainties about the number, location, and structure of acid sites during catalysis, the challenges inherent in the unambiguous experimental assessment of acid strength, and measured rates and selectivities that are seldom interpreted in terms of chemical mechanisms have contributed to the pervasive controversies about the strength of acids and about the consequences of acid strength for rates and selectivities of specific reactions and for catalysis in general.

Deprotonation energies (DPE) reflect the ionic and covalent interactions between a proton (H^+) and its conjugate base. These interactions must be overcome to transfer this proton to the intermediates and transition states that mediate transformations catalyzed by acids. DPE values represent a rigorous and probe-independent measure of acid strength; it is accessible to density functional theory (DFT) treatments for well-defined solid acids, such as Keggin polyoxometalate (POM) clusters (1087 - 1143 kJ mol^{-1} for $H_{8-n}X^{n+}W_{12}O_{40}$; X = P, Si, Al, or Co in order of increasing DPE) [2,3] and zeolites with different frameworks [4] and heteroatoms [5].

The effects of DPE, and consequently of acid strength, on alkanol dehydration [3,6,7] and n-hexene isomerization [8] rate constants (per accessible H^+) on Keggin POM

clusters ($H_{8-n}X^{n+}W_{12}O_{40}$; X = P, Si, Al, or Co) indicate that the ion-pair transition states (TS) that mediate the kinetically-relevant elementary steps are lower in energy with respect to fully protonated clusters on stronger acids, in part, because of their more stable conjugate anions. Differences in the amount and localization of cationic charge at kinetically relevant TS relative to those properties for the most abundant surface intermediates (MASI) determine the sensitivity of measured rate constants to acid strength [7,8]. Cations that are small and contain a highly localized charge resemble H^+ and interact most effectively with the conjugate anion [9]; as a result, proton-like TS structures attenuate the effects of acid strength on reactivity most effectively, by recovering most of the energy required to separate the proton. These studies have shown that the effects of acid strength on reactivity reflect differences in interaction energies between the TS and the conjugate anion and those between the MASI species and the conjugate anion.

Here, we assess the effects of acid strength on isomerization turnover rates of hexane and hexene isomers with different backbone structures on bifunctional catalyst mixtures consisting of well-defined Brønsted acids (W-based Keggin POM clusters) and metal sites (here Pt/Al_2O_3). In such mixtures, Pt sites equilibrate alkanes and alkenes with a given backbone structure via fast hydrogenation-dehydrogenation reactions when such sites are present in sufficient amounts; in such cases, reactant alkenes are present throughout the catalyst mixture at low and constant concentrations; such low concentrations cannot be detected but are known from thermodynamic data at each given temperature and H_2 and alkane pressures. These alkenes undergo skeletal isomerization on acid sites and the alkene isomers formed rapidly equilibrate with the respective alkanes upon contact with Pt sites [10–12].

Isomerization rate constants (per H^+) were measured for the conversion of 2-methylpentane, 3-methylpentane, 2,3-dimethylbutane, and n-hexane reactants through mechanistic interpretations of rate data and measurements of the number of accessible protons by titrations with organic bases during catalysis. These rate constants reflect TS energies relative to unoccupied Brønsted acid sites and gaseous alkene reactants. Selectivities to isomerization products formed from reactant-derived alkenes after only a single sojourn at an acid site cannot be estimated directly from measured selectivities, because secondary interconversions of alkene products and hydrogenation reactions occur at comparable rates; hydrogenation occurs, either locally within acid domains via hydrogen transfer from alkane reactants or via reactions with H_2 after diffusion of alkene isomer products through such acid domains to reach Pt sites. Such selectivities to 3-methylpentene isomer products from 2-methylpentane derived alkenes, which reflect the stability of methyl shift TS relative to those for TS that vary backbone length, were determined— without the use of measured selectivities—from the measured isomerization rate constants for the conversion of each hexane isomer through mechanistic interpretations of rate data. We find that acid strength influences the isomerization rates and selectivities of all skeletal isomers to a similar extent, suggesting that charge distributions are also similar among the ion-pairs that mediate each of these reactions. We conclude that the preferential formation of certain isomers reflects the different proton affinities among the gaseous analogs of their respective transition states; these differences and the extent to which deprotonation energies are recovered by interactions of such TS structures with the conjugate anion are

not affected, however, by the stability of the conjugate anion and thus do not depend on the strength of the solid acid catalyst.

1.2. Experimental Methods

1.2.1. Catalyst synthesis and characterization

$H_3PW_{12}O_{40}$ (Sigma-Aldrich; reagent grade; CAS #12501-23-4), $H_4SiW_{12}O_{40}$ (Aldrich; >99.9 %; CAS #12027-43-9), $H_5AlW_{12}O_{40}$ (as prepared in [13]), and $H_6CoW_{12}O_{40}$ (prepared as in [14,15]) were supported on amorphous SiO_2 (Cab-O-Sil HS-5; 310 m^2 g^{-1}; 1.5 cm^3 g^{-1} pore volume) by incipient wetness impregnation with ethanol as the solvent. SiO_2 was washed three times with 1 M HNO_3 and treated in flowing dry air (UHP Praxair; 0.5 cm^3 g^{-1} s^{-1}) at 573 K for 5 h before impregnation. Ethanolic POM solutions (ethanol, Sigma-Aldrich; >99.5 %; anhydrous) were added to pretreated SiO_2 (1.5 cm^3 solution [g dry SiO_2]$^{-1}$) and impregnated samples were stored in closed vials for > 24 h before treatment in flowing dry air (UHP Praxair; 0.5 cm^3 g^{-1} s^{-1}) by heating from ambient temperature to 323 K at 0.033 K s^{-1} and holding for 24 h. SiO_2-supported POM clusters are denoted as "H_nXW/SiO_2", where n is the stoichiometric number of protons per cluster and X is the central atom. POM concentrations in the impregnation solutions were set to give a surface density of 0.04 POM [nm-SiO_2]$^{-2}$ (~5.0 % wt) for all central atoms, unless noted otherwise. ^{31}P-MAS-NMR spectra of H_3PW/SiO_2 (Figure S.1. in Supporting Information) confirmed that the procedures used to disperse POM clusters on SiO_2 did not alter their Keggin structures. Transmission electron micrographs (Figure S.2. in Supporting Information) showed that, prior to their exposure to reaction conditions, POM clusters were present as isolated clusters or small two-dimensional oligomers on SiO_2 at the surface densities used in this study.

Pt/Al_2O_3 (1.5 % wt.), used as a co-catalyst in physical mixtures with POM/SiO_2 Brønsted acids, was prepared by incipient wetness impregnation of γ-Al_2O_3 (Sasol SBa-200; 193 m^2 g^{-1}, 0.57 cm^3 g^{-1} pore volume) with aqueous H_2PtCl_6 (Aldrich; CAS #16941-12-1; 0.57 cm^3 g^{-1} dried Al_2O_3) solution. The γ-Al_2O_3 was treated in dry air (UHP Praxair; 0.5 cm^3 g^{-1} s^{-1}) at 923 K for 5 h prior to impregnation. The impregnated sample was treated in dry air (Praxair UHP, 0.7 cm^3 g^{-1} s^{-1}) at 383 K for 10 h before heating to 823 K at 0.033 K s^{-1} and holding for 3 h in flowing dry air (Praxair UHP, 0.7 cm^3 g^{-1} s^{-1}). This sample was then treated in H_2 (Praxair 99.999%; 0.2 cm^3 g^{-1} s^{-1}) by heating to 723 K at 0.083 K s^{-1} and holding for 2 h. After cooling to 303 K in He (UHP Praxair; 0.7 cm^3 g^{-1} s^{-1}), the Pt/Al_2O_3 was treated in a dry air/He mixture (2.1 % mol O_2, 7.9 % mol N_2, 90 % mol He, 0.7 cm^3g^{-1} s^{-1} total flow) for 2 h.

The Pt dispersion in Pt/Al_2O_3 (0.92; defined as the fraction of Pt-atoms located at the surfaces of Pt particles) was determined by H_2 uptakes at 298 K using a volumetric chemisorption unit and a 1:1 H-atom:Pt_S adsorption stoichiometry (Pt_S, surface Pt-atom). Pt/Al_2O_3 was treated in H_2 (99.999 % Praxair) at 598 K for 1 h and then held under vacuum at 598 K for 0.5 h before chemisorption measurements. A H_2 adsorption isotherm (99.999% Praxair) was measured at 298 K from 0.1 to 50 kPa H_2. The cell was then evacuated for 0.25 h at 298 K and a second isotherm was measured under the same conditions. The amount of chemisorbed H_2 was calculated from the difference between the first and second

isotherms after their respective extrapolations to zero pressure. The Pt dispersion was also determined by CO chemisorption at 298 K using similar pretreatments, a single CO (99.5% Praxair) adsorption isotherm extrapolated to zero pressure, and by assuming a 1:1 CO:Pt_S adsorption stoichiometry (0.78 Pt_S/Pt_{total}). Their average (0.85) was used to calculate (Pt_S/H^+) ratios of acid-metal mixtures.

Pt/Al_2O_3 samples were mixed with POM/SiO_2 (P, Si, Al, and Co central atoms) in a mortar and pestle (< 100 μm Al_2O_3 and SiO_2 particles) and then pressed into wafers, crushed, and sieved to retain 125-180 μm aggregates. The compositions of these mixtures are reported here as the ratio of Pt_S (from the average dispersion from H_2 and CO chemisorption) to accessible H^+ (measured by titration during catalysis; Section 1.3.1.1); this ratio (Pt_S/H^+) was varied between 6.2 and 22.9 to determine the ratios required to achieve reactant alkane-alkene equilibrium during isomerization catalysis (Section 1.3.1.2.).

1.2.2. Alkane isomerization rate measurements and titrations with 2,6-di-*tert*-butylpyridine

2-Methylpentane (2MP), 3-methylpentane (3MP), 2,3-dimethylbutane (23DMB), and n-hexane (nH) isomerization rates were measured on catalyst mixtures (0.01 - 0.3 g) held within a quartz tubular flow reactor (1.0 cm I.D.) using a porous quartz disk and maintained at 473 K by resistive heating (Watlow Series 982 controller). Temperatures were measured using a K-type thermocouple (Omega; ± 0.2K) held within an indentation at the reactor wall. Mixtures of POM/SiO_2 and Pt/Al_2O_3 were heated to 473 K at 0.083 K s^{-1} in flowing He (UHP Praxair; 0.83 cm^3 s^{-1}) and held for 1 h before catalytic measurements

Liquid 2-methylpentane (Fluka; > 99.5 % analytical standard), 3-methylpentane (Fluka; > 99.5 % analytical standard), 2,3-dimethylbutane (Fluka; > 99.5 % analytical standard), and n-hexane (Fluka; > 99.0 % GC standard) reactants were evaporated into a flowing He (UHP Praxair) and H_2 (99.999 % Praxair) stream using a syringe pump (Cole-Palmer 74900 Series). All transfer lines were kept at 423 K to prevent reactants, products, or titrants from condensing. Flow rates of He and H_2 were metered using electronic mass flow controllers (Porter, Model 201). Molar flow rates of alkanes, H_2, and He were controlled to give desired H_2 pressures and (alkane/H_2) molar ratios and to maintain low reactant conversions (< 7%). H_2 pressures between 60 and 90 kPa were used and (alkane/H_2) reactant ratios were varied between 0.01 and 0.3 (higher ratios led to significant deactivation over the course of kinetic experiments). Reactant and product concentrations in the reactor effluent were measured by gas chromatography using flame ionization detection (Agilent 6890N GC; 50 m HP-1 column). All reactant alkanes contained one or more of the product alkanes as impurities (< 0.7% carbon selectivity); impurity concentrations were subtracted from those in the reactor effluent when calculating their formation rates. Formation rates of each product were corrected for approach to equilibrium with each reactant using:

$$r_{forward} = r_{net} \left(1 - \left(\frac{P_{prod}}{P_{react}} \right) K_{prod,react}^{-1} \right)^{-1} \qquad (1)$$

in which (P_{prod}/P_{react}) is the ratio of product and reactant pressures within the reactor effluent and $K_{prod,react}$ is their equilibrium constant at 473 K obtained from tabulated thermodynamic data [16]. Moderate catalyst deactivation (< 20% over 36 h) occurred on some catalysts during kinetic experiments. All rates were corrected for any intervening deactivation by periodic rate measurements at reference conditions (75 kPa H_2 and 1.9 kPa alkane).

Titration experiments were conducted by dissolving 2,6-di-*tert*-butylpyridine (DTBP, Aldrich; > 97% ; CAS #585-48-8) in liquid 2MP reactants (between 2.4 x 10^{-2} and 8.6 x 10^{-2} % mol) and evaporating this mixture into a flowing H_2/He stream (UHP Praxair; 75 % mol H_2) to give DTBP pressures between 0.45 and 2.6 Pa. Isomerization rates and DTBP uptakes at 473 K were calculated from the concentrations of 2MP, its isomerization products, and DTBP in the reactor effluent. Isomerization rates were extrapolated to zero linearly to determine the number of DTBP molecules required to fully suppress isomerization rates. The extrapolated value was assumed to reflect the number of H^+ accessible during catalysis (using a 1:1 H^+:DTBP adsorption stoichiometry) [17].

1.3. Results and Discussion

1.3.1. 2-Methylpentane, 3-Methylpentane, 2,3-dimethylbutane, and n-hexane isomerization turnover rates on POM/SiO$_2$ mixtures with Pt/Al$_2$O$_3$

2-Methylpentane (2MP), 3-methylpentane (3MP), 2,3-dimethylbutane (23DMB), and n-hexane (nH) isomerization turnover rates were measured on SiO_2-supported POM clusters ($H_{8-n}X^{n+}W_{12}O_{40}/SiO_2$) with different central atoms (X^{n+} = P^{5+}, Si^{4+}, Al^{3+}, Co^{2+}), each present as physical mixtures with Pt/Al$_2$O$_3$ co-catalysts. 2MP isomerization predominantly formed 3MP, 23DMB, and nH products at all conditions and on all catalysts. 2MP isomerization rates were much higher on these bifunctional mixtures than on Pt/Al$_2$O$_3$ (by factors > 100), indicating that only acid sites contribute to the formation of these isomer products. Measured 2MP isomerization selectivities to 3MP (80% - 97% for all conditions and catalyst mixtures) were much higher than to 23DMB or nH (0.1% - 14.5% and 2.3% - 5.4%, respectively). Traces of 2,2-dimethylbutane (22DMB) were detected (< 0.55 % carbon selectivity), but selectivities extrapolated to zero at zero conversion (varied by changing residence time; Figure S.3., Supporting Information), indicating that 22DMB forms only through secondary reactions of primary isomers along the catalyst bed.

On all catalyst mixtures, 3MP isomerization predominantly formed 2MP (> 85 % carbon selectivity) and small amounts of 23DMB and nH. Traces of 22DMB were also detected with 3MP reactants (< 1.1 % carbon selectivity) on these mixtures, but its selectivity also extrapolated to zero at short residence times (Figure S.4. in Supporting Information). nH isomerization at short residence times on these catalyst mixtures formed 2MP and 3MP in amounts consistent with their interconversion equilibrium (2MP/3MP =

1.4 - 1.6), much smaller concentrations of 23DMB (< 1.0 % carbon selectivity), and only traces of 22DMB (< 0.1 % selectivity). 23DMB reactants on these catalyst mixtures formed predominantly 2MP and 3MP at constant ratios (2MP/3MP = 2.0 - 2.3), moderate concentrations of 22DMB (~ 6 % carbon selectivity), and smaller concentrations of nH (< 1.0 % carbon selectivity) at short residence times. 2MP, 3MP, and nH isomerization formed 22DMB with low selectivities that decreased monotonically with decreasing residence time, indicating that 22DMB forms only from 23DMB-derived alkenes, from which it can form via a single methyl shift along the backbone without the need to lengthen or shorten the length of the backbone.

These measured selectivities are consistent with elementary isomerization events that only change the number of pendant methyl groups and length of the backbone by one or none when the shifting methyl group is originally attached to tertiary, secondary, or primary carbon atoms, and not at all when the shifting methyl group is originally attached to quaternary carbon atoms. Scheme 1 depicts a reaction network for hexane isomer rearrangements that is consistent with nH forming only from 2MP and 3MP, and 22DMB forming only from 23DMB. According to Scheme 1, comparisons of the absolute and relative stabilities of TS that mediate the interconversions of 2MP, 3MP, nH, and 23DMB, require that we remove the 22DMB formation rate from the measured rate of conversion of 23DMB reactants, which reflect only the stability of the TS for 22DMB and 23DMB interconversion. Thus, isomerization rate constants reported here represent the rate of forming mono-branched products, which reflect the stability of the TS that mediate 23DMB conversion to 2MP and 3MP.
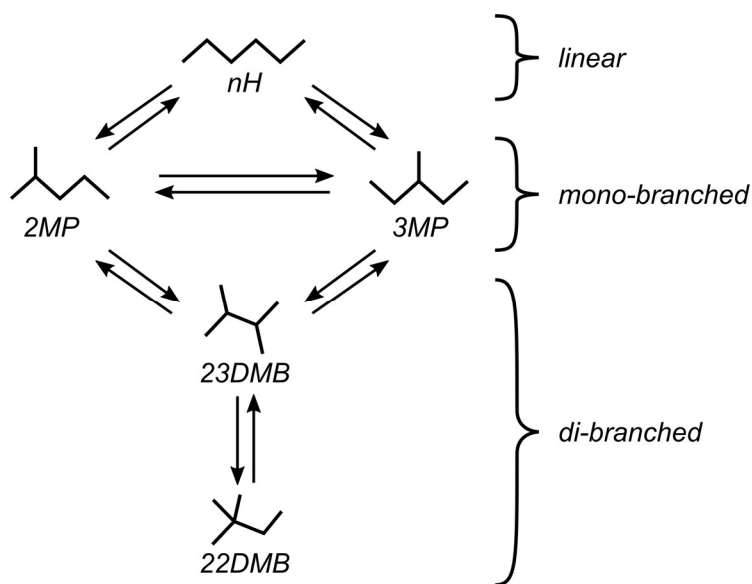
Scheme 1. Isomerization reaction network for gaseous hexane/hexene isomers on POM/SiO$_2$ mixtures with Pt/Al$_2$O$_3$

1.3.1.1. Titrations of protons by 2,6-di-tert-butylpyridine (DTBP) during 2-methylpentane isomerization catalysis

2,6-di-*tert*-Butylpyridine (DTBP) is a selective titrant of Brønsted acid sites because it is protonated irreversibly but cannot coordinate to Lewis acid sites because of steric constraints [17]. Figure 1 shows 2MP isomerization rates (per POM) as a function of time or of cumulative DTBP uptake (per POM) before and during DTBP introduction, respectively, on H_3PW/SiO_2-Pt/Al_2O_3 and H_4SiW/SiO_2-Pt/Al_2O_3 mixtures. Isomerization rates decreased linearly with increasing DTBP uptake on both catalysts and reached undetectable levels upon titration of all protons in each sample. These data show that 2MP isomerization occurs only at Brønsted acid sites and that DTBP titrates all protons accessible to reactants. As a result, isomerization turnover rates are reported here as measured rates normalized by the number of protons (H^+) titrated by DTBP in each sample (assuming a 1:1 H^+:DTBP adsorption stoichiometry) during 2MP isomerization catalysis.
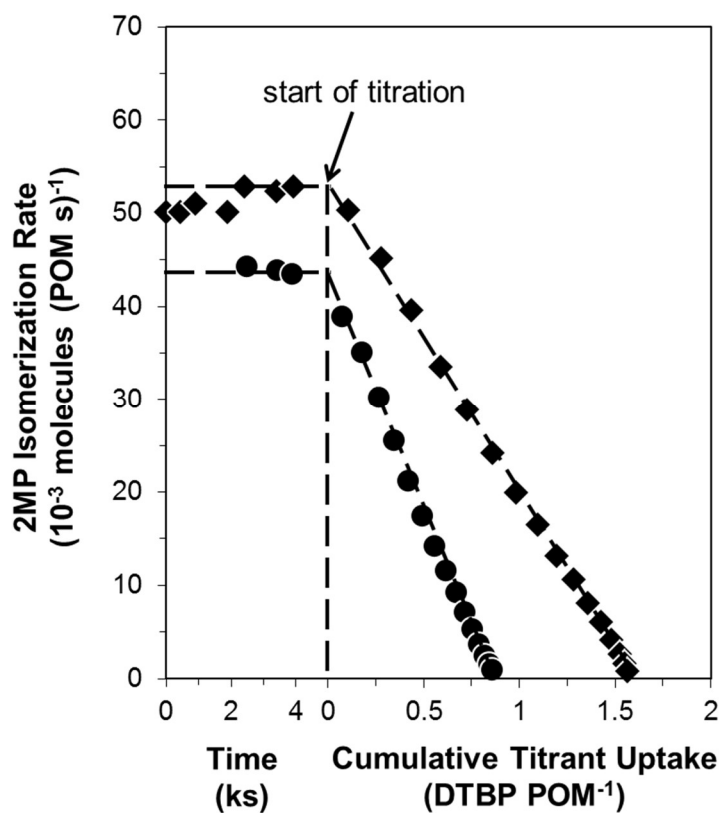
Figure 1. 2-Methylpentane isomerization rates (per POM) on (●) H_3PW/SiO_2-Pt/Al_2O_3 (Pt_S/H^+ = 11.7) and (◆) H_4SiW/SiO_2-Pt/Al_2O_3 (Pt_S/H^+ = 4.8) mixtures as a function of time before 2,6-di-*tert*-butylpyridine introduction (473 K, 1.9 kPa 2MP, 75 kPa H_2) and as a function of cumulative titrant uptake (473 K, 1.9 kPa 2MP, 75 kPa H_2, 0.45 Pa DTBP).

7

The number of titrated H^+ (per POM; Table 1) was smaller than expected from the POM stoichiometry (i.e., 8-x where x is the valence of the central atom) by factors of 2 to 3.5 for all POM cluster compositions. Secondary structures of POM clusters can prevent DTBP and nonpolar reactants from accessing H^+ located in interstitial spaces within the cubic packing of such secondary structures [8,18], leading to lower DTBP uptakes than expected for isolated fully accessible POM clusters. POM features evident in TEM images of 0.04 POM $(nm-SiO_2)^{-2}$ (< 2 nm; Figure S.2. in Supporting Information) are much smaller than the secondary POM structures that would have had to exist to account for the proton counts shown in Table 1 (~ 15 - 20 nm diameters assuming POM anions with 1.2 nm diameters and rhombic dodecahedron secondary structures with bcc crystal structure). Substoichiometric DTBP uptakes may instead reflect intracluster POM dehydroxylation, which removes some H^+ and POM O-atoms as H_2O, or similar reactions between OH groups in POM clusters and surface OH groups on SiO_2 surfaces under the anhydrous conditions of isomerization catalysis [19–21]. Unsupported POM clusters lose H^+ as water at significantly higher temperatures (623 K for $H_3PW_{12}O_{40}$ [22]) than isomerization reaction temperatures (473 K), suggesting that low H^+ counts (Table 1) are caused instead by reactions with silanols. DTPB uptakes varied among $H_3PW_{12}O_{40}/SiO_2$-Pt/Al_2O_3 mixtures containing the same 5 wt% $H_3PW_{12}O_{40}/SiO_2$ catalysts (Table 1) with different amounts of Pt/Al_2O_3, yet their isomerization turnover rates were identical (Figure 2), indicating that such dehydroxylation reactions do not influence the reactivity, and by inference the acid strength, of those protons which remain accessible to DTBP. Therefore, we conclude that DTBP uptakes accurately reflect the actual number of accessible Brønsted acid sites *during* catalysis needed to rigorously normalize rates.

1.3.1.2. Potential effects of diffusional restrictions on isomerization turnover rates and selectivities measured on POM/SiO2-Pt/Al2O3 mixtures

Alkane isomerization rates on bifunctional metal-acid catalysts are limited by the isomerization of alkene intermediates on Brønsted acid sites when (i) the metal function maintains alkane-alkene thermodynamic equilibrium [23] outside acid domains (defined here as the proton-containing regions devoid of metal sites) and (ii) there are no concentration gradients of reactant-derived alkenes within such acid domains. On such mixtures, transport restrictions do not corrupt measured rates of reactant depletion and calculated rate constants reflect the kinetic and thermodynamic properties of the acid sites. Next, we confirm that conditions (i) and (ii) are met for the catalyst mixtures studied here.

H_3PW/SiO_2-Pt/Al_2O_3 mixtures with (Pt_S/H^+) ratios of 6.2, 11.7 and 22.9 gave similar 2MP isomerization turnover rates (per H^+) at all conditions (Figure 2; 0.75 - 22.5 kPa 2MP, 75 kPa H_2). The isomerization turnover rates (per H^+) for 3MP, 23DMB, and nH reactants were also unaffected by (Pt_S/H^+) ratios (Table 3; 1.9 kPa alkane, 75 kPa H_2). These results indicate that Pt sites can maintain alkane dehydrogenation-hydrogenation equilibrium for all reactants in these physical mixtures, which contain the POM acid with the highest turnover rate, thus satisfying requirement (i) above.

Reactant alkene concentration gradients within acid domains were ruled out by the similar measured 2MP, 3MP, 23DMB, and nH isomerization turnover rates on H_3PW/SiO_2-Pt/Al_2O_3 mixtures with very different proton densities (0.03 and 0.34 H^+ $(nm-SiO_2)^{-2}$) within acid domains (Figure 2 and Table 3; Pt_S/H^+ = 10.5 and 11.7, respectively).

Any intraparticle concentration gradients of reactant alkenes would have been more severe on samples with higher H^+ densities and would have led to concomitantly lower turnover rates, because isomerization rates are nearly proportional to reactant alkene concentrations at the conditions of these experiments [24]. All rate data used to determine kinetic parameters on H_3PW were obtained on samples with 0.03 H^+ nm^{-2} acid site densities and a (Pt_S/H^+) ratio of 11.7 to ensure strict kinetic control and the absence of any diffusional corruptions of measured rates and rate constants.
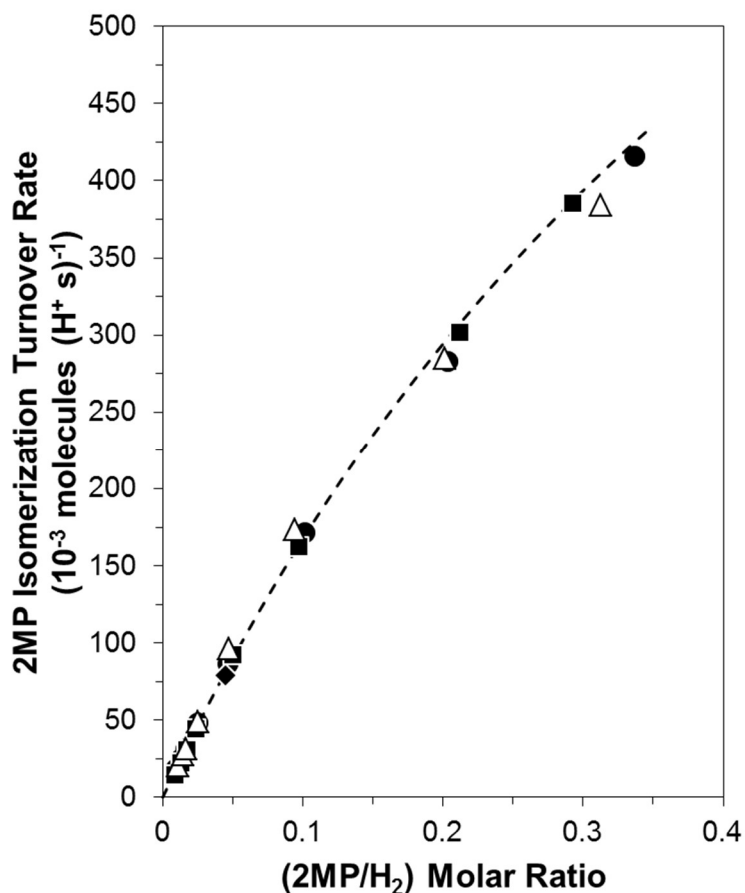
Figure 2. 2-Methylpentane isomerization turnover rates as a function of (2MP/H_2) ratios on H_3PW/SiO_2-Pt/Al_2O_3 mixtures with (◆) 0.03 H^+ [nm-SiO_2]$^{-2}$ and Pt_S/H^+ = 6.2, (●) 0.03 H^+ [nm-SiO_2]$^{-2}$ and Pt_S/H^+ = 11.7, (△) 0.04 H^+ [nm-SiO_2]$^{-2}$ and Pt_S/H^+ = 22.9, and (■) 0.34 H^+ [nm-SiO_2]$^{-2}$ and Pt_S/H^+ = 10.5 (reaction conditions: 473 K, 0.5 – 25 kPa 2MP, 75 kPa H_2). Dashed lines represent the regression of the data to the functional form of Eq. 4.

Bifunctional mixtures with (Pt_S/H^+) ratios smaller than 11.7 were used for the other POM acids (Pt_S/H^+ = 4.8, 5.0, and 5.9 for H_4SiW/SiO_2-Pt/Al_2O_3, H_5AlW/SiO_2-Pt/Al_2O_3, and H_6CoW/SiO_2-Pt/Al_2O_3 mixtures, respectively), which have lower isomerization turnover rates than H_3PW/SiO_2-Pt/Al_2O_3 mixtures (Figure 4). Such ratios were chosen to avoid any contributions to rates from Pt-catalyzed isomerization reactions (Section 1.3.1).

These mixtures have (Pt_s/H^+) ratios similar to (and isomerization turnover rates lower than) the H_3PW/SiO_2-Pt/Al_2O_3 mixture with a (Pt_s/H^+) ratio of 6.2, for which such ratios were sufficient to maintain alkane dehydrogenation-hydrogenation equilibrium for 2MP reactants, suggesting that the metal function in these samples are also sufficient to maintain alkane-alkene equilibrium outside acid domains. Transport restrictions within acid domains for reactant alkenes would have been less severe for these other POM acids supported with 0.04 POM (nm-SiO_2)$^{-2}$ surface densities (which were used for kinetic experiments) than for the H_3PW/SiO_2 sample with a 0.20 POM (nm-SiO_2)$^{-2}$ surface density, because they have much lower isomerization rates than the H_3PW/SiO_2 sample when normalized by the pellet volume of the silica support (~ 8 - 140 fold), yet similar diffusion rates because of the similar size and porous structure of the silica domains that contain the acid sites. Thus, isomerization turnover rates measured on these H_4SiW/SiO_2-Pt/Al_2O_3, H_5AlW/SiO_2-Pt/Al_2O_3, and H_6CoW/SiO_2-Pt/Al_2O_3 mixtures are not corrupted by transport restrictions.

Measured alkane isomerization selectivities on bifunctional metal-acid catalysts reflect the relative rates of product formation from reactant alkenes after only a single sojourn at an acid site only when rates of secondary interconversions of alkene products are much lower than their respective hydrogenation rates, either locally within acid domains via hydrogen transfer from alkane reactants or via reactions with H_2 after their diffusion through such acid domains to reach Pt sites. Only on such mixtures, transport restrictions would not corrupt measured selectivities and calculated rate constants for *individual* product formation would rigorously reflect the kinetic and thermodynamic properties of the isomerization TS that mediates each respective formation reactions. Selectivities measured on such mixtures at differential conditions are expected to be independent of rates of product alkene hydrogenation and, consequently, reactant alkane pressure. Figure 3 shows 2MP isomerization selectivities to 23DMB ($S_{meas,23}$) and nH ($S_{meas,nH,}$) products as a function of 2MP pressure and 75 kPa H_2 on H_3PW/SiO_2-Pt/Al_2O_3 mixtures with very different acid site densities (0.03 and 0.34 H^+ (nm-SiO_2)$^{-2}$). $S_{meas,23}$ and $S_{meas,nH}$ values decrease with increasing 2MP pressure on these samples suggesting they depend, to some extent, on rates of product alkene hydrogenation via hydride transfer from alkane reactants. Increasing 2MP pressure increases rates of hydrogenation locally within acid domains, decreasing the concentration of product alkenes in such acid domains and, concomitantly, rates of secondary interconversions of alkene products. $S_{meas,nH}$ values in Figure 3 appear to approach constant values at high 2MP pressures (>10 kPa) suggesting that at such high 2MP pressures increasing rates of hydrogenation locally within acid domains is not effective at changing the net rate of secondary interconversions among 3MP and nH derived alkene products. Decreasing the acid site density of the H_3PW/SiO_2-Pt/Al_2O_3 mixtures, which decrease rates of secondary interconversions and hydrogenation via hydride transfer from alkane reactants within such domains but not the rates of diffusion of product alkenes through acid domains, gave higher $S_{meas,nH}$ values (by 1.4 factors) at high 2MP pressures (>10 kPa in Figure 3). These data indicate that transport restrictions indeed influence measured selectivities on these samples for the range of 2MP and H_2 pressures in Figure 3 (including 2MP pressures >10 kPa); as a result, secondary interconversions of alkene products at these conditions occur at rates similar to their hydrogenation, both locally within acid domains via hydrogen transfer from alkane reactants and via reactions with H_2 after their diffusion through such acid domains to reach

Pt sites. In such cases, rates and selectivities for isomerization reactions to *individual* primary products (defined as those formed from reactant alkenes in one surface sojourn) cannot be inferred directly from measured selectivities. These constraints preclude the determination of such *individual* product formation rates for most of the isomer products formed; as we show in Section 1.3.1.3, such formation rates and, as a result, selectivities for 3-methylpentene formation as a primary product from 2-methylpentene can be determined explicitly for any given catalyst mixture from measured isomerization turnover rates for 2MP, 3MP, 23DMB, and nH reactants. Next, such isomerization turnover rates measured on H_3PW/SiO_2-Pt/Al_2O_3, H_4SiW/SiO_2-Pt/Al_2O_3, H_5AlW/SiO_2-Pt/Al_2O_3, and H_6CoW/SiO_2-Pt/Al_2O_3 mixtures are interpreted mechanistically.
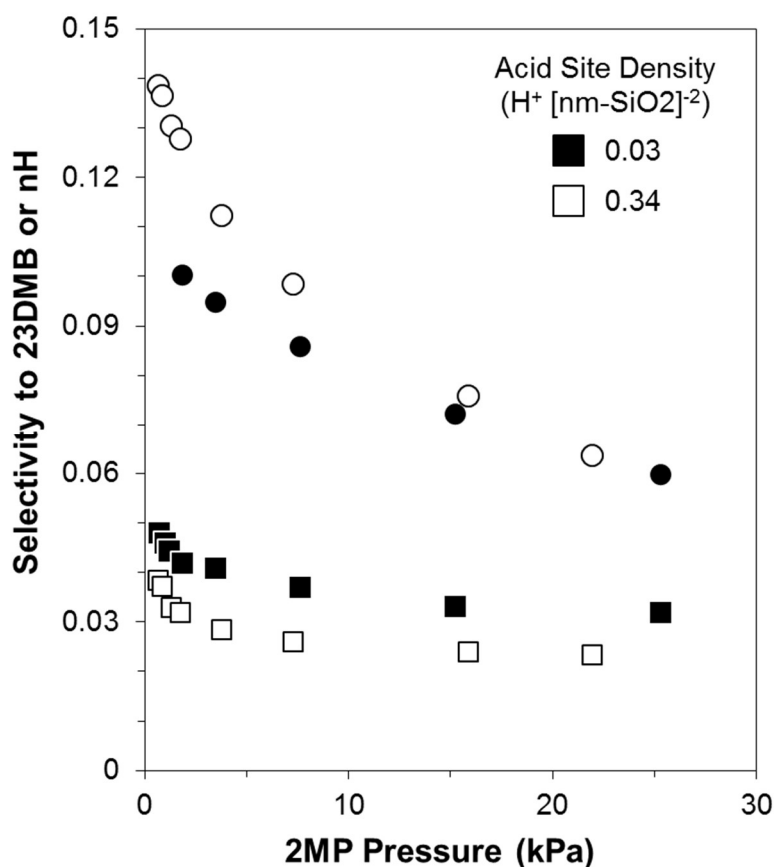
Figure 3. Isomerization selectivities to 23DMB (●) and nH (■) products for 2MP reactants on H_3PW/SiO_2-Pt/Al_2O_3 (Pt_S/H^+ = 10.5 - 11.7; H^+ [nm-SiO_2]$^{-2}$ = 0.03 - 0.34) as a function of 2MP pressure (473 K, 0.7 - 25 kPa 2MP, 75 kPa H_2).

1.3.1.3. Mechanistic interpretation of isomerization turnover rate data for POM/SiO2-Pt/Al2O3 mixtures

Figure 4a shows 2MP isomerization turnover rates (per H^+) as a function of (2MP/H_2) ratio (a surrogate for the concentration of the alkene regioisomers with the 2-methyl backbone in equilibrium with 2MP reactants) on POM/SiO_2-Pt/Al_2O_3 mixtures with P, Si, Al, and Co central atoms ((Pt_s/H^+) = 4.8 - 11.7). 2MP isomerization turnover rates (at a given reaction condition) increased as the valence of the POM central atom decreased. Turnover rates also increased with increasing (2MP/H_2) ratios on each sample, linearly at first and then more gradually at higher reactant ratios (Figure 4a). 2MP isomerization rates depend only on (2MP/H_2) ratios and not on the individual values of the 2MP or H_2 pressures (60 - 90 kPa H_2) used to obtain these ratios on all POM/SiO_2-Pt/Al_2O_3 mixtures.
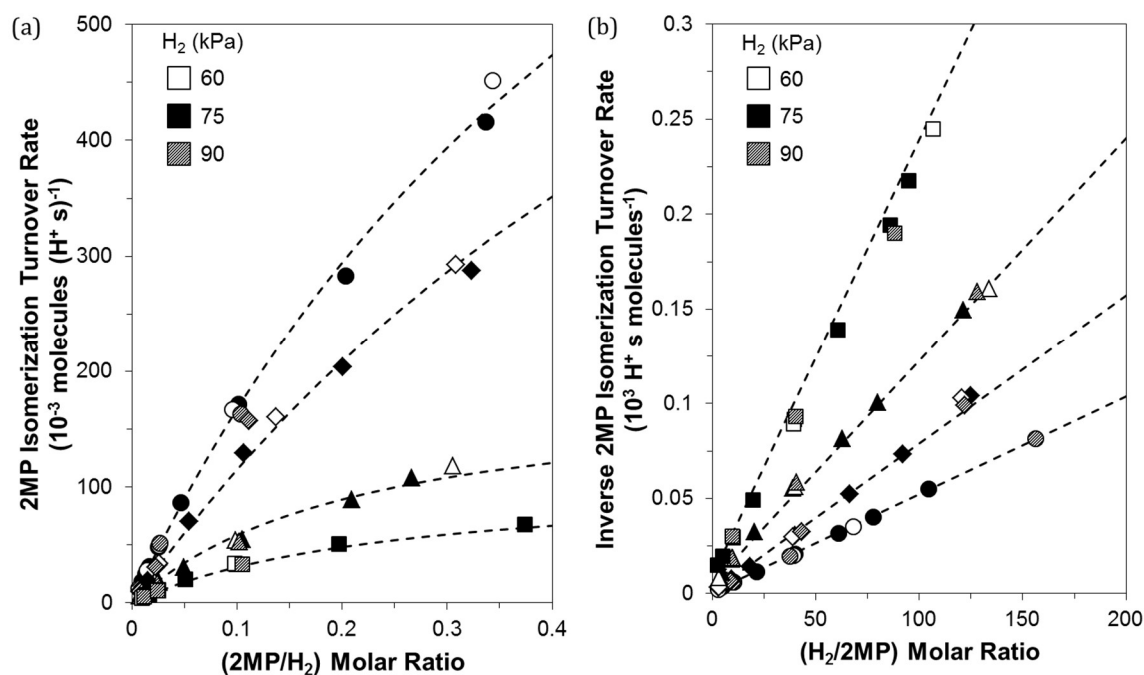
Figure 4. (a) 2-Methylpentane isomerization turnover rates as functions of the (2MP/H_2) ratio and (b) inverse 2-methylpentane isomerization turnover rates as a function of the (H_2/2MP) ratio on mixtures of Pt/Al_2O_3 with (●) H_3PW/SiO_2 (Pt_S/H^+ = 11.7), (◆) H_4SiW/SiO_2 (Pt_S/H^+ = 4.8), (▲) H_5AlW/SiO_2 (Pt_S/H^+ = 5.0), and (■) H_6CoW/SiO_2 (Pt_S/H^+ = 5.9) (reaction conditions: 473 K, 0.5 - 25 kPa 2MP, 60 – 90 kPa H_2). Dashed lines represent the regression of the data to the functional form of Eq. 4.

The elementary steps in Scheme 2 may be used to derive a rate equation consistent with these measured effects of (2MP/H_2) ratios on isomerization rates, as shown previously for other bifunctional isomerization catalysts [8,23,25]. Pt sites equilibrate 2MP with all 2-methylpentene regioisomers (Scheme 2, Step 1 illustrated for the case of 2-methylpent-2-ene); as a result, alkene pressures are proportional to (2MP/H_2) ratios and to their respective dehydrogenation equilibrium constants ($K_{dehy,2}$). Quasi-equilibrated protonation of 2-methylpentene isomers at acid sites forms adsorbed 2-methylpentoxide isomers with backbone attachments to surfaces at locations prescribed by their relative thermodynamic

12

stability (Scheme 2, Step 2 shown for 2-methylpent-2-ene and 2-methypent-3-oxide). Adsorbed 2-methylpentoxides then isomerize in irreversible steps to alkoxides with a different backbone structure (Scheme 2, Step 3 for the case of 3-methylpent-2-oxide). These backbone rearrangements are mediated by cationic TS that resemble cyclopropyl carbenium ions (or cyclobutyl carbenium ions for interconversions of 3-methylpentoxides and 2,3-dimethylpentoxides) in which C-C bonds (and C-H bonds, for cyclopropyl carbenium ion TS that change the number of pendant methyls) bonds cleave and form in concerted steps [26–30]. Product alkoxides either deprotonate to form their gaseous alkenes (Scheme 2, Step 4 shown for 3-methylpent-2-ene) or hydrogenate via hydrogen transfer from 2MP to form their respective gaseous alkane isomer and a 2-methylpentoxide (Scheme 2, Step 5 shown for 3-methylpent-2-oxide and 2-methylpent-3-oxide). Gaseous alkene products may re-protonate at acid sites (Scheme 2, Step 4) or diffuse to Pt sites and undergo hydrogenation reactions with H_2 to form the respective gaseous alkane isomer (Scheme 2, Step 6 shown for 3MP). Alkenes (and alkoxides) with a given backbone but different double-bond positions can be rigorously treated in all kinetic analyses as a lumped chemical pseudo-species, because of their rapid interconversions. These alkene (and alkoxide) pseudo-species are denoted henceforth by the superscript symbol "=" (and "*") without specifying the position of the double bond in the gaseous alkene and of the surface attachment in the alkoxides (e.g., 2-methylpentane, 2-methylpentene isomers, and 2-methylpentoxide isomers are denoted as 2MP, 2MP$^=$, and 2MP* respectively).
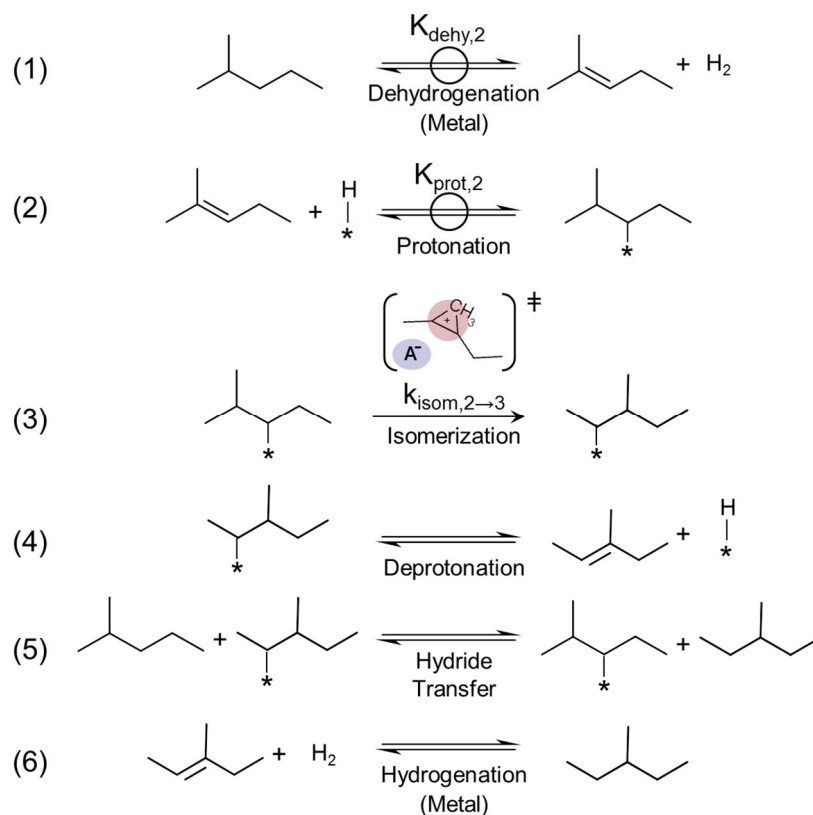
Scheme 2. Elementary steps and chemical reactions involved in 2-methylpentane isomerization on metal-acid mixtures that establish 2-methylpentane/2-methylpentene equilibrium. Chemical reactions are shown for the (de)hydrogenation on metal sites (Pt/Al$_2$O$_3$) and elementary steps for acid-catalyzed routes on H$_{8-n}$X^{n+}W$_{12}$O$_{40}$/SiO$_2$ (X = P^{5+}, Si^{4+}, Al^{3+}, Co^{2+}). Steps 3 - 6 are illustrated using 3-methylpentane as the product, but analogous steps are involved in 2,3-dimethylbutane and n-hexane formation. Bonds to the Brønsted active site are denoted as "*" in molecular structures.

The assumptions of pseudo-steady-state for alkoxides and of equilibrated hydrogenation-dehydrogenation and protonation-deprotonation steps, taken together with 2MP* and H$^+$ as the most abundant surface intermediates (MASI) and irreversible skeletal isomerization of 2MP*, lead to a rate equation for 2MP isomerization to each alkane product isomer "P" ($r_{isom,2\rightarrow P}$; P = 3MP (3), 23DMB (23), or nH; full derivation in Section S.3. of Supporting Information):

$$\frac{r_{isom,2\rightarrow P}}{[H^+]} = \frac{k_{isom,2\rightarrow P}K_{prot,2}K_{dehy,2}\left(\dfrac{2MP}{H_2}\right)}{1 + K_{prot,2}K_{dehy,2}\left(\dfrac{2MP}{H_2}\right)} \tag{2}$$

Here, [H$^+$] is the number of accessible H$^+$ (from DTBP titration data, Section 1.3.1.1), K$_{prot,2}$ is the equilibrium constant for 2MP$^=$ protonation to 2MP* (2-methylpent-3-oxide

14

used as example in Scheme 2), and $k_{isom,2\rightarrow P}$ is the alkoxide isomerization rate constant that forms product "P". The first and second terms in the denominator of Equation 2 reflect the relative numbers of active sites present as unoccupied H^+ and 2MP*, respectively; the coverage by product-derived alkoxides is much smaller than that by 2MP*, because of the low concentrations of product-alkenes at the low conversions of these experiments. All product formation rate equations have the same denominator (with terms only for H^+ and 2MP* species) because all products form on the same Brønsted acid sites. The sum of rate equations similar in functional form to Equation 2 but for each 3MP, 23DMB, and nH product gives an equation for the total 2MP isomerization rate ($r_{isom,2}$) at 2MP-2MP$^=$ equilibrium:

$$\frac{r_{isom,2}}{[H^+]} = \frac{k_{isom,2}K_{prot,2}K_{dehy,2}\left(\dfrac{2MP}{H_2}\right)}{1+K_{prot,2}K_{dehy,2}\left(\dfrac{2MP}{H_2}\right)} \tag{3a}$$

in terms of the sum of the individual rate constants for the isomerization to form each product

$$k_{isom,2} = k_{isom,2\rightarrow 3} + k_{isom,2\rightarrow 23} + k_{isom,2\rightarrow nH} \tag{3b}$$

$K_{prot,2}K_{dehy,2}$ values in Equation 3a are independent of the product being formed because all isomerization events originate from the same pool of equilibrated surface alkoxide species (2MP*). These equations describe the rate data shown in Figure 2, because 2MP$^=$ concentrations remain at equilibrium with 2MP reactants at all acid sites throughout the reactor.

2MP isomerization rates that depend inversely on (H_2/2MP) ratios (Figure 4b) and lie along a single curve at all H_2 pressures (60 - 90 kPa H_2; Figures 4a and 4b) are consistent with the form of Equation 3a and with 2MP-2MP$^=$ equilibration:

$$\left(\frac{r_{isom,2}}{[H^+]}\right)^{-1} = \frac{1}{k_{isom,2}K_{prot,2}K_{dehy,2}}\left(\frac{H_2}{2MP}\right)+\frac{1}{k_{isom,2}} \tag{4}$$

The slope and intercept of linear rate data shown in Figure 4b, therefore, reflect the values of the kinetic and thermodynamic parameters in Equation 4. The values of the first-order rate constant for alkene isomerization ($k_{isom,2}K_{prot,2}$) were regressed from the data in Figure 4b for each POM acid to the functional form of Equation 4 using thermodynamic data [16,31] for the gas phase equilibrium constant for alkane-alkene equilibration ($K_{dehy,2}$ = 1.10 Pa at 473 K); their values are shown in Table 2. The zero-order rate constant for alkene isomerization ($k_{isom,2}$) and the equilibrium constant for the formation of alkoxide species at acid sites from gaseous alkenes ($K_{prot,2}$) were regressed from the data in Figure 4a to the functional form of Equation 3a using the determined $k_{isom,2}K_{prot,2}$ value for each POM acid. These rate data provide accurate values for $k_{isom,2}K_{prot,2}$, but not for $k_{isom,2}$ (or $K_{prot,2}$) (e.g.,

linear regressions of rate data measured on POM clusters give errors for $k_{isom,2}K_{prot,2}$ $<\pm0.8\%$ of the reported values, but up to $\pm120\%$ of the values reported for $k_{isom,2}$). The form and mechanistic interpretation of Equation 4 indicate that accurate $k_{isom,2}$ estimates would require (H_2/2MP) ratios that cause detectable contributions from its intercept and, as a result, lead to kinetically-detectable alkoxide coverages (the second term in the denominator of Equation 3b). Such small (H_2/2MP) ratios favor bimolecular alkene-alkoxide oligomerization reactions that can form unreactive oligomers that bind irreversibly to acid sites leading to catalyst deactivation. As a result, regressions were limited in this study to (2MP/H_2) ratios below ~ 0.1 (i.e., when the second term is much smaller than unity in the denominator of Equation 3a) and become less accurate at higher (2MP/H_2) ratios (dashed curves in Figure 4a).

Figure 5a shows 2MP, 3MP, 23DMB, and nH total isomerization turnover rates (normalized by H^+ titrated with DTBP, Table 1) as a function of (alkane/H_2) ratios on H_3PW/SiO_2-Pt/Al_2O_3 mixtures with 0.03 H^+ nm^{-2} surface density and 11.7 (Pt_s/H^+) ratios. Turnover rates increased with increasing (alkane/H_2) ratios for all reactants, linearly at first and then more gradually at higher reactant ratios (Figure 4a). Isomerization turnover rates at different H_2 pressures lie along a single curve for each reactant (Figures 5a and 5b), as expected from alkane-alkene equilibration (as in the case of 2MP reactants; Fig. 3a and 3b). These data show that the elementary steps in Scheme 2 accurately represent the isomerization pathways for all hexane isomers used as reactants and that all rate data can be described by:

$$\frac{r_{isom,R}}{[H^+]} = \frac{k_{isom,R}K_{prot,R}K_{dehy,R}\left(\frac{[R]}{H_2}\right)}{1 + K_{prot,R}K_{dehy,R}\left(\frac{[R]}{H_2}\right)} \qquad (5)$$

Here, $K_{dehy,R}$ is the dehydrogenation equilibrium constant for reactant "R" (R = 2MP (2), 3MP (3), 23DMB (23), or nH (nH)) calculated from tabulated thermodynamic data [31] ($K_{dehy,3} = 1.15$ Pa, $K_{dehy,23} = 1.67$ Pa, and $K_{dehy,nH} = 0.28$ Pa at 473 K). $K_{prot,R}$ is the equilibrium constant for the formation of a given alkoxide regioisomer group ($[R^*]$) from the equilibrated alkene lump, $[R^=]$, for reactant "R"; $k_{isom,R}$ is the isomerization rate constant for the total conversion of $[R^*]$ to all isomer products. The dashed curves in Figures 5a and 5b represent the regression of these data to Equation 5 using the method described above for 2MP reactants to obtain $k_{isom,R}K_{prot,R}$, $K_{prot,R}$, and $K_{dehy,R}$ values. As in the case of 2MP reactants, $k_{isom,R}K_{prot,R}$ values for 3MP, 23DMB, and nH reactants can be determined more accurately than $k_{isom,R}$ values (or $K_{prot,R}$) (e.g., linear regressions of data in Figure 5b give errors for $k_{isom,R}K_{prot,R}$ $<\pm0.9\%$ of the reported values, but errors for $k_{isom,R}$ up to $\pm430\%$ of the reported values). The $k_{isom,R}K_{prot,R}$ values for 3MP, 23DMB, and nH reactants on POM/SiO_2-Pt/Al_2O_3 mixtures with Si, Al, and Co central atoms were obtained by regression of rate data to the functional form of Equation 5 at low (alkane/H_2) ratios (75 kPa H_2, < 1.9 kPa alkane).
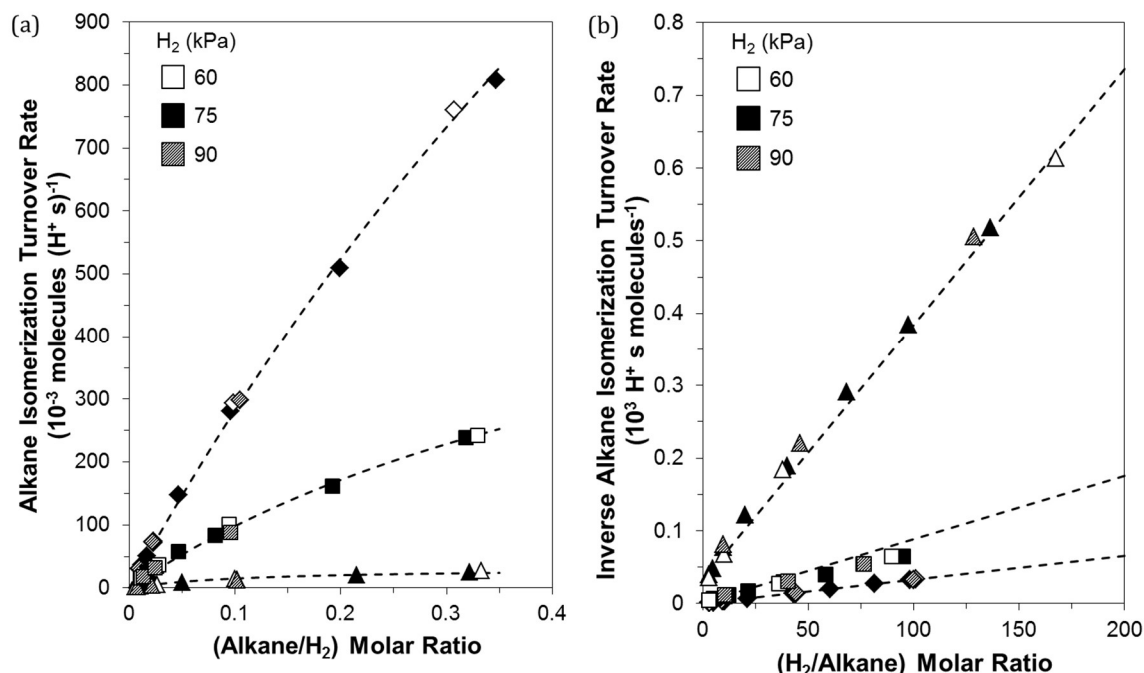
Figure 5. (a) Isomerization turnover rates as functions of the ([R]/H$_2$) ratio and (b) inverse isomerization turnover rates as functions of the (H$_2$/[R]) ratio for (◆) 3-methylpentane, (■) 2,3-dimethylbutane, and (▲) n-hexane reactants on H$_3$PW/SiO$_2$-Pt/Al$_2$O$_3$ (Pt$_s$/H$^+$ = 11.7) (reaction conditions: 473 K, 0.5 – 25 kPa alkane, 60 – 90 kPa H$_2$). Dashed lines represent the regression of the data to the functional form of Eq. 5.

A rigorous analysis of the effects of acid strength on isomerization rate constants and selectivities requires that we dissect $k_{isom,R}K_{prot,R}$ values into those for the formation of each *individual* isomer product ($k_{isom,R\rightarrow P}K_{prot,R}$). The data and discussion in Section 1.3.1.2 showed that measured alkane isomerization selectivities vary with reactant alkane pressure and do not reflect the selectivity for the formation of *primary* isomers (defined as those formed from reactant alkenes in one sojourn at an acid site); therefore, these selectivities cannot be used to calculate the individual formation rate for each isomer and to determine, in this manner, the $k_{isom,R\rightarrow P}K_{prot,R}$ values. This constraint precludes the determination of each $k_{isom,R\rightarrow P}K_{prot,R}$ value for most *individual* isomer products formed from each reactant (except approximately when one isomer predominates among products). As we show next, however, $k_{isom,2\rightarrow3}K_{prot,2}$ values, and consequently 2MP isomerization selectivities to 3MP and the ratio of those selectivities to those for isomerization products that vary backbone length, can be determined explicitly, without the use of measured product selectivities, from the measured lumped $k_{isom,R}K_{prot,R}$ values for each isomer reactant.

The functional form of Equation 3b for each reactant allows one to expand $k_{isom,R}K_{prot,R}$ values for each reactant "R" in terms of $k_{isom,R\rightarrow P}K_{prot,R}$ values for each product "P" formed from reactant "R" (noting that 22DMB formation is excluded from 23DMB conversion rates):

$$k_{isom,2}K_{prot,2} = k_{isom,2\rightarrow3}K_{prot,2} + k_{isom,2\rightarrow23}K_{prot,2} + k_{isom,2\rightarrow nH}K_{prot,2} \tag{6a}$$

17

$$k_{isom,3}K_{prot,3} = k_{isom,3\to2}K_{prot,3} + k_{isom,3\to23}K_{prot,3} + k_{isom,3\to nH}K_{prot,3} \qquad (6b)$$

$$k_{isom,23}K_{prot,23} = k_{isom,23\to2}K_{prot,23} + k_{isom,23\to3}K_{prot,23} \qquad (6c)$$

$$k_{isom,nH}K_{prot,nH} = k_{isom,nH\to2}K_{prot,nH} + k_{isom,nH\to3}K_{prot,nH} \qquad (6d)$$

These forward and reverse isomerization rate constants ($k_{isom,2\to23}K_{prot,2}$ and $k_{isom,23\to2}K_{prot,23}$ for example) are measured at reaction conditions where unoccupied H^+ sites are the *single* most abundant surface species and alkoxide isomerization is the *single* kinetically-relevant step. In such cases, forward and reverse isomerization events are mediated by the same kinetically relevant transition state and must obey the principle of microscopic reversibility even when the isomerization reactions are far from equilibrium [31]. The ratio of the rate constants that describe such reactions is given by the equilibrium constant ($K_{ene,R\leftrightarrow P}$) for the overall reaction (i.e. formation of the equilibrated $[R^=]$ lump for product "P" from the equilibrated $[R^=]$ lump for reactant "R"), which may be calculated from tabulated gas phase thermodynamic data at the given reaction temperature (473 K):

$$K_{ene,2\leftrightarrow3} = \frac{k_{isom,2\to3}K_{prot,2}}{k_{isom,3\to2}K_{prot,3}} \qquad (7a)$$

$$K_{ene,2\leftrightarrow23} = \frac{k_{isom,2\to23}K_{prot,2}}{k_{isom,23\to2}K_{prot,23}} \qquad (7b)$$

$$K_{ene,2\leftrightarrow nH} = \frac{k_{isom,2\to nH}K_{prot,2}}{k_{isom,nH\to2}K_{prot,nH}} \qquad (7c)$$

$$K_{ene,23\leftrightarrow3} = \frac{k_{isom,23\to3}K_{prot,23}}{k_{isom,3\to23}K_{prot,3}} \qquad (7d)$$

$$K_{ene,nH\leftrightarrow3} = \frac{k_{isom,nH\to3}K_{prot,nH}}{k_{isom,3\to nH}K_{prot,3}} \qquad (7e)$$

These relations can be used to simplify Equation 6a-d to:

$$k_{isom,2\to3}K_{prot,2} = k_{isom,2}K_{prot,2} - k_{isom,2\to23}K_{prot,2} - k_{isom,2\to nH}K_{prot,2} \qquad (8a)$$

$$k_{isom,2\to3}K_{prot,2} = k_{isom,3}K_{prot,3}K_{ene,2\leftrightarrow3} - k_{isom,3\to23}K_{prot,3}K_{ene,2\leftrightarrow3} - k_{isom,3\to nH}K_{prot,3}K_{ene,2\leftrightarrow3} \qquad (8b)$$

$$0 = -k_{isom,23}K_{prot,23}K_{ene,2\leftrightarrow23} + k_{isom,2\to23}K_{prot,2} + k_{isom,3\to23}K_{prot,3}K_{ene,2\leftrightarrow3} \qquad (8c)$$

$$0 = -k_{isom,nH}K_{prot,nH}K_{ene,2\leftrightarrow nH} + k_{isom,2\rightarrow nH}K_{prot,2} + k_{isom,3\rightarrow nH}K_{prot,3}K_{ene,2\leftrightarrow 3} \qquad (8d)$$

Adding Equations 8a to 8d, gives an explicit expression for $k_{isom,2\rightarrow 3}K_{prot,3}$ in terms of the measurable $k_{isom,R}K_{prot,R}$ and $K_{ene,2\leftrightarrow R}$ values for each reactant:

$$k_{isom,2\rightarrow 3}K_{prot,2} = \frac{1}{2}\left(\begin{array}{c} k_{isom,2}K_{prot,2} + k_{isom,3}K_{prot,3}K_{ene,2\leftrightarrow 3} \\ -k_{isom,23}K_{prot,23}K_{ene,2\leftrightarrow 23} - k_{isom,nH}K_{prot,nH}K_{ene,2\leftrightarrow nH} \end{array}\right) \qquad (9)$$

The selectivity to methyl-shift isomerization events relative to those events that vary backbone length (s_{MS}) can then be calculated from $k_{isom,2}K_{prot,2}$ and $k_{isom,2\rightarrow 3}K_{prot,2}$ values:

$$s_{MS} = \frac{r_{isom,2\rightarrow 3}}{r_{isom,2\rightarrow 23} + r_{isom,2\rightarrow nH}} = \frac{k_{isom,2\rightarrow 3}K_{prot,2}}{k_{isom,2}K_{prot,2} - k_{isom,2\rightarrow 3}K_{prot,2}} \qquad (10)$$

Here, $r_{isom,2\rightarrow 3}$, $r_{isom,2\rightarrow 23}$, and $r_{isom,2\rightarrow nH}$ are, respectively, rates of methyl shift, branching, and chain lengthening isomerization events from $2MP^=$.

We conclude that first-order alkene isomerization rate constants measured on POM/SiO$_2$-Pt/Al$_2$O$_3$ mixtures ($k_{isom,R}K_{prot,R}$; Figure 6a) reflect the reactivity of gaseous [R$^=$] species in equilibrium with the reactant alkane at H$^+$. From this mechanistic analysis, we can determine $k_{isom,2\rightarrow 3}K_{prot,2}$ values and selectivities for 3MP formation from 2MP explicitly and also the ratio of methyl shift events to those that lengthen or shorten the backbone (s_{MS}) without the use of measured isomerization selectivities that reflect, in part, transport restrictions of product alkenes within acid domains instead of the rate constants for the formation of *individual* products from measured $k_{isom,R}K_{prot,R}$ values for each reactant. Values of $k_{isom,2\rightarrow 3}K_{prot,2}$ reflect the free energy barrier for forming the transition state that mediates 2MP and 3MP interconversion from gaseous $2MP^=$; these values are used in Section 1.3.3 to assess the effects of acid strength on the stability of such transition states. Values of s_{MS} indicate the tendency for 2MP reactants to methyl shift rather than branch or chain lengthen, thus providing a measure of isomerization product selectivities that is free of transport corruptions. In Section 1.3.4, s_{MS} values determined for POM/SiO$_2$-Pt/Al$_2$O$_3$ mixtures with P, Si, Al, and Co central atoms are used to probe the effects of acid strength on isomerization selectivities.

1.3.2. Mechanistic assessment of the effects of acid strength on isomerization rates

Figure 6a shows $k_{isom,R}K_{prot,R}$ values (in a logarithmic scale) for 2MP, 3MP, 23DMB, and nH reactants on POM/SiO$_2$-Pt/Al$_2$O$_3$ mixtures as a function of DPE values previously reported for POM clusters with P, Si, Al, and Co central atoms [3]. The $k_{isom,R}K_{prot,R}$ value for each hexane isomer reactant decreases exponentially with increasing DPE. POM clusters with fewer protons (and higher-valent central atoms) have more stable conjugate anions and thus smaller DPE values, because the partial charge in protons leads to lower electron density for clusters with fewer protons and, consequently, higher electron affinity. The exponential effects of DPE on rate constants predominantly reflect concomitant effects on activation energies, instead of activation entropies [3,8] because

isomerization TS structures are similar on POM clusters with different central atom [8]. When DPE predominantly influences activation energies, the effects of DPE on $k_{isom,R}K_{prot,R}$ can be expressed in terms of derivatives as:

$$\frac{d\left(\ln\left(k_{isom,R}K_{prot,R}\right)\right)}{d\left(DPE\right)} = \frac{1}{k_{isom,R}K_{prot,R}}\frac{d\left(k_{isom,R}K_{prot,R}\right)}{d\left(DPE\right)} = -\frac{1}{RT}\frac{d\left(E_{A,R}\right)}{d\left(DPE\right)} \tag{11}$$

Here, $E_{A,R}$ is the measured activation barrier for reactant "R". The linear dependence of $\ln(k_{isom,R}K_{prot,R})$ on DPE (Figure 6a) indicates that $d(E_{A,R})/d(DPE)$ values for all hexane isomer reactants are essentially independent of DPE on these POM clusters. The small values of the slopes of the dashed lines in Figure 6a ($d(\ln(k_{isom,R}K_{prot,R}))/d(DPE)$ = -0.03 mol kJ^{-1} for all reactants) and the functional form of Equation 11 indicate that the measured activation energies vary in magnitude much less than the concomitant changes in DPE. Measured activation energies for all hexane isomer reactants were similarly sensitive to changes in DPE ($d(E_{A,R})/d(DPE)$ = 0.11), for which $k_{isom,R}K_{prot,R}$ rate constants vary by about a factor of 4 for each POM composition. Similar sensitivities of $k_{isom,R}K_{prot,R}$ rate constants to changes in DPE for these different isomer reactants that form different sets of isomer products provides qualitative evidence that all isomerization events are similarly-dependent on DPE.

Isomerization leads to multiple products and $k_{isom,R}K_{prot,R}$ is a lumped rate constant reflecting the total rate of isomerization of the gaseous equilibrated alkene lump for reactant "R" to each individual product "P" with rate constant $k_{isom,R\rightarrow P}K_{prot,R}$ (Eq. 6a-d). Therefore, the effects of DPE on $k_{isom,R}K_{prot,R}$ are given by the summation of those on $k_{isom,R\rightarrow P}K_{prot,R}$ rate constants for each product "P" of reactant "R":

$$\frac{d\left(k_{isom,R}K_{prot,R}\right)}{d\left(DPE\right)} = \sum_P \frac{d\left(k_{isom,R\rightarrow P}K_{prot,R}\right)}{d\left(DPE\right)} \tag{12}$$

Equation 11 and equations analogous to Equation 11 that describe the effects of DPE on each $k_{isom,R\rightarrow P}K_{prot,R}$ rate constant may be solved implicitly for each of the derivatives in Equation 12. Filling these solutions into Equation 12 shows that measured $d(E_{A,R})/d(DPE)$ values are given by the rate-average (or selectivity-average) of those for each isomer product that a reactant forms:

$$\frac{d\left(E_{A,R}\right)}{d\left(DPE\right)} = \frac{\sum_P k_{isom,R\rightarrow P}K_{prot,R}\dfrac{d\left(E_{A,R\rightarrow P}\right)}{d\left(DPE\right)}}{k_{isom,R}K_{prot,R}} = \sum_P S_{R\rightarrow P}\frac{d\left(E_{A,R\rightarrow P}\right)}{d\left(DPE\right)} \tag{13}$$

Here, $E_{A,R\rightarrow P}$ is the activation barrier to form the TS that gives the isomer product "P" from reactant "R" and $S_{R\rightarrow P}$ is the selectivity to isomer product "P" from reactant "R". According to Equation 13, $d(E_{A,R})/d(DPE)$ values that are similar for each reactant and essentially independent of DPE require the stability of all isomerization TS to be similarly sensitive to DPE (with $(E_{A,R\rightarrow P})/d(DPE)$=0.11 for all kinetically relevant isomerization steps). Such

similar sensitivities would lead, in turn, to isomerization selectivities ($S_{R \to P}$) that cannot depend on DPE (and acid strength) for acid POM clusters.

The relative stabilities of the ensembles of TS structures that mediate the isomerizations between 2MP, 3MP, 23DMB, and nH reactants cannot be compared directly from their $E_{A,R}$ values because these activation energies are referenced to different reactants. The gaseous alkene reactant lumps ($[R^=]$) have different gas-phase stabilities related to the equilibrium constant for the formation of the given equilibrated $[R^=]$ lump from a common reference equilibrated lump. In the context of transition state theory, $k_{isom,R \to P}K_{prot,R}$ values reflect free energy barriers ($\Delta G^{\ddagger}_{R \to P}$) given by the difference between the free energies for the TS that mediates the conversion of "R" to "P" (or "P" to "R", $G^{\ddagger}_{P \leftrightarrow R}$) and for the gaseous alkene reactant lump ($G_{ene,R}$):

$$\Delta G^{\ddagger}_{R \to P} = G^{\ddagger}_{R \leftrightarrow P} - G_{ene,R} = -RT \ln \left(\frac{h}{k_B T} k_{isom,R \to P} K_{prot,R} \right) \tag{14}$$

Here, k_B and h are the Boltzmann and Planck constants, respectively. Free energy barriers calculated in this manner using $k_{isom,R}K_{prot,R}$ rate constants ($\Delta G^{\ddagger}_R$) can be related to those for each product formed using the functional form of Eq. 3b for the given reactant "R" and Equation 14 (shown in Scheme 3 for 2MP, 3MP and 23DMB reactants):

$$\Delta G^{\ddagger}_R = -RT \ln \left(\sum_P \exp \left(\frac{-\left(G^{\ddagger}_{R \leftrightarrow P} - G_{ene,R} \right)}{RT} \right) \right) = -RT \ln \left(\frac{h}{k_B T} k_{isom,R} K_{prot,R} \right) \tag{15}$$

Here, $\Delta G^{\ddagger}_R$ accounts for the additive contributions of all TS to measured $k_{isom,R}K_{prot,R}$ values. The free energy difference between the gaseous alkene lump ($[R^=]$) species and the gaseous 2MP$^=$ ($\Delta G_{ene,2 \leftrightarrow R}$) can be added to both sides of Equation 15 to make all TS energies relative to the same reference state (gaseous 2MP$^=$):

$$\Delta G^{\ddagger}{}'_R = \Delta G^{\ddagger}_R + \Delta G_{ene,2 \leftrightarrow R} = -RT \ln \left(\sum_P \exp \left(\frac{-\left(G^{\ddagger}_{R \leftrightarrow P} - G_{ene,2} \right)}{RT} \right) \right) \tag{16}$$

In this case, $\Delta G^{\ddagger}{}'_R$ is the free energy barrier for the ensemble of TS accessible to reactant "R" referenced to gaseous 2MP$^=$ (shown in Scheme 3 for 2MP$^=$, 3MP$^=$ and 23DMB$^=$ reactants) and $G_{ene,2}$ is the free energy for the gaseous 2MP$^=$. We can then compare $\Delta G^{\ddagger}{}'_R$ values for each reactant to those for 2MP by taking the ratio of the isomerization rate constant for each reactant isomer ($k_{isom,R}K_{prot,R}$) (normalized by the equilibrium constant for forming the gaseous reactant alkene lump $[R^=]$ from gaseous 2MP$^=$ ($K_{ene,2 \leftrightarrow R}$)) to the isomerization rate constant for 2MP ($k_{isom,2}K_{prot,2}$):

$$\alpha_{R,2} = \frac{k_{isom,R} K_{prot,R} K_{ene,2 \leftrightarrow R}}{k_{isom,2} K_{prot,2}} = \exp \left(\frac{-\left(\Delta G^{\ddagger}{}'_R - \Delta G^{\ddagger}_2 \right)}{RT} \right) \tag{17}$$

The value of $\alpha_{R,2}$ reflects the free energy difference between that for the isomerization TS structures accessible to reactant "R" and that for the TS structures accessible to $2MP^=$, thus providing a rigorous assessment of the relative stability of the two ensembles of transition states ($\Delta G^{\ddagger}{}'_R$ - $\Delta G^{\ddagger}_2$). The $\alpha_{R,2}$ values determined for 3MP, 23DMB and nH reactants are essentially independent of DPE on W-POM acids with different central atoms (Figure 6b) because $k_{isom,R}K_{prot,R}$ values for each alkane reactant depend similarly on acid strength. Values of $\alpha_{R,2}$ are near unity for 3MP because 2MP and 3MP predominantly form each other during their respective isomerization reactions via the same transition state. The $\alpha_{R,2}$ values for 23DMB and nH reactants are much smaller than unity (0.20 ± 0.02 and 0.068 ± 0.008 for 23DMB and nH, respectively) because the transition states for chain lengthening and shortening (the predominant isomerization events for 23DMB and nH reactants, respectively) are less stable than those that mediate methyl shifts (the predominant isomerization event for 2MP reactants). Equation 17 indicates gives free energy barrier differences that indicate free energy barriers are 6.3 ± 0.4 kJ mol^{-1} and 10.5 ± 0.4 kJ mol^{-1} lower for 2MP isomerization than for 23DMB and nH isomerization, respectively.
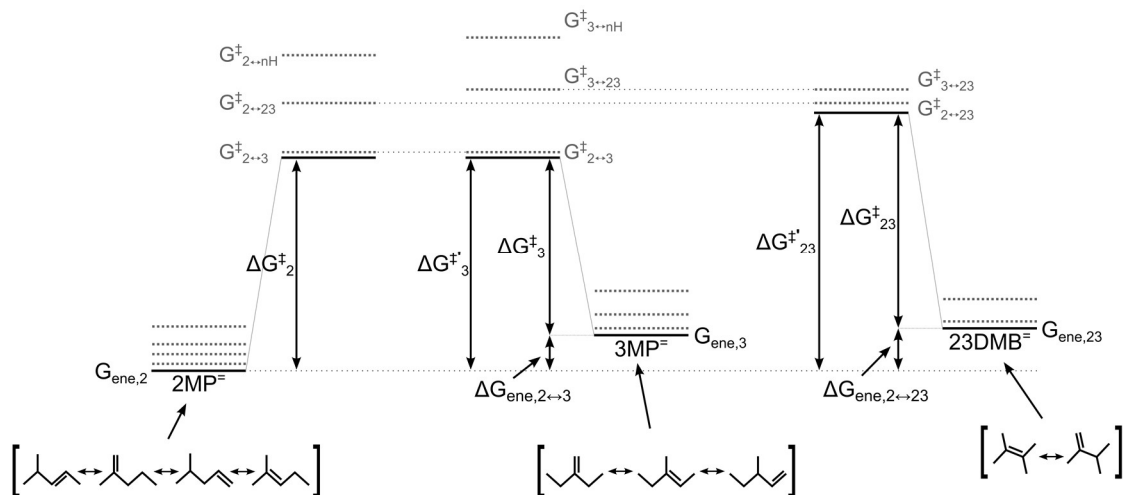
Scheme 3. Reaction coordinate diagram depicting the free energies of $2MP^=$ ($G_{ene,2}$), $3MP^=$ ($G_{ene,3}$), and $23DMB^=$ ($G_{ene,23}$) regioisomer isomer groups and the free energies of the isomerization transition states accessible to each of these groups ($2MP^=$: $G^{\ddagger}_{2\leftrightarrow3}$, $G^{\ddagger}_{2\leftrightarrow23}$, and $G^{\ddagger}_{2\leftrightarrow nH}$; $3MP^=$: $G^{\ddagger}_{2\leftrightarrow3}$, $G^{\ddagger}_{3\leftrightarrow23}$ and $G^{\ddagger}_{3\leftrightarrow nH}$; $23DMB^=$: $G^{\ddagger}_{2\leftrightarrow23}$ and $G^{\ddagger}_{3\leftrightarrow23}$). Free energy barriers for $k_{isom,2}K_{prot,2}$ ($\Delta G^{\ddagger}_2$), $k_{isom,3}K_{prot,3}$ ($\Delta G^{\ddagger}_3$), $k_{isom,23}K_{prot,23}$ ($\Delta G^{\ddagger}_{23}$), $k_{isom,3}K_{prot,3}K_{ene,2\leftrightarrow3}$ ($\Delta G^{\ddagger}{}'_3$), and $k_{isom,23}K_{prot,23}K_{ene,2\leftrightarrow23}$ ($\Delta G^{\ddagger}{}'_{23}$) and free energy differences for $K_{ene,2\leftrightarrow3}$ ($\Delta G_{ene,2\leftrightarrow3}$) and $K_{ene,2\leftrightarrow23}$ ($\Delta G_{ene,2\leftrightarrow23}$) are also shown.
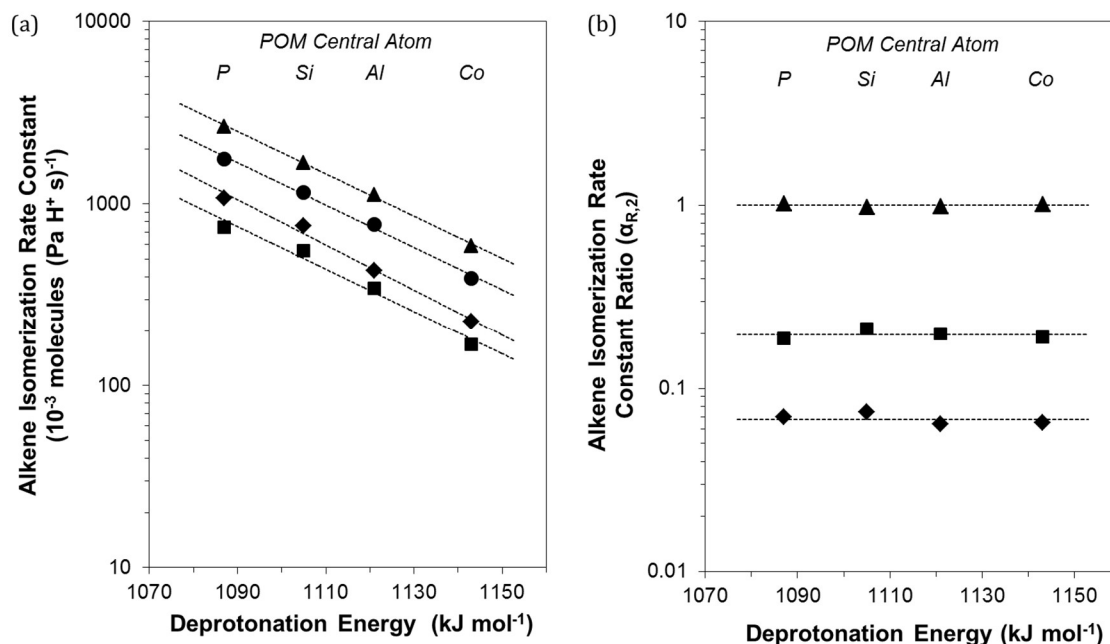
Figure 6. (a) Alkene isomerization rate constants ($k_{isom,R}K_{prot,R}$) for ($\bullet$) 2-methylpentane, ($\blacktriangle$) 3-methylpentane, ($\blacksquare$) 2,3-dimethylbutane, and ($\blacklozenge$) n-hexane reactants and (b) $k_{isom,R}K_{prot,R}K_{ene,2\leftrightarrow R}/k_{isom,2}K_{prot,2}$ ratios for ($\blacktriangle$) 3-methylpentane, ($\blacksquare$) 2,3-dimethylbutane, and ($\blacklozenge$) n-hexane reactants as functions of deprotonation energy for $H_{8-n}X^{n+}W_{12}O_{40}$ (X = P, Si, Al, Co) (473 K). The dashed lines in (a) are exponential fits of the data to deprotonation energies for Keggin clusters and in (b) are the averages of the data for each ratio.

1.3.3. Mechanistic assessment of the effects of acid strength on isomerization transition state energies

The following discussion assesses calculated $k_{isom,2\rightarrow3}K_{prot,2}$ values (Eq. 9) mechanistically, then further analyzes their values in more detail using thermochemical cycles. In doing so, we seek to probe how specific catalyst properties determine the stability of *individual* isomerization transition states and what causes the significant attenuation of DPE effects on activation barriers for such transition states. Figure 7 shows values of $k_{isom,2\rightarrow3}K_{prot,2}$, calculated from $k_{isom}K_{prot,R}$ values using the functional form of Equation 9, for 2MP, 3MP, 23DMB, and nH reactant on POM clusters with P, Si, Al, and Co central atoms as a function of their DPE. The slope of the dashed line for the $k_{isom,2\rightarrow3}K_{prot,2}$ data in Figure 7 ($d(\ln(k_{isom,2\rightarrow3}K_{prot,2}))/d(DPE)$= -0.03 mol kJ^{-1}) is much smaller than unity, indicating, according to an equation analogous to Equation 11 describing the effects of DPE on $k_{isom,2\rightarrow3}K_{prot,2}$, that activation barriers for methyl shift isomerization transition states differ in energy among catalysts much less than their concomitant changes in DPE ($d(E_{A,2\rightarrow3})/d(DPE) = 0.11 < 1$). Scheme 4 shows the reaction coordinate for 2MP$^=$ (shown as 2-methylpent-2-ene as the example) conversion to 3MP$^=$ and the energies that determine the activation barrier reflected in its lumped kinetic parameter ($k_{isom,2\rightarrow3}K_{prot,2}$). Activation energies for $k_{isom,2\rightarrow3}K_{prot,2}$ include the energies to protonate the lumped gaseous 2MP$^=$ species by reaction with protons at POM Brønsted acid sites (E_{prot} in Scheme 4) and to rearrange 2MP* species to form the transition state that mediates methyl shifts for the

23

equilibrated mixtures of adsorbed alkoxides ($E_{isom,3MP}$ in Scheme 4). Thermochemical cycles are used next to dissect these methyl shift activation energies into those for a sequence of hypothetical steps, for which experiments or calculations can provide accurate energies, using a formalism previously applied to alkanol dehydration [3,7] and n-hexane isomerization [8] reactions on solid acids.
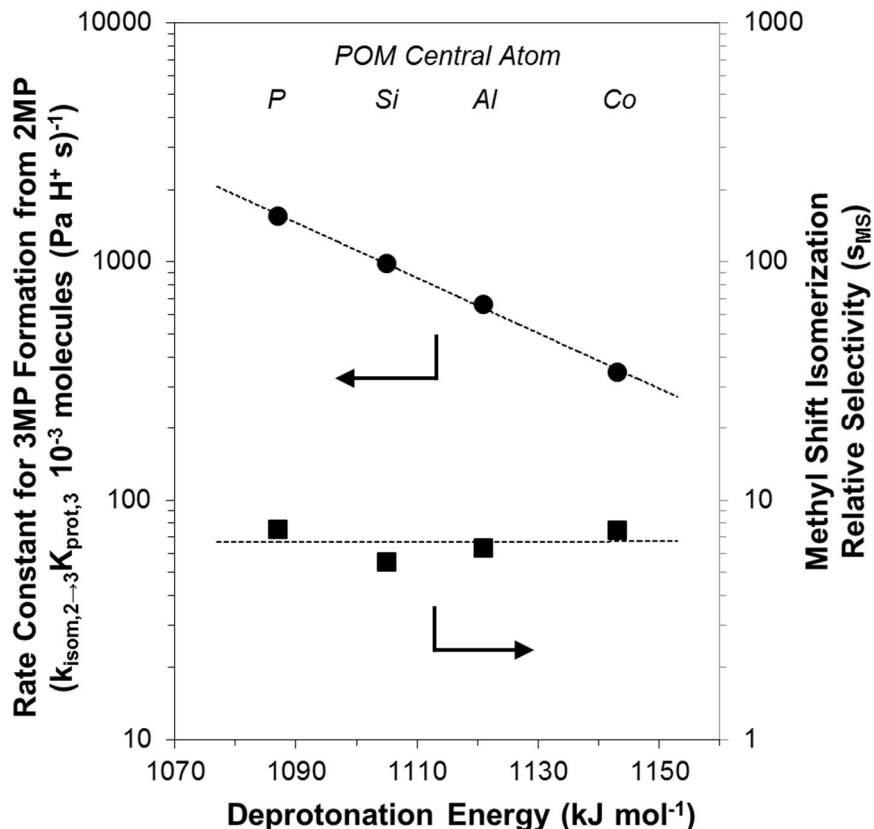
Figure 7. Rate constants for 2-methylpentene isomerization to 3-methylpentene ($k_{isom,2\rightarrow3}K_{prot,2}$, ●) and selectivities for methyl shift isomerization events relative to isomerization events that vary backbone length (s_{MS}, ■) at 473 K as a function of deprotonation energy for $H_{8-n}X^{n+}W_{12}O_{40}$ (X = P, Si, Al, Co). The dashed lines are an exponential fit of $k_{2\rightarrow3}$ values to deprotonation energies and the average of s_{MS} values for Keggin clusters.

A thermochemical cycle that converts gaseous $2MP^=$ species into the methyl shift transition state (Scheme 4) involves deprotonation (DPE) of the POM clusters by overcoming interactions of H^+ with conjugate anion, formation of gaseous cycloalkyl carbenium ions resembling the TS cation (structure resembles Scheme 4 (A) for 2MP-3MP interconversion) by reactions of gaseous H^+ and $2MP^=$ ($E_{gas,2\rightarrow3}$), and the interaction energy between the gaseous TS cations and the conjugate anion of the POM solid acid at the TS ($E_{int,2\rightarrow3}$):

$$E_{A,2\rightarrow3} = DPE + E_{gas,2\rightarrow3} + E_{int,2\rightarrow3}$$

(18)

24

Here, DPE and $E_{int,2\rightarrow3}$ reflect ion-pair interactions of H^+ and TS cation, respectively, with the same POM anion. Such interactions typically involve an ionic component reflecting classical electrostatic interactions between ions, when they approach each other, and a covalent component reflecting structural and electronic relaxation induced by ions in close proximity with each other [9]. The $E_{gas,2\rightarrow3}$ value is the energy required to form the gaseous analog of the relevant cycloalkyl carbenium ion transition state ($[C_6H_{13}^{\ddagger}]^+_{(g)}$) from gaseous $2MP^=$ and a free gaseous H^+:

$$2MP^=_{(g)} + H^+_{(g)} \rightarrow \left[C_6H_{13}^{\ddagger} \right]^+_{(g)} \tag{19}$$
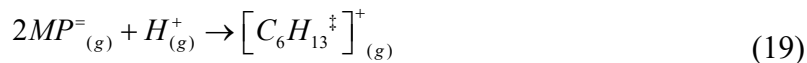
The sensitivity of each energy term in the thermochemical cycle (Eq. 18) to DPE ultimately accounts for the observed effects of DPE on $k_{isom,2\rightarrow3}K_{prot,2}$ values (Figure 7):

$$\frac{d\left(E_{A,2\rightarrow3} \right)}{d\left(DPE \right)} = 1 + \frac{d\left(E_{int,2\rightarrow3} \right)}{d\left(DPE \right)} \tag{20}$$

The term for $d(E_{gas,2\rightarrow3})/d(DPE)$ is absent in Equation 20 (even though it appears in Equation 18), because $E_{gas,2\rightarrow3}$ is a property of the gaseous species (Eq. 19) and thus unaffected by the identity or DPE of the acid catalyst. Activation energies of methyl shift isomerizations ($E_{A,2\rightarrow3}$) increase less than the commensurate changes in DPE because interactions between the conjugate anion and cationic moieties at TS recover a large fraction of the additional energy needed to deprotonate weaker acids, as also shown previously for acid catalyzed reactions that are mediated by ion-pair transition states [3,7]. Thus, weaker acids have larger DPE values and more negative values of $E_{int,2\rightarrow3}$ that offset each other in activation energies.
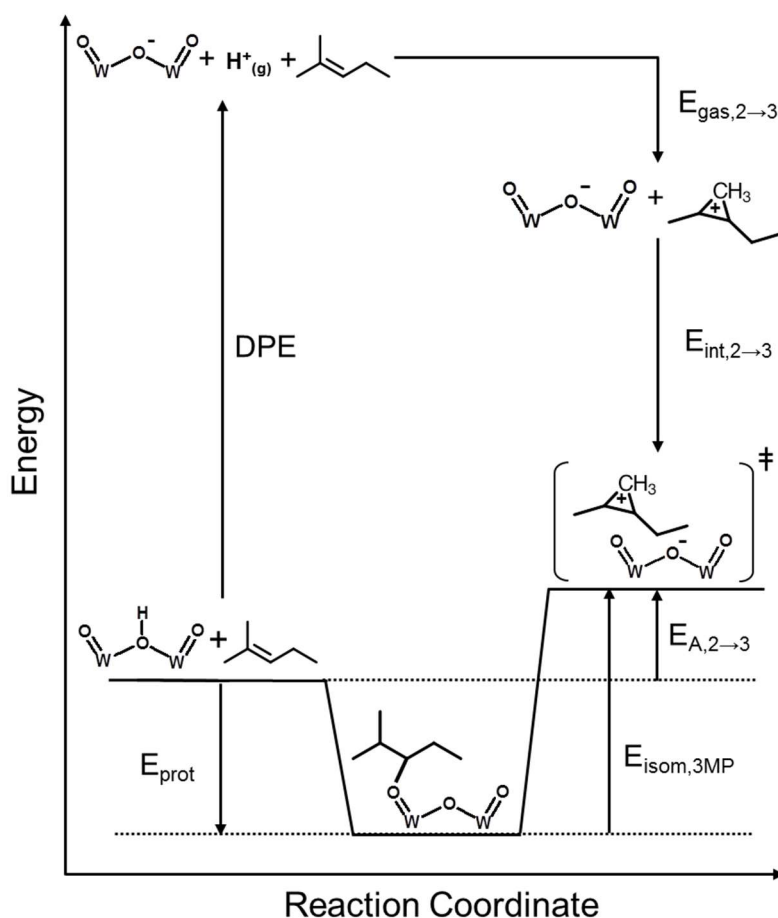
Scheme 4. Thermochemical cycle accounting for activation energies of Brønsted acid-catalyzed isomerization reactions (shown for 3MP products). Activation energies of $k_{isom,2 \to 3}K_{prot,2}$ ($E_{A,2 \to 3}$) are the sum of the intrinsic isomerization activation energies ($E_{isom,3MP}$) and 2-methylpentene protonation energies at the acid site (E_{prot}). $E_{A,2 \to 3}$ values depend on catalyst deprotonation energies (DPE), gas-phase protonation of the alkene to form the gaseous analog of the transition state ($E_{gas,2 \to 3}$), and transition state interaction energies ($E_{int,2 \to 3}$).

Mechanistic assessments of rate constants for the formation of other *individual* isomerization products from $2MP^=$ or any of the other alkenes ($k_{isom,R \to P}K_{prot,R}$) lead to similar thermochemical cycles and consequently to equations similar to that for $k_{isom,2 \to 3}K_{prot,2}$ (Eq. 20). The replacement of the $d(E_{A,R \to P})/d(DPE)$ term in Equation 13 with equations analogous to Equation 20 for each hexane isomer shows that the attenuation of the effects of DPE on the activation barriers ($d(E_{A,R})/d(DPE) < 1$) for $k_{isom,R}K_{prot,R}$ rate constants ($E_{A,R}$) reflect the selectivity-average of those for $k_{isom,R \to P}K_{prot,R}$ for each reactant

$$\frac{d\left(E_{A,R}\right)}{d\left(DPE\right)} = 1 + \sum_P \frac{k_{isom,R \to P}K_{prot,R}}{k_{isom,R}K_{prot,R}} \frac{d\left(E_{int,R \to P}\right)}{d\left(DPE\right)} = 1 + \sum_P S_{R \to P} \frac{d\left(E_{int,R \to P}\right)}{d\left(DPE\right)} \qquad (21)$$

Here, $E_{int,R \to P}$ values reflect the ionic and covalent interactions between the conjugate anion and the TS that is kinetically relevant for the conversion of each reactant "R" to each product "P" and $S_{R \to P}$ is the selectivity to isomer product "P" from reactant "R". The linear dependence of $\ln(k_{isom,R}K_{prot,R})$ on DPE (Figure 6a) indicates, according to the functional form of Equation 11, that $d(E_{A,R})/d(DPE)$ values and, in turn, the right side of Equation 21 are similar for all hexane isomer reactants and essentially independent of DPE on these POM clusters. These results suggests that $E_{int,R \to P}$ values for all the transitions states that interconvert all hexene isomers depend similarly on DPE (with $d(E_{int,R \to P})/d(DPE)=-0.89$ for every one of the isomerization reactions); consequently, isomerization selectivities ($S_{R \to P}$) are independent DPE on these POM clusters. The factors responsible for such similar DPE effects on selectivities are discussed in the next section.

1.3.4. Mechanistic assessment of the effects of acid strength on isomerization selectivities

In this section, calculated s_{MS} values for 2MP reactants (Eq. 10) are assessed mechanistically, and then analyzed in more detail using the thermochemical cycles of Section 1.3.3. Figure 7 shows measured s_{MS} values for 2MP reactants on POM/SiO$_2$-Pt/Al$_2$O$_3$ mixtures (P, Si, Al, Co central atoms) as a function of their DPE values. Values of s_{MS} were greater than unity and essentially independent of DPE on these POM mixtures, having a mean value of 6.7 ± 1.5 (95% confidence interval). Such s_{MS} values greater than unity suggest that the cycloalkyl carbenium ion transition states that form 23DMB and nH from 2MP reactants (Scheme 4 (B) and (C), respectively) are less stable than those that form 3MP from 2MP reactants (Scheme 4 (A)), consistent with lower DFT-derived activation barriers for reactions on an aluminosilicate site that form 3-methyl-2-pentene from 2-methylpent-2-ene (71 kJ/mol) [27] than those forming 2,3-dimethyl-2-butene from 2-methylpent-2-ene (117 kJ/mol) [27].
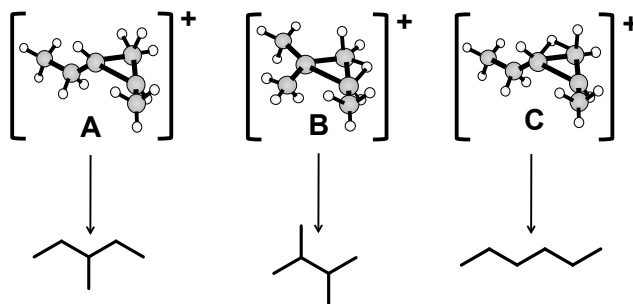
Scheme 5. Proposed cyclopropyl carbenium ions at isomerization transition states forming (A) 3-methylpentane, (B) 2,3-dimethylbutane, and (C) n-hexane [27]. 3-Methylpentane transition states involve cleavage and formation of C-C bonds to shift the methyl group along the hydrocarbon backbone. 2,3-Dimethylbutane and n-hexane transition states involve concerted cleavage and formation of C-C and C-H bonds to rearrange the hydrocarbon backbone.

The significant role of $E_{gas,R \to P}$ in determining the magnitude of activation energies (Eq. 18), but not their dependence on DPE (Eq. 20), indicates that reactions that are more

demanding (i.e., have larger activation energies) do not necessarily sense acid strength more strongly (i.e., exhibit a larger slope with DPE). The effects of acid strength on isomerization selectivities reflect only the relative ability of these cationic transition states to recover differences in DPE among acids through concomitant changes in their interaction energies with the conjugate anions of these acids. "Proton-like" transition states with localized positive charges that can closely approach the anion interact more strongly with the anion, which leads to weaker DPE effects on their activation energies than that of larger transition states with more diffuse positive charges.

When pre-exponential factors are essentially independent of DPE (Section 1.3.2), the effects of DPE on s_{MS} values is given by:

$$\frac{d\left(\ln\left(s_{MS}\right)\right)}{d\left(DPE\right)} = -\frac{1}{RT}\left(\frac{d\left(E_{int,2\to3}\right)}{d\left(DPE\right)} - \frac{d\left(E_{int,2\to23+nH}\right)}{d\left(DPE\right)}\right) \tag{22}$$

because DPE effects on isomerization activation barriers depend only on the concomitant effects on transition state interaction energies (Eq. 17). Here, $E_{int,2\to23+nH}$ is the rate-averaged interaction energy for the transition states that mediate nH and 23DMB formation from 2MP defined by:

$$E_{int,2\to23+nH} = \frac{k_{isom,2\to23}}{k_{isom,2\to23}+k_{isom,2\to nH}}E_{int,2\to23} + \frac{k_{isom,2\to nH}}{k_{isom,2\to23}+k_{isom,2\to nH}}E_{int,2\to nH} \tag{23}$$

The s_{MS} values are essentially independent of DPE (Figure 7), indicating that interaction energies are similarly sensitive to changes in DPE for the transition states that mediate methyl shift, branching, and chain lengthening isomerizations events ($d(E_{int,2\to3})/d(DPE)=d(E_{int,2\to23+nH})/d(DPE)=-0.89$ in Eq. 22). The similar amount and location of cationic charge at these TS causes them to recover a similar fraction of the DPE changes among these clusters. In such cases, the specific kinetic hurdles for a given isomerization event (reflected in the magnitude of $E_{gas,R\to P}$ for that reaction in Eq. 18) does not influence how this activation barrier varies with acid strength.

This mechanistic analysis shows that s_{MS} values rigorously reflect the differences in free energy barriers between TS that shift the methyl group and those that vary backbone length of 2MP reactants, and, as a result, provide a probe of *primary* product selectivities (defined as those formed from reactant alkenes in one surface sojourn) free of transport artifacts. The value of s_{MS}, or the tendency of alkenes with 2MP backbones to form alkenes with 3MP, nH, or 23DMB backbones, is unaffected by the DPE, and thus the acid strength, of POM clusters because of the similar amount and localization of cationic charge at all isomerization TS. In such cases, acid strength alone cannot be used to improve the selective isomerization to any one of these hexane isomers from a given reactant, nor can it be used for any other conversion where TS cations in competing pathways have similar charge amount and localization.

1.4. Conclusions

The effects of acid strength on reactivity and selectivity are demonstrated using 2-methylpentane (2MP), 3-methylpentane (3MP), 2,3-dimethylbutane (23DMB), and n-hexane (nH) isomerization routes on well-defined solid Brønsted acids in mixtures with Pt/Al_2O_3 co-catalysts. Fast dehydrogenation-hydrogenation reactions at Pt sites equilibrate alkanes and all alkene isomers of a given backbone structure at these sites providing a low and constant concentration of alkenes that disfavor oligomerization reactions at acid sites that can lead to catalyst deactivation. Alkenes isomerize to one another through alkoxide backbone rearrangements at acid sites via similar elementary steps and with similar rate expressions. Alkene isomerization rate constants for each hexane isomer ($k_{isom,R}K_{prot,R}$) were measured on Keggin polyoxometalate (POM) clusters using mechanism-based interpretations of rate data and titrations that count the number of reactive H^+. These rate constants reflect the stabilities of cycloalkyl carbenium ion transition states, which mediate kinetically-relevant alkoxide isomerization steps, relative to an equilibrated lump of gaseous reactant alkenes and unoccupied sites; rate constants decrease exponentially with increasing deprotonation energies (DPE) on Keggin POM for all reactants because ion-pair transition states contain less stable conjugate anions on weaker acids. Such transition states attenuate changes in DPE on activation barriers because interactions between the conjugate anion and cationic moieties at these transition states recover most of the additional energy needed to deprotonate weaker acids, resulting in large changes in DPE having relatively small impacts on activation energies ($d(E_{A,R})/d(DPE) = 0.11$).

Measured selectivities reflected, in part, transport restrictions of product alkenes within acid domains instead of the rate constants for the formation of *individual* products from each reactant. In such cases, selectivities to isomerization products formed from reactant-derived alkenes after only a single sojourn at an acid site cannot be estimated directly from measured selectivities, because secondary interconversions of alkene products are similar in rates to their hydrogenation, both locally within acid domains via hydrogen transfer from alkane reactants or via reactions with H_2 after their diffusion through such acid domains to reach Pt sites. The rate constant for the formation of 3MP from 2MP reactants, and consequently the 2MP isomerization selectivity to 3MP and the ratio of this to that for isomerization products that vary backbone length (s_{MS}), were determined explicitly, without the use of measured product selectivities, from mechanism-based interpretations of measured turnover rates for all hexane isomer reactants on each catalyst mixture. Determined s_{MS} values and, consequently, the tendency for alkenes to methyl-shift, branch, or chain lengthen were unaffected by the DPE, and thus the acid strength, of POM clusters because of the similar amount and localization of cationic charge at all isomerization transition states.

These findings show unequivocally that the demanding or facile nature of a given reaction, which is a property of the stability of the organic cations at ion pair transition states, is not necessarily relevant to how these catalytic reactions "sense" acid strength changes; this depends on the amount and localization of cationic charge at such transition states. These concepts suggest changing acid strength will lead to more selective conversions of reactant mixtures only when competing pathways are mediated by transition states with different amount or localization of cationic charge, thus showing that

isomerization selectivities, often used to assess acid strength, are inappropriate probes of acid strength in the context proposed by, and used in, the previous literature. Although shown here for isomerization reactions, these concepts apply in general to reactions mediated by ion-pairs at transition states.

1.5. Tables

Table 1. Number of accessible H^+ per POM cluster measured by chemical titration with 2,6-di-*tert*-butylpyridine[a] during 2-methylpentane isomerization[b] on $HXW_{12}O_{40}/SiO_2$-Pt/Al_2O_3 (X = P, Si, Al, Co) mixtures.

Catalyst	POM Content (% wt.)	POM Surface Density (POM nm^{-2})	Accessible H^+ (per POM)
$H_3PW_{12}O_{40}$	5	0.04	0.72^c, 0.73^d, 1.1^e
$H_3PW_{12}O_{40}$	25	0.20	1.6
$H_4SiW_{12}O_{40}$	5	0.04	1.6
$H_5AlW_{12}O_{40}$	5	0.04	1.45
$H_6CoW_{12}O_{40}$	5	0.04	0.25

[a] Assuming a 1:1 DTBP:H^+ adsorption stoichiometry
[b] 1.9 kPa 2-methylpentane, 75 kPa H_2, 473 K
[c] Pt_S/H^+ = 11.7
[d] Pt_S/H^+ = 6.2
[e] Pt_S/H^+ = 22.9

Table 2. 2-Methylpentane isomerization rate constants ($k_{isom,2}K_{prot,2}$ and $k_{isom,2}$) and protonation equilibrium constants ($K_{prot,2}$) measured on $HXW_{12}O_{40}/SiO_2$-Pt/Al_2O_3 (X = P, Si, Al, Co) mixtures (473 K)

Catalyst	$k_{isom,2}K_{prot,2}$[a,d]	$k_{isom,2}$[b,d]	$K_{prot,2}$[c,d]
$H_3PW_{12}O_{40}$	1759 ± 5	1200 ± 170	1.5 ± 0.2
$H_4SiW_{12}O_{40}$	1159 ± 9	1100 ± 1300	1.0 ± 1.2
$H_5AlW_{12}O_{40}$	771 ± 4	187 ± 11	4.1 ± 0.2
$H_6CoW_{12}O_{40}$	393 ± 3	108 ± 14	3.6 ± 0.5

[a] 10^{-3} molecules (Pa H^+ s)$^{-1}$
[b] 10^{-3} molecules (H^+ s)$^{-1}$
[c] Pa^{-1}
[d] Errors represent the 95% confidence intervals of parameter in Eq. 4 obtained from the method of least-squares.

Table 3. 3MP, 23DMB, and nH isomerization rates measured on H_3PW/SiO_2-Pt/Al_2O_3 mixtures

Surface Density (POM nm^{-2})	Pt_s/H^+ Ratio	3MP Turnover Rate[a,b]	23DMB Turnover Rate[a,b]	nH Turnover Rate[a,b]
0.04	11.7	75	32	7.5
0.04	22.9	80	30	9.4
0.25	10.5	73	32	7.2

[a] 10^{-3} molecules (H^+ s)$^{-1}$
[b] 1.9 kPa alkane, 75 kPa H_2, 473 K

1.6. Supporting Information

1.6.1. MAS-^{31}P-NMR of silica-supported $H_3PW_{12}O_{40}$

Solid-state MAS-^{31}P-NMR spectra of SiO_2-supported $H_3PW_{12}O_{40}$ (H_3PW/SiO_2) were recorded on a Bruker DSX-500 spectrometer equipped with a Bruker 4mm CPMAS probe. Samples were loaded into a ZrO_2 rotor at ambient conditions and spun at 14 kHz at ambient temperature. An operating frequency of 202.2 MHz was used for ^{31}P nuclei and small angle rf pulses (1 ms-15 degree) were used with a recycle time of 100 s because of the long spin-lattice relaxation of ^{31}P nuclei in Keggin clusters. MAS-^{31}P-NMR signals were also examined with delay times up to 3000 s to check for the presence of slow relaxing components. Chemical shifts are referenced to 85% H_3PO_4 for ^{31}P nuclei.

The MAS-^{31}P-NMR spectrum of $H_3PW_{12}O_{40}/SiO_2$, prepared by the methods described in Section 1.2.1, is shown in Figure S.1. This spectrum has a single sharp peak located at -14.9 ppm. The chemical shift of this peak is in excellent agreement with the ^{31}P nucleus signal for Keggin $[PW_{12}O_{40}]^{3-}$ anions in the aqueous-phase ($\delta(^{31}P) = -14.9$ ppm) [32]. There are also no peaks at chemical shifts that have been reported for non-Keggin (Wells-Dawson $[P_2W_{18}O_{62}]^{6-}$, $\delta(^{31}P) = -12.7$ ppm) [**SError! Bookmark not defined.**] or lacunary Keggin ($[PW_{11}O_{39}]^{7-}$, $\delta(^{31}P) = -10.4$ ppm) structures. Thus, we conclude that the Keggin structure persists on the silica support and is not degraded during grafting procedures.
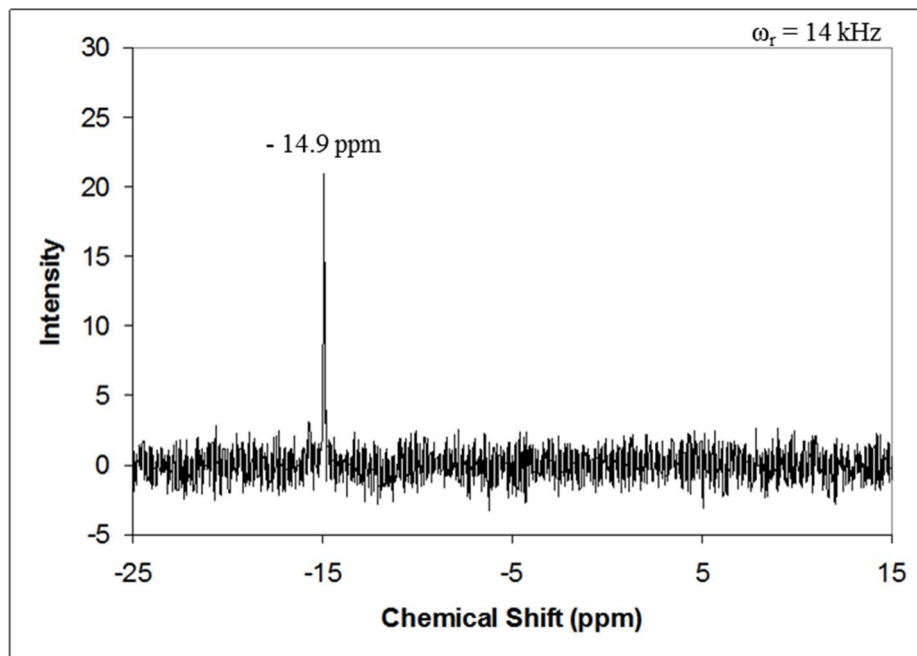
Figure S.1. MAS-^{31}P-NMR of 0.04 POM nm^{-2} $H_3PW_{12}O_{40}/SiO_2$ referenced to 85 wt% H_3PO_4.

1.6.2. Transmission Electron Micrographs (TEM) of silica-supported $H_4SiW_{12}O_{40}$

TEM samples were prepared by grinding $H_4SiW_{12}O_{40}/SiO_2$ (as prepared in Section 2.1) into a fine powder (< 50 μm) using a mortar and pestle. Approximately 0.002 g of powder was suspended in 1 cm^3 of CHCl$_3$ (Sigma-Aldrich, >99%) by sonication for 1 min before evaporating the mixture onto an ultrathin carbon film on a 400 mesh copper TEM grid (Ted Pella, Inc.). TEM images were obtained on FEI Tecnai 12 (120 kV accelerating voltage, bright field) transmission electron microscope using an internal charge-coupled device (CCD) camera. Figure S.2 shows a typical TEM image of $H_4SiW_{12}O_{40}$ (small dark circular features approximately 1-5 nm in diameter) supported on amorphous silica particles (medium gray) at 0.04 POM nm^{-2} surface density. The size of these features relative to the diameter of a single Keggin cluster (~1.2 nm) indicates that supported POM clusters exist as isolated clusters or as small aggregates (< 15 POM clusters). Edges of silica particles do not reveal large multi-layer structures; thus, small aggregates of clusters are only two-dimensional.
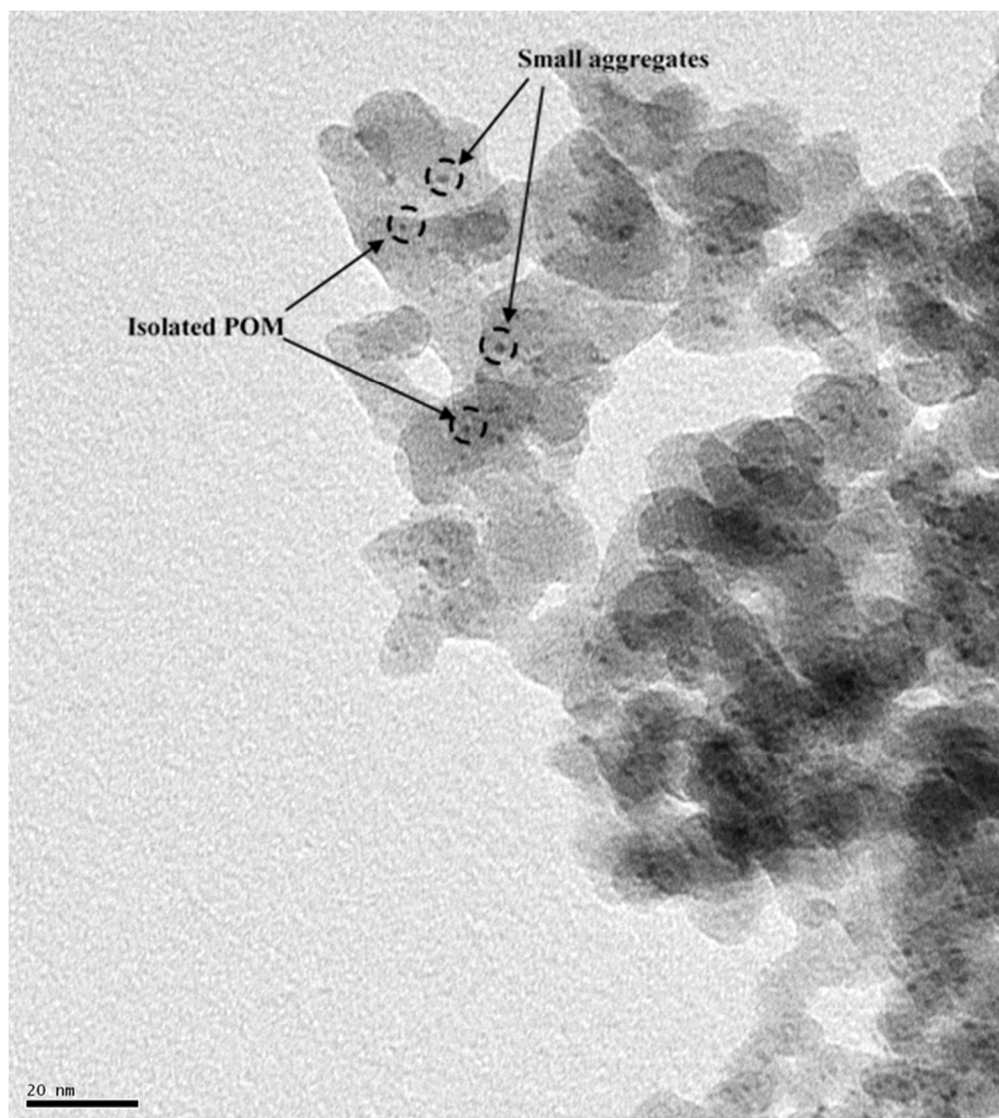
Figure S.2. Transmission electron micrograph of 0.04 POM nm^{-2} H$_4$SiW$_{12}$O$_{40}$/SiO$_2$. Dark circular features are isolated or small two-dimensional aggregates of Keggin POM on the silica support, examples of which are indicated in the micrograph.

1.6.3. Effects of space velocities on 2-methylpentane and 3-methylpentane isomerization rates

Figure S.3 shows ratios of 2,3-dimethylbutane (23DMB), n-hexane (nH), and 2,2-dimethylbutane (22DMB) formation rates to formation rates for 3-methylpentane (3MP) (per POM) as a function of 2-methylpentane (2MP) conversion (2 – 20%) on H$_3$PW/SiO$_2$-Pt/Al$_2$O$_3$ (Pt$_s$/H$^+$ = 1). All ratios decreased with decreasing 2MP conversion indicating a decrease in the extent of secondary reactions between 3MP and the other products. 22DMB ratios nearly extrapolate to zero at low conversions, indicating that it is formed almost exclusively by secondary isomerizations.
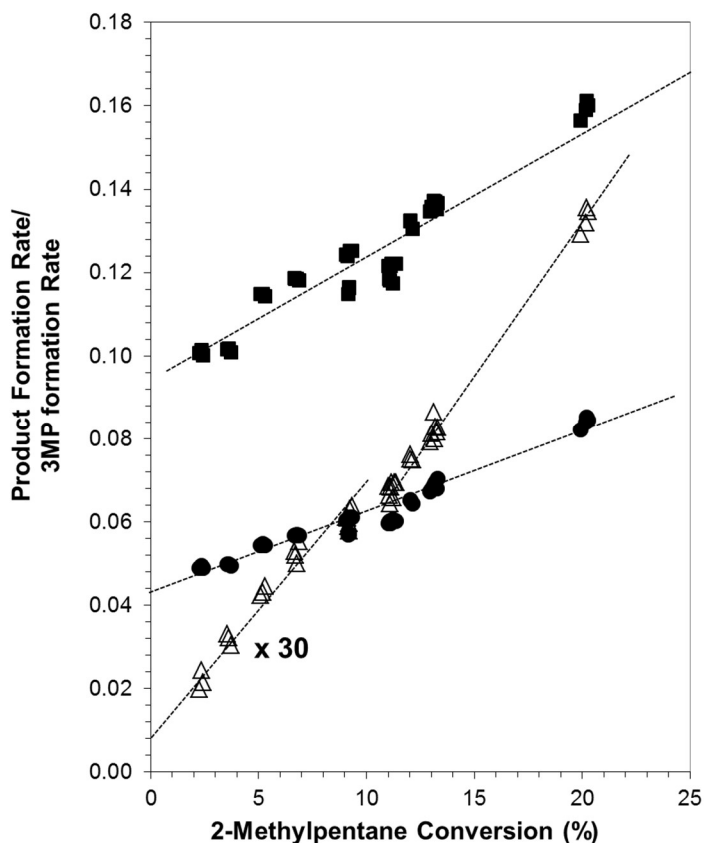
Figure S.3. Ratios of (■) 2,3-dimethylbutane, (●) n-hexane, and (△) 2,2-dimethylbutane formation rates to the formation rate of 3-methylpentane as functions of 2-methylpentane conversion on H_3PW/SiO_2-Pt/Al_2O_3 (Pt_s/H^+ = 1.0) (473 K, 30 kPa H_2, 3 kPa 2MP). Dashes lines show qualitative trends in the data.

Figure S.4 shows ratios of 2,3-dimethylbutane (23DMB), n-hexane (nH), and 2,2-dimethylbutane (22DMB) formation rates to formation rates for 2-methylpentane (2MP) (per POM) as a function of 3-methylpentane (3MP) conversion (3 – 18%) on H_3PW/SiO_2-Pt/Al_2O_3 (Pt_s/H^+ = 2). All ratios decreased with decreasing 3MP conversion indicating a decrease in the extent of secondary reactions between 2MP and the other products. 22DMB ratios nearly extrapolate to zero at low conversions, indicating that it is formed almost exclusively by secondary isomerizations.
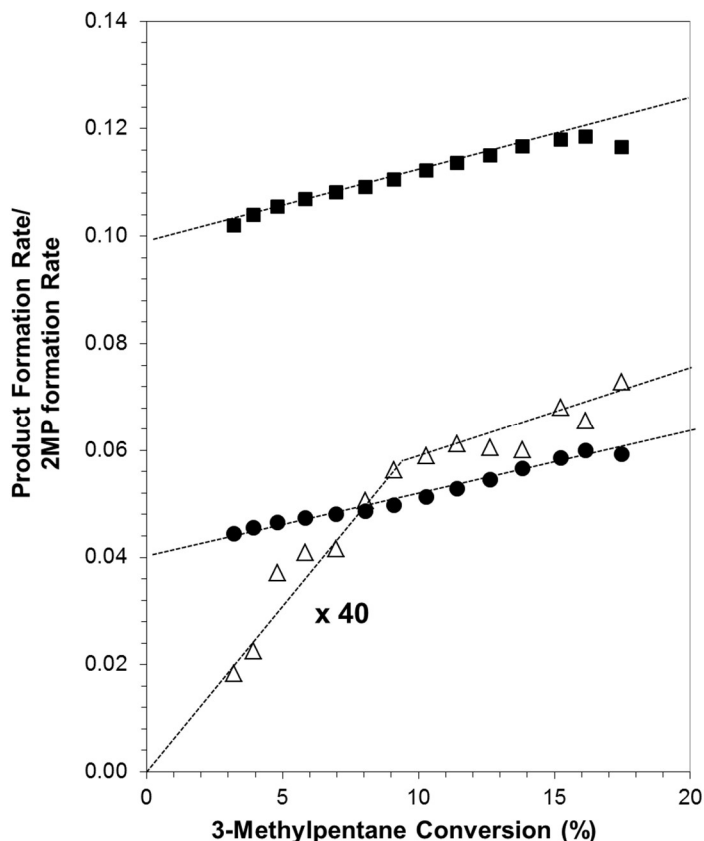
Figure S.4. Ratios of (■) 2,3-dimethylbutane, (●) n-hexane, and (△) 2,2-dimethylbutane formation rates to the formation rate of 2-methylpentane as functions of 3-methylpentane conversion on H_3PW/SiO_2-Pt/Al_2O_3 ($Pt_S/H^+ = 2.0$) (473 K, 30 kPa H_2, 1.3 kPa 3MP). Dashes lines show qualitative trends in the data.

1.6.4. Derivations of rate expressions for 2-methylpentane isomerization

Here, we derive the rate expressions used throughout the main text, and additional equations used to justify our assumptions, by using kinetic analyses of elementary steps. Throughout this section, concentrations of surface intermediates are denoted by square brackets and pressures of gas-phase species are denoted by parenthesis. Surface intermediates at metal and acid sites are denoted by "#" and "*"respectively.

1.6.4.1. Pseudo-steady-state treatment of alkenes

The pseudo-steady-state hypothesis (PSSH) may be applied to reactive intermediates when their concentrations (C_i) change by much less than reactant and/or product concentrations (C_r and C_p, respectively):

$$\left|\frac{dC_r}{dt}\right| \approx \left|\frac{dC_p}{dt}\right| \gg \left|\frac{dC_i}{dt}\right| \approx 0 \tag{S-1}$$

This assumption is valid for all surface intermediates because active sites carry out many turnovers at all detectable conversions. Alkene concentrations may also be treated by PSSH under the conditions used here because they are never detected in the reactor effluent, but product alkanes are detected. Here we use PSSH to derive the concentrations of alkenes and their dependences on (Pt/H$^+$) ratios and isomerization rates.

Metal sites dehydrogenate alkanes and hydrogenate alkenes by the proposed set of elementary steps shown in Scheme S.1. Alkanes (AH$_2$) adsorb dissociatively at neighboring vacant metal sites (#) to form chemisorbed hydrogen atoms (H#) and adsorbed alkyl fragments (AH#) (Scheme S.1, Step 1). Alkyl fragments lose another H-atom to form "adsorbed alkenes" (A#) (Scheme S.1, Step 2), which desorb as alkenes (A=) (Scheme S.1, Step 3). Two H# desorb associatively as H$_2$ in quasi-equilibrated steps (Scheme S.1, Step 4).

Alkane dehydrogenation rates (r_{dehy}) are given by:

$$r_{dehy} = k_{des,AH_2}[A\#] \tag{S-2}$$

The PSSH for A#, AH#, and H# are:

$$\left|\frac{d[A\#]}{dt}\right| = k_{dehy,AH\#}[AH\#]\frac{[\#]}{[Pt]} - k_{hy,A\#}[A\#]\frac{[H\#]}{[Pt]} - k_{des,A\#}[A\#] \approx 0 \tag{S-3}$$

$$\left|\frac{d[AH\#]}{dt}\right| = k_{dehy,AH_2}(AH_2)\frac{[\#]^2}{[Pt]} + k_{hy,A\#}[A\#]\frac{[H\#]}{[Pt]} - k_{hy,AH\#}[AH\#]\frac{[H\#]}{[Pt]} - k_{dehy,AH\#}[AH\#]\frac{[\#]}{[Pt]} \approx 0 \tag{S-4}$$

$$[H\#] = \sqrt{K_H(H_2)}[\#] \tag{S-5}$$

and may be solved to substitute [A#] into Equation (S-2). If all steps are reversible and equilibrated (i.e., $k_{des,A\#} \ll k_{hy,A\#}\sqrt{K_H(H_2)}\frac{[\#]}{[Pt]}$), Equation (S-2) becomes:

$$\frac{r_{dehy}}{[Pt]} = \frac{k_{des,A\#}k_{dehy,AH\#}k_{dehy,AH2}}{k_{hy,A\#}k_{hy,AH\#}}\left(\frac{AH_2}{H_2}\right)\frac{[\#]}{[Pt]} \tag{S-6}$$

If alkane adsorption at metal sites is equilibrated (i.e., $k_{dehy,AH\#} \ll k_{hy,AH\#}\sqrt{K_H(H_2)}$) and the second H-atom abstraction is irreversible (i.e., $k_{des,A\#} \gg k_{hy,A\#}\sqrt{K_H(H_2)}\frac{[\#]}{[Pt]}$), then Equation (S-2) becomes:

$$\frac{r_{dehy}}{[Pt]} = \frac{k_{dehy,AH\#}k_{dehy,AH_2}}{k_{hy,AH\#}K_H}\frac{(AH_2)}{(H_2)^{1/2}}\left(\frac{[\#]}{[Pt]}\right)^2 \tag{S-7}$$

If alkane adsorption is irreversible (i.e., $k_{dehy,AH\#} \gg k_{hy,AH\#}\sqrt{K_H(H_2)}$ and

$k_{des,A\#} \gg k_{hy,A\#}\sqrt{K_H(H_2)}\dfrac{[\#]}{[Pt]}$), the dehydrogenation rate is:

$$\frac{r_{dehy}}{[Pt]} = k_{dehy,AH_2}\left(AH_2\right)\left(\frac{[\#]}{[Pt]}\right)^2 \tag{S-8}$$

The fraction of metal sites that are vacant ([#]/[Pt]) in Eqs. (S-6) - (S-8) is determined by a surface Pt-atom site balance:

$$[Pt] = [\#] + [H\#] + [AH\#] + [A\#] \tag{S-9}$$

Surface species derived from alkanes and alkenes are presumed to be at low surface concentrations for the low alkene pressures used during this study (< 1.25 Pa), simplifying the site balance to:

$$[Pt] = [\#](1+\sqrt{K_H(H_2)}) \tag{S-10}$$

which can be substituted into Eqs. (S-6) - (S-8) to obtain dehydrogenation rate expressions. Rigorous thermodynamic treatments of rates far away from equilibrium [33] show that alkene hydrogenation rates (r_{hy}) are given by:

$$\frac{r_{hy}}{[Pt]} = r_{dehy}\left(\frac{\dfrac{(A=)(H_2)}{(AH_2)}}{\dfrac{k_{dehy,AH_2}k_{dehy,AH\#}k_{des,A\#}}{k_{ads,A=}k_{hy,A\#}k_{hy,AH\#}K_H}}\right) \tag{S-11}$$

Dehydrogenation rates are first-order in alkane pressure for all cases discussed above and have a H_2 pressure dependence (ranging from zero to inverse second order) that is determined by the kinetic-relevance of the H-abstraction steps and the H# coverage. Alkene hydrogenation rates are always first-order in alkene pressure. In the absence of further mechanistic knowledge regarding the kinetic-relevance of individual elementary steps for dehydrogenation-hydrogenation, we will assume that alkane dehydrogenation and alkene hydrogenation rates follow the rate expressions:

$$\frac{r_{dehy}}{[Pt]} = k_{dehy}\left(\frac{AH_2}{H_2}\right) \tag{S-12a}$$

$$\frac{r_{hy}}{[Pt]} = k_{hy}\left(A=\right) \tag{S-12b}$$

These results are used next to determine the pseudo-steady-state concentrations of 2MP= under reaction conditions for POM/SiO$_2$-Pt/Al$_2$O$_3$ mixtures. Isomerization rates are linear with 2MP= pressure at low pressures and bend over at higher pressures (Figure 4 in the main text). At low pressures rates are given by (derived in Section 1.6.3.2):

$$\frac{r_{isom,2}}{\left[H^+\right]} = k_{isom,2} K_{prot,2} \left(2MP=\right) \tag{S-13a}$$

$$k_{isom,2} K_{prot,2} = k_{isom,2\rightarrow3} K_{prot,2} + k_{isom,2\rightarrow23} K_{prot,2} + k_{isom,2\rightarrow nH} K_{prot,2} \tag{S-13b}$$

where the rate and equilibrium constants are defined by the elementary steps shown in Scheme 1 of the main text. The PSSH for 2MP= is therefore:

$$\left|\frac{d(2MP=)}{dt}\right| = k_{dehy}\left(\frac{2MP}{H_2}\right)[Pt] - k_{hy}\left(2MP=\right)[Pt] - k_{isom,2} K_{prot,2}\left(2MP=\right)[H^+] \approx 0 \tag{S-14}$$

which defines the pseudo-steady-state concentration of 2MP=:

$$\left(2MP=\right) = \frac{K_{dehy,2}\left(\dfrac{2MP}{H_2}\right)}{1 + \dfrac{k_{isom,2} K_{prot,2}}{k_{hy}}\dfrac{[H^+]}{[Pt]}} \tag{S-15}$$

Saturation of protons by alkoxides at higher 2MP= pressures causes isomerization rates that are zero-order in 2MP= pressure so that Equation (S-15) represents the lower bound for 2MP= pressures. Pt sites equilibrate 2MP= and 2MP at high (Pt_S/H^+) ratios and isomerization rates approach the dehydrogenation-hydrogenation equilibrium solution (Eq. (3a)):

$$\frac{r_{isom,2}}{\left[H^+\right]} = \frac{k_{isom,2} K_{prot,2} K_{dehy,2}\left(\dfrac{2MP}{H_2}\right)}{1 + K_{prot,2} K_{dehy,2}\left(\dfrac{2MP}{H_2}\right)} \tag{S-16}$$

Equation (S-15) shows that proportional changes in isomerization rate constants and (Pt/H^+) ratios do not change the extent of 2MP-2MP= equilibration. Such proportional changes are discussed in the main text (Section 1.3.1.2) to reduce the effects of Pt-catalyzed isomerization routes, while maintaining equilibrium 2MP= pressures.
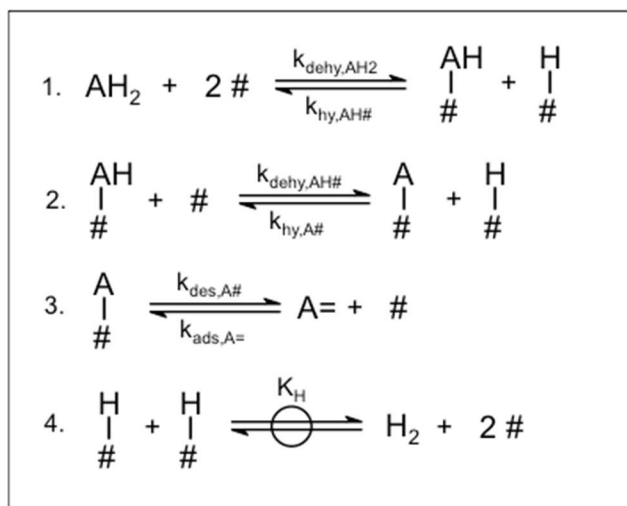
Scheme S.1. Elementary steps for alkane (AH$_2$) dehydrogenation and alkene (A=) hydrogenation at metal sites (#).

1.6.4.2. Isomerization rates at alkane-alkene equilibrium

Here we derive the rate expression for the formation of product isomer "P" under conditions of alkane-alkene equilibrium (the criterion for which is derived and shown in Section 1.6.3.1). At high (Pt$_S$/H$^+$) ratios and low 2MP conversions, rapid deprotonation of product alkoxides and hydrogenation of the resulting alkenes make isomerization steps irreversible. The formation rate of product "P" ($r_{isom,2 \to P}$) is then:

$$r_{isom,2 \to P} = k_{isom,2 \to P}\left[2MP*\right]$$

(S-17)

where [2MP*] is the concentration of the pool of equilibrated 2-methylpentoxide isomers at acid sites (shown as 2-methylpent-3-oxide in Step 3 of Scheme 1), $k_{isom,2 \to P}$ is the isomerization rate constant for forming product "P" from [2MP*]. When alkene protonation and alkoxide deprotonation is equilibrated (Scheme 1, Step 2), [2MP*] can be defined by its equilibrium with the equilibrated pool of 2MP= double bond isomers or any one of those isomers (shown for 2-methylpent-2-ene in Scheme 1) in the contacting gas-phase:

$$\left[2MP*\right] = K_{prot,2}(2MP=)[*]$$

(S-18)

where K$_{prot,2}$ is the protonation equilibrium constant forming [2MP*] from the equilibrated pool of 2MP= double bond isomers. The concentration of vacant protons in Equation (S-18) is given by the acid site balance:

$$[H^+] = [*] + [2MP*] = [*]\left(1 + K_{prot,2}(2MP=)\right)$$

(S-19)

The complete expression for "P" formation is achieved by combining Equation (S-17) – (S-19):

$$\frac{r_{isom,2}}{\left[H^+\right]} = \frac{k_{isom,2}K_{prot,2}(2MP=)}{1 + K_{prot,2}(2MP=)} \tag{S-20}$$

Equation 2 in the main text is obtained from Equation (S-20) by relating the 2MP= and 2MP pressures via the 2MP= dehydrogenation equilibrium constant ($K_{dehy,2}$ in Eq. 2 and Scheme 1).

1.7. References

[1] A. Corma, *Chem. Rev.* 95 (1995) 559–614.

[2] M.J. Janik, J. Macht, E. Iglesia, M. Neurock, *J. Phys. Chem. C.* 113 (2009) 1872–1885. doi:10.1021/jp8078748

[3] J. Macht, M.J. Janik, M. Neurock, E. Iglesia, *J. Am. Chem. Soc.* 130 (2008) 10369–79. doi:10.1021/ja803114r

[4] M. Brändle, J. Sauer, *J. Am. Chem. Soc.* 120 (1998) 1556–1570.

[5] A.J. Jones, R.T. Carr, S.I. Zones, E. Iglesia, *J. Catal.* 312 (2014) 58–68. doi:10.1016/j.jcat.2014.01.007

[6] J. Macht, M.J. Janik, M. Neurock, E. Iglesia, *Angew. Chem. Int. Ed.* 46 (2007) 7864–8. doi:10.1002/anie.200701292

[7] R.T. Carr, M. Neurock, E. Iglesia, *J. Catal.* 278 (2011) 78–93. doi:10.1016/j.jcat.2010.11.017

[8] J. Macht, R.T. Carr, E. Iglesia, *J. Am. Chem. Soc.* 131 (2009) 6554–6565.

[9] P. Deshlahra, R.T. Carr, E. Iglesia, *J. Am. Chem. Soc.* 136 (2014) 15229–15247. doi:10.1021/ja506149c

[10] P.B. Weisz, E.W. Swegler, *Science (80-.).* 126 (1957) 31–32. doi:10.1126/science.126.3262.31

[11] M. Guisnet, F. Alvarez, G. Giannetto, G. Perot, *Catal. Today.* 1 (1987) 415–433.

[12] G.D. Pirngruber, K. Seshan, J. a. Lercher, *J. Catal.* 186 (1999) 188–200. doi:10.1006/jcat.1999.2554

[13] J. Cowan, C.L. Hill, R. Reiner, I. Weinstock, *Inorg. Synth.* 33 (2002) 18–26.

[14] L. Baker, T. McCutcheon, *J. Am. Chem. Soc.* 78 (1956) 4503–4510.

[15] L. Baker, B. Loev, T. McCutcheon, *J. Am. Chem. Soc.* 72 (1950) 2374–2377.

[16] D. Scott, "Chemical Thermodynamic Properties of Hydrocarbons and Related Substances: properties of the alkane hydrocarbons, C1 through C10, in the ideal gas state from 0 to 1500 K," Washington, 1974.

[17] C. Baertsch, *J. Catal.* 205 (2002) 44–57. doi:10.1006/jcat.2001.3426

[18]   Noritaka Mizuno and Makoto Misono, *Chem. Rev.* 98 (1998) 199–217. doi:10.1021/cr960401q

[19]   B.B. Bardin, R.J. Davis, *Appl. Catal. A-Gen.* 200 (2000) 219–231.

[20]   M.J. Janik, B.B. Bardin, R.J. Davis, M. Neurock, *J. Phys. Chem. B*. 110 (2006) 4170–8. doi:10.1021/jp0553176

[21]   X. Rozanska, P. Sautet, F. Delbecq, F. Lefebvre, S. Borshch, H. Chermette, et al., *Phys. Chem. Chem. Phys.* 13 (2011) 15955–9. doi:10.1039/c1cp21171d

[22]   T. Okuhara, N. Mizuno, M. Misono, *Adv. Catal.* 41 (1996) 113–252.

[23]   G. Djega-Mariadassou, M. Boudart, *J. Catal.* 216 (2003) 89–97. doi:10.1016/S0021-9517(02)00099-4

[24]   R. Madon, M. Boudart, *Ind. Eng. Chem. Fundam.* 21 (1982) 438–447. doi:10.1021/i100008a022

[25]   J. Macht, R.T. Carr, E. Iglesia, *J. Catal.* 264 (2009) 54–66. doi:10.1016/j.jcat.2009.03.005

[26]   V. Kazansky, *Accounts Chem. Res.* 24 (1991) 379–383.

[27]   M. Natal-Santiago, R. Alcalá, J. Dumesic, *J. Catal.* 181 (1999) 124–144.

[28]   M. Boronat, P. Viruela, A. Corma, *J. Phys. Chem.* 100 (1996) 633–637. doi:10.1002/chin.199620056

[29]   T. Demuth, X. Rozanska, L. Benco, J. Hafner, R.A. Van Santen, H. Toulhoat, *J. Catal.* 214 (2003) 68–77. doi:10.1016/S0021-9517(02)00074-X

[30]   a L.L. East, T. Bucko, J. Hafner, *J. Phys. Chem. A*. 111 (2007) 5945–7. doi:10.1021/jp072327t

[31]   R.A. Alberty, C.A. Gehrig, *J. Phys. Chem. Ref. Data*. 14 (1985) 803–820.

[32]   R. Massart, R. Contant, J.-M. Fruchart, J.-P. Ciabrini, M. Fournier, *Inorg. Chem.* 16 (1977) 2916–2921.

[33]   M. Boudart, *Ind. Eng. Chem. Fundam.* 25 (1986) 70–75.

Chapter 2.

Acid Strength and Metal-Acid Proximity Effects on Methylcyclohexane Ring Contraction Turnover Rates and Selectivities

Abstract

Methylcyclohexane ring contraction reactions on bifunctional (metal-acid) catalysts are used to probe the effects of acid strength and metal-acid proximity on turnover rates and selectivities. Keggin type polyoxometalates (POM) clusters with different central atoms provide Brønsted acid catalysts with well-defined structures and diverse acid strengths. Titrations of Brønsted acid sites with non-coordinating bases during catalysis and mechanistic interpretations of rate data on bifunctional catalysts containing POM acids and sufficient metal function to maintain cycloalkane-cycloalkene equilibrium in reactants and products give ring contraction rate constants that decrease exponentially with increasing deprotonation energy (DPE). Density functional theory (DFT) calculations indicate that transition state structures containing corner-protonated bicyclo[3.1.0]hexyl carbenium ion fragments mediate kinetically relevant ring contraction steps. Mechanistic interpretations of selectivity data using diffusion-reaction formalisms and DFT results give intrinsic ring contraction selectivities that are independent of acid strength. The sensitivities of rate constants for forming individual ring contraction isomers to acid strength are the same because their respective transition states have cations with similar amounts and distributions of charge that benefit to the same extent from more stable conjugate anions on stronger acids. Observed product selectivities, even at differential conditions, reflect, in part, the effects of diffusion-enhanced interconversions of product alkylcyclopentenes within acid domains that depend on the strength and density of acid sites in acid domains and the size and diffusive properties of such domains. Increasing activity per catalyst volume increases the extent of diffusion-enhanced secondary interconversions that move product selectivities in the direction of their preferred thermodynamic prevalence and away from those determined by kinetics.

2.1. Introduction

The ring contraction of methylcyclohexane to alkylcyclopentanes on heterogeneous bifunctional catalysts consisting of Brønsted acid and metal functions has been suggested as an informative probe reaction to determine the number and strength of acid sites and the shape selective properties of the confining voids in amorphous and crystalline solid acid catalysis [1–4]; yet, rigorous connections between measured reactivities and selectivities and these physicochemical properties have remained elusive. In many cases, these hurdles are imposed by the uncertain density and strength of the acid sites and their unknown distance from the metal function, as well as by measured rates and selectivities that are seldom interpreted in terms of the relevant elementary steps. We resolve these uncertainties

here by using Brønsted acid catalysts of known structure and a broad range of acid strengths and a second metal function that is able to maintain cycloalkane-cycloalkene equilibrium in reactants and products, by measuring the number of accessible protons by titrations with organic bases during catalysis, and by interpreting rate and selectivity data in terms of the elementary steps that mediate the isomerization reactions.

Tungsten polyoxometalate (POM) clusters with Keggin structures and charge-balancing protons ($H_{8-n}X^{n+}W_{12}O_{40}$) are Brønsted acids that exhibit uniform and well-defined cluster size and atomic connectivity, and provide diverse chemical compositions ($X^{n+} = P^{5+}$, Si^{4+}, Al^{3+}, Co^{2+}) [5]. The identity of their central atom influences their acid strength and, consequently, their catalytic reactivity by changing the number of protons and the stability of anionic charge in the conjugate base [6]. Deprotonation energies (DPE) reflect the energy required for the heterolytic cleavage of a proton from the conjugate base, thus providing a rigorous and probe-independent measure of acid strength; these energies can be determined using density functional theory (DFT) treatments for solids with known structures, such as the Keggin POM clusters examined here (1087 - 1143 kJ mol^{-1} for $H_{8-n}X^{n+}W_{12}O_{40}$; X = P, Si, Al, or Co in order of increasing DPE) [6,7].

Our recent studies have shown that first-order alkene isomerization rate constants [8] and rate constants for alkanol dehydration [5,9] (per accessible H^+) decrease exponentially with increasing DPE (decreasing acid strength) for Keggin POM clusters with different central atoms (P, Si, Al, Co); such trends reflect ion-pair transition states (TS) that benefit from the more stable conjugate anions. The sensitivity of alkene isomerization rate constants to DPE is similar for different hexene isomer reactants, because the amount and location of the positive charge is similar for the transition states that mediate such reactions. Consequently, the selectivity of alkene isomerization reaction does not depend on acid strength, because it solely reflects the stability of the gaseous analogs of each isomerization TS. Measured alkane isomerization selectivities, however, do not reflect the intrinsic selectivity of the alkene interconversions, because of fast secondary alkene interconversions that occur locally within porous acid domains, before alkenes convert to alkanes via hydrogen transfer at acid sites or reactions with H_2 at a second metal function in bifunctional catalysts [8].

Here, ring contraction rate constants (per H^+) were determined for the conversion of methylcyclohexane reactants through mechanistic interpretations of rate data and measurements of the number of accessible protons by titrations with organic bases during catalysis. Differences between measured and intrinsic ring contraction selectivities at differential conversions are shown to reflect diffusion-enhanced interconversions of product alkylcyclopentenes that depend on the strength and density of acid sites in acid domains and the size and diffusive properties of such domains. Experimental and theoretical results indicate that intrinsic selectivities among ring-contraction products are independent of acid strength, consistent with their transition states being full ion-pairs. Consequently, the use of selectivities, even at differential conversion, as evidence for a preference for more demanding reactions on stronger acids or in microporous acids [1,2,10,11] (that impose a larger diffusive barrier, thus enhancing secondary reactions) is inappropriate, because such selectivities merely reflect the predominant initial formation of the more "facile" isomer, followed by subsequent diffusion-enhanced secondary

interconversions that move products in the direction of their preferred thermodynamic prevalence.

2.2. Methods

2.2.1. Catalyst Preparation

Detailed catalyst preparation procedures have been reported elsewhere [11]. $H_3PW_{12}O_{40}$ (Sigma-Aldrich; reagent grade; CAS #12501-23-4), $H_4SiW_{12}O_{40}$ (Aldrich; >99.9%; CAS #12027-43-9), $H_5AlW_{12}O_{40}$ (prepared according to [14]), and $H_6CoW_{12}O_{40}$ (prepared according to [15,16]) were supported on amorphous SiO_2 (Cab-O-Sil HS-5; 310 m^2 g^{-1}; 1.5 cm^3 g^{-1} pore volume) at loadings of 0.04 and 0.20 POM $(nm^2\text{-}SiO_2)^{-1}$ using incipient wetness impregnation methods. SiO_2-supported POM clusters will be denoted herein as "H_nXW/SiO_2", where n is proton stoichiometry. ^{31}P-MAS-NMR spectra showed that their dispersion onto the SiO_2 support and their use in catalysis retain the essential features of the NMR spectra of intact $H_3PW_{12}O_{40}$ Keggin structures [11]. Transmission electron micrographs showed that POM clusters are present as isolated clusters with a minority of two-dimensional aggregates at these POM surface densities (0.033 - 0.067 POM $(nm^2\text{-}SiO_2)^{-1}$) [11].

Pt/Al_2O_3 (1.5 wt% Pt) was prepared by incipient wetness impregnation of treated $\gamma\text{-}Al_2O_3$ (Sasol SBa-200; 193 m^2 g^{-1}, 0.57 cm^3 g^{-1} pore volume; treated in dry air (UHP Praxair; 0.5 cm^3 g^{-1} s^{-1}) at 923 K for 18 ks) with aqueous H_2PtCl_6 solutions (Aldrich; CAS #16941-12-1) [11]. The Pt dispersion (90%) was determined by H_2 chemisorption at 313 K (Quantasorb analyzer; Quantachrome Corp.) using a 1:1 H:Pt stoichiometry [11]. Pt/Al_2O_3 and H_nXW/SiO_2 (X=P, Si, Al, or Co) catalysts were mixed as intimate aggregates (<20 μm) using a mortar and pestle; these fine powders were pressed into wafers and then crushed and sieved to retain 125-180 μm aggregates. The composition of these mixtures is reported as the ratio of surface Pt-atoms (from H_2 chemisorption) to H^+ in POM clusters (from titrations with 2,6-di-*tert*-butylpyridine during catalysis; Section 2.2.2).

2.2.2. Ring Contraction Rate Measurements and Titrations of Protons with 2,6-di-*tert*-butylpyridine During Catalysis

Reaction rates and selectivities were measured on samples (0.040-0.103 g) packed within a stainless steel tubular reactor (3/8 in. O.D.) with plug-flow hydrodynamics. Reactor temperatures were measured with two K-type thermocouples (Omega; ± 0.2K), one held against the external reactor wall and the other held within a 1/16 in. stainless steel sheath aligned axially along the bed; temperatures were maintained controlled using a resistively-heated furnace and PID control strategies (Watlow Serues 982 controller). Transfer lines were kept at 423 K to prevent condensation of reactants, products, and titrants. A backpressure regulator was used to control pressure (Equilibar, model EB1LF2). Physical mixtures Pt/Al_2O_3 and H_nXW/SiO_2 were treated in flowing H_2 (Praxair UHP) at 2 bar (0.16 cm^3 s^{-1} at STP) by heating to 473 K at 0.083 K s^{-1} and holding for 4 ks before catalytic measurements. Liquid methylcyclohexane (MCH; Sigma Aldrich; >99%) was used without further purification and vaporized at 523 K evaporated into a flowing H_2 (UHP Praxair) stream using a liquid syringe pump (Cole-Palmer 74900 Series). Molar

MCH and H_2 flow rates were set using electronic mass flow controllers to maintain a given (MCH/H_2) molar ratio and low MCH conversions (<10%).

Reactants and products in the reactor effluent were separated chromatographically (HP-1 column; 0.32 mm ID x 50 m, 1.05 μm film; Agilent) and detected using flame ionization (Agilent 6890N GC). The predominant products detected were: ethylcyclopentane (ECP), *cis*-1,3-dimethylcyclopentane (c13DMCP), *trans*-1,3-dimethylcyclopentane (t13DMCP), *tran*-1,2-dimethylcyclopentane (t12DMCP), 1,1-dimethylcyclopentane (11DMCP), several acyclic heptane isomers, methylcyclopentane. *cis*-1,2-Dimethylcyclopentane (c12DMCP) and MCH did not elute separately from the column; therefore, c12DMCP formation rates were calculated from its equilibrium constant with t12DMCP at 473 K [17]. 13DMCP chemical isomers (c13DMCP and t13DMCP) were detected at a nearly constant ratio ([c13DMCP]/[t13DMCP] = 1.071 ± 0.008), leading us to assume similar equilibration for cis and trans 12DMCP. The c12DMCP and t12DMCP isomers (and the c13DMCP and t13DMCP isomers) are treated as a 12DMCP (and 13DMCP) lumped products. The concentration of any product (t12DMCP, c12DMCP, and ECP) present as trace impurities (< 0.0013 % mol) in MCH reactants was subtracted from those detected in the effluent in determining product formation rates. The rates of formation of each product were also corrected for their approach to equilibrium for the reactions that forms them from MCH using:

$$r_{forward} = r_{net} \left(1 - \left(\frac{P_{prod}}{P_{mch}} \right) K_{mch,prod}^{-1} \right)^{-1} \tag{1}$$

in which (P_{prod}/P_{mch}) is the ratio of product and MCH pressures in the effluent and $K_{mch,prod}$ is their equilibrium constant at 473 K, derived from reported thermodynamic data [17,18]. Catalyst deactivation (half-lives between 14 and 72 ks) was observed on all catalysts during kinetic experiments. Rates measured periodically at a standard condition (4 kPa MCH and 235 kPa H_2) were used to correct all rate data for any intervening deactivation.

Titrations during catalysis were performed by dissolving 2,6-di-*tert*-butylpyridine (DTBP, Aldrich; > 97% ; CAS #585-48-8) in liquid MCH reactants (between 7.7 x 10^{-6} and 1.1 x 10^{-3} % mol) and vaporizing this mixture into flowing H_2 stream (UHP Praxair) at 523 K to give DTBP pressures between 0.03 and 4.4 Pa. Ring contraction rates and DTBP uptakes were determined using the chromatographic protocols described above. The number of DTBP titrants required to suppress MCH conversion rates reflects the number of H^+ present in POM/SiO_2 samples during catalysis [19] and the complete suppression of the rates confirms that these isomerization reactions occur only on Brønsted acid sites.

2.2.3. Computational Methods

The structures and energies of gaseous reactants, adsorbed surface species, and transition states (TS) on Keggin POM clusters ($H_{8-n}X^{n+}W_{12}O_{40}$) with different central atoms ($X^{n+} = P^{5+}$, Si^{4+}, Al^{3+}, and Co^{2+}) were calculated using periodic gradient-corrected density functional theory (DFT) as implemented in the Vienna ab initio simulation package (VASP) [20–23]. Wavefunctions for valence electrons were represented using a periodic plane-wave basis-set expansion to a cutoff energy of 396.0 eV and electron-core interactions were described using the projector augmented-wave method (PAW) [24,25].

Exchange and correlation energies within the generalized-gradient approximation were calculated using the Perdew-Wang (PW91) [26] functional. A $1 \times 1 \times 1$ k-point mesh [27] and specified integer band occupancies were used for optimization calculations. Electronic structures were converged self-consistently to energies within 1×10^{-6} eV for each step in both structural optimizations. Spin-restricted calculations were used for all POM compositions except those with Co central atoms, which were performed with spin polarization and three unpaired electrons, corresponding to the Co^{2+} electronic configurations.

A cubic unit cell with an edge-length of 3 nm was for calculating the structures and energies of Keggin clusters (~1.2 nm diameter) and gaseous molecules to avoid interactions among clusters in adjacent unit cells [10,12,28]. Uniform background charges were used in calculations of charged species to maintain neutral unit cells, and the resulting energies were corrected using methods [29] implemented in VASP. Dipole and quadrupole moments, with the center of charge located at the center of the unit cell corrected long-range interactions among atoms in neighboring unit cells in charged and neutral systems. Structures were relaxed until the maximum force on any atom was within 0.05 eV Å^{-1}. Converged wave functions of optimized structures were transformed into a set of localized quasiatomic orbitals (QUAMBO) [30–33], which were used in Löwdin population analyses to determine charges on individual atoms [34,35].

Nudged elastic band (NEB) methods[36] with structures converged to energies within 1×10^{-4} eV and forces to within 0.3 eV Å^{-1} were used for calculating minimum energy reaction paths and starting TS structures and reaction modes for Dimer calculations. Dimer calculations [37] with convergence criteria of 1×10^{-6} eV for energies and 0.05 eV Å^{-1} for forces on each atom were used to identify TS structures. Frequency calculations performed on TS structures gave one large imaginary frequency mode (larger than -150 cm^{-1}), confirming the structures are at saddle points on the potential energy surface and that they reflect those of a transition states.

2.3. Results and Discussion

2.3.1. Elementary Steps, Rates, and Selectivities for Methylcyclohexane Ring Contraction

Methylcyclohexane (MCH) ring contraction rates and selectivities were measured on silica-supported POM clusters (H_nXW/SiO_2) with different central atoms (X = P, Si, Al, and Co) as bifunctional physical mixtures with Pt/Al_2O_3. MCH ring contraction reactions predominately formed ECP, 12DMCP, and 13DMCP at all conditions and on all catalysts (> 98 % carbon selectivity), with trace amounts of 11DMCP (< 1 % carbon selectivity at short residence times). Ring contraction rates were much higher on bifunctional mixtures containing H_nXW/SiO_2 than on monofunctional Pt/Al_2O_3 or H_nXW/SiO_2 (by factors > 100), indicating that ring contraction occurs on acid sites. Titration with 2,6-di-*tert*-butylpyridine (DTBP) during reaction gave rates that decreased with increasing DTBP uptakes on all catalysts and ultimately reached undetectable levels after all protons were titrated (shown for H_4SiW/SiO_2 in Figure SI-1; supporting information (SI)). Thus, MCH ring contraction occurs only at Brønsted acid sites and DTBP titrates all protons in

H_nXW/SiO_2 co-catalysts. Ring contraction turnover rates are reported here on the basis of the number of H^+ titrated by DTBP in each sample.

MCH ring contraction rates on bifunctional mixtures containing H_nXW/SiO_2 and Pt/SiO_2 are limited by the ring isomerization of methylcyclohexenes ($MCH^=$) on Brønsted acid sites when the metal function maintains hydrogenation-dehydrogenation thermodynamic equilibrium [13] at the external boundaries of the acid domains (the proton-containing regions devoid of metal sites) and the depletion of $MCH^=$ species is not fast enough to impose concentration gradients of $MCH^=$ species within these acid domains. The first-order rate constants for $MCH^=$ ring contraction (per H^+) were nearly ten or more times smaller than those reported for 2-methylpentene isomerization (per H+) (Figure 9; [11]); the latter values did not depend on either (Pt_S/H^+) ratios ((Pt_S/H^+) = 6.2 - 22.9 for H_3PW/SiO_2-Pt/Al_2O_3 mixtures) or H^+ densities (0.006 and 0.070 H^+ $(nm^3$-$SiO_2)^{-1}$ for H_3PW/SiO_2-Pt/Al_2O_3 mixtures). Therefore, the (Pt_s/H^+) ratio ((Pt_S/H^+) = 5.4) and proton density (0.022 H^+ $(nm^3$-$SiO_2)^{-1}$) for the H_3PW/SiO_2-Pt/Al_2O_3 mixture, and those for the mixtures containing the other POM acids (<0.022 H^+ $(nm^3$-$SiO_2)^{-1}$ and (Pt_S/H^+) > 1.7), which have lower MCH ring contraction turnover rates (per H^+) than H_3PW (Figure 1), are sufficient to maintain alkane dehydrogenation-hydrogenation equilibrium for MCH reactants outside acid domains and to avoid corruption of measured ring contraction turnover rates by transport restriction.

Table 1. Number of accessible H^+ per POM cluster measured by chemical titration with 2,6-di-*tert*-butylpyridine[a] during methylcyclohexane isomerization[b] on $H_nXW_{12}O_{40}/SiO_2$-Pt/Al_2O_3 ($X = P$, Si, Al, Co) mixtures.

Catalyst	POM Content (% wt.)	POM Areal Density (POM $(nm^2$-$SiO_2)^{-1})$	Accessible H^+ (per POM)	H^+ Volumetric Density (H^+ $(nm^3$-$SiO_2)^{-1})$	Pt_s/H^+ Ratio
$H_3PW_{12}O_{40}$	10	0.067	1.6	0.022	5.4
$H_4SiW_{12}O_{40}$	5	0.034	2.6	0.018	3.3
$H_5AlW_{12}O_{40}$	5	0.033	2.5	0.020	1.7
$H_6CoW_{12}O_{40}$	5	0.039	0.22	0.002	38

[a] Assuming a 1:1 DTBP:H^+ adsorption stoichiometry

[b] 4 kPa methylcyclohexane, 218 kPa H_2, 473 K

Figure 1 shows MCH ring contraction turnover rates (per H^+) as a function of (MCH/H_2) inlet molar ratios on H_nXW/SiO_2-Pt/Al_2O_3 mixtures with P, Si, Al, and Co central atoms ((Pt_s/H^+) = 3.2 - 30.1). MCH ring contraction turnover rates increased with increasing (MCH/H_2) ratios, linearly at first and then more gradually at higher reactant ratios; rates did not depend on H_2 pressures (60 - 90 kPa H_2) for a given (MCH/H_2) ratio on any of the H_nXW/SiO_2-Pt/Al_2O_3 mixtures (Figure 1). These data are consistent with the full equilibration of methylcyclohexane and all methylcyclohexene isomers on Pt sites and with ring contraction rates that depend only on the concentration of these $MCH^=$ species, as shown next by a discussion of plausible ring contraction elementary steps.
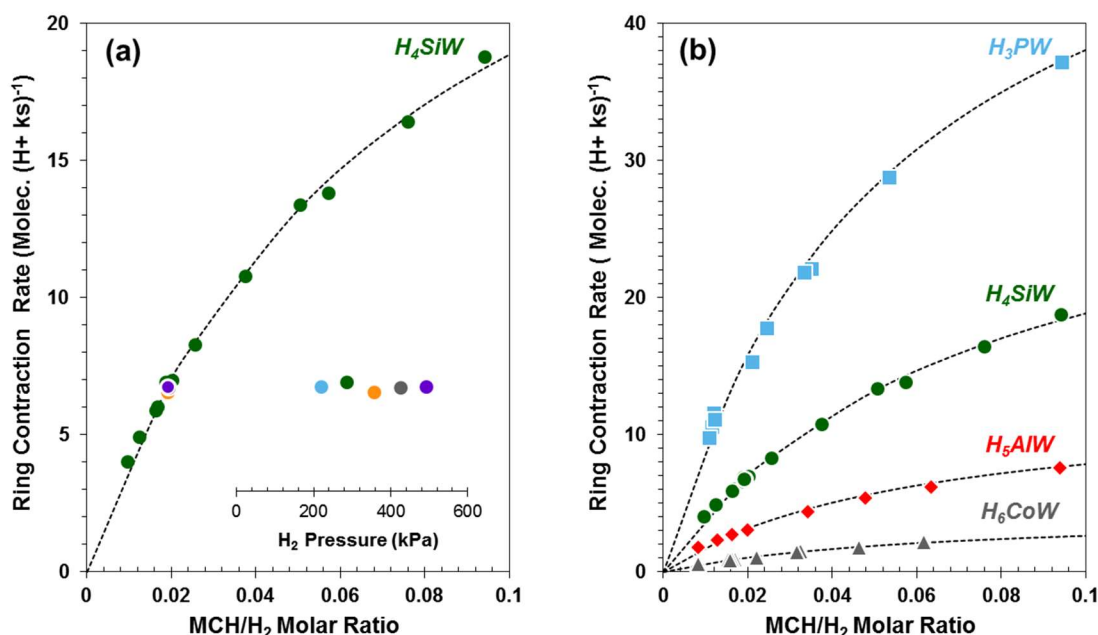
Figure 1. (a) Methylcyclohexane ring contraction turnover rate as functions of the (MCH/H_2) ratio and H_2 pressure (inset) on a H_4SiW/SiO_2 mixture with Pt/Al_2O_3 (Pt_S/H^+ = 3.3, 0.018 H^+ (nm^3-SiO_2)$^{-1}$) and (b) as functions of the (MCH/H_2) ratio on Pt/Al_2O_3 mixtures with H_3PW/SiO_2 (Pt_S/H^+ = 5.4, 0.022 H^+ (nm^3-SiO_2)$^{-1}$; ■), H_4SiW/SiO_2 (Pt_S/H^+ = 3.3, 0.018 H^+ (nm^3-SiO_2)$^{-1}$; ●), H_5AlW/SiO_2 (Pt_S/H^+ = 1.7, 0.020 H^+ (nm^3-SiO_2)$^{-1}$; ◆), and H_6CoW/SiO_2 (Pt_S/H^+ = 38, 0.002 H^+ (nm^3-SiO_2)$^{-1}$; ▲) (reaction conditions: 473 K, 191 – 442 kPa H_2). Dashed lines represent the regression of the data to the functional form of Equation 2.

Scheme 1 shows a sequence of elementary steps and the overall stoichiometric MCH ring contraction reactions on metal-acid mixtures at conditions of MCH/H_2/MCH$^=$ equilibration on Pt sites for all methylcyclohexene regioisomers (Scheme 1, Step 1 shown for 1-methylcyclohexene); MCH$^=$ concentrations therefore depend only on (MCH/H_2) ratios and their respective equilibrium constants ($K_{d,mch}$). Methylcyclohexenes diffuse into acid domains (Scheme 1, Step 2) where they equilibrate with H^+ to form the corresponding alkoxides in quasi-equilibrated steps (Scheme 1, Step 3). Methylcyclohexoxides with different attachment points equilibrate by rapid hydride shifts in alkoxides. These methylcyclohexoxides then isomerize to form ethylcyclopentoxides and dimethylcyclopentoxides (Scheme 1). Steps 4a-c illustrates the specific formation of the ethylcyclohex-2-oxide, 1,2-dimethylcyclohex-3-oxide, and 1,3-dimethylcyclohex-2-oxide isomers, respectively. These ring contraction events are mediated by ion-pair transition states containing corner-protonated bicyclo[3.1.0]hexyl carbenium ions (shown in Figure 6) in which C-C bonds cleave and form in concerted steps [39–46]. Product cyclopentoxides deprotonate in quasi-equilibrated steps (except for *1-1-DMCP; see Section 2.3.2) to form their respective gaseous alkylcyclopentene isomers (Scheme 1, Steps 5a-c shown for ethylcyclopent-1-ene, 1,2-dimethylcyclopent-1-ene, and 1,4-dimethylcyclopent-1-ene isomers, respectively); the latter can readsorb on H^+ sites as they diffuse through acid domains and then undergo secondary isomerizations to form other alkylcyclopentoxides and alkyl cyclopentenes. Step 6a (Scheme 1) shows these reactions

51

for ethylcyclohex-2-oxide and 1,2-dimethylcyclopent-1-oxide interconversions and Step 6b for 1,2-dimethylcyclopent-1-oxide and 1,3-dimethylcyclohex-2-oxide interconversions. Gaseous alkylcyclopentene isomers that leave an acid domain (Scheme 1, Step 7a-c shown for ethylcyclopent-1-ene, 1,2-dimethylcyclopent-1-ene, and 1,4-dimethylcyclopent-1-ene, respectively) hydrogenate on Pt sites and equilibrate with their respective cycloalkane isomers (Scheme 1, Step 8a-c for ECP, 12DMCP, and 13DMCP formation, respectively). Alkene (and alkoxide) regioisomers with the same carbon backbone are treated here as lumped chemical pseudo-species because of their equilibrated interconversions. The lumped cycloalkenes with a given backbone are denoted here by a superscript "=" and their respective alkoxides by "*", in both cases without specifying the location of the surface attachment or the C=C bond (e.g., MCH, MCH$^=$, and MCH* for methylcyclohexane, methylcyclohexene isomers, and methylcyclohexoxide isomers).
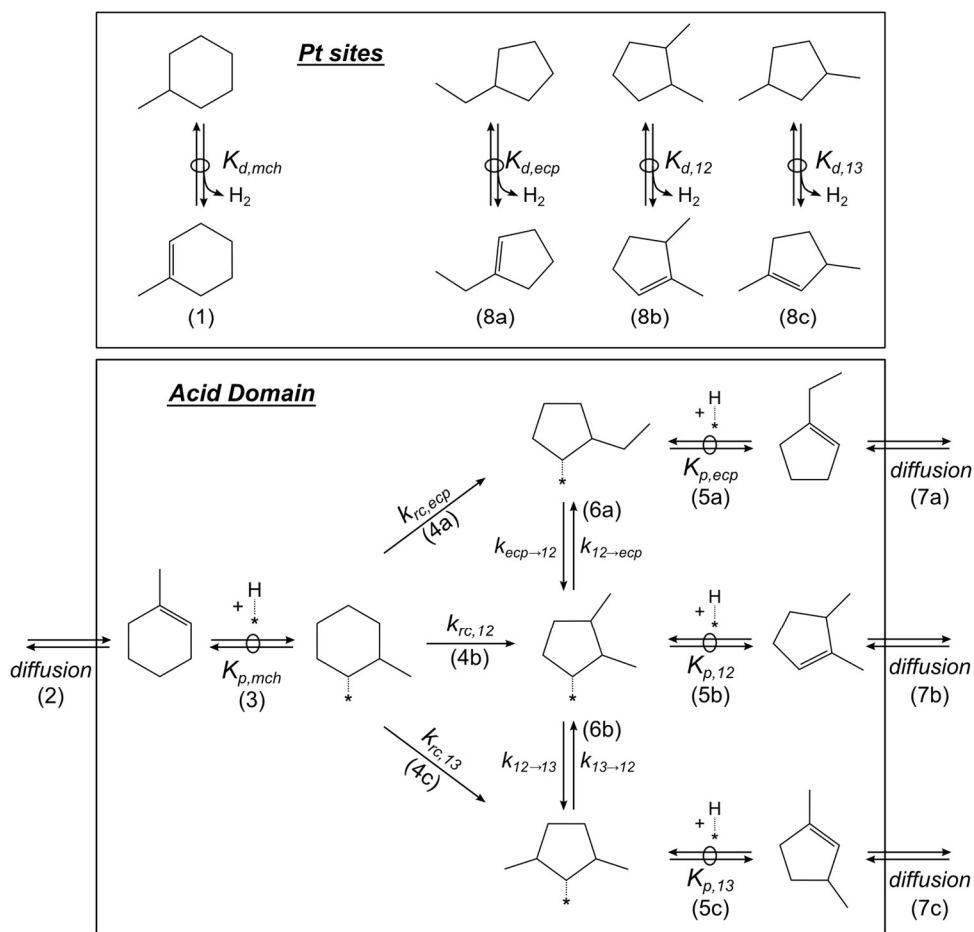
Scheme 1. Elementary steps and chemical reactions involved in methylcyclohexane ring contraction on metal-acid mixtures that establish methylcyclohexane/methylcyclohexene equilibrium. Chemical reactions are shown for the (de)hydrogenation on metal sites (Pt/Al$_2$O$_3$) and elementary steps for acid-catalyzed routes on H$_n$XW/SiO$_2$ (X = P, Si, Al, Co). Bonds to the Brønsted active site are denoted as "*" in molecular structures.

The pseudo-steady-state assumption for alkoxides and the quasi-equilibrium among MCH$^=$ isomers and their MCH* counterparts, taken together with MCH* and H$^+$ as the most abundant surface intermediates (MASI), gives an equation for MCH ring contraction rates for the formation all alkylcyclopentene isomers:

$$\frac{r_{rc}}{[H^+]} = \frac{k_{rc}K_{p,mch}K_{d,mch}\left(\dfrac{[MCH]}{[H_2]}\right)}{1 + K_{p,mch}K_{d,mch}\left(\dfrac{[MCH]}{[H_2]}\right)} \qquad (2)$$

where

$$k_{rc} = k_{rc,ecp} + k_{rc,12} + k_{rc,13} \qquad (3)$$

represents the sum of rate constants for MCH* ring contraction to form each skeletal isomer (each with equilibrated double-bond locations and cis-trans configurations). Here, [H$^+$] is the total number of protons, $K_{p,mch}$ is the equilibrium constant for MCH* formation from MCH$^=$ (illustrated for methylcyclohex-1-oxide in Scheme 1) and $k_{rc,P}$ is the rate constant for MCH* ring contraction to form a given product ($k_{rc,ecp}$, $k_{rc,12}$, and $k_{rc,13}$ for ECP$^=$, 12DMCP$^=$, and 13DMCP$^=$ formation, respectively). The first two terms in the denominator reflect the relative numbers of MCH* and unoccupied H$^+$; terms corresponding to bound alkylcyclopentoxides are much smaller at the low prevalent concentration of gaseous products. The dashed curves in Figure 1 represent the regression of these rate data to the functional form of Equation 2 with the reported thermodynamics for MCH-MCH$^=$ equilibration ($K_{d,mch}$ = 5.0 Pa at 473 K [47–50]); the regressed k_{rc}, and $K_{p,mch}$ values and their product are shown in Table 2 on all H$_n$XW$_{12}$O$_{40}$/SiO$_2$ acids.

Table 2. Methylcyclohexane ring contraction rate constants ($k_{rc}K_{p,mch}$ and k_{rc}) and protonation equilibrium constants ($K_{p,mch}$) measured on H$_n$XW$_{12}$O$_{40}$/SiO$_2$-Pt/Al$_2$O$_3$ (X = P, Si, Al, Co) mixtures (473 K)

Catalyst	$k_{rc}K_{p,mch}$[a]	k_{rc}[b]	$K_{p,mch}$[c]
H$_3$PW$_{12}$O$_{40}$	215.6	58.9	3.7
H$_4$SiW$_{12}$O$_{40}$	88.1	33.0	2.7
H$_5$AlW$_{12}$O$_{40}$	42.3	12.4	3.4
H$_6$CoW$_{12}$O$_{40}$	13.9	4.3	3.3

[a] molec. (H$^+$ ks Pa)$^{-1}$
[b] molec. (H$^+$ ks)$^{-1}$
[c] Pa^{-1}.

Product selectivities are defined as formation rate of a given product "P" ($r_{rc,P}$) divided by the combined rate MCH conversion to all products (r_{rc}):

$$S_{m,P} = \frac{r_{rc,p}}{r_{rc}} \qquad (4)$$

("P" = ecp, 12, or 13 for ECP, 12DMCP, and 13DMCP). Figure 2 shows ECP, 13DMCP, and 12DMCP selectivities as functions of space velocity (mol MCH (ks mol $[H^+])^{-1}$) for different H^+ densities (densities varied by allowing deactivation to occur) on H_4SiW/SiO_2-Pt/Al_2O_3 at differential MCH conversions (< 2.1%). A decrease in H^+ densities led to higher ECP selectivity and lower 12DMCP and 13DMCP selectivities, even though variations in conversion imposed by changes in space velocity (for a given H^+ density) did not affect selectivities. Figure 3a shows ECP, 13DMCP, and 12DMCP selectivities as a function of MCH conversion at different total reactant molar flow rates on H_4SiW/SiO_2-Pt/Al_2O_3. MCH conversions at each molar flowrate were smaller at longer times-on-stream (more catalyst deactivation) and higher [MCH]/[H_2] molar ratios (more acid sites covered by [MCH*]). Such changes in MCH conversion (at each given total molar flow rate) increased ECP selectivity and decreased 12DMCP and 13DMCP selectivities, and resulted in selectivity curves for each total molar flow rate that depended only on MCH conversion. The predominant effects of H^+ density and not space velocity on measured selectivities (Figure 2), suggest that decreasing reactant flow rates (and increasing MCH conversion) simply shifts selectivities to higher MCH conversions. Therefore, the observed differences in measured selectivities (at a given MCH conversion) in Figure 3a for different reactant flow rates reflect differences in the time-on-stream or the $MCH^=$ pressure at which the data was taken, which respectively determine the number of acid sites not yet lost to catalyst deactivation and the fraction of those that are covered by MCH* ($K_{p,mch}[MCH^=]$).
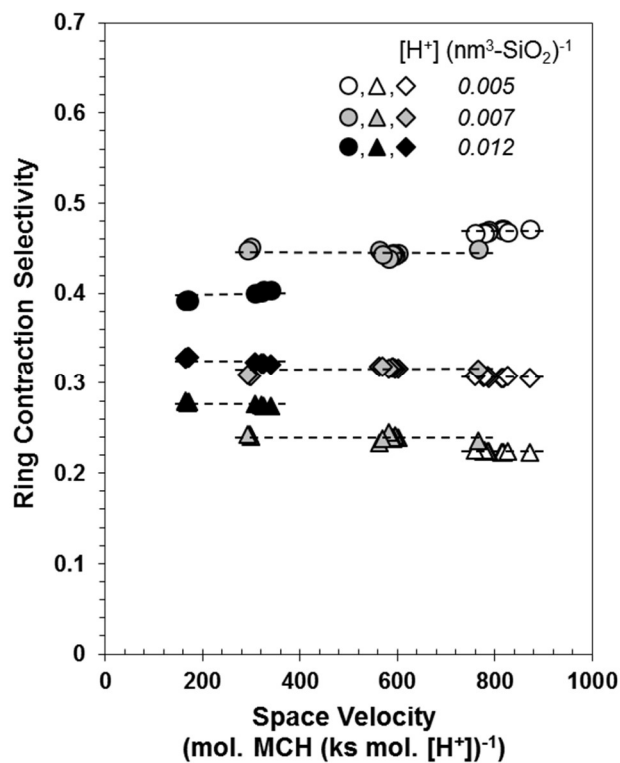
Figure 2. Measured ethylcyclopentane (●), 1,3-dimethylcyclopentane (▲), and 1,2-dimethylcyclopentane (◆) selectivities as functions of space velocity for different H^+ densities (0.005, 0.007 and 0.012 [H^+] (nm^3-SiO_2)$^{-1}$) on H_4SiW/SiO_2-Pt/Al_2O_3 ($Pt_S/[H^+]_0 =$ 3.3) at differential MCH conversions (< 2.1%), [MCH]/[H_2] ratios below 0.026, total reactant flowrates between 3.5 – 7.0 mmol ks^{-1}, pressures between 220 - 500 kPa, and 473 K. The dashed lines are the average selectivity for each product at each H^+ density.
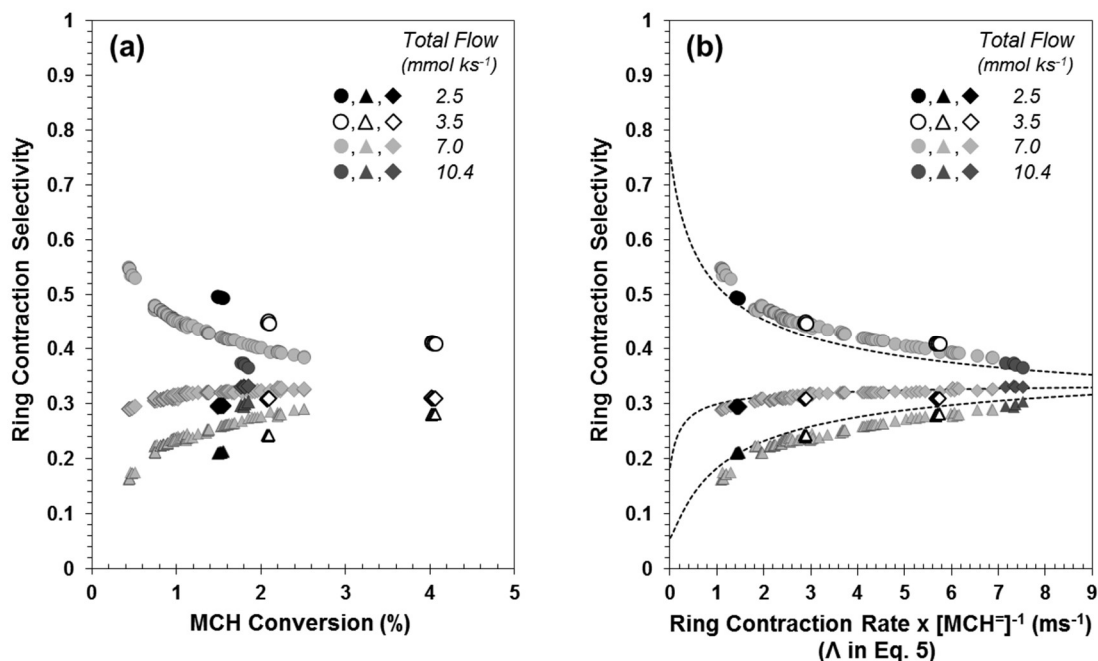
Figure 3. Measured ethylcyclopentane ($\bullet$), 1,3-dimethylcyclopentane ($\blacktriangle$), and 1,2-dimethylcyclopentane ($\blacklozenge$) selectivities as functions of (a) methylcyclohexane conversion and (b) measured ring contraction rate per volume of silica divided to the molar concentration of $MCH^=$ (Λ in Eq. 5) for different total reactant molar flow rates (2.5, 3.5, 7.0 and 10.4 mmol ks^{-1}) on H_4SiW/SiO_2-Pt/Al_2O_3 (Pt$_S$/[H$^+$]$_0$ = 3.3, 0.018 [H$^+$]$_0$ (nm^3-SiO$_2$)$^{-1}$) at several [MCH]/[H$_2$] ratios (0.01 - 0.10) and system pressures (220 - 500 kPa) at 473 K. The dashed lines in (b) are best fits of selectivity data measured on all catalysts (Figure 4) to the functional form of Equation 13.

Ring contraction rates per volume of silica divided by $MCH^=$ concentrations (calculated from the [MCH]/[H$_2$] ratio and $K_{d,mch}$):

$$\Lambda = \frac{r_{rc}}{V_{cat}[MCH^=]} \tag{5}$$

serve as a better benchmark than MCH conversion for comparisons of measured selectivities on different catalysts, because they depend on the activity and coverage of acid sites (like MCH conversion), but are independent of reactant flow rate (unlike MCH conversion). Figure 3b depicts the same data as in Figure 3a, but as a function of Λ instead of MCH conversion. All selectivity ratios are shown to be single-valued functions of Λ, and independent of MCH conversion, [MCH]/[H$_2$] ratio, or pressure. Selectivities are also independent of the central atom in H$_n$XW/SiO$_2$-Pt/Al$_2$O$_3$ mixtures (P, Si, Al, and Co central atoms; (Pt$_s$/H$^+$) = 1.7 - 38) for a given Λ value (Figure 4). These data show that diffusion-enhanced secondary interconversions of primary alkylcyclopentenes isomers (Scheme 1, Steps 5 and 6 shown for 12DMCP$^=$ and ECP$^=$ interconversion) occur within acid domains, driven by their intra-domain concentration gradients, before they convert to alkylcyclopentanes via hydrogen transfer locally at acid sites or via hydrogenation on Pt clusters present at the outer boundary of the acid domain (Scheme 1, Steps 7 and 8). These

56

diffusion-enhanced interconversions obfuscate determinations of intrinsic ring contraction selectivities ($S_{rc,P}$; "P" = ecp, 12, or 13 for ECP, 12DMCP, and 13DMCP) that reflect the ratio of the rate constants for the conversion of $MCH^=$ intermediates to each alkylcyclopentene isomer ($k_{rc,P}K_{p,mch}$) during one surface sojourn to sum of rate constants that combine to give total $MCH^=$ conversion rates ($k_{rc}K_{p,mch}$):

$$S_{rc,P} = \frac{k_{rc,P}}{k_{rc}} .$$ (6)

It is those ratios that we seek here, because they reflect the relative stabilities of the transition states that mediate each of these isomerization events. In what follows, we relate measured selectivities in Figure 3 and Figure 4 to the volumetric MCH conversion rates (Λ) by using diffusion-reaction treatments that also provide a method for extracting intrinsic (i.e. primary) selectivities to the various ring contraction products, while also providing predictive models to describe the selectivities observed in practical implementations of ring contraction catalysis.
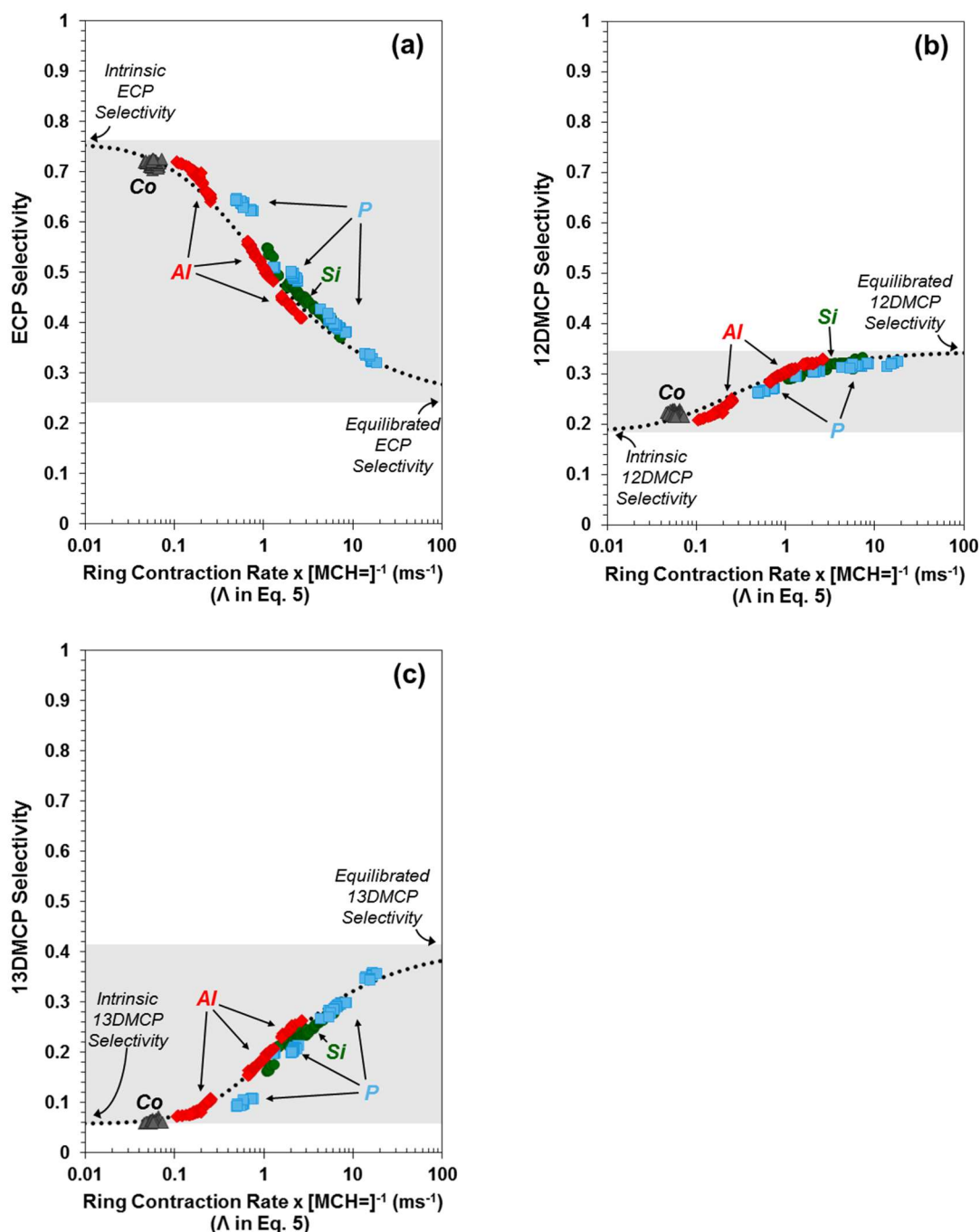
Figure 4. Measured selectivities to (a) ethylcyclopentane, (b) 1,2-dimethylcyclopentane, and (c) 1,3-dimethylcyclopentane among ring contraction products from methylcyclohexane reactants ($S_{m,ecp}$, $S_{m,12}$, and $S_{m,13}$, respectively) as functions of the measured ring contraction rate per volume of catalyst normalized to the molar concentration of MCH$^=$ (Λ, Eq. 5) on Pt/Al$_2$O$_3$ mixtures with H$_3$PW/SiO$_2$ (Pt$_S$/H$^+$ = 5.4, 0.022 H$^+$ (nm^3-SiO$_2$)$^{-1}$; ■), H$_4$SiW/SiO$_2$ (Pt$_S$/H$^+$ = 3.3, 0.018 H$^+$ (nm^3-SiO$_2$)$^{-1}$; ●), H$_5$AlW/SiO$_2$ (Pt$_S$/H$^+$ = 1.7, 0.020 H$^+$ (nm^3-SiO$_2$)$^{-1}$; ◆), and H$_6$CoW/SiO$_2$ (Pt$_S$/H$^+$ = 38, 0.002 H$^+$ (nm^3-SiO$_2$)$^{-1}$; ▲) (reaction conditions: 473 K, 191 – 442 kPa H$_2$). Dotted lines are best fits of the data to the functional form of Equation 13. Shaded regions reflect the range of selectivities accessible to each of the products by changing Λ.

58

The extent of secondary isomerization within acid domains determines, in part, the observed product selectivities; such contributions from secondary reactions depend on the volumetric density of protons within acid domains (ρ_a), on the proclivity for isomerization of each alkylcyclopentene (e.g. $k_{ecp \to 12}K_{p,ecp}$ for ECP$^=$), and on the size and diffusion properties of acid aggregates in bifunctional catalysts. The size and diffusion properties of the aggregates determine the extent to which protons (where primary alkylcyclopentenes form) communicate with metal clusters (where they become less reactive by converting to alkylcyclopentanes), thus controlling the characteristic lifetime of reactive alkylcyclopentene isomers before their conversion to less reactive alkylcyclopentanes. Such "site proximity" effects are seldom enforced or rigorously determined measured in the bound extrudates used in the practice of bifunctional isomerization catalysis.

A more rigorous treatment of such diffusional constraints and of alkylcyclopentene isomers within acid domains requires diffusion-reaction formalisms that identify the relevant dimensionless parameters, in this case, the Thiele modulus (Φ). It is defined for ECP$^=$ consumption (Φ_{ecp}) according to Scheme 1 as:

$$\Phi_{ecp}^2 = \frac{\rho_a R^2}{D_{ecp}} \left(\frac{k_{ecp \to 12}K_{p,ecp}}{1 + K_{p,mch}K_{d,mch}\left(\frac{[MCH]}{[H_2]}\right)} \right) \tag{7}$$

where R is the characteristic distance that defines the diffusion length of acid domains and D_{ecp} is the effective ECP$^=$ diffusivity within these acid domains. This treatment assumes equilibration of MCH-H$_2$-MCH$^=$ and MCH$^=$-MCH*, as well of alkylcyclopentenes with their respective alkoxides; it also considers the surface reactions that convert MCH* to C$_5$ ring alkoxides to be irreversible and the isomerization of ECP* to 13DMCP* to occur only after intervening conversion to one of the other alkoxide isomers because isomerizations events shift alky groups along backbones by one carbon at a time. Thiele moduli for 13DMCP$^=$ and 12DMCP$^=$ are related to that for ECP$^=$ by:

$$\frac{\Phi_{13}^2}{\Phi_{ecp}^2} = \frac{D_{ecp}}{D_{13}} \left(\frac{k_{13 \to 12}K_{p,13}}{k_{ecp \to 12}K_{p,ecp}} \right) = \frac{D_{ecp}}{D_{13}} \frac{K_{13,ecp}}{\sigma_{ecp}} \tag{8}$$

$$\frac{\Phi_{12}^2}{\Phi_{ecp}^2} = \frac{D_{ecp}}{D_{12}} \left(\frac{(k_{12 \to ecp} + k_{12 \to 13})K_{p,12}}{k_{ecp \to 12}K_{p,ecp}} \right) = \frac{D_{ecp}}{D_{12}} \left(\frac{1 + \sigma_{ecp}}{\sigma_{ecp}} \right) K_{12,ecp} \tag{9}$$

Here, $K_{13,ecp}$ and $K_{12,ecp}$ are the equilibrium constants for 13DMCP$^=$-ECP$^=$ and 12DMCP$^=$-ECP$^=$ equilibration, D_{13} and D_{12} are the effective diffusivities of 13DMCP$^=$ and 12DMCP$^=$ within the mesoporous acid domains, and σ_{ecp} is the ratio of the rate constants for the surface elementary steps that convert 12DMCP* to ECP* and 13DMCP* alkoxide isomers:

$$\sigma_{ecp} = \frac{k_{12 \to ecp}}{k_{12 \to 13}}. \tag{10}$$

The Thiele moduli in Equations 7-9, and thus the alkylcyclopentene isomerization rate constants, cannot be determined directly from measured rates and selectivities, as a result of the inherent diffusional corruption of intrinsic selectivities. Substituting Equation 2 into Equation 5 leads to an equation for the volumetric rate of methylcyclohexane ring contraction (to all alkylcyclopentanes) divided by the MCH$^=$ concentration of (Λ) that is consistent with Scheme 1

$$\Lambda = \frac{k_{rc} K_{p,mch}}{1 + K_{p,mch} K_{d,mch} \left(\dfrac{[MCH]}{[H_2]} \right)} \rho_a \tag{11}$$

For a given catalyst, the Thiele modulus for ECP$^=$ consumption (Φ_{ecp}; Eq. 7) is proportional to $\Lambda^{1/2}$:

$$\Phi_{ecp} = \left(\Lambda \frac{R^2}{D_{ecp}} \left(\frac{k_{ecp \rightarrow 12} K_{p,ecp}}{k_{rc} K_{p,mch}} \right) \right)^{1/2} = \Lambda^{1/2} \alpha_{ecp}^{1/2} . \tag{12}$$

The constant of proportionality in Equation 12 (α_{ecp}) depends on the characteristic time for ECP$^=$ diffusion in the mesoporous acid aggregates (R^2/D_{ecp}) and the ratio of the rate constant for ECP$^=$ isomerization to 12DMCP$^=$ ($k_{ecp \rightarrow 12} K_{p,ecp}$) to that for MCH$^=$ ring contraction to all products ($k_{rc} K_{p,mch}$); it does not depend on the H$^+$ density, the MCH or H$_2$ pressures, or the relative magnitude of the two terms in the denominator of Equation 2 (or in Equation 11).

Next, we combine a kinetic treatment based on the elementary steps in Scheme 1 with the diffusion-reaction construct that led to Equations 7-12 and their respective Thiele moduli to develop selectivity expressions for each of the alkylcyclopentene products. In what follows, equilibrium is assumed to prevail among MCH-H$_2$-MCH$^=$ gaseous molecules and MCH$^=$-MCH* and between each alkylcyclopentene isomer and its respective alkoxides. MCH* ring contraction steps are taken to be irreversible and no direct ECP*-13DMCP* interconversion routes are taken into account; all alkylcyclopentenes are assumed to have the same diffusivity within the porous acid domains.

These assumptions lead to selectivities ($S_{m,P}$) for each alkylcyclopentane isomer (derivation in Section 2.6.2):

$$S_{m,P} = S_{rc,P} + \Delta S_P (1 - \eta_+) + \Theta_P (\eta_- - \eta_+) \tag{13}$$

where

$$\Delta S_P = \frac{K_{P,ecp}}{1 + K_{12,ecp} + K_{13,ecp}} - S_{rc,P} \tag{14}$$

is the mole fraction of product "P" among the equilibrated pool of alkylcyclopentene products minus its intrinsic (kinetic) selectivity, η_+ and η_- are the effectiveness factors that describe the extent of secondary isomerization reactions within acid domains, and Θ_P is a

constant that is unique to product "P" and reflects the changes in selectivity due to secondary influences. Equation 13 depends on two effectiveness factors (η_+ and η_-) because secondary isomerization reactions occur via two distinct paths: 12DMCP*-ECP* and 12DMCP*-13DMCP* interconversions (Scheme 1, Step 6a and 6b). The values of η_+ and η_- in Equation 13 do not depend on the identity of P but are sensitive to the value of Φ_{ecp} (Eq. 7) through the relation:

$$\eta_\pm = \frac{3\left(\zeta_\pm \Phi_{ecp} \coth\left(\zeta_\pm \Phi_{ecp}\right) - 1\right)}{\zeta_\pm^2 \Phi_{ecp}^2} \tag{15}$$

for the case of quasi-spherical acid domains. The parameters ζ_+ and ζ_- depend only on σ_{ecp}, $K_{13,ecp}$ and $K_{12,ecp}$:

$$
\begin{aligned}
\zeta_\pm^2 = \frac{1}{2}&\left(1 + \frac{(1+\sigma_{ecp})}{\sigma_{ecp}} K_{12,ecp} + \frac{K_{13,ecp}}{\sigma_{ecp}}\right) \\
&\pm \frac{1}{2}\sqrt{\begin{aligned}&1 + \left(\frac{(1+\sigma_{ecp})}{\sigma_{ecp}} K_{12,ecp}\right)^2 + \left(\frac{K_{13,ecp}}{\sigma_{ecp}}\right)^2 \\ &+ 2\frac{K_{12,ecp}}{\sigma_{ecp}}\left(\frac{K_{13,ecp}}{\sigma_{ecp}} + \sigma_{ecp} - \left(1 + K_{13,12} + K_{13,ecp}\right)\right)\end{aligned}}
\end{aligned} \tag{16}
$$

The choice of Φ_{ecp} in Equation 15, instead of the moduli for 12DMCP$^=$ or 13DMCP$^=$, is arbitrary because all moduli differ only by a constant factor (Eqs. 8 and 9); the alternate use of Φ_{12} or Φ_{13} would change the form and values of ζ_+ and ζ_-, but neither η_+ or η_- (details in Section 2.6.2). The Θ_P term in Equation 13 influences selectivities for intermediate η values (Eq. 12), the value of Θ_P depends on σ_{ecp}, $K_{13,ecp}$, $K_{12,ecp}$, and ΔS_P for two out of the three ring contraction products (the third being calculated by differences because they add up to unity). In the case of ECP$^=$ this relation is:

$$\Theta_{ecp} = \left(\zeta_-^2 - \frac{K_{13,ecp}}{\sigma_{ecp}}\right)\frac{\sigma_{ecp}\Delta S_{13}\left(\zeta_+^2 - \frac{K_{13,ecp}}{\sigma_{ecp}}\right) - \Delta S_{ecp}\left(\zeta_+^2 - 1\right)}{\left(1 - \frac{K_{13,ecp}}{\sigma_{ecp}}\right)\left(\zeta_+^2 - \zeta_-^2\right)} \tag{17}$$

The Θ_P value for 13DMCP$^=$ is proportional to that for ECP$^=$:

$$\Theta_{13} = \Theta_{ecp}\left(\frac{\zeta_-^2 - 1}{\sigma_{ecp}\left(\zeta_-^2 - \frac{K_{13,ecp}}{\sigma_{ecp}}\right)}\right) \tag{18}$$

and the third Θ_P value (Θ_{12}) is calculated by differences ($\Theta_{12} = -(\Theta_{ecp} + \Theta_{13})$). Equations 13 -18 predict that observed selectivities (at differential conditions) depend on more than just the intrinsic selectivities for ring contraction products ($S_{rc,P}$), they also depend on the thermodynamic and kinetic constants for the interconversion of alkylcyclopentenes, and on the characteristic diffusion time in acid domains (R^2/D). Equations 11 and 12 indicate

that measured total volumetric rates of MCH conversion divided by [MCH$^=$] (Λ) reflect catalyst activity per volume of support and the magnitude of the kinetic constants for the interconversion of alkylcyclopentenes. The dashed curves in Figure 3b and the dotted curves in Figure 4 (a-c) represent the regressed fit of the selectivities data in Figure 4 (a-c) over a broad range of MCH and H$_2$ pressures on POM/SiO$_2$-Pt/Al$_2$O$_3$ mixtures with P, Si, Co and Al central atoms to the functional form of Equation 13 while keeping the values of the six independent parameters in Equations 12-18 ($S_{rc,ecp}/S_{rc,12}$, $S_{rc,13}/S_{rc,12}$, $K_{13,ecp}$, $K_{12,ecp}$, α_{ecp}, and σ_{ecp}) constant with composition; the fitted values of the constants are shown in Table 3. The shaded regions in Figure 4 (a-c) reflect the range of selectivities prescribed by Equation 13 for each product according to the values of the fitted parameters in Table 3.

The regressed ($S_{rc,ecp}/S_{rc,12}$) and ($S_{rc,13}/S_{rc,12}$) values in Table 3 are indicative of the predominant formation of non-branching ECP products ($S_{rc,ecp} = 0.76$; $S_{rc,12} = 0.18$; $S_{rc,13} = 0.06$), suggesting that the TS that forms ECP* is more stable than those that form 12DMCP* and 13DMCP* from MCH*. These results are consistent with non-branching C6 alkene isomerizations being more facile than those that change the degree of branching [8,38] and non-branching TS having more substituted and, consequently, more stable cyclopropyl backbones than branching TS (shown in Scheme 2 for MCH$^=$ isomerizations) [2,49]. The values of $K_{12,ecp}$ and $K_{13,ecp}$ are near unity (0.70 and 0.58, respectively) indicating similar concentrations of gaseous alkenes with ECP, 12DMCP, or 13DMCP backbones at equilibrium (and equilibrated C=C bond locations). Values of σ_{ecp} near unity ($\sigma_{ecp} = 0.90$) indicate that the TS for interconverting 12DMCP* and ECP* is similarly as stable as those interconverting 12DMCP* and 13DMCP*.

For diffusion in porous solids resembling partially overlapped sphere packings at large Knudson numbers, effective diffusivities (D_{eA}) can be estimated from the void fraction (ϕ), tortuosity factor (τ), and surface area per unit volume (a_v) of the solid [50]:

$$D_{eA} = \frac{4}{3} \frac{\phi^2}{\tau a_v} \left(\frac{8RT}{\pi M_A} \right)^{1/2} \tag{19}$$

where M_A is the is the molecular weight of the molecule. The assumptions of mesoporous acid domains having diameters approximate to the size of the aggregates used for intimate mixtures prior to pellet formation (~20 μm in diameter), surface areas per unit volume equal to that of the support (0.21 nm^{-1}), and being made up of quasi-spherical particles with a porosity of 0.4 and tortuosity factor of 3 (approximate to those typically measured for spherical packings [51]) and Equation 19 predict a characteristic time for ECP$^=$ diffusion in acid domains (0.6 ms; R^2/D_{ecp} in Equation 12) that is less than 1/50 of the regressed value of α_{ecp} (30.8 ms) and, consequent to Equation 12, rate constants for ECP$^=$ conversion to 12DMCP$^=$ that are ~50 times larger than those for conversion of MCH$^=$ to all ring contraction products. Diffusion limitations corrupt measured selectivities and not measured ring contraction rates because ECP$^=$, 12DMCP$^=$, and 13DMCP$^=$ have much shorter characteristic times for their reaction (($k_{R \to P} K_{p,R}$)$^{-1}$) in acid domains than MCH$^=$ (($k_{rc} K_{p,mch}$)$^{-1}$) and, consequently, much larger Thiele moduli for their consumption.

Table 3. Values of select parameters from Equations 12-18 determined by the regression of the data in Figure 4 (a-c) to the functional form of Equation 13.

	$ECP^=$	$12DMCP^=$	$13DMCP^=$
α_{ecp}	30.8 ms		
σ_{ecp}	0.90		
$K_{12,ecp}$	0.70		
$K_{13,ecp}$	0.58		
$S_{rc,ecp}/S_{rc,12}$	4.20		
$S_{rc,13}/S_{rc,12}$	0.31		
intrinsic selectivity ($S_{rc,P}$)	0.76	0.18	0.06
thermodynamic selectivity ($S_{rc,P}+\Delta S_P$)	0.28	0.35	0.37
Θ_P	0.40	0.04	-0.44

The data in Figure 4 (a-c) suggest that for a given size, proton density, and diffusive properties of an acid domain size, acid strength influences <u>observed (but not intrinsic)</u> selectivities because of concomitant changes in the rate constants for surface elementary steps that interconvert 12DMCP*, ECP*, and 13DMCP* (i.e. σ_{ecp} in Eq. 10 is independent of acid strength) and therefore in the Thiele moduli for secondary reactions (Φ_{ecp}, Eq. 7). This leads to a different extent of secondary interconversions within acid domains acid domains given by η_+ and η_- values in Equation 15, in spite of relative rates of alkylcyclopentoxide formation and interconversion reactions that are unaffected by acid strength. The form of Equation 12 and the data in Figure 4 show that higher and Φ_{ecp} values move selectivities closer to their equilibrium values (the asymptotic selectivity value at the right edge of Figure 4), while asymptotic selectivities at low Φ_{ecp} values reflect the intrinsic kinetics of $MCH^=$ ring contraction after a single surface sojourn at a proton. Similar trends and conclusions are evident for any catalyst property that changes the value of Φ_{ecp}. This includes the distance between metal and acid sites (because the location of the metal defines the edge of the acid domain) (R), the difficulty in traversing the intervening path (effective diffusivity of the porous acid domain) (D_{ecp}), and the proton density (ρ_a). In a manner less obvious from the treatment here for reactions occurring at low $MCH^=$ concentration on an essentially bare ensemble of protons, the extent of interconversion reactions also decreases as such protons become increasingly covered by methylcyclopentoxides ($K_{p,mch}[MCH^-]$), because all reaction rates are lower than in the first-order kinetic regime.

We note that these selectivity effects caused by secondary interconversion artifacts have been often misconstrued in the literature as evidence for a preference for more demanding reactions on stronger acids or in zeolites (that impose a larger diffusive barrier, thus enhancing secondary reactions). Such effects merely reflect the predominant initial formation of the "facile" isomer and diffusion-enhanced secondary interconversions that move products in the directions of their thermodynamic prevalence. Thus, the use of selectivity in probe reactions to assess the acid strength of materials, even at differential conversion, is inappropriate, unless diffusion-enhanced interconversions are eliminated, something that we have been unable to achieve for any materials for two quintessential probe reactions, the bifunctional isomerizations of acyclic [8] and cyclic (this study) alkanes and the acid-catalyzed interconversions of their alkene homologs.

2.3.2. Stabilities of TS Containing Corner-Protonated Bicyclo[3.1.0]hexyl Carbenium Ions

TS structures containing protonated bicyclo[3.1.0]hexyl species were previously proposed for ring contraction reactions of gaseous cyclohexylium [42,52], methylcyclohexylium [41], and 1,2-dimethylcyclohexylium [43] cations and of cyclohexene in zeolite [44] on the basis of DFT calculations. Figure 5 shows the optimized TS structure that mediates cyclohexoxide (CH*) conversion to 1-cyclopentane-methoxide (MCP*) (TS1) on $H_3PW_{12}O_{40}$ clusters. The alkyl shift involves simultaneous breaking of the C_P–C_β bond and forming of the C_P–C_α, therefore C_P, C_α, and C_β, have a triangular geometry at TS1 with C_P being similarly distant to C_α (C_P–C_α = 1.94 Å) and C_β (C_P–C_β = 1.79 Å). The C_α and C_β centers in TS1 have nearly trigonal planar geometries and the C_P center having a trigonal pyramidal geometry, consistent with the short C_α–C_β bond length (C_α–C_β = 1.40 Å) and with C_P needing to act as a nucleophile in attacking C_α during the alkyl shift. The large negative charge for the POM conjugate anion in TS1 (-0.8627 e charge) and the long O_T–C_β and O_B–C_α bond lengths (O_T–C_β = 2.32 Å and O_B–C_α = 2.71 Å; Figure 5) indicate nearly full transfer of the proton to the organic moiety at the TS, consistent with isomerization TS that are ion-pairs [8].
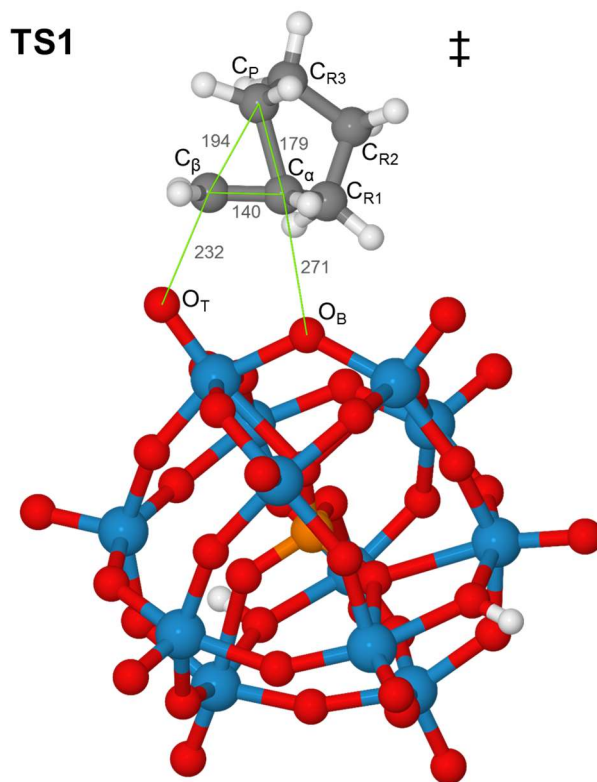
Figure 5. Structure of bicyclo[3.1.0]hexyl type transition state mediating 1-cyclohexoxide (CH*) conversion to 1-cyclopentane-methoxide (MCP*) on $H_3PW_{12}O_{40}$ (TS1). Distances shown in pm.

TS structures that mediate MCH$^=$ conversions to different alkylcyclopentoxide isomers are analogous to TS1 (Figure 5) with one H-atom replaced by a methyl group (Figure 6). The C-atom at which the additional methyl group attaches dictates the stability of the TS and the identity of the product isomer (Scheme 2). Methylation of TS1 at either C_α or C_β gives TS structures with smaller activation energies (referenced to a bare cluster and 1-methylcylcohexene(g)) (68 kJ mol^{-1} and 62 kJ mol^{-1} for TS2 and TS3 on H$_3$PW$_{12}$O$_{40}$, receptively; Scheme 2) than those for TS formed from methylation at other C-atoms (72-82 kJ mol^{-1} for TS4, TS5, TS6, and TS7 on H$_3$PW$_{12}$O$_{40}$; Scheme 2) because the C_α–C_β bond in TS1 resembles a C–C double bond – both of its C centers have sp2 hybridization and its bond length (1.39 Å; Figure 5) is close to that for the C-C double bond in ethene (1.34 Å; [53]) – and benefits similarly from greater amounts of substitution. The smaller activation barrier for ECP* formation (62 kJ mol^{-1} on H$_3$PW$_{12}$O$_{40}$; TS3) relative to those for 12DMCP* formation (75 kJ mol^{-1} and 82 kJ mol^{-1}; TS4 and TS5 on H$_3$PW$_{12}$O$_{40}$, respectively) or 13DMCP* formation (72 kJ mol^{-1} and 74 kJ mol^{-1}; TS6 and TS7 on H$_3$PW$_{12}$O$_{40}$, respectively) is consistent with the predominant formation of non-branching ECP$^=$ products from MCH$^=$ on POM clusters ($S_{rc,ecp} = 0.76$; $S_{rc,12} = 0.18$; $S_{rc,13} = 0.06$; Table 3). The activation barrier for TS2 (68 kJ mol^{-1} on H$_3$PW$_{12}$O$_{40}$), which mediates the formation of 1-methyl-1-methoxide-cyclopentane (1*-1-DMCP), is not kinetically relevant for 11DMCP$^=$ formation since deprotonation of 1*-1-DMCP is extremely difficult as it has quaternary carbon at its β position that cannot undergo β-eliminations. The small amounts of 11DMCP detected during MCH ring contraction reactions on all of the POM samples (< 1 % carbon selectivity at short residence times) suggest that the barrier for 1*-1-DMCP desorption is much larger than those for any of the transition states in Scheme 2 (TS2-TS7).
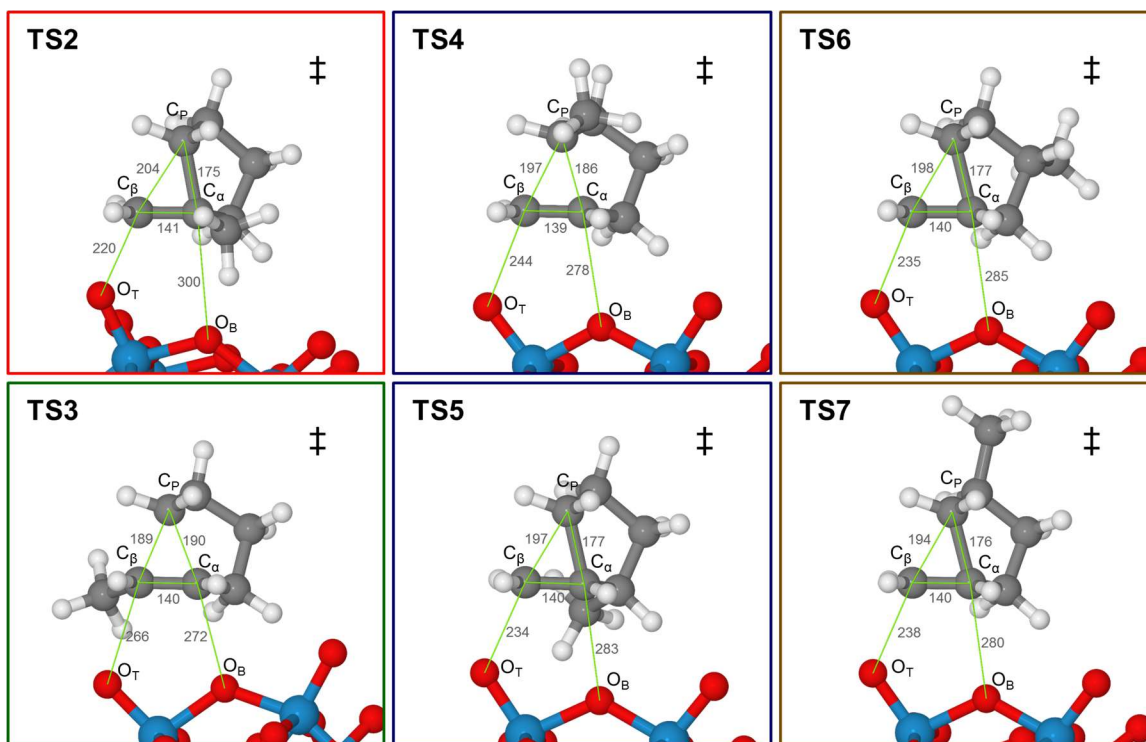
Figure 6. Structures of TS mediating $MCH^=$ ring contractions to 1*-1-DMCP (TS2), ECP* (TS3), 12DMCP* (TS4 and TS5), and 13DMCP* (TS6 and TS7) on $H_3PW_{12}O_{40}$. Distances shown in pm.
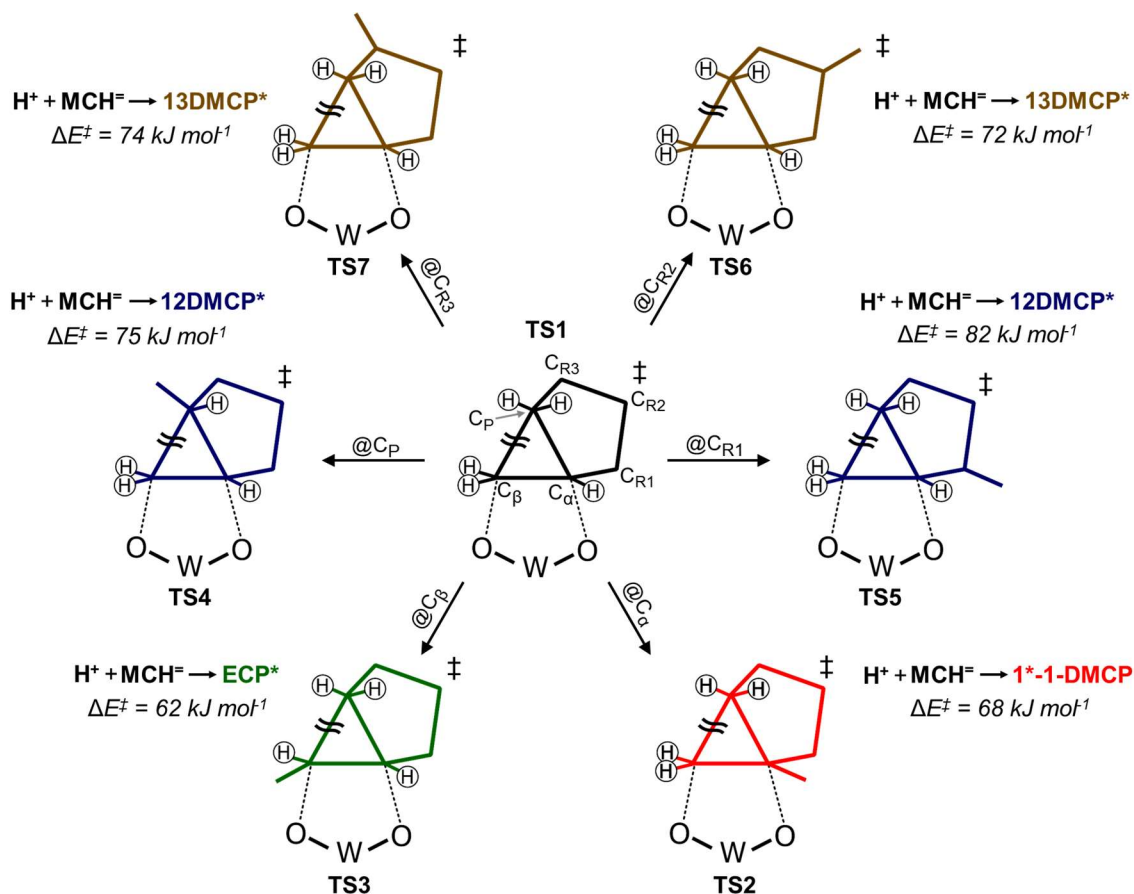
Scheme 2. Formation of MCH$^=$ ring contraction TS by methylation at different carbons atoms in the TS structure for cyclohexoxide (CH*) ring contraction to methylcyclopentoxides (MCP*) (TS1; Figure 5). Activation energies ($\Delta E^{\ddagger}$) are for forming TS on $H_3PW_{12}O_{40}$ and are relative to a bare protons (H$^+$) and gaseous 1-methylcylcohexene and have units of kJ mol^{-1}.

Figure 7 shows the energies of the ring contraction transition states that mediate MCH$^=$ conversion to ECP$^=$ (TS3), 12DMCP$^=$ (TS4 and TS5), and 13DMCP$^=$ (TS6 and TS7) formation (referenced to a bare POM proton and gaseous 1-methylcylcohexene) as a function of DPE for $H_{8-n}X^{n+}W_{12}O_{40}$ clusters (X^{n+} = P^{5+}, Si^{4+}, Al^{3+}, and Co^{2+}). Energy barriers for all ring contraction TS structures are larger on weaker acids, because of their less stable conjugate anions at these ion-pair transition states. Differences in energy barriers among TS structures are nearly independent of acid composition and, thus, acid strength for the POM clusters (as shown by their TS energies being similarly sensitive to DPE in Figure 7), indicating that the difficulty of a ring contraction reaction is not indicative of the sensitivity of its energy barrier to changes in DPE. Furthermore, the similar sensitivities of activation energies for all ring contraction TS to changes in DPE indicate that intrinsic ring contraction selectivities, which reflect the kinetics of MCH$^=$ ring contraction after a single surface sojourn at a proton, are independent of acid strength, consistent with the similar selectivity curves in Figure 4 for the different POM clusters that were accurately described

(the dashed lines in Figure 4) using the same set of intrinsic selectivities for each of the acids.
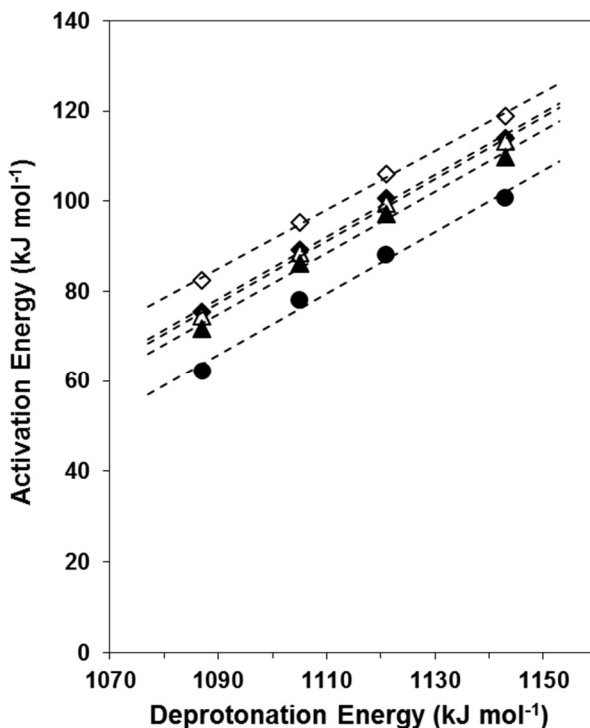
Figure 7. Calculated activation energies as functions of DPE for MCH$^=$ ring contractions to ECP$^=$ (●; TS3), 12DMCP$^=$ (◆ and ◇; TS4 and TS5, respectively), and 13DMCP$^=$ (▲ and △; TS6 and TS7, respectively) on H$_{8-n}$X^{n+}W$_{12}$O$_{40}$ (X^{n+} = P^{5+}, Si^{4+}, Al^{3+}, and Co^{2+}). Activation energies are with respect to bare clusters (H$^+$) and 1-methylcylcohene (g). TS structures are shown in Figure 6.

2.3.3. Acid Strength Effects on Methylcyclohexene Ring Contraction Rates

The interpretation of observed selectivities in terms of individual MCH* isomerization routes allows us to examine next the effects of acid strength (varied though changes in the POM central atom) on overall and individual isomerization rate constants. Figure 8 shows $k_{rc}K_{p,mch}$ and $K_{p,mch}$ values for each POM/SiO$_2$-Pt/Al$_2$O$_3$ mixture (regressed from data in Figure 1 to the form of Eq. 2) as a function of their calculated DPE values [5]. POM clusters with higher-valent central atoms (and fewer protons) give smaller DPE, because of their lower electron density, which leads to more stable conjugate anions. The values of $k_{rc}K_{p,mch}$ increase exponentially with decreasing DPE values (Figure 8) because the full ion-pairs at ring contraction TS (see Section 2.3.2) benefit from more stable conjugate anions. In contrast, $K_{p,mch}$ values are essentially insensitive to DPE because

methylcyclohexoxides are largely uncharged and thus unaffected by the stability of conjugate anions.
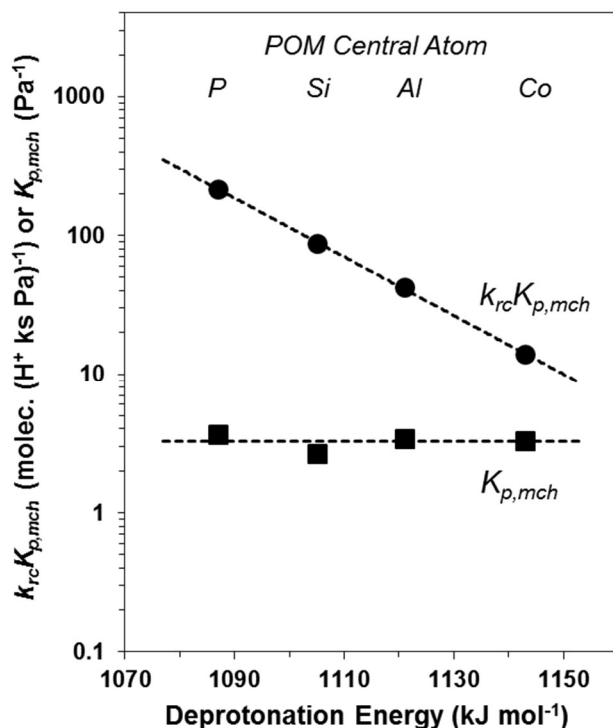
Figure 8. Measured methylcyclohexene ring contraction rate constants ($k_{rc}K_{p,mch}$; ●) and equilibrium constants for MCH⁼ protonation to MCH* ($K_{p,mch}$; ■) for methylcyclohexane reactants as a function of deprotonation energies for $H_{8-n}X^{n+}W_{12}O_{40}$ (X = P, Si, Al, Co) (473 K) mixtures with Pt/SiO$_2$. The upper dashed line is the regressed linear fit of $k_{rc}K_{p,mch}$ values and the lower one the average of $K_{p,mch}$ values.

Scheme 3 shows the reaction coordinate for MCH⁼ ring contraction on Brønsted acid sites and the terms that determine the free energy barrier for the lumped kinetic parameter ($k_{rc}K_{p,mch}$). In the formalism of transition state theory, free-energy barriers for $k_{rc}K_{p,mch}$ ($\Delta G^{\ddagger}_{app}$ in Scheme 3) include the free energies for protonation of the lumped gaseous MCH⁼ isomers for form MCH* lumped alkoxide species ($\Delta G_{p,mch}$ in Scheme 3) and to rearrange these MCH* species to form an ensemble of TS structures able to mediate ring contraction events from an equilibrated mixture of adsorbed MCH* alkoxides ($\Delta G^{\ddagger}_{rc}$ in Scheme 3). The $k_{rc}K_{p,mch}$ value reflects the sum of rate constants for the formation of each ring contraction product ($k_{rc,P}K_{p,mch}$, Eq. 3), while $\Delta G^{\ddagger}_{app}$ reflects the additive contributions of the free energies of all ring contraction TS structures ($G^{\ddagger}_{mch\leftrightarrow P}$ in Scheme 3,) relative to those for lumped gaseous MCH⁼ isomers and to an uncovered H⁺ (G_{mch} in Scheme 3):

$$\Delta G^{\ddagger}_{app} = -RT \ln \left(\sum_P \exp \left(\frac{-\left(G^{\ddagger}_{mch \leftrightarrow P} - G_{mch} \right)}{RT} \right) \right) = -RT \ln \left(\sum_P \exp \left(\frac{-\Delta G^{\ddagger}_{app,P}}{RT} \right) \right) \quad (20)$$

The observed exponential effects of DPE on $k_{rc}K_{p,mch}$ can then be interpreted in terms of:

$$-RT \frac{d\left(\ln \left(k_{rc}K_{p,mch} \right) \right)}{d(DPE)} = \frac{d\left(\Delta G^{\ddagger}_{app} \right)}{d(DPE)} = \sum_P S_{rc,P} \frac{d\left(\Delta G^{\ddagger}_{app,P} \right)}{d(DPE)} \quad (21)$$

where $\Delta G^{\ddagger}_{app,P}$ is the apparent free-energy barrier to form the TS that gives the ring contraction product "P" and $S_{rc,P}$ is the intrinsic selectivity to form product "P" from MCH$^=$. The right side of Equation 21 shows that measured $d(\Delta G^{\ddagger}_{app})/d(DPE)$ values are given by the selectivity-weighted average of these derivatives for each ring contraction product. Ring contraction TS structures (Scheme 2) are similar on POM clusters with different central atom [8,54]; consequently, $d(\Delta G^{\ddagger}_{app})/d(DPE)$ values predominantly reflect concomitant effects of DPE on activation energies, because of their similar activation entropies [5,54] and Equation 21 becomes:

$$-RT \frac{d\left(\ln \left(k_{rc}K_{p,mch} \right) \right)}{d(DPE)} = \frac{d\left(E_{app} \right)}{d(DPE)} = \sum_P S_{rc,P} \frac{d\left(E_{app,P} \right)}{d(DPE)} \quad (22)$$

Here, E_{app} and $E_{app,P}$ are the respective apparent activation barriers for $k_{rc}K_{p,mch}$ and the $k_{rc,P}K_{p,mch}$ terms for each product "P". The linear dependence of $\ln(k_{rc}K_{p,mch})$ on DPE (Figure 8) demonstrates that $d(E_{app})/d(DPE)$ does not depend on acid strength for POM clusters that differ in reactivity ($k_{rc}K_{p,mch}$) by a factor of 15. Measured $d(E_{app})/d(DPE)$ values (0.19; Figure 8) are much smaller than unity, indicating that E_{app} values change vary by less than the concomitant changes in DPE, therefore, ring contraction TS are able to partially attenuate the effects of changes in DPE on activation barriers. The form of Equation 22 indicates that $d(E_{app})/d(DPE)$ values that are insensitive to DPE require that the stability of all ring contraction TS depend similarly on DPE (with $d(E_{app,P})/d(DPE) =$ 0.19 for all products). As a result, intrinsic ring contraction selectivities ($S_{rc,P}$) cannot depend on DPE (and acid strength). This is consistent with the similar selectivity curves in Figure 4 for the different POM clusters that were accurately described by the same set of intrinsic selectivities (the dashed lines in Figure 4) and with calculated activation energies for all ring-contraction TS structures being similarly sensitive to changes in DPE (Figure 7).
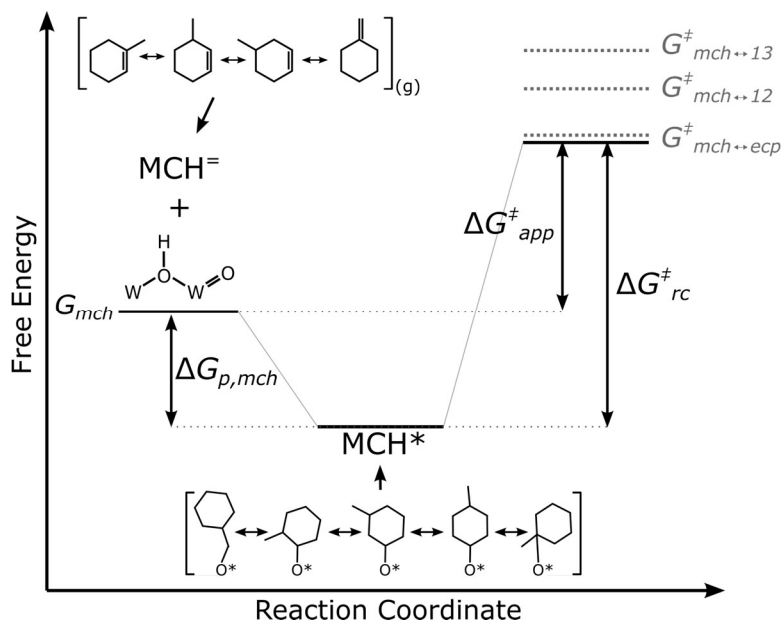
Scheme 3. Reaction coordinate diagram depicting the free energies of MCH$^=$ and MCH* regioisomer groups and the free energies of the ring contraction transition states accessible to MCH*. Free energy barriers for $k_{rc}K_{p,mch}$ ($\Delta G^\ddagger_{rc,app}$) and k_{rc} ($\Delta G^\ddagger_{rc}$) and the free energy difference for $K_{p,mch}$ ($\Delta G_{p,mch}$) are also shown.

Born-Haber thermochemical cycles provide instructive constructs to dissect activation barriers into those for hypothetical steps that correspond to properties of the catalysts (e.g., DPE) and molecules (e.g. proton affinities of gaseous species) involved [8,54–57]. Specifically, activation barriers for MCH$^=$ conversion to ECP$^=$ includes hypothetical steps (Scheme 4) that deprotonate the POM cluster (*DPE*), reacts a gaseous H$^+$ with MCH$^=$(g) to form a gaseous analog of the cation at the TS ($E_{gas,ecp}$), and the interaction of the latter with POM conjugate anion to form ion-pair TS for ring contraction ($E_{int,ecp}$):

$$E_{app,ecp} = DPE + E_{gas,ecp} + E_{int,ecp} \qquad (23)$$

Thus, DPE effects on $E_{app,ecp}$ solely reflect its concomitant effects on $E_{int,ecp}$ and reflects the extent to which the TS cation recovers through interactions with the conjugate anion the energy required to deprotonate the acid moiety. Such interactions recover a large fraction of the ionic component of DPE values (the classical electrostatic interactions as ions move relative to one another) and a much smaller fraction of covalent component of DPE (any reorganization, structural or electronic, induced by the proximity of two species at their equilibrium distances) [58].

The replacement of $E_{app,P}$ in Equation 22 with the analogs of Equation 23 for each ring contraction product leads to an equation for the sensitivity of $k_{rc}K_{p,mch}$ values to DPE:

$$\frac{d\left(E_{app}\right)}{d\left(DPE\right)} = 1 + \sum_{P} S_{rc,P} \frac{d\left(E_{int,P}\right)}{d\left(DPE\right)} \tag{24}$$

The individual $d(E_{gas,P})/d(DPE)$ term for each product is absent because $E_{gas,P}$ is a property of gaseous species (Eq. 19). In Section 3.3, we showed that intrinsic $MCH^=$ ring contraction selectivities ($S_{rc,P}$ in Eq. 24) did not depend on DPE. The $\ln(k_{rc}K_{p,mch})$ values depend linearly on DPE (Figure 8), confirming that $d(E_{app})/d(DPE)$ and all terms in the summation in Equation 21 are constants that do not depend on DPE. We conclude, as inferred earlier, that $E_{int,P}$ values and $MCH^=$ ring contraction TS energies for all products depend similarly on DPE. Equation 24 then becomes:

$$\frac{d\left(E_{app}\right)}{d\left(DPE\right)} = 1 + \frac{d\left(E_{int,P}\right)}{d\left(DPE\right)} \tag{25}$$

The value of $d(\ln(k_{rc}K_{p,mch}))/d(DPE)$ (Figure 8; 473 K) corresponds to a $d(E_{int,P})/d(DPE)$ value of -0.8 indicating that each ring contraction TS recovers 80% of the DPE difference among these acids. These values of $d(E_{int,P})/d(DPE)$ (smaller than -1) reflect gaseous protons that interact more effectively with POM anions than the cationic moieties at ring contraction TS; such interactions depend, in large part, to the extent to which the positive charge is localized at the proton and the TS. The similar effects of DPE on the stability of ion-pairs that mediate the different ring contraction events indicates that the charge is similarly distributed among their organic cations.
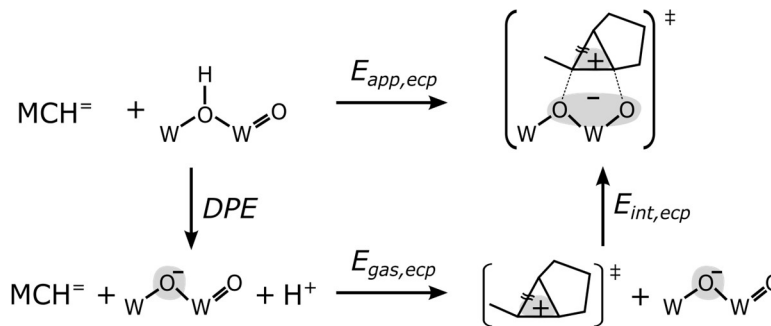
Scheme 4. Thermochemical cycle for formation of the ring contraction transition state leading to ethylcyclopentene on POM acid catalysts.

2.3.4. Contrasting DPE Effects on Isomerization of Methylcyclohexene and Hexenes Rate Constants

Rate constants for ring contraction of $MCH^=$ to all products ($k_{rc}K_{p,mch}$; Figure 9) depend more sensitively on DPE than for 2-methylpentene ($2MP^=$) isomerization ($k_{isom}K_{p,2mp}$; values from [8] shown in Figure 9) on the same POM/SiO$_2$-Pt/Al$_2$O$_3$ bifunctional catalysts, suggesting that the TS that mediate $2MP^=$ isomerization reactions

are able to recover a larger fraction of changes in DPE. Therefore, differences between $2MP^=$ and $MCH^=$ rate constants are larger on weaker acids with larger DPE.

As in the case of the TS structures that mediate $MCH^=$ ring contraction (Section 3.2), those for $2MP^=$ isomerization are expected to involve entropy changes that do not depend on the POM central atom [8], making pre-exponential factors similar on all acid catalysts. As a result, the exponential effects of DPE on $k_{isom}K_{p,2mp}$ and $k_{rc}K_{p,mch}$ (Figure 9) reflect the sensitivity of their apparent activation barriers to changes in DPE ($d(E_{app})/d(DPE)$; Eq. 22). The data in Figure 9 give $d(E_{app})/d(DPE)$ values of 0.10 and 0.19 for $k_{isom}K_{p,2mp}$ and $k_{rc}K_{p,mch}$; values much less than unity suggest that isomerization and ring contraction TS attenuate the effects of DPE changes on activation barriers.

Smaller $d(E_{app})/d(DPE)$ values for $2MP^=$ than $MCH^=$ and Equation 25 indicate that interactions between cationic moieties and conjugate anions at $2MP^=$ isomerization TS recover a larger fraction of the additional energy required to deprotonate weaker acids than those at $MCH^=$ ring contraction TS ($d(E_{int})/d(DPE)$ = -0.89 for $2MP^=$ (89% recovered) and -0.81 for $MCH^=$ (81% recovered)). The ability of cationic moieties at TS to interact with POM anions depends, in part, on the degree to which positive charge is delocalized on these cations. TS involving cationic moieties with more localized positive charges and that place those charges nearer to the POM anion interact more strongly with the anion, and their energies are less affected by changes in DPE, than transition states involving cationic moieties with more diffuse positive charges. Therefore, $k_{isom}K_{p,2mp}$ values that are less sensitive than $k_{rc}K_{p,mch}$ values to changes in DPE suggest that $2MP^=$ isomerization TS contain cationic moieties that are more "proton-like" than those for $MCH^=$ ring contraction TS.
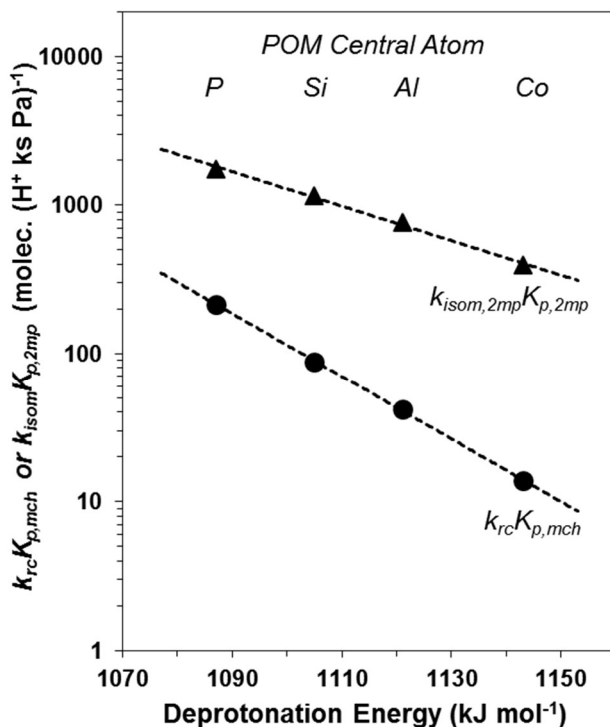
Figure 9. Methylcyclohexene ring contraction rate constants ($k_{rc}K_{p,mch}$; ●) reported here and 2-methylpentene isomerization rate constants ($k_{isom}K_{p,2mp}$; ▲) reported in [8] as a function of deprotonation energies for $H_{8-n}X^{n+}W_{12}O_{40}$ (X = P, Si, Al, Co) (473 K) mixtures with Pt/SiO$_2$. The dashed lines are the regressed linear fits of rate constant values.

2.4. Conclusions

The effects of acid strength on reactivity and of acid strength and site proximity on selectivity are demonstrated using methylcyclohexane ring contraction reactions on well-defined solid Brønsted acids in mixtures with Pt/Al$_2$O$_3$ co-catalysts. When present in sufficient amounts, metal sites equilibrate dehydrogenation-hydrogenation reactions of reactant and product alkanes-alkenes and provide a low and constant concentration of alkenes outside of all acid domains. Measured rate-data were interpreted mechanistically in order to determine rate constants for the total conversion of methylcyclohexene ring contraction ($k_{rc}K_{p,mch}$) normalized to the number of reactive H$^+$ on Keggin POM clusters. These rate constants reflect the stabilities of ion-pair transition states, which mediate kinetically-relevant methylcycloalkoxide ring contraction steps, relative to an equilibrated pool of gaseous reactant methylcyclohexenes and unoccupied acid sites. Activation barriers for ring contraction reactions to all products increase with increasing DPE on Keggin POM because cationic organic fragments at all ring contraction transition states recover only a portion of the additional energy required to deprotonate weaker acids.

74

Activation barriers for ring contraction reactions are more sensitive to changes in DPE than those reported previously [8] for 2-methylpentene isomerization because ring contraction transition states have greater positive charge delocalization on their cationic organic fragments than those that mediate 2-methylpentene isomerization reactions.

Measured ring contraction selectivities at differential methylcyclohexane conversions depend only on the total ring contraction rate per volume of catalyst divided by [MCH^-] (a surrogate for the density and activity of acid sites in acid domains) for Keggin POM clusters supported on mesoporous SiO_2. This reflects intrinsic ring contraction selectivities for branched and un-branched products and those for secondary isomerizations that interconvert ring contraction products that are independent of acid strength. Changes in acid strength affect measured ring contraction selectivities only when such changes also change the value of the Thiele moduli for $ECP^=$ consumption (Φ_{ecp}) and, concomitantly, the extent of secondary isomerization reactions among ring contraction products within acid not by changing the relative rates of alkylcyclopentoxide formation from methylcyclohexene at acid sites. At low values of Φ_{ecp}, measured selectivities approach those predicted by the intrinsic rates of alkylcyclopentoxide formation from methylcyclohexene, and at high values measured selectivities approach those predicted for an equilibrated mixture of alkylcyclopentene products. Such effects are expected for any change in catalyst property that changes Φ_{ecp}. Consequently, increasing site proximity among metal and acid sites, which decreases the characteristic length of the acid domain, decreasing density of acid sites in the acid domain, increasing the diffusivity of products in the catalyst support, decreasing the fraction of uncovered acid sites covered, or decreasing the acid strength of the catalyst will all shift measured selectivities in the same direction: towards those predicted by the intrinsic rates of alkylcyclopentoxide formation from methylcyclohexene.

2.5. Abbreviations

12DMCP$^=$, 13DMCP$^=$, ECP$^=$, MCH$^=$	Lumped chemical pseudo-species made up of alkene regioisomers that share the same carbon skeleton and only differ in the position of the double bond.
12DMCP*, 13DMCP*, ECP*, MCH*	Lumped chemical pseudo-species made up of alkoxide regioisomers that share the same carbon skeleton and only differ in the position of the surface attachment.
a_v	Surface area per unit volume of the mesoporous acid aggregate (here silica).
D_P	Effective diffusivity of product "P" ("P" = ecp, 12, or 13 for ECP$^=$, 12DMCP$^=$, and 13DMCP$^=$, respectively) in the mesoporous acid aggregate.
$K_{d,mch}$	Equilibrium constant for MCH dehydrogenation to MCH$^=$.
$K_{p.mch}$	Equilibrium constant for MCH$^=$ protonation to MCH*.
$K_{p,P}$	Equilibrium constant for product "P" protonation. ("P" = ecp, 12, or 13 for ECP$^=$ to ECP*, 12DMCP$^=$ to 12DMCP*, and 13DMCP$^=$ to 13DMCP*, respectively).
$K_{P,P'}$	Equilibrium constant for the equilibration of product "P" and product "P'" ("P" or "P'" = ecp, 12, or 13 for ECP$^=$, 12DMCP$^=$, and 13DMCP$^=$, respectively)
$k_{P \rightarrow P'}$	Rate constant for "P" isomerization to product "P'" ("P" or "P'" = ecp, 12, or 13 for ECP*, 12DMCP*, and 13DMCP*, respectively)
k_{rc} k_{rc}	Rate constant for MCH* ring contraction to all products.
$k_{rc,P}$	Rate constant for MCH* ring contraction to product "P".
R	Characteristic length of acid domains.
r_{rc}	Rate of MCH ring contraction to all alkylcyclopentane isomers.
$r_{rc,P}$	Rate of MCH ring contraction to product "P"
$S_{m,P}$	Measured selectivity to product "P".
$S_{rc,P}$	Intrinsic MCH* ring contraction selectivity to product "P"
V_{cat}	Total volume of the acid catalyst.
α_{ecp}	Ratio of the Thiele modulus for ECP$^=$ consumption squared to Λ.

ζ_+ and ζ_-	Constants that relate the Thiele modulus for ECP$^=$ consumption to those for all secondary isomerization reactions. The values of these constants depend explicitly on σ_{ecp} and $S_{eq,P}$.
η_+ and η_-	Effectiveness factors that describe the extent of secondary isomerization reactions within acid domains.
Θ_P	A constant unique to product "P" that affects selectivities to product "P" when η_+ and η_- are between extremes.
Λ	Rate of MCH ring contraction to all alkylcyclopentane isomers per volume of acid catalyst divided by the concentration of MCH$^=$
ρ_a	Volumetric density of Brønsted acid sites in acid domains.
σ_{ecp}	Ratio of the rate constant for 12DMCP* isomerization to ECP* over that for 12DMCP* isomerization to 13DMCP*.
τ	Tortuosity factor in the mesoporous acid aggregate.
ϕ	Void fraction in the mesoporous acid aggregate.
Φ_P	Thiele modulus for consumption of product "P" via secondary isomerization reactions.

2.6. Supporting Information

2.6.1. Titration results for H4SiW.
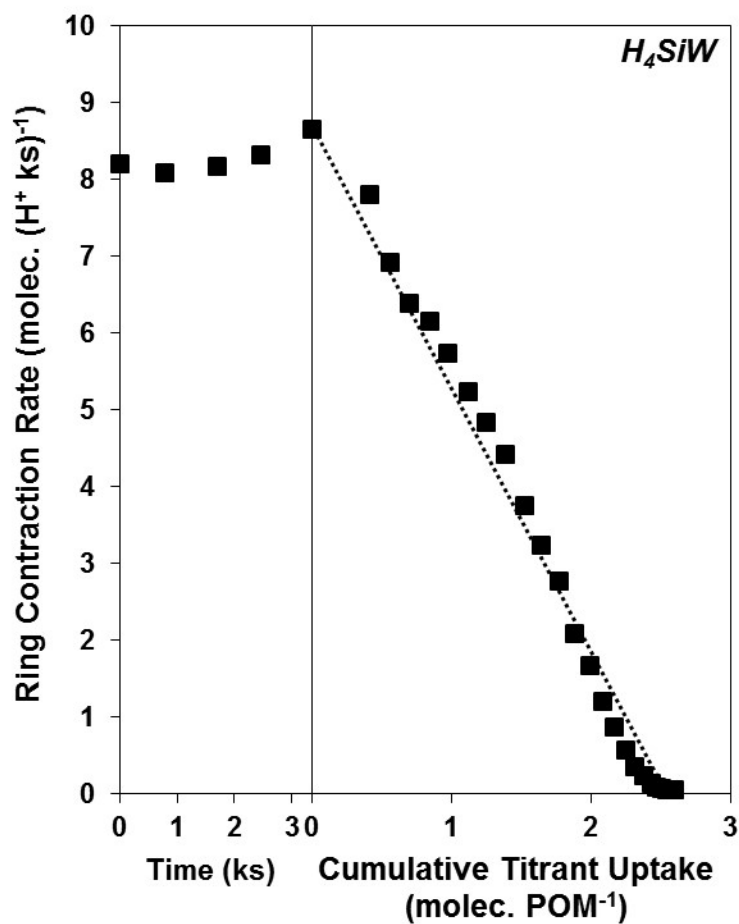
Figure S1-1. Total dehydration turnover rates on H_4SiW/SiO_2 as a function of time before 2,6-di-*tert*-butylpyridine injection (4.0 kPa MCH and 218 kPa H_2) and as a function of cumulative titrant uptake (4.0 kPa MCH and 218 kPa H_2, 1 Pa 2,6-di-*tert*-butylpyridine).

2.6.2. Derivation of Ring Contraction Selectivity Equations

Here we show the derivation for Equation 13 from the continuity equations for each product. Here, equilibrium is assumed to prevail among MCH-H_2-MCH$^=$ gaseous molecules and MCH$^=$-MCH* and between each alkylcyclopentene isomer and its respective alkoxides. We further assume that ring contraction reactions are irreversible, and that there are no concentration gradients of MCH$^=$ in acid domains. In the following $[a]_{r,z}$ gives the concentration of species "a" at radius r inside an acid domain located at point z along the catalyst bed and $[a]_{R,z}$ gives the concentration of species "a" at the outer radius of an acid domain located at point z along the catalyst bed.

Acid Domain
Dimensionless Concentrations:

$$\frac{\left[ECP^=\right]_{r,z}}{\phi_{ecp}^s} = \frac{\left[MCH^=\right]_{R,z} k_{rc,ecp} K_{p,mch}}{k_{ecp\to12} K_{p,ecp}}$$

$$\frac{\left[12DMCP^=\right]_{r,z}}{\phi_{12}^s} = \frac{\left[MCH^=\right]_{R,z} k_{rc,12} K_{p,mch}}{k_{ecp\to12} K_{p,ecp} K_{12,ecp} + k_{12\to13} K_{p,12}}$$

$$\frac{\left[13DMCP^=\right]_{r,z}}{\phi_{13}^s} = \frac{\left[MCH^=\right]_{R,z} k_{rc,13} K_{p,mch}}{k_{12\to13} K_{p,12} K_{12,13}}$$

(26)

Simplify Naming:

$$MCH^= \to a \;;\; ECP^= \to b \;;\; 12DMCP^= \to c \;;\; 13DMCP^= \to d$$

$$\frac{[b]_{r,z}}{\phi_b^s} = \frac{[a]_{R,z} k_{ab}}{k_{bc}}$$

$$\frac{[c]_{r,z}}{\phi_c^s} = \frac{[a]_{R,z} k_{ac}}{k_{bc} K_{cb} + k_{cd}}$$

(27)

$$\frac{[d]_{r,z}}{\phi_d^s} = \frac{[a]_{R,z} k_{ad}}{k_{cd} K_{cd}}$$

Dimensionless Length:

$$\xi = \frac{r}{R}$$

(28)

Thiele Moduli:

$$\Phi_b^2 = \frac{\rho_a R^2}{D_b} k_{bc}$$

$$\Phi_c^2 = \frac{\rho_a R^2}{D_c}\left(k_{bc} K_{cb} + k_{cd}\right)$$

(29a-c)

$$\Phi_d^2 = \frac{\rho_a R^2}{D_d} k_{cd}\left(K_{cd}\right)^{-1}$$

where R is the radius of the acid domain, ρ_a the density of acid sites in silica support, D_b, D_c, and D_d are respectively the effective diffusivities of ECP=, 12DMCP=, and 13DMCP= in the silica support.

Non-dimensional parameters:

$$\alpha_{cb} = \left(\frac{k_{ab}}{k_{ac}}\right) \quad \alpha_{cd} = \left(\frac{k_{ad}}{k_{ac}}\right) \quad \sigma_{cb} = \left(\frac{k_{cb}}{k_{cb} + k_{cd}}\right) \tag{30}$$

Continuity Equations (slab geometry):

$$\frac{d^2 \phi_b^s}{d\xi^2} = -\Phi_b^2 \left(1 + \left(\frac{\sigma_{cb}}{\alpha_{cb}}\right) \phi_c^s - \phi_b^s\right)$$

$$\frac{d^2 \phi_c^s}{d\xi^2} = -\Phi_c^2 \left(1 + \alpha_{cb}\, \phi_b^s + \alpha_{cd}\, \phi_d^s - \phi_c^s\right) \tag{31}$$

$$\frac{d^2 \phi_d^s}{d\xi^2} = -\Phi_d^2 \left(1 + \left(\frac{1 - \sigma_{cb}}{\alpha_{cd}}\right) \phi_c^s - \phi_d^s\right)$$

Continuity Equations (spherical geometry):

$$\frac{1}{\xi^2}\frac{d}{d\xi}\left[\xi^2 \frac{d\phi_b^s}{d\xi}\right] = -\Phi_b^2 \left(1 + \left(\frac{\sigma_{cb}}{\alpha_{cb}}\right) \phi_c^s - \phi_b^s\right)$$

$$\frac{1}{\xi^2}\frac{d}{d\xi}\left[\xi^2 \frac{d\phi_c^s}{d\xi}\right] = -\Phi_c^2 \left(1 + \alpha_{cb}\, \phi_b^s + \alpha_{cd}\, \phi_d^s - \phi_c^s\right) \tag{32}$$

$$\frac{1}{\xi^2}\frac{d}{d\xi}\left[\xi^2 \frac{d\phi_d^s}{d\xi}\right] = -\Phi_d^2 \left(1 + \left(\frac{1 - \sigma_{cb}}{\alpha_{cd}}\right) \phi_c^s - \phi_d^s\right)$$

Boundary Conditions:

$$\left.\frac{d\phi_b^s}{d\xi}\right|_{\xi=0} = \left.\frac{d\phi_c^s}{d\xi}\right|_{\xi=0} = \left.\frac{d\phi_d^s}{d\xi}\right|_{\xi=0} = 0$$

$$\phi_b^s(1) = \frac{[b]_{R,z}\, k_{bc}}{[a]_{R,z}\, k_{ab}} = G_b$$

$$\phi_c^s(1) = \frac{[c]_{R,z}\, (k_{bc}K_{cb} + k_{cd})}{[a]_{R,z}\, k_{ac}} = G_c \tag{33}$$

$$\phi_d^s(1) = \frac{[d]_{R,z}\, k_{cd}\, (K_{cd})^{-1}}{[a]_{R,z}\, k_{ad}} = G_d$$

Rates (moles/site):

$$r_b = -\left(\frac{s_a}{V_{cat}}\right)\frac{D_b}{\rho_a}\frac{d\,[b]_{r,z}}{dr}\bigg|_{r=R} = -\frac{[a]_{R,z}\,k_{ab}}{\Phi_b^2}\frac{d\phi_b^s}{d\xi}\bigg|_{\xi=1} = -\frac{[a]_{R,z}\,k_{ac}\,(\alpha_{cb})}{\Phi_b^2}\frac{d\phi_b^s}{d\xi}\bigg|_{\xi=1}$$

$$r_d = -\frac{[a]_{R,z}\,k_{ad}}{\Phi_d^2}\frac{d\phi_d^s}{d\xi}\bigg|_{\xi=1} = -\frac{[a]_{R,z}\,k_{ac}\,(\alpha_{cd})\,K_{cd}}{\Phi_c^2}\frac{d\phi_d^s}{d\xi}\bigg|_{\xi=1} \tag{34}$$

$$r_{tot} = -\frac{[a]_{R,z}\,k_{ac}}{\Phi_c^2}\left(\frac{d\phi_c^s}{d\xi}\bigg|_{\xi=1} + \left(\frac{\alpha_{cb}K_{cb}}{\sigma_{cb}}\right)\frac{d\phi_b^s}{d\xi}\bigg|_{\xi=1} + \frac{\alpha_{cd}K_{cd}}{(1-\sigma_{cb})}\frac{d\phi_d^s}{d\xi}\bigg|_{\xi=1}\right)$$

Differential Selectivity towards b:

$$\frac{dS_{b,meas}}{dX} = -\left(\frac{k_{ab}}{k_{ab}+k_{ac}+k_{ad}}\right)\frac{1}{\Phi_b^2}\frac{d\phi_b^s}{d\xi}\bigg|_{\xi=1} = -\frac{S_{b,0}}{\Phi_b^2}\frac{d\phi_b^s}{d\xi}\bigg|_{\xi=1} \tag{35}$$

We are unable to solve the coupled BVP directly, therefore, we guess a solution for the functional form of the concentration profiles based on the solution found for simpler systems (i.e. a system in which only two products form and can interconvert).

Guess of functional forms of concentration profiles and their derivatives for a slab geometry:

$$\phi_x^s(\xi) = \varepsilon_x\,\xi^2 + \omega_x + \gamma_{x1}\left(\frac{\cosh(\xi\cdot\Phi_{eff,1})}{\cosh(\Phi_{eff,1})}\right) + \gamma_{x2}\left(\frac{\cosh(\xi\cdot\Phi_{eff,2})}{\cosh(\Phi_{eff,2})}\right) \tag{36}$$

$$\phi_x^s{}'(\xi) = 2\varepsilon_x\,\xi + \gamma_{x1}\Phi_{eff,1}\left(\frac{\sinh(\xi\cdot\Phi_{eff,1})}{\cosh(\Phi_{eff,1})}\right) + \gamma_{x2}\Phi_{eff,2}\left(\frac{\sinh(\xi\cdot\Phi_{eff,2})}{\cosh(\Phi_{eff,2})}\right) \tag{37}$$

$$\phi_x^s{}''(\xi) = 2\varepsilon_x + \gamma_{x1}\Phi_{eff,1}^2\left(\frac{\cosh(\xi\cdot\Phi_{eff,1})}{\cosh(\Phi_{eff,1})}\right) + \gamma_{x2}\Phi_{eff,2}^2\left(\frac{\cosh(\xi\cdot\Phi_{eff,2})}{\cosh(\Phi_{eff,2})}\right) \tag{38}$$

or a spherical geometry:

$$\phi_x^s(\xi) = \varepsilon_x\,\xi^2 + \omega_x + \frac{\gamma_{x1}}{\xi}\left(\frac{\sinh(\xi\cdot\Phi_{eff,1})}{\sinh(\Phi_{eff,1})}\right) + \frac{\gamma_{x2}}{\xi}\left(\frac{\sinh(\xi\cdot\Phi_{eff,2})}{\sinh(\Phi_{eff,2})}\right) \tag{39}$$

$$\frac{d\phi_x^s}{d\xi} = 2\xi\varepsilon_x + \frac{\gamma_{x1}}{\xi^2}\left[\Phi_{eff,1}\xi\left(\frac{\cosh(\xi\cdot\Phi_{eff,1})}{\sinh(\Phi_{eff,1})}\right) - \left(\frac{\sinh(\xi\cdot\Phi_{eff,1})}{\sinh(\Phi_{eff,1})}\right)\right]$$

$$+ \frac{\gamma_{x2}}{\xi^2}\left[\Phi_{eff,2}\xi\left(\frac{\cosh(\xi\cdot\Phi_{eff,2})}{\sinh(\Phi_{eff,2})}\right) - \left(\frac{\sinh(\xi\cdot\Phi_{eff,2})}{\sinh(\Phi_{eff,2})}\right)\right] \tag{40}$$

$$\frac{1}{\xi^2}\frac{d}{d\xi}\left[\xi^2\frac{d\phi_x^s}{d\xi}\right] = 6\varepsilon_x + \Phi_{eff,1}^2\frac{\gamma_{x1}}{\xi}\left(\frac{\sinh(\xi\cdot\Phi_{eff,1})}{\sinh(\Phi_{eff,1})}\right)$$

$$+ \Phi_{eff,2}^2\frac{\gamma_{x2}}{\xi}\left(\frac{\sinh(\xi\cdot\Phi_{eff,2})}{\sinh(\Phi_{eff,2})}\right) \tag{41}$$

Here, we added a second effective Thiele modulus term to the solution for the simpler system because we are dealing with two distinct isomerization TS (the TS that interconverts ECP$^{=}$ and 12DMCP$^{=}$ and the one that interconverts 12DMCP$^{=}$ and 13DMCP$^{=}$). Both effective Thiele modulus terms are required for all product concentration profiles because all products are linked via a single or set of reactions.

Next, the continuity equations (Eq. 31 and 32) and boundary conditions (Eq. 33) are used to determine the unknown coefficients in either Equations 36 - 38 or 39 - 41.

Substitution of the dimensionless concentrations in the continuity equation for product b (Eq. 31 for a slab geometry) with their respective guessed concentration profile (Eq. 36 for a slab geometry) leads to an equation made up 4 distinct sets of coefficients that depend uniquely on the dimensionless length:

$$\phi_b^s{''}(\xi) = -\Phi_b^2\left(1 + \left(\frac{\sigma_{cb}}{\alpha_{cb}}\right)\phi_c^s(\xi) - \phi_b^s(\xi)\right)$$

where,

$$\phi_b^s{''}(\xi) = 2\varepsilon_b + \gamma_{b1}\Phi_{eff,1}^2\left(\frac{\cosh(\xi\cdot\Phi_{eff,1})}{\cosh(\Phi_{eff,1})}\right) + \gamma_{b2}\Phi_{eff,2}^2\left(\frac{\cosh(\xi\cdot\Phi_{eff,2})}{\cosh(\Phi_{eff,2})}\right)$$

$$\phi_b^s(\xi) = \varepsilon_b\xi^2 + \omega_b + \gamma_{b1}\left(\frac{\cosh(\xi\cdot\Phi_{eff,1})}{\cosh(\Phi_{eff,1})}\right) + \gamma_{b2}\left(\frac{\cosh(\xi\cdot\Phi_{eff,2})}{\cosh(\Phi_{eff,2})}\right)$$

$$\phi_c^s(\xi) = \varepsilon_c\xi^2 + \omega_c + \gamma_{c1}\left(\frac{\cosh(\xi\cdot\Phi_{eff,1})}{\cosh(\Phi_{eff,1})}\right) + \gamma_{c2}\left(\frac{\cosh(\xi\cdot\Phi_{eff,2})}{\cosh(\Phi_{eff,2})}\right) \tag{42}$$

after replacing,

$$0 = \left[1 + 2\varepsilon_b\Phi_b^{-2} - \omega_b + \left(\frac{\sigma_{cb}}{\alpha_{cb}}\right)\omega_c\right] + \left(\frac{\cosh(\xi\cdot\Phi_{eff,1})}{\cosh(\Phi_{eff,1})}\right)\left[\left(\Phi_{eff,1}^2\Phi_b^{-2} - 1\right)\gamma_{b1} + \left(\frac{\sigma_{cb}}{\alpha_{cb}}\right)\gamma_{c1}\right]$$

$$+ \left(\frac{\cosh(\xi\cdot\Phi_{eff,2})}{\cosh(\Phi_{eff,2})}\right)\left[\left(\Phi_{eff,2}^2\Phi_b^{-2} - 1\right)\gamma_{b2} + \left(\frac{\sigma_{cb}}{\alpha_{cb}}\right)\gamma_{c2}\right] + \xi^2\left[\left(\frac{\sigma_{cb}}{\alpha_{cb}}\right)\varepsilon_c - \varepsilon_b\right]$$

Similar analysis for a spherical geometry leads to another equation made up 4 distinct sets of coefficients that depend uniquely on the dimension less length:

82

$$\frac{1}{\xi^2}\frac{d\left[\xi^2\phi_b^s{}'(\xi)\right]}{d\xi} = -\Phi_b{}^2\left(1+\left(\frac{\sigma_{cb}}{\alpha_{cb}}\right)\phi_c^s(\xi)-\phi_b^s(\xi)\right)$$

where,

$$\frac{1}{\xi^2}\frac{d\left[\xi^2\phi_b^s{}'(\xi)\right]}{d\xi} = 6\varepsilon_b + \gamma_{b1}\Phi_{eff,1}^2\frac{1}{\xi}\left(\frac{\sinh(\xi\cdot\Phi_{eff,1})}{\sinh(\Phi_{eff,1})}\right)+\gamma_{b2}\Phi_{eff,2}^2\frac{1}{\xi}\left(\frac{\sinh(\xi\cdot\Phi_{eff,2})}{\sinh(\Phi_{eff,2})}\right)$$

$$\phi_b^s(\xi) = \varepsilon_b\,\xi^2 + \omega_b + \gamma_{b1}\frac{1}{\xi}\left(\frac{\sinh(\xi\cdot\Phi_{eff,1})}{\sinh(\Phi_{eff,1})}\right)+\gamma_{b2}\frac{1}{\xi}\left(\frac{\sinh(\xi\cdot\Phi_{eff,2})}{\sinh(\Phi_{eff,2})}\right)$$

$$\phi_c^s(\xi) = \varepsilon_c\,\xi^2 + \omega_c + \gamma_{c1}\frac{1}{\xi}\left(\frac{\sinh(\xi\cdot\Phi_{eff,1})}{\sinh(\Phi_{eff,1})}\right)+\gamma_{c2}\frac{1}{\xi}\left(\frac{\sinh(\xi\cdot\Phi_{eff,2})}{\sinh(\Phi_{eff,2})}\right)$$

after replacing,

$$\quad(43)$$

$$0 = \left[1+6\varepsilon_b\,\Phi_b^{-2}-\omega_b+\left(\frac{\sigma_{cb}}{\alpha_{cb}}\right)\omega_c\right]$$

$$+\frac{1}{\xi}\left(\frac{\sinh(\xi\cdot\Phi_{eff,1})}{\sinh(\Phi_{eff,1})}\right)\left[\left(\Phi_{eff,1}^2\Phi_b^{-2}-1\right)\gamma_{b1}+\left(\frac{\sigma_{cb}}{\alpha_{cb}}\right)\gamma_{c1}\right]$$

$$+\frac{1}{\xi}\left(\frac{\sinh(\xi\cdot\Phi_{eff,2})}{\sinh(\Phi_{eff,2})}\right)\left[\left(\Phi_{eff,2}^2\Phi_b^{-2}-1\right)\gamma_{b2}+\left(\frac{\sigma_{cb}}{\alpha_{cb}}\right)\gamma_{c2}\right]$$

$$+\xi^2\left[\left(\frac{\sigma_{cb}}{\alpha_{cb}}\right)\varepsilon_c-\varepsilon_b\right]$$

In order for Equation 42 or 43 to be true at all dimensionless lengths each set of coefficients must also be equal to 0. Substitutions of the dimensionless concentrations into the other continuity equations in Equation 31 or 32 and into the boundary conditions (Eq. 33) leads to 14 independent equations able to determine the 14 unknown coefficients suggested by the functional form of Equation 36 or 39 for each of the products for a slab geometry:

Dependent Variables (14): $\omega_b, \omega_c, \omega_d, \gamma_{b1}, \gamma_{c1}, \gamma_{d1}, \gamma_{b2}, \gamma_{c2}, \gamma_{d2}, \varepsilon_b, \varepsilon_c, \varepsilon_d, \Phi_{eff1}, \Phi_{eff2}$

Independent Equations (14):

a) $\omega_b = 1 + 2\varepsilon_b \, \Phi_b^{-2} + \left(\dfrac{\sigma_{cb}}{\alpha_{cb}}\right)\omega_c$

d) $\varepsilon_b = \left(\dfrac{\sigma_{cb}}{\alpha_{cb}}\right)\varepsilon_c$

b) $\omega_c = 1 + 2\varepsilon_c \, \Phi_c^{-2} + \alpha_{cb}\,\omega_b + \alpha_{cd}\,\omega_d$

e) $\varepsilon_c = \alpha_{cb}\,\varepsilon_b + \alpha_{cd}\,\varepsilon_d$

c) $\omega_d = 1 + 2\varepsilon_d \, \Phi_d^{-2} + \left(\dfrac{1-\sigma_{cb}}{\alpha_{cd}}\right)\omega_c$

(redundant) $\varepsilon_d = \left(\dfrac{1-\sigma_{cb}}{\alpha_{cd}}\right)\varepsilon_c$

f) $0 = \gamma_{b1}\left(1 - \Phi_{eff,1}^2\Phi_b^{-2}\right) - \left(\dfrac{\sigma_{cb}}{\alpha_{cb}}\right)\gamma_{c1}$

i) $0 = \gamma_{b2}\left(1 - \Phi_{eff,2}^2\Phi_b^{-2}\right) - \left(\dfrac{\sigma_{cb}}{\alpha_{cb}}\right)\gamma_{c2}$
$\qquad$ (44a-n)

g) $0 = \gamma_{d1}\left(1 - \Phi_{eff,1}^2\Phi_d^{-2}\right) - \left(\dfrac{1-\sigma_{cb}}{\alpha_{cd}}\right)\gamma_{c1}$

j) $0 = \gamma_{d1}\left(1 - \Phi_{eff,2}^2\Phi_d^{-2}\right) - \left(\dfrac{1-\sigma_{cb}}{\alpha_{cd}}\right)\gamma_{c2}$

h) $0 = \gamma_{c1}\left(1 - \Phi_{eff,1}^2\Phi_c^{-2}\right) - \alpha_{cb}\,\gamma_{b1} - \alpha_{cd}\,\gamma_{d1}$
k) $0 = \gamma_{c1}\left(1 - \Phi_{eff,2}^2\Phi_c^{-2}\right) - \alpha_{cb}\,\gamma_{b2} - \alpha_{cd}\,\gamma_{d2}$

l) $G_b = \gamma_{b1} + \gamma_{b2} + \omega_b + \varepsilon_b$

m) $G_c = \gamma_{c1} + \gamma_{c2} + \omega_c + \varepsilon_c$

n) $G_d = \gamma_{d1} + \gamma_{d2} + \omega_d + \varepsilon_d$

or a spherical geometry:

Dependent Variables (14): $\omega_b, \omega_c, \omega_d, \gamma_{b1}, \gamma_{c1}, \gamma_{d1}, \gamma_{b2}, \gamma_{c2}, \gamma_{d2}, \varepsilon_b, \varepsilon_c, \varepsilon_d, \Phi_{eff1}, \Phi_{eff2}$

Independent Equations (14):

a) $\omega_b = 1 + 6\varepsilon_b \, \Phi_b^{-2} + \left(\dfrac{\sigma_{cb}}{\alpha_{cb}}\right)\omega_c$

d) $\varepsilon_b = \left(\dfrac{\sigma_{cb}}{\alpha_{cb}}\right)\varepsilon_c$

b) $\omega_c = 1 + 6\varepsilon_c \, \Phi_c^{-2} + \alpha_{cb}\,\omega_b + \alpha_{cd}\,\omega_d$

e) $\varepsilon_c = \alpha_{cb}\,\varepsilon_b + \alpha_{cd}\,\varepsilon_d$

c) $\omega_d = 1 + 6\varepsilon_d \, \Phi_d^{-2} + \left(\dfrac{1-\sigma_{cb}}{\alpha_{cd}}\right)\omega_c$

(redundant) $\varepsilon_d = \left(\dfrac{1-\sigma_{cb}}{\alpha_{cd}}\right)\varepsilon_c$

f) $0 = \gamma_{b1}\left(1 - \Phi_{eff,1}^2\Phi_b^{-2}\right) - \left(\dfrac{\sigma_{cb}}{\alpha_{cb}}\right)\gamma_{c1}$

i) $0 = \gamma_{b2}\left(1 - \Phi_{eff,2}^2\Phi_b^{-2}\right) - \left(\dfrac{\sigma_{cb}}{\alpha_{cb}}\right)\gamma_{c2}$
$\qquad$ (45a-n)

g) $0 = \gamma_{d1}\left(1 - \Phi_{eff,1}^2\Phi_d^{-2}\right) - \left(\dfrac{1-\sigma_{cb}}{\alpha_{cd}}\right)\gamma_{c1}$

j) $0 = \gamma_{d1}\left(1 - \Phi_{eff,2}^2\Phi_d^{-2}\right) - \left(\dfrac{1-\sigma_{cb}}{\alpha_{cd}}\right)\gamma_{c2}$

h) $0 = \gamma_{c1}\left(1 - \Phi_{eff,1}^2\Phi_c^{-2}\right) - \alpha_{cb}\,\gamma_{b1} - \alpha_{cd}\,\gamma_{d1}$
k) $0 = \gamma_{c1}\left(1 - \Phi_{eff,2}^2\Phi_c^{-2}\right) - \alpha_{cb}\,\gamma_{b2} - \alpha_{cd}\,\gamma_{d2}$

l) $G_b = \gamma_{b1} + \gamma_{b2} + \omega_b + \varepsilon_b$

m) $G_c = \gamma_{c1} + \gamma_{c2} + \omega_c + \varepsilon_c$

n) $G_d = \gamma_{d1} + \gamma_{d2} + \omega_d + \varepsilon_d$

It should be noted that equations d-n are identical for both slab and spherical geometries.

At differential conditions the non-dimensional concentrations of the products (G_b, G_c, and G_d) are approximately zero. At such conditions, Equations 44a-n lead to the following solution for the 14 unknown coefficients for a slab geometry:

a) $\varepsilon_c = -\dfrac{(1+\alpha_{cb}+\alpha_{cd})\,\Phi_b^2\Phi_c^2\Phi_d^2}{(1-\sigma_{cb})\,\Phi_b^2\Phi_c^2+\Phi_b^2\Phi_d^2+\sigma_{cb}\Phi_c^2\Phi_d^2}\,\dfrac{1}{2}$ b) $\varepsilon_b = \varepsilon_c\,\dfrac{\sigma_{cb}}{\alpha_{cb}}$ c) $\varepsilon_d = \varepsilon_c\,\dfrac{(1-\sigma_{cb})}{\alpha_{cd}}$

d) $\gamma_{c1} = \dfrac{-\left(\Phi_{eff,1}^2-\Phi_d^2\right)\left(\Phi_{eff,1}^2-\Phi_b^2\right)}{\sigma_{cb}(1-\sigma_{cb})\,\Phi_{eff1}^2\left(\Phi_{eff,1}^2-\Phi_{eff,2}^2\right)\left(\Phi_b^2-\Phi_d^2\right)}\dfrac{\Phi_{eff,2}^2\begin{pmatrix}(\alpha_{cb}+\sigma_{cb})(1-\sigma_{cb})\Phi_b^2\Phi_c^2\\[2pt]-(1+\alpha_{cd}-\sigma_{cb})\sigma_{cb}\Phi_c^2\Phi_d^2\\[2pt]-(\alpha_{cd}\sigma_{cb}-\alpha_{cb}(1-\sigma_{cb}))\Phi_b^2\Phi_d^2\end{pmatrix}-\alpha_{cb}(1-\sigma_{cb})\left(\Phi_d^2+(1-\sigma_{cb})\Phi_c^2\right)\Phi_b^4+\alpha_{cd}\sigma_{cb}\left(\Phi_b^2+\sigma_{cb}\Phi_c^2\right)\Phi_d^4-(\alpha_{cb}-\alpha_{cd})\sigma_{cb}(1-\sigma_{cb})\Phi_b^2\Phi_c^2\Phi_d^2}{(1-\sigma_{cb})\Phi_b^2\Phi_c^2+\Phi_b^2\Phi_d^2+\sigma_{cb}\Phi_c^2\Phi_d^2}$

e) $\gamma_{b1} = -\gamma_{c1}\,\dfrac{\sigma_{cb}\Phi_b^2}{\alpha_{cb}\left(\Phi_{eff,1}^2-\Phi_b^2\right)}$ f) $\gamma_{d1} = -\gamma_{c1}\,\dfrac{(1-\sigma_{cb})\Phi_d^2}{\alpha_{cd}\left(\Phi_{eff,1}^2-\Phi_d^2\right)}$

g) $\gamma_{c2} = \dfrac{\left(\Phi_{eff,2}^2-\Phi_d^2\right)\left(\Phi_{eff,2}^2-\Phi_b^2\right)}{\sigma_{cb}(1-\sigma_{cb})\,\Phi_{eff,2}^2\left(\Phi_{eff,1}^2-\Phi_{eff,2}^2\right)\left(\Phi_b^2-\Phi_d^2\right)}\dfrac{\Phi_{eff,1}^2\begin{pmatrix}(\alpha_{cb}+\sigma_{cb})(1-\sigma_{cb})\Phi_b^2\Phi_c^2\\[2pt]-(1+\alpha_{cd}-\sigma_{cb})\sigma_{cb}\Phi_c^2\Phi_d^2\\[2pt]-(\alpha_{cd}\sigma_{cb}-\alpha_{cb}(1-\sigma_{cb}))\Phi_b^2\Phi_d^2\end{pmatrix}-\alpha_{cb}(1-\sigma_{cb})\left(\Phi_d^2+(1-\sigma_{cb})\Phi_c^2\right)\Phi_b^4+\alpha_{cd}\sigma_{cb}\left(\Phi_b^2+\sigma_{cb}\Phi_c^2\right)\Phi_d^4-(\alpha_{cb}-\alpha_{cd})\sigma_{cb}(1-\sigma_{cb})\Phi_b^2\Phi_c^2\Phi_d^2}{(1-\sigma_{cb})\Phi_b^2\Phi_c^2+\Phi_b^2\Phi_d^2+\sigma_{cb}\Phi_c^2\Phi_d^2}$

(46a-n)

h) $\gamma_{b2} = -\gamma_{c2}\,\dfrac{\sigma_{cb}\Phi_b^2}{\alpha_{cb}\left(\Phi_{eff,2}^2-\Phi_b^2\right)}$ i) $\gamma_{d2} = -\gamma_{c2}\,\dfrac{(1-\sigma_{cb})\Phi_d^2}{\alpha_{cd}\left(\Phi_{eff,2}^2-\Phi_d^2\right)}$

j) $\Phi_{eff,1}^2 = \dfrac{1}{2}\left(\Phi_b^2+\Phi_c^2+\Phi_d^2+\sqrt{\Phi_b^4+\Phi_c^4+\Phi_d^4+2(2\sigma_{cb}-1)\Phi_b^2\Phi_c^2+2(1-2\sigma_{cb})\Phi_c^2\Phi_d^2-2\Phi_b^2\Phi_d^2}\right)$

k) $\Phi_{eff,2}^2 = \dfrac{1}{2}\left(\Phi_b^2+\Phi_c^2+\Phi_d^2-\sqrt{\Phi_b^4+\Phi_c^4+\Phi_d^4+2(2\sigma_{cb}-1)\Phi_b^2\Phi_c^2+2(1-2\sigma_{cb})\Phi_c^2\Phi_d^2-2\Phi_b^2\Phi_d^2}\right)$

l) $\omega_b = -\left(\gamma_{b1}+\gamma_{b2}+\varepsilon_b\right)$

m) $\omega_c = -\left(\gamma_{c1}+\gamma_{c2}+\varepsilon_c\right)$

n) $\omega_d = -\left(\gamma_{d1}+\gamma_{d2}+\varepsilon_d\right)$

and for a spherical geometry, Equation 45a-n lead to the following solution for the 14 unknown coefficients:

a) $\varepsilon_c = -\dfrac{\left(1+\alpha_{cb}+\alpha_{cd}\right)\Phi_b^2\Phi_c^2\Phi_d^2}{\left(1-\sigma_{cb}\right)\Phi_b^2\Phi_c^2+\Phi_b^2\Phi_d^2+\sigma_{cb}\Phi_c^2\Phi_d^2}\dfrac{1}{6}$ b) $\varepsilon_b = \varepsilon_c\dfrac{\sigma_{cb}}{\alpha_{cb}}$ c) $\varepsilon_d = \varepsilon_c\dfrac{\left(1-\sigma_{cb}\right)}{\alpha_{cd}}$

d) $\gamma_{c1} = \dfrac{-\left(\Phi_{eff,1}^2-\Phi_d^2\right)\left(\Phi_{eff,1}^2-\Phi_b^2\right)}{\sigma_{cb}\left(1-\sigma_{cb}\right)\Phi_{eff1}^2\left(\Phi_{eff,1}^2-\Phi_{eff,2}^2\right)\left(\Phi_b^2-\Phi_d^2\right)}\dfrac{\begin{pmatrix}\Phi_{eff,2}^2\begin{pmatrix}\left(\alpha_{cb}+\sigma_{cb}\right)\left(1-\sigma_{cb}\right)\Phi_b^2\Phi_c^2\\-\left(1+\alpha_{cd}-\sigma_{cb}\right)\sigma_{cb}\Phi_c^2\Phi_d^2\\-\left(\alpha_{cd}\sigma_{cb}-\alpha_{cb}\left(1-\sigma_{cb}\right)\right)\Phi_b^2\Phi_d^2\end{pmatrix}\\-\alpha_{cb}\left(1-\sigma_{cb}\right)\left(\Phi_d^2+\left(1-\sigma_{cb}\right)\Phi_c^2\right)\Phi_b^4\\+\alpha_{cd}\sigma_{cb}\left(\Phi_b^2+\sigma_{cb}\Phi_c^2\right)\Phi_d^4\\-\left(\alpha_{cb}-\alpha_{cd}\right)\sigma_{cb}\left(1-\sigma_{cb}\right)\Phi_b^2\Phi_c^2\Phi_d^2\end{pmatrix}}{\left(1-\sigma_{cb}\right)\Phi_b^2\Phi_c^2+\Phi_b^2\Phi_d^2+\sigma_{cb}\Phi_c^2\Phi_d^2}$

e) $\gamma_{b1} = -\gamma_{c1}\dfrac{\sigma_{cb}\Phi_b^2}{\alpha_{cb}\left(\Phi_{eff,1}^2-\Phi_b^2\right)}$ f) $\gamma_{d1} = -\gamma_{c1}\dfrac{\left(1-\sigma_{cb}\right)\Phi_d^2}{\alpha_{cd}\left(\Phi_{eff,1}^2-\Phi_d^2\right)}$

(47a-n)

g) $\gamma_{c2} = \dfrac{\left(\Phi_{eff,2}^2-\Phi_d^2\right)\left(\Phi_{eff,2}^2-\Phi_b^2\right)}{\sigma_{cb}\left(1-\sigma_{cb}\right)\Phi_{eff,2}^2\left(\Phi_{eff,1}^2-\Phi_{eff,2}^2\right)\left(\Phi_b^2-\Phi_d^2\right)}\dfrac{\begin{pmatrix}\Phi_{eff,1}^2\begin{pmatrix}\left(\alpha_{cb}+\sigma_{cb}\right)\left(1-\sigma_{cb}\right)\Phi_b^2\Phi_c^2\\-\left(1+\alpha_{cd}-\sigma_{cb}\right)\sigma_{cb}\Phi_c^2\Phi_d^2\\-\left(\alpha_{cd}\sigma_{cb}-\alpha_{cb}\left(1-\sigma_{cb}\right)\right)\Phi_b^2\Phi_d^2\end{pmatrix}\\-\alpha_{cb}\left(1-\sigma_{cb}\right)\left(\Phi_d^2+\left(1-\sigma_{cb}\right)\Phi_c^2\right)\Phi_b^4\\+\alpha_{cd}\sigma_{cb}\left(\Phi_b^2+\sigma_{cb}\Phi_c^2\right)\Phi_d^4\\-\left(\alpha_{cb}-\alpha_{cd}\right)\sigma_{cb}\left(1-\sigma_{cb}\right)\Phi_b^2\Phi_c^2\Phi_d^2\end{pmatrix}}{\left(1-\sigma_{cb}\right)\Phi_b^2\Phi_c^2+\Phi_b^2\Phi_d^2+\sigma_{cb}\Phi_c^2\Phi_d^2}$

h) $\gamma_{b2} = -\gamma_{c2}\dfrac{\sigma_{cb}\Phi_b^2}{\alpha_{cb}\left(\Phi_{eff,2}^2-\Phi_b^2\right)}$ i) $\gamma_{d2} = -\gamma_{c2}\dfrac{\left(1-\sigma_{cb}\right)\Phi_d^2}{\alpha_{cd}\left(\Phi_{eff,2}^2-\Phi_d^2\right)}$

j) $\Phi_{eff,1}^2 = \dfrac{1}{2}\left(\Phi_b^2+\Phi_c^2+\Phi_d^2+\sqrt{\Phi_b^4+\Phi_c^4+\Phi_d^4+2\left(2\sigma_{cb}-1\right)\Phi_b^2\Phi_c^2+2\left(1-2\sigma_{cb}\right)\Phi_c^2\Phi_d^2-2\Phi_b^2\Phi_d^2}\right)$

k) $\Phi_{eff,2}^2 = \dfrac{1}{2}\left(\Phi_b^2+\Phi_c^2+\Phi_d^2-\sqrt{\Phi_b^4+\Phi_c^4+\Phi_d^4+2\left(2\sigma_{cb}-1\right)\Phi_b^2\Phi_c^2+2\left(1-2\sigma_{cb}\right)\Phi_c^2\Phi_d^2-2\Phi_b^2\Phi_d^2}\right)$

l) $\omega_b = -\left(\gamma_{b1}+\gamma_{b2}+\varepsilon_b\right)$

m) $\omega_c = -\left(\gamma_{c1}+\gamma_{c2}+\varepsilon_c\right)$

n) $\omega_d = -\left(\gamma_{d1}+\gamma_{d2}+\varepsilon_d\right)$

It should be noted here that only parts a-c and l-n are different between Equations 46 and 47, thus the values, and, consequently the chemical significance of parts d-k are independent of system geometry.

Substitution of the Thiele moduli for b and d (Eq. 29) into Equations 46 j and k (or 47 j and k) shows that the effective Thiele moduli are proportional to the Thiele modulus for product c:

$$a)\ \Phi_{eff,1}^2 = \frac{\Phi_c^2}{2K_{cb}K_{cd}} \left(K_{cb}\left(1 + K_{cd} - \sigma_{cb}\right) + K_{cd}\sigma_{cb} + \sqrt{\begin{array}{l} K_{cb}^2\left(1 + K_{cd}\right)^2 \\ -2K_{cb}\left(K_{cb} + K_{cd} + 3K_{cb}K_{cd} + K_{cd}^2\right)\sigma_{cb} \\ +\left(K_{cb} + K_{cd}\right)\left(K_{cb} + K_{cd} + 4K_{cb}K_{cd}\right)\sigma_{cb}^2 \end{array}} \right)$$

$$b)\ \Phi_{eff,2}^2 = \frac{\Phi_c^2}{2K_{cb}K_{cd}} \left(K_{cb}\left(1 + K_{cd} - \sigma_{cb}\right) + K_{cd}\sigma_{cb} - \sqrt{\begin{array}{l} K_{cb}^2\left(1 + K_{cd}\right)^2 \\ -2K_{cb}\left(K_{cb} + K_{cd} + 3K_{cb}K_{cd} + K_{cd}^2\right)\sigma_{cb} \\ +\left(K_{cb} + K_{cd}\right)\left(K_{cb} + K_{cd} + 4K_{cb}K_{cd}\right)\sigma_{cb}^2 \end{array}} \right)$$

(48a,b)

Substitution of the dimensionless concentration in Equation 35 with those given by the functional form of Equation 36 and with the values of the unknown coefficients given by Equation 46a-n leads to an expression for the measured differential selectivity towards product b for a slab geometry:

$$S_{b,m} = S_{b,0} + \left(S_{b,eq} - S_{b,0}\right)\left(1 - \frac{\tanh\left(\Phi_{eff,1}\right)}{\Phi_{eff,1}}\right) + \Theta_b\left(\frac{\tanh\left(\Phi_{eff,2}\right)}{\Phi_{eff,2}} - \frac{\tanh\left(\Phi_{eff,1}\right)}{\Phi_{eff,1}}\right) \qquad (49)$$

or for a spherical geometry (via substitution of the dimensionless concentration in Equation 35 with those given by the functional form of Equation 39 and with the values of the unknown coefficients given by Equations 46a-n):

$$S_{b,meas} = S_{b,0} + \left(S_{b,eq} - S_{b,0}\right)\left(1 - \frac{3\left(\Phi_{eff,1}\coth\left(\Phi_{eff,1}\right) - 1\right)}{\Phi_{eff,1}^2}\right)$$
$$+\Theta_b\left[\left(\frac{3\left(\Phi_{eff,2}\coth\left(\Phi_{eff,2}\right) - 1\right)}{\Phi_{eff,2}^2}\right) - \left(\frac{3\left(\Phi_{eff,1}\coth\left(\Phi_{eff,1}\right) - 1\right)}{\Phi_{eff,1}^2}\right)\right] \qquad (50)$$

where $S_{b,eq}$ is the mole fraction of product b when at equilibrium with products c and d, $S_{b,0}$ is the intrinsic selectivity to product b, and Θ_b is a constant (see Equations 17 and 18) that depends on σ_{bc} (analogous to σ_{ecp}), the intrinsic product selectivities, and the equilibrium selectivities, but is independent of Φ_c. Substituting Equation 15 into Equation 50 returns an equation analogous to Equation 13 but for product b:

$$S_{b.meas} = S_{b,0} + \Delta S_b\left(1 - \eta_+\right) + \Theta_b\left(\eta_- - \eta_+\right) \qquad (51)$$

2.7. References

[1]   T. Prasomsri, S. Jongpatiwut, M. Santikunaporn, D.E. Resasco, Selectivity of Ring-Contraction Products in the Hydroisomerization of Methylcyclohexane, in: 2007 Spring Meet. 3rd Glob. Congr. Process Saf. 10th Top. Conf. Refin. Process., Houston, 2007.

[2]   G.B. McVicker, O.C. Feeley, J.J. Ziemiak, D.E.W. Vaughan, K.C. Strohmaier, W.R. Kliewer, et al., *J. Phys. Chem. B*. 109 (2005) 2222–6. doi:10.1021/jp040205k

[3]   C. Nguyen, C. Sonwane, S. Bhatia, D. Do, *Langmuir*. 7463 (1998) 4950–4952.

[4]   E.G. Derouane, J.C. Védrine, R.R. Pinto, P.M. Borges, L. Costa, M.A.N.D.A. Lemos, et al., *Catal. Rev.* 55 (2013) 454–515. doi:10.1080/01614940.2013.822266

[5]   J. Macht, M.J. Janik, M. Neurock, E. Iglesia, *J. Am. Chem. Soc.* 130 (2008) 10369–79. doi:10.1021/ja803114r

[6]   J. Macht, M.J. Janik, M. Neurock, E. Iglesia, *Angew. Chem. Int. Ed.* 46 (2007) 7864–8. doi:10.1002/anie.200701292

[7]   M.J. Janik, J. Macht, E. Iglesia, M. Neurock, *J. Phys. Chem. C*. 113 (2009) 1872–1885. doi:10.1021/jp8078748

[8]   W. Knaeble, R.T. Carr, E. Iglesia, *J. Catal.* 319 (2014) 283–296. doi:10.1016/j.jcat.2014.09.005

[9]   R.T. Carr, M. Neurock, E. Iglesia, *J. Catal.* 278 (2011) 78–93. doi:10.1016/j.jcat.2010.11.017

[10]   H.S. Cerqueira, P.C. Mihindou-Koumba, P. Magnoux, M. Guisnet, *Ind. Eng. Chem. Res.* 40 (2001) 1032–1041. doi:10.1021/ie000730f

[11]   M. Santikunaporn, W.E. Alvarez, D.E. Resasco, *Appl. Catal. A Gen.* 325 (2007) 175–187. doi:10.1016/j.apcata.2007.03.029

[12]   J. Cowan, C.L. Hill, R. Reiner, I. Weinstock, *Inorg. Synth.* 33 (2002) 18–26.

[13]   L. Baker, B. Loev, T. McCutcheon, *J. Am. Chem. Soc.* 72 (1950) 2374–2377.

[14]   L. Baker, T. McCutcheon, *J. Am. Chem. Soc.* 78 (1956) 4503–4510.

[15]   B.M.B. Epstein, G.M. Barrow, K.S. Pitzer, F.D. Rossini, *J. Res. Natl. Bur. Stand. (1934)*. 43 (1949) 245–250.

[16] J.E. Kilpatrick, H. Werner, C. Beckett, K.S. Pitzer, F.D. Rossini, *J. Res. Natl. Bur. Stand. (1934).* 39 (1947) 523–543.

[17] C. Baertsch, *J. Catal.* 205 (2002) 44–57. doi:10.1006/jcat.2001.3426

[18] G. Kresse, J. Furthmüller, *Phys. Rev. B.* 54 (1996) 11169–11186.

[19] G. Kresse, J. Hafner, *Phys. Rev. B.* 47 (1993) 558–561.

[20] G. Kresse, J. Hafner, *Phys. Rev. B.* 49 (1994) 14251–14269. doi:10.1103/PhysRevB.49.14251

[21] G. Kresse, J. Furthmüller, *Comput. Mater. Sci.* 6 (1996) 15–50. doi:10.1016/0927-0256(96)00008-0

[22] P.E. Blöchl, *Phys. Rev. B.* 50 (1994) 17953–17979. doi:10.1103/PhysRevB.50.17953

[23] G. Kresse, *Phys. Rev. B.* 59 (1999) 1758–1775. doi:10.1103/PhysRevB.59.1758

[24] J. Perdew, J. Chevary, S. Vosko, *Phys. Rev. B.* 46 (1992) 6671–6687.

[25] H.J. Monkhorst, J.D. Pack, *Phys. Rev. B.* 13 (1976) 5188–5192. doi:10.1103/PhysRevB.13.5188

[26] P. Deshlahra, R.T. Carr, S.-H. Chai, E. Iglesia, *ACS Catal.* 5 (2015) 666–682. doi:10.1021/cs501599y

[27] G. Makov, M. Payne, *Phys. Rev. B.* 51 (1995) 4014–4022. doi:10.1103/PhysRevB.51.4014

[28] W.C. Lu, C.Z. Wang, M.W. Schmidt, L. Bytautas, K.M. Ho, K. Ruedenberg, *J. Chem. Phys.* 120 (2004) 2629. doi:10.1063/1.1638731

[29] W.C. Lu, C.Z. Wang, T.L. Chan, K. Ruedenberg, K.M. Ho, *Phys. Rev. B.* 70 (2004) 041101. doi:10.1103/PhysRevB.70.041101

[30] T.-L. Chan, Y.X. Yao, C.Z. Wang, W.C. Lu, J. Li, X.F. Qian, et al., *Phys. Rev. B.* 76 (2007) 205119. doi:10.1103/PhysRevB.76.205119

[31] X. Qian, J. Li, L. Qi, C.-Z. Wang, T.-L. Chan, Y.-X. Yao, et al., *Phys. Rev. B.* 78 (2008) 245112. doi:10.1103/PhysRevB.78.245112

[32] P.-O. Löwdin, *J. Chem. Phys.* 18 (1950) 365. doi:10.1063/1.1747632

[33] P.-O. Löwdin, On the Nonorthogonality Problem, in: Adv. Quantum Chem., 1970: pp. 185–199. doi:10.1016/S0065-3276(08)60339-1

[34] G. Henkelman, B.P. Uberuaga, H. Jónsson, *J. Chem. Phys.* 113 (2000) 9901–9904. doi:10.1063/1.1329672

[35] G. Henkelman, H. Jónsson, *J. Chem. Phys.* 111 (1999) 7010. doi:10.1063/1.480097

[36] F. Alvarez, A. Montes, G. Perot, M. Guisnet, *Stud. Surf. Sci. Catal.* 49 (1989) 1367–1376. doi:10.1016/S0167-2991(08)62021-2

[37] V. Kazansky, *Accounts Chem. Res.* 24 (1991) 379–383.

[38] M. Natal-Santiago, R. Alcalá, J. Dumesic, *J. Catal.* 181 (1999) 124–144.

[39] M. Boronat, P. Viruela, A. Corma, *J. Phys. Chem.* 100 (1996) 633–637. doi:10.1002/chin.199620056

[40] R.T. LaLonde, A.D. Debboli, *J. Org. Chem.* 35 (1970) 2657–2661. doi:10.1021/jo00833a038

[41] I.D. Mackie, J. Govindhakannan, *J. Mol. Struct. THEOCHEM.* 939 (2010) 53–58. doi:10.1016/j.theochem.2009.09.040

[42] I.D. Mackie, J. Govindhakannan, G.A. Dilabio, O.P. Drive, C. Tg, *J. Phys. Chem. A.* 112 (2008) 4004–10. doi:10.1021/jp710656f

[43] V. Vrček, M. Saunders, O. Kronja, *J. Org. Chem.* 68 (2003) 1859–1866. doi:10.1021/jo020694p

[44] Y. V. Joshi, K.T. Thomson, *J. Catal.* 230 (2005) 440–463. doi:10.1016/j.jcat.2004.12.016

[45] R. a. Alberty, Y.S. Ha, *J. Phys. Chem. Ref. Data.* 14 (1985) 1107. doi:10.1063/1.555741

[46] R. a. Alberty, *J. Phys. Chem. Ref. Data.* 14 (1985) 177. doi:10.1063/1.555745

[47] M.B. Epstein, K.S. Pitzer, F.D. Rossini, *J. Res. Natl. Bur. Stand. (1934).* 42 (1949) 379. doi:10.6028/jres.042.031

[48] M. Peereboom, B. van de Graaf, J.M.A. Baas, *Recl. Des Trav. Chim. Des Pays-Bas.* 101 (1982) 336–338. doi:10.1002/recl.19821011003

[49] J.A. Martens, P.A. Jacobs, "Introduction to Zeolite Science and Practice," Elsevier,

2001. doi:10.1016/S0167-2991(01)80256-1

[50]   J.M. Zalc, S.C. Reyes, E. Iglesia, *Chem. Eng. Sci.* 59 (2004) 2947–2960. doi:10.1016/j.ces.2004.04.028

[51]   S.C. Reyes, E. Iglesia, *J. Catal.* 129 (1991) 457–472. doi:10.1016/0021-9517(91)90049-A

[52]   Y. V Joshi, A. Bhan, K.T. Thomson, *J. Phys. Chem. B*. 108 (2004) 971–980. doi:10.1021/jp036205m

[53]   G. Herzberg, "Molecular spectra and molecular structure. Vol.3: Electronic spectra and electronic structure of polyatomic molecules," 1966.

[54]   J. Macht, R.T. Carr, E. Iglesia, *J. Am. Chem. Soc.* 131 (2009) 6554–6565.

[55]   A. Corma, *Chem. Rev.* 95 (1995) 559–614.

[56]   W.E. Farneth, R.J. Gorte, *Chem. Rev.* 95 (1995) 615–635. doi:10.1021/cr00035a007

[57]   R.J. Gorte, *Catal. Letters*. 62 (1999) 1–13.

[58]   P. Deshlahra, R.T. Carr, E. Iglesia, *J. Am. Chem. Soc.* 136 (2014) 15229–15247. doi:10.1021/ja506149c

Chapter 3.

Kinetic and Theoretical Insights into the Mechanism of Alkanol Dehydration on Solid Brønsted Acid Catalysts

Abstract

Elementary steps that mediate ethanol dehydration to alkenes and ethers are determined here from rate and selectivity data on solid acids of diverse acid strength and known structure and free energies derived from density functional theory (DFT). Measured ethene and ether formation rates that differed from those expected from accepted monomolecular and bimolecular routes led to our systematic enumeration of plausible dehydration routes and to a rigorous assessment of their contributions to the products formed. H-bonded monomers, protonated alkanol dimers, and alkoxides are the prevalent bound intermediates at conditions relevant to the practice of dehydration catalysis. We conclude that direct and sequential (alkoxide-mediated) routes contribute to ether formation via S_N2-type reactions, alkenes form preferentially from sequential routes via monomolecular and bimolecular syn-E2-type eliminations, and alkoxides form via bimolecular S_N2-type substitutions. The prevalence of these elementary steps and their kinetic relevance are consistent with measured kinetic and thermodynamic parameters, which agree with values from DFT-derived free energies and with the effects of acid strength on rates, selectivities, and rate constants; such effects reflect the relative charges in transition states and their relevant precursors. Dehydration turnover rates, but not selectivities, depend on acid strength, because transition states are more highly charged than their relevant precursors, but similar in charge for transition states that mediate the competing pathways responsible for selectivity.

3.1. Introduction

The recent increase in demand for renewable carbon sources [1] has led to a concomitant increase in ethanol (EtOH) production (ten-fold from 1995 to 2014 in the U.S. [2]). EtOH has also emerged as an attractive feedstock to produce hydrocarbon fuels (via deoxygenation-oligomerization)[1] and chemical intermediates, such as ethylene (EY) and diethyl ether (DEE) (via dehydration on solid Brønsted acids) [3–7]. EtOH dehydration rates and selectivities have been widely reported [3–5,7–14], but only on solids with acid sites uncertain in number, type, location, or local structure, obfuscating reactivity comparisons among catalysts and mechanistic elucidation. In the absence of clear mechanistic insights, the role of acid strength and confinement on reactivity (as turnover rates) and selectivity, required for systematic catalyst improvements, have remained unclear and not rigorously demonstrated.

Tungsten polyoxometalate (POM) clusters with Keggin structures and charge-balancing protons ($H_{8-n}X^{n+}W_{12}O_{40}$) are used in practice to convert EtOH to EY [15–17]. These solids also represent a family of Brønsted acids with uniform and well-defined

atomic arrangements and diverse chemical composition ($X^{n+}=P^{5+}$, Si^{4+}, Al^{3+}, Co^{2+}) [18]. The identity of the central atom (X) influences acid strength and consequently the reactivity of the protons, through changes in their number and in the stability of the conjugate anion formed upon deprotonation of the solid acid [19]. Deprotonation energies (DPE) reflect the energy required to heterolytically cleave a proton from its conjugate base, thus providing a rigorous and probe-independent measure of acid strength; their magnitude can be determined using density functional theory (DFT) because of the known and stable structure of these catalysts [19,20].

Methanol (MeOH) can form only bimolecular dehydration products (dimethyl ether), while larger 1-butanol and 2-butanol reactants (BuOH) predominantly convert via monomolecular routes (to butenes) on Keggin POM clusters and acid forms of zeolites [19–22]. Consequently, these reactants cannot probe reactions (and transition states) of different molecularity involved in the two dehydration paths. EtOH reacts via monomolecular (to EY) and bimolecular (to DEE) routes on Brønsted acids at conditions relevant to the practice of dehydration catalysis, thus providing a unique opportunity to explore these mechanisms in concert.

Here, alcohol dehydration routes to alkenes and ethers are explored by combining EtOH rate and selectivity data on Brønsted acids of known structure and a broad range of acid strength ($H_{8-n}X^{n+}W_{12}O_{40}$) with density functional theory (DFT) treatments of acid strength and plausible elementary steps. Total EtOH dehydration rate data can be made consistent with several mechanistic interpretations, including one that is often implicated, in which monomolecular and bimolecular elementary steps mediate EY and DEE formation, respectively. The measured ratios of formation rates (r_{DEE}/r_{EY}), however, are inconsistent with these accepted pathways. It is such inconsistencies that motivate our reassessment of alkanol dehydration pathways. Such an assessment, if it is to be rigorous and complete, requires that we enumerate each plausible sequence of elementary steps, that we calculate their rates through accurate estimates of Gibbs free energies for all intermediates and transition states (instead of only their enthalpies), and that we systematically evaluate their respective contributions to measured rates, using protocols based on sensitivity and rate-of-production analyses. These protocols replace the customary visual inspection of graphical reaction coordinate depictions with a more complete theoretical framework suitable for quantitative comparisons. Such strategies are used here, using constants predicted from DFT-derived free energies, to reduce the number of relevant species and connecting reactions by retaining only those consequential for the formation of EY and DEE at conditions relevant to the practice of catalytic dehydration. The resulting reduced mechanism is consistent with all measured rates and selectivities; the measured rate and equilibrium constants agree well with those obtained from DFT-derived free energies on all POM acids.

3.2. Methods

3.2.1. Catalyst synthesis

Catalyst synthesis details have been reported elsewhere [23]. $H_3PW_{12}O_{40}$ (Sigma-Aldrich; reagent grade; CAS #12501-23-4), $H_4SiW_{12}O_{40}$ (Aldrich; >99.9%; CAS #12027-43-9), $H_5AlW_{12}O_{40}$ [24], and $H_6CoW_{12}O_{40}$ [25,26] were dispersed onto colloidal SiO_2 (Cab-O-Sil HS-5; 310 m^2 g^{-1}; 1.5 cm^3 g^{-1} pore volume) using incipient wetness impregnation at 0.04 POM [nm-SiO_2]$^{-2}$ surface densities (~5.0 % wt), unless noted otherwise. SiO_2-supported POM clusters are denoted here as "H_nXW/SiO_2", where n is proton stoichiometry. ^{31}P-MAS-NMR spectra showed that H_3PW Keggin structures were unchanged upon dispersion onto the SiO_2 support and after use in catalysis [23]; transmission electron micrographs showed that POM clusters were present as isolated clusters with two-dimensional aggregates as minority species at these surface densities [23].

3.2.2. Dehydration rate measurements and titrations with 2,6-di-tert-butylpyridine

Ethanol (EtOH) dehydration rates and selectivities were measured on samples (0.02 - 0.7 g) held within a packed-bed stainless steel tubular reactor (3/8 in. O.D.) with plug-flow hydrodynamics. Reactor temperatures were controlled using a resistively-heated furnace and measured with two K-type thermocouples (Omega; ± 0.2K), one held within a 1/16 in. stainless steel sheath aligned axially along the bed and another held against the external reactor wall. Pressure was controlled with a backpressure regulator (Equilbar, model EB1LF2).

Liquid ethanol (EtOH; Sigma-Aldrich; ≥ 99.5 %, anhydrous) was evaporated into a flowing He stream (UHP Praxair) using a syringe pump (Cole-Palmer 74900 Series). All transfer lines were kept at 423 K to prevent condensation of reactants, products, and titrants. He flow rates were metered using electronic mass flow controllers (Porter, Model 201). Molar flow rates of EtOH and He were controlled to give the desired EtOH pressures and maintain low EtOH conversions (< 15%). Reactant and product concentrations were measured by gas chromatography using flame ionization detection (Agilent 6890N GC; 50 m HP-1 column). Diethyl ether (DEE) and ethylene (EY) were the only products detected on all catalysts; no products were detected when reactants streams were exposed to empty reactors. Moderate catalyst deactivation was observed on H_5AlW/SiO_2 (< 25 % after 5 h time on stream) and H_6CoW/SiO_2 (< 50 % after 5 h time on stream) catalysts. In such cases, rates were corrected for any intervening deactivation by periodic rate measurements at a reference condition (1.0 kPa EtOH).

The number of Brønsted acid sites (H^+) accessible during catalysis was measured by titration with a non-coordinating base during catalysis. Titrations were conducted by dissolving 2,6-di-*tert*-butylpyridine (DTBP, Aldrich; > 97% ; CAS #585-48-8) in EtOH (0.024-0.086 % mol) and introducing the mixture into a He stream (UHP Praxair) to give 0.45 or 2.6 Pa DTBP pressures. EtOH dehydration rates and DTBP uptakes were determined from EtOH, EY, DEE, and DTBP concentrations in the reactor effluent. The number of DTBP molecules required to fully suppress dehydration rates was used to determine the number of H^+ responsible for measured rates [27].

3.2.3. Computational Methods

Periodic gradient-corrected density functional theory (DFT) was used as implemented in the Vienna ab initio simulation package (VASP) [28–31] to calculate structures and energies of gaseous reactants and products and of bound stable intermediates and transition states (TS) on Keggin POM clusters ($H_{8-n}X^{n+}W_{12}O_{40}$) with different central atoms ($X^{n+} = P^{5+}$, Si^{4+}, Al^{3+}, and Co^{2+}). A periodic plane-wave basis-set expansion to a cutoff energy of 396.0 eV was used to represent the wavefunctions for valence electrons. Projector augmented-wave method (PAW) [32,33] was used to describe electron-core interactions. The Perdew-Wang (PW91) [34] functional was used to calculate exchange and correlation energies within the generalized-gradient approximation. Electronic structures were converged self-consistently to energies within 1×10^{-6} eV with a $1 \times 1 \times 1$ Monkhorst−Pack [35] sampling of the first Brillouin zone (k-point mesh) and specified integer band occupancies (appropriate for the non-periodic molecular systems treated here) for each step in both structural optimizations and single-point calculations. All calculations for POM clusters with Co central atoms were performed with spin polarization and three unpaired electrons, corresponding to the Co^{2+} electronic configurations. Spin-restricted calculations were used for all other compositions.

The structures and energies of Keggin clusters (~1.2 nm diameter) and gaseous molecules were calculated by placing them at the center of a cubic unit cell with an edge-length of 3 nm to provide an intervening vacuum region sufficiently large to prevent interactions among clusters in adjacent unit cells [20,36,37]. Calculations of charged species were performed with uniform background charges to maintain neutral unit cells, and the resulting energies were corrected using methods[38] implemented in VASP. Long-range interactions among atoms in neighboring unit cells in charged and neutral systems were corrected using dipole and quadrupole moments, with the center of charge located at the center of the unit cell. Structures were relaxed until forces on all atoms were within 0.05 eV $Å^{-1}$. The charges at individual atoms were determined by Löwdin population analyses,[39,40] after transforming converged wave functions of optimized structures into a set of localized quasiatomic orbitals (QUAMBO) [41–44].

Minimum energy reaction paths were calculated using nudged elastic band (NEB) methods[45] with structures converged to energies within 1×10^{-4} eV and forces to within 0.3 eV $Å^{-1}$ to identify starting structures for TS structures and reaction modes. NEB TS structures were refined using Dimer calculations [46] with convergence criteria of within 1×10^{-6} eV for energies and 0.05 eV $Å^{-1}$ for forces on each atom. The structures of bound intermediate and TS were determined at the proton location labeled H_B in Figure 3 for $H_3PW_{12}O_{40}$.

Deprotonation energies (DPE) are defined as the energy an isolated proton (H+) and a structurally relaxed and isolated anion (A-) relative to that for an intact acid (HA):

$$DPE = E^{H^+} + E^{A^-} - E^{HA} \tag{1}$$

DPE values reported are for protons located at the bridging O-atom labeled as H_B in Figure 3 for $H_3PW_{12}O_{40}$.

For all reactant, product, and transition states reported here, enthalpies:

$$H = E_0 + ZPVE + H_{vib} + H_{trans} + H_{rot} \tag{2}$$

and free energies:

$$G = E_0 + ZPVE + G_{vib} + G_{trans} + G_{rot} \tag{3}$$

include contributions from electronic energies (E_0), zero-point vibrational energies (ZPVE), vibrational enthalpies and free energies (H_{vib} and G_{vib}), and for gaseous molecules their translational and rotational enthalpies (H_{trans} and H_{rot}) and free energies (G_{trans} and G_{rot}) . ZPVE, H_{vib}, and G_{vib} values were determined from the frequencies in optimized structures [47]. Low-frequency modes of weakly-bound adsorbates give rise to significant inaccuracies in vibrational contributions to free energies;[37] they were excluded from Gibbs free energy calculations. These modes were assumed instead to retain a fraction (0.7) of the translational and rotational entropies estimated by statistical mechanics for gaseous EtOH (3.15×10^{-4} eV/K), which was shown to provide accurate estimates of adsorption entropies for adsorbed molecules on oxide surfaces [48]. H_{trans}, H_{rot}, G_{trans}, and G_{rot} values for gaseous species were computed using statistical mechanics formalisms [47].

Rate constants for elementary steps were estimated from differences in free energies between each TS and its relevant precursors ($\Delta G^{\ddagger}$):

$$k = \frac{k_B T}{h} \exp\left(-\frac{\Delta G^{\ddagger}}{RT} \right) \tag{4}$$

where k_B is Boltzmann's constant and h is Planck's constant [49,50].

3.3. Results and Discussion

EtOH dehydration rates were measured on silica-supported Keggin POM clusters (H_nXW/SiO_2) with different central atoms (X = P, Si, Al, and Co). EtOH formed bimolecular and monomolecular dehydration products (DEE and EY, respectively) at all conditions and on all catalysts. Total dehydration rates are defined here as the combined molar rates of DEE and EY formation ($r_{total} = r_{DEE} + r_{EY}$). Titration with DTBP led to dehydration rates that decreased with increasing DTBP uptakes and were fully suppressed after all protons were titrated (Figure 1; H_3PW/SiO_2 and H_4SiW/SiO_2). These data indicate that Brønsted acid sites account for all DEE and EY products formed and that DTBP titrates all protons in POM/SiO_2 catalysts. DTBP uptakes (per POM; Table 1) are smaller than stoichiometric values (i.e., 8-x where x is the valence of the central atom) for all POM catalysts, suggesting that some protons inaccessible to EtOH or DTBP or are not present at reaction conditions; this may reflect intracluster or intercluster POM dehydroxylations, which remove some H^+ and POM O-atoms as H_2O, or condensation reactions of OH groups

in POM clusters with silanols.[51–53] Total dehydration turnover rates for each sample are reported here normalized by the number of H^+ titrated by DTBP during catalysis.

Table 1. Number of accessible H^+ per POM cluster measured by chemical titration with 2,6-di-*tert*-butylpyridine[a] during ethanol dehydration[b] on $H_nXW_{12}O_{40}/SiO_2$ (X = P, Si, Al, and Co) catalysts.

Catalyst	POM Content (% wt.)	POM Surface Density (POM $(nm^2\ SiO_2)^{-1}$)	Accessible H^+ (per POM)	H^+ Surface Density (H^+ $(nm^2\ SiO_2)^{-1}$)
$H_3PW_{12}O_{40}$	5	0.034	2.5	0.09
	10	0.067	2.9	0.18
$H_4SiW_{12}O_{40}$	5	0.034	1.9	0.06
$H_5AlW_{12}O_{40}$	5	0.033	2.7	0.09
$H_6CoW_{12}O_{40}$	5	0.039	2.5	0.10

[a] Assuming a 1:1 DTBP:H^+ adsorption stoichiometry

[b] $H_3PW_{12}O_{40}/SiO_2$ (5wt%): 0.08 kPa EtOH, 409 K. Other catalysts: 1 kPa EtOH, 409 K.
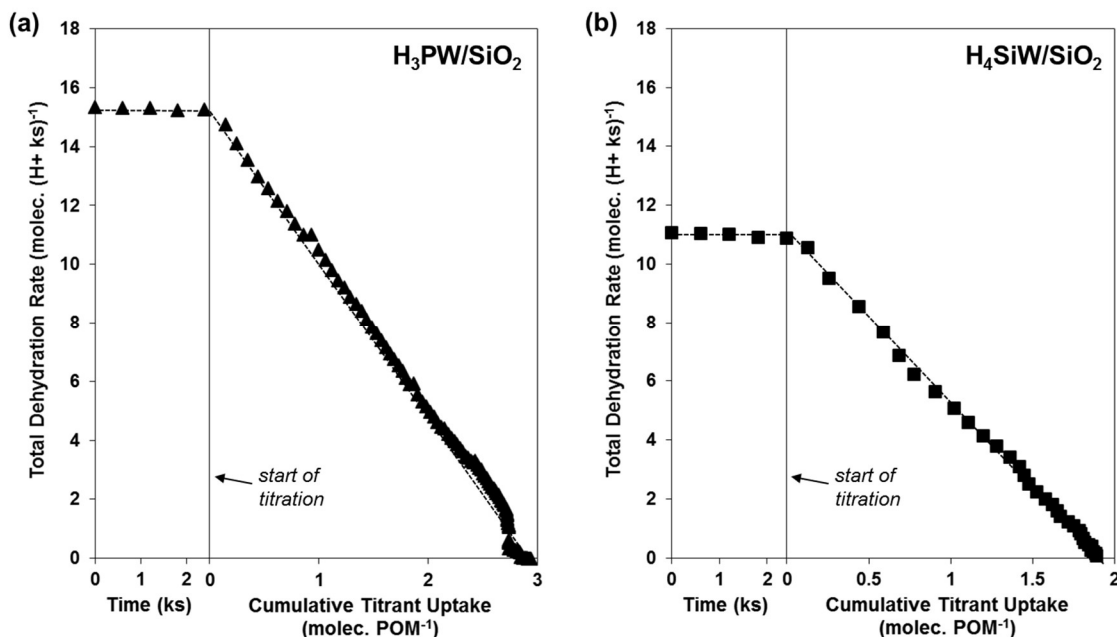
Figure 1. Total dehydration turnover rates on (a) H_3PW/SiO_2 and (b) H_4SiW/SiO_2 as a function of time before 2,6-di-*tert*-butylpyridine injection (1.0 kPa EtOH) and as a function of cumulative titrant uptake (1 kPa EtOH, 0.3 Pa 2,6-di-*tert*-butylpyridine).

Figure 2a shows measured total dehydration turnover rates (per accessible H^+) as a function of EtOH pressure on each POM/SiO_2 catalyst. Turnover rates are initially proportional to EtOH pressure but become insensitive to EtOH at higher pressures, a transition that occurs at higher pressures on POM clusters with lower-valent central atoms. The areal density of protons (0.09–0.18 H^+ $(nm^2\ SiO_2)^{-1}$) did not influence turnover rates on H_3PW/SiO_2 catalysts (Figure 2a), suggesting that measured rates are unaffected by

intraparticle ethanol concentration gradients, which would become stronger with increasing H^+ density. The lower reactivity of POM clusters with central atoms other than P on the same silica support precludes any effects of transport corruptions on these other catalysts.
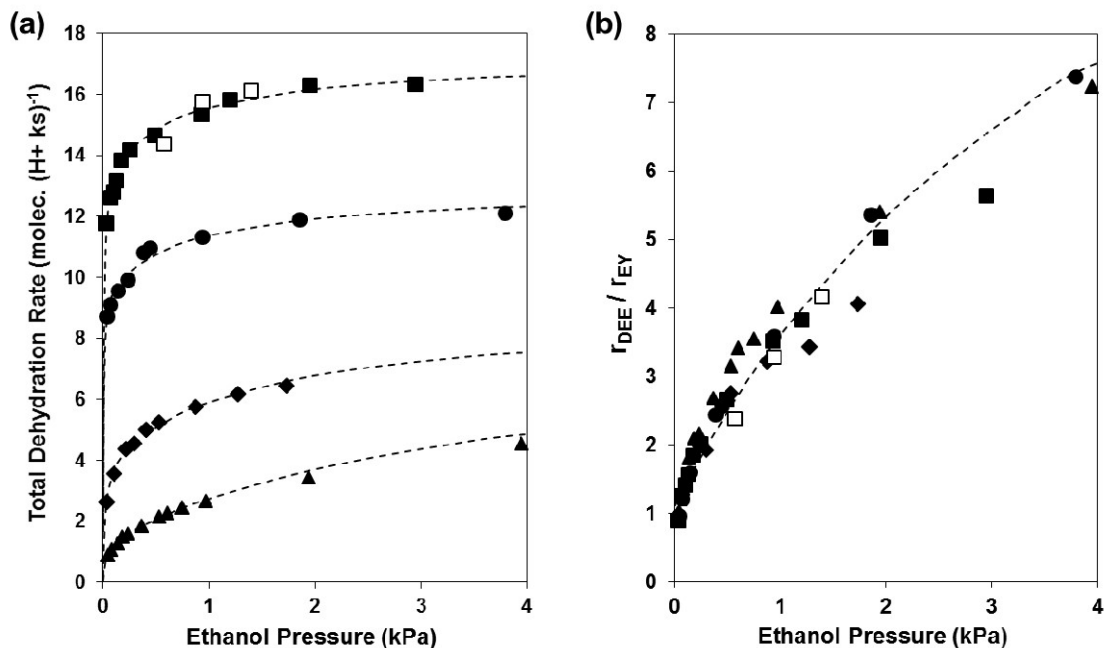
Figure 2. Measured (a) total EtOH dehydration turnover rates and (b) ratios of the rate of DEE formation to the rate of EY formation (r_{DEE}/r_{EY}) as functions EtOH pressure (kPa) on H_3PW/SiO_2 (H^+ [nm-SiO_2]$^{-2}$ = 0.09 (■) and 0.18 (□)), H_4SiW/SiO_2 (●), H_5AlW/SiO_2 (◆), and H_6CoW/SiO_2 (▲) (reaction conditions: 409 K, 0.02–4 kPa EtOH). Dashed lines represent the regression of the data to the functional form of Equations 15 and 16.

The ratios of DEE formation to EY formation rates (r_{DEE}/r_{EY}) are shown in Figure 2b as a function of EtOH pressure on all H_nXW/SiO_2 samples. These rate ratios increase sharply with increasing EtOH pressure at first and them more gradually at higher pressures; their values were similar for H_nXW/SiO_2 samples with different central atoms and did not depend of areal H^+ density (Figure 2b), indicating that selectivities are unaffected by diffusion-enhanced interconversions of EY and DEE products within acid domains. Consequently, the non-linear relationship between EtOH pressure and r_{DEE}/r_{EY} in Figure 2b, and the non-zero EY formation rates at high EtOH pressures of practical applications, are kinetic in origin.

3.3.1. Mechanism for EY and DEE formation

Conventional mechanisms that propose only monomolecular elementary steps for EY formation and bimolecular steps for DEE formation predict a simple linear relation between EtOH pressure and r_{DEE}/r_{EY} with a zero intercept,

$$\frac{r_{DEE}}{r_{EY}} = \frac{k_{DEE}[EtOH]}{k_{EY}} \qquad (5)$$

in sharp contrast with the data in Figure 2b. Therefore, the elementary steps must include at least two distinct pathways (with different EtOH pressure effects) to form one or both dehydration products. In what follows, we assemble a comprehensive set of plausible elementary steps for EY and DEE formation (Scheme 1) and evaluate their kinetic relevance using systematic protocols based on sensitivity and rate-of-production analyses together with thermodynamic and kinetic constants derived from density functional theory.

These plausible EtOH dehydration catalytic sequences (Scheme 1) include direct and sequential (alkoxide-mediated) routes (Steps 1-5,8,9,11). These steps account for EY and DEE formation from ethanol [3,5,11,12,54–58] and for the direct formation of EY from protonated EtOH dimers (Step 6), also proposed in the case of butanol dehydration on MFI zeolites[59]; additional steps, first proposed herein, account for bimolecular ethoxide formation and EtOH-assisted ethoxide deprotonation (Steps 7 and 10, respectively). The mechanism depicted in Scheme 1 involves five surface intermediates (bare protons (*), EtOH monomers (M*), protonated EtOH dimers (D*), ethoxides (X*), and ethoxide/EtOH site pairs (MX*)), three quasi-equilibrated steps (Steps 1-3), and eight irreversible steps (Steps 4-11). The reverse reactions for Steps 4-11 all depend on the concentrations of one or more dehydration product (EY, DEE, or H_2O). The irreversibility of these steps is evident from total dehydration rates and product formation rate ratios that do not depend on space velocity and, consequently, on the concentrations of dehydration products on H_4SiW/SiO_2 at differential EtOH conversions (Fig. S1-1 in Section 3.6), indicating that Steps 4-11 do not proceed at detectable rates in their reverse direction at the conditions of our experiments.

In these pathways, EtOH physisorbs at unoccupied Brønsted acid sites (Step 1; quasi-equilibrated) by forming an H-bond between the O-atom in EtOH and a proton. This H-bonded EtOH (or EtOH monomer) then protonates and reorients to eliminate H_2O to form a π-bonded EY that desorbs without protonation (Step 4) or an ethoxide at a terminal O-atom (Step 5). This ethoxide can form EY directly by cleaving its covalent C-O bond, leaving the H^+ at a bridging O-atom (Step 9). The adsorption of another EtOH at an O-atom adjacent to an EtOH monomer (Step 2; quasi-equilibrated) leads to the full transfer of the proton to the EtOH monomer to form protonated EtOH dimers, which can rearrange and release H_2O to form a protonated DEE that deprotonates and desorbs (Step 8); these dimers can also form a π-bonded EY adjacent to an adsorbed EtOH (from which EY desorbs; Step 6) or an ethoxide bound to a terminal O-atom with an adjacent EtOH (Step 7). EtOH adsorption next to an ethoxide (Step 3, quasi-equilibrated) forms a weak H-bond between the OH in EtOH and a bridging O-atom on the POM acid. The co-adsorbed EtOH molecule can react with the bound ethoxide by either a substitution reaction, in which the EtOH O-atom forms a bond with the α-carbon atom of the ethoxide while displacing the POM terminal O-atom to form DEE (Step 11), or acting as a proton shuttle in assisting EY formation (Step 10).
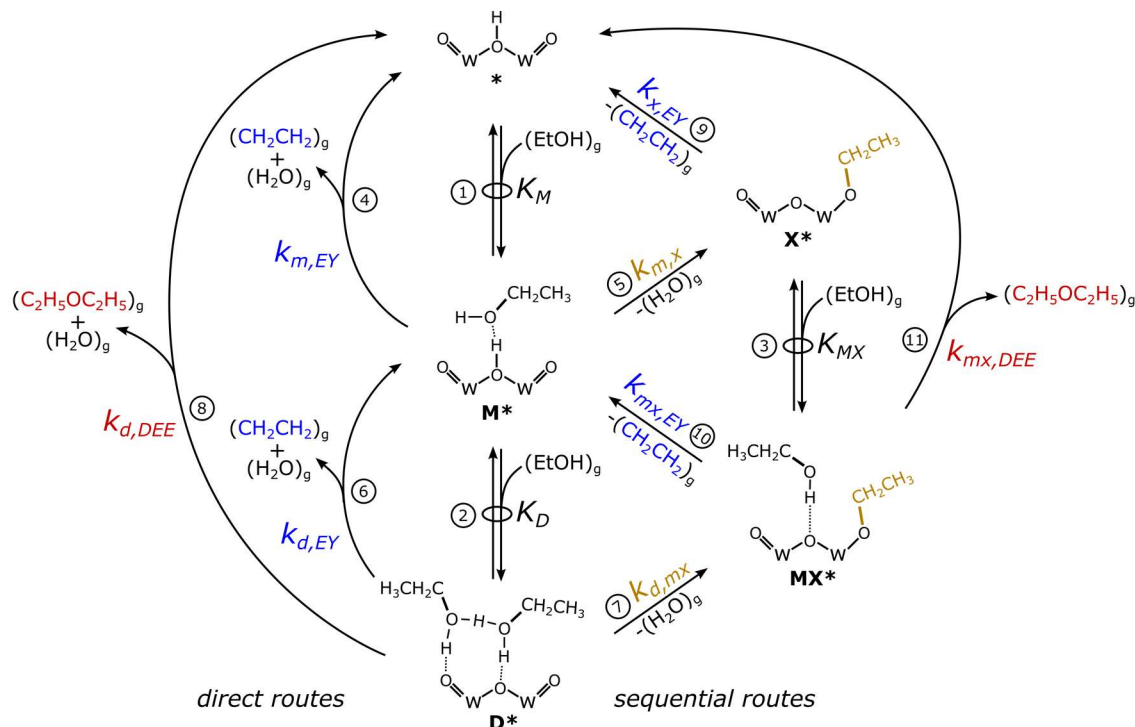
Scheme 1. Plausible sequences of elementary steps for the formation of EY and DEE from EtOH on Brønsted acid sites. Surface intermediate labels correspond to bare protons (*), EtOH monomers (M*), protonated EtOH dimers (D*), ethoxides (X*), and ethoxide/EtOH site pairs (MX*). Label colors indicate elementary steps that form DEE (red), EY (blue), and ethoxides (gold).

     The elementary steps depicted in Scheme 1 taken together with the assumptions of quasi-equilibrated EtOH physisorption at H^+ and at O-atoms vicinal to ethoxides or EtOH monomers (Steps 1-3), of irreversible elimination and substitution steps (Steps 4-11), and of pseudo-steady-state for all bound species give equations for the rates of EY formation:

$$\frac{r_{EY}}{[H^+]} = \frac{\left[k_{m,EY} + k_{d,EY}K_D[\text{EtOH}] + \left(k_{m,x} + k_{d,mx}K_D[\text{EtOH}]\right)\left(1 - f_{x\to DEE}\right)\right]K_M[\text{EtOH}]}{1 + (1+\beta)\,K_M[\text{EtOH}] + \left(K_D + \beta K_{MX}\right)K_M[\text{EtOH}]^2} \quad (6)$$

and DEE formation:

$$\frac{r_{DEE}}{[H^+]} = \frac{\left[k_{d,DEE}K_D[\text{EtOH}] + \left(k_{m,x} + k_{d,mx}K_D[\text{EtOH}]\right)f_{x\to DEE}\right]K_M[\text{EtOH}]}{1 + (1+\beta)\,K_M[\text{EtOH}] + \left(K_D + \beta K_{MX}\right)K_M[\text{EtOH}]^2} \quad (7)$$

In these equations, $f_{x\to DEE}$ is given by:

100

$$f_{x \to DEE} = \frac{k_{mx,DEE} K_{MX}[\text{EtOH}]}{k_{x,EY} + \left(k_{mx,EY} + k_{mx,DEE}\right) K_{MX}[\text{EtOH}]} \qquad (8)$$

and represents the fraction of the ethoxide consumed that forms DEE. The β term, in turn, is given by:

$$\beta = \frac{k_{m,x} + k_{d,mx} K_D[\text{EtOH}]}{k_{x,EY} + \left(k_{mx,EY} + k_{mx,DEE}\right) K_{MX}[\text{EtOH}]} \qquad (9)$$

and reflects the ratio of ethoxide to EtOH monomer at surfaces. The rate constants are (i) $k_{m,EY}$ and $k_{m,x}$ for H_2O elimination from monomers for EY (Step 4) and for ethoxide formation (Step 5); (ii) $k_{d,DEE}$, $k_{d,EY}$, and $k_{d,mx}$ for H_2O elimination from EtOH dimers to form DEE (Step 8), EY (Step 6), and ethoxide (Step 7); (iii) $k_{x,EY}$ and $k_{mx,EY}$ for EY formation from ethoxides via unassisted (Step 9) and EtOH-assisted (Step 10) routes; and (iv) $k_{mx,DEE}$ for DEE formation from ethoxides (Step 11). The K_M, K_D, and K_{MX} parameters denote, respectively, the equilibrium constants for EtOH physisorption at protons (Step 1) and at O-atoms vicinal to EtOH monomers (Step 2) or ethoxides (Step 3). [H^+] represents the total number of protons, determined by titration with 2,6-di-*tert*-butyl pyridine during EtOH dehydration (Table 1).

In Section 3.3.2, DFT-derived free energies for intermediates and transition states are used together with sensitivity analysis protocols to determine the magnitude of the rate and equilibrium constants in Equations 6-9 and the respective contributions of each of the routes in Scheme 1 to the observed rates of formation of EY and DEE.

3.3.2. Theoretical treatments of intermediates and transition states in ethanol dehydration on POM clusters

3.3.2.1. EtOH adsorption at protons and at O-atoms vicinal to EtOH monomers and ethoxides

EtOH interacts with protons attached to O-atoms in POM clusters (Step 1 in Scheme 1) to form a strong bond between the POM proton (H_B; nomenclature defined in Figure 3) and the O-atom in EtOH (O_E) (M*; Figure 3); the O_B–O_E distance in M* (2.50–2.55 Å; Table 2) is much shorter than in H-bonded alkanols (2.74 Å),[36,60,61] suggesting that the POM proton is partially transferred to the EtOH molecule. The O_B–H_B bond in M* resembles that in the bare POM cluster (O_B–H_B = 0.97 Å vs. 1.04–1.06 Å for M*; Table 2) and is much shorter than the bond between the O-atom in EtOH and H_B (O_E–H_B = 1.44–1.51 Å for M*; Table 2), indicating that adsorbed EtOH monomers are not fully protonated by POM clusters, because proton transfer would result in to longer O_B-H_B and shorter O_E-H_B bonds than in M*. Yet, the charge on the H_B atom decreases from 0.443–0.452 in the bare proton to 0.376–0.379 in M* (Table 2) and the POM conjugate anion becomes more negatively charged (0.443–0.452 in *; 0.539–0.568 in M*) with the additional net positive charge residing at the adsorbed EtOH (0.160–0.192 in M*), consistent with significant electronic reorganization upon formation of the H-bond. EtOH adsorption enthalpies were more negative on POM clusters with smaller DPE values (stronger acids; Figure 4a),

ranging from -75.5 kJ mol^{-1} on the weakest acid (H$_6$CoW$_{12}$O$_{40}$, DPE = 1141 kJ mol^{-1}) to -86.7 kJ mol^{-1} on the strongest acid (H$_3$PW$_{12}$O$_{40}$, DPE = 1085 kJ mol^{-1}); these trends are consistent with the higher energetic cost of charge separation and the lower stability of the negative charge at the conjugate base for the weaker acids. EtOH adsorption enthalpies vary by less than concomitant changes in DPE (ΔH_{ads} = 11.2 kJ mol^{-1} vs ΔDPE = 56 kJ mol^{-1} going from H$_3$PW$_{12}$O$_{40}$ to H$_6$CoW$_{12}$O$_{40}$) because negative charges on POM anions decrease (0.568–0.539 for M*) as acids weaken, thus attenuating the greater energetic costs of charge separation in weaker acids. These adsorption enthalpies indicate that the interactions between EtOH and POM protons are much stronger than for H-bonding among gaseous EtOH molecules (-21 kJ mol^{-1} per H-bond),[62] as a consequence of electrostatic interactions between the partially charged H$_B$ and the O-atom in EtOH. EtOH adsorption entropies are negative (Figure 4b) because EtOH(g) loses significant mobility upon adsorption. These entropy losses are smaller on weaker acids because the O$_B$–H$_B$ distances (Table 2) and the partial charges in adsorbed EtOH (Table 2) are smaller than on stronger acids to offset the higher costs of charge separation on weaker acids; as a result, the H$_B$–O$_E$ bond is weaker and the adsorbed EtOH less rigid.

A second EtOH molecule can adsorb at an O-atom adjacent to the EtOH monomer (Step 2 in Scheme 1) to form additional H-bonds with the O-atom and the co-adsorbed EtOH. The most stable structure of these EtOH dimers (D* in Figure 3) contains an O$_{E1}$–H$_S$–O$_{E2}$ bridge between the two EtOH molecules, as well as a H-bond between each EtOH and a POM O-atom. The O–O distances between the two EtOH molecules (O$_{E1}$–O$_{E2}$ = 2.44–2.46 Å; Table 2) are shorter than for O$_{E1}$–O$_B$ and O$_{E2}$–O$_{T1}$ bonds between EtOH and the surface (2.50–2.60 Å and 2.60–2.66 Å, respectively; Table 2). These dimers (EtOH–H$_S$–EtOH) are more cationic than EtOH monomers (0.701–0.776 for D* vs. 0.539–0.568 for M*, range for POM clusters with different central atoms; Table 2), consistent with the more complete transfer of the proton upon dimer formation. The dimer formation enthalpies (from EtOH monomers and EtOH(g)) are large and negative (-74.1 to -85.9 kJ mol^{-1}; Figure 4a) and become less negative with increasing DPE (Figure 4a), because the concomitant increase in energetic costs of charge separation are offset only in part by their smaller charge in the conjugate anion (0.776–0.701 for D*). Dimer formation entropies are negative (Figure 4b) as a result of the binding of the second EtOH molecule, and more so than for EtOH monomer formation (Figure 4b), because the O$_{E1}$–H$_S$–O$_{E2}$ bridge in dimers (Figure 3) makes the bound EtOH molecules more rigid. Entropy losses are larger on weaker acids, consistent with their shorter O$_B$–H$_{E1}$ and O$_{T1}$–H$_{E2}$ bonds (Table 2), which compensate for the higher cost of charge separation in weaker acids by decreasing the amount and the separation of charges, thus making dimers slightly more rigid on weaker acids.

The adsorption of an EtOH molecule at an O-atom adjacent to an ethoxide (Step 3; Scheme 1) forms a bond between the H-atom in the EtOH hydroxyl group and an O-atom in the POM cluster (MX*; Figure 3). W$_2$–O$_{T2}$–C$_\alpha$ bond angles in ethoxides (X*; Figure 3) increased slightly upon EtOH co-adsorption to form MX* ($\angle$W$_2$–O$_{T2}$–C$_\alpha$ = 149.5–154.8° for MX* vs. 145.0–150.2° for X*; Figure 4, Table 2). The enthalpies of MX* formation (from X* and EtOH(g)) (-29.6 to -34.8 kJ mol^{-1}; Figure 4a) resemble those in the H-bonds prevalent among gaseous EtOH molecules (21 kJ mol^{-1}),[62] but are much less negative that for EtOH adsorption at POM protons (-75.5 to -86.7 kJ mol^{-1}; Figure 4a) or at POM

O-atoms adjacent to EtOH monomers (-74.1 to -85.9 kJ mol^{-1}; Figure 4a). These weak ethoxide-EtOH interactions give rise to large O_E–O_B distances (2.86–2.93 Å; Table 2), to slightly negative charges on the EtOH group (-0.010 to -0.032; Table 2, and to smaller entropy losses upon adsorption than for EtOH adsorption on protons or adjacent to EtOH monomers (Figure 4b). The enthalpies and entropies for the formation of EtOH/ethoxide moieties become slightly more negative as DPE increases because the higher electron densities in the weaker POM acids lead to stronger interactions with the H-atom at the OH group in EtOH.

In Section 3.3.2.4, these adsorption enthalpies and entropies (Figure 4) are used to estimate the relative abundance of these bound species, which interconvert via the quasi-equilibrated steps shown in Scheme 1 (*–M*–D*; Steps 1,2; X*–MX*; Step 3). In contrast with quasi-equilibrium concentrations of these species, the concentration of ethoxides (X*, MX*) relative to those interacting with bare protons or EtOH(g) (M*, D*) reflect their relative rates of formation (Steps 5, 7) and consumption (Steps 9-11), as prescribed by the pseudo-steady-state-hypothesis.
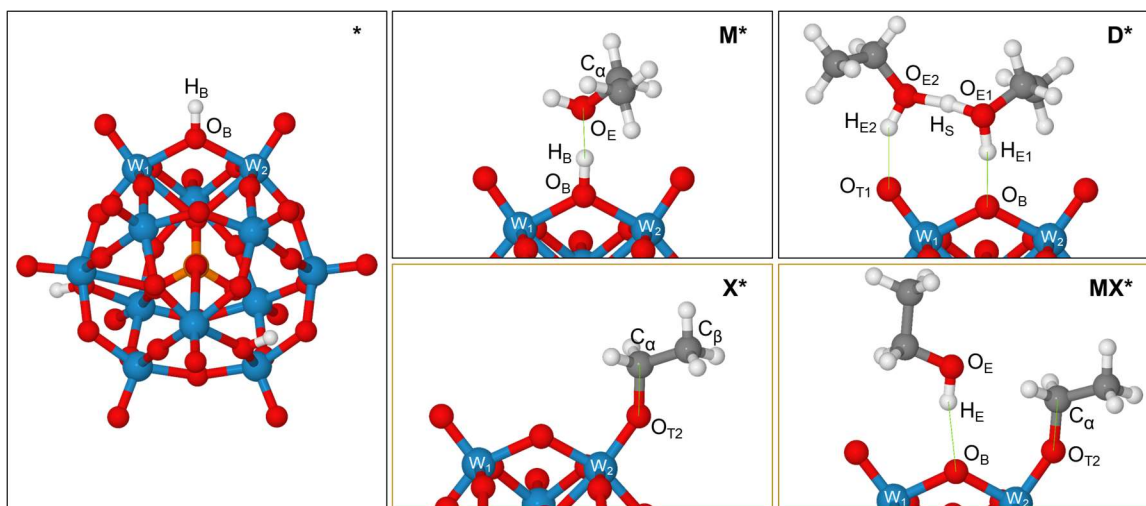
Figure 3. Structures for surface intermediates in Scheme 1 on $H_3PW_{12}O_{40}$: bare protons (*), EtOH monomers (M*), protonated EtOH dimers (D*), ethoxides (X*), and ethoxide/EtOH site pairs (MX*).

Table 2. Atomic distances (Å), bond and dihedral angles (degrees), and charges (electron charges) of surface intermediates on Keggin POM clusters.

species[a]	central atom			
	P	Si	Al	Co
bare cluster (*)				
O_B-H_B	0.97	0.97	0.97	0.97
charge – H_B	0.452	0.451	0.449	0.443
EtOH monomer (M*)				
O_B-O_E	2.50	2.52	2.53	2.55
O_B-H_B	1.06	1.05	1.05	1.04
O_E-H_B	1.44	1.48	1.48	1.51
C_α-O_E	1.47	1.46	1.46	1.46
charge – H_B	0.376	0.379	0.379	0.379
charge – EtOH	0.192	0.176	0.173	0.160
charge – EtOH+H_B	0.568	0.555	0.552	0.539
protonated EtOH dimer (D*)				
O_{E1}-O_{E2}	2.45	2.45	2.44	2.46
O_{E1}-H_S	1.11	1.10	1.10	1.08
O_{E2}-H_S	1.35	1.36	1.35	1.39
O_{E1}-O_B	2.60	2.57	2.56	2.50
O_{E1}-H_{E1}	1.03	1.04	1.04	1.07
O_B-H_{E1}	1.58	1.53	1.53	1.44
O_{E2}-O_{T1}	2.66	2.63	2.60	2.60
O_{E2}-H_{E2}	1.00	1.00	1.00	1.00
O_{T1}-H_{E2}	1.74	1.71	1.67	1.66
$\angle O_B$-H_{E1}-O_{E1}	172.3°	171.4°	168.7°	169.3°
$\angle O_{E1}$-H_S-O_{E2}	171.9°	171.8°	171.5°	171.5°
$\angle O_{E2}$-H_{E2}-O_{T1}	151.6°	151.8°	153.8°	154.4°
charge – EtOH dimer	0.776	0.754	0.741	0.701
ethoxide (X*)				
O_{T2}-C_α	1.45	1.44	1.44	1.43
C_α-C_β	1.51	1.51	1.51	1.51
H_β-C_β	1.10	1.10	1.10	1.10
$\angle W_2$-O_{T2}-C_α	145.0°	147.1°	147.4°	150.2°
charge – ethyl ($C_\alpha H_2 C_\beta H_3$)	0.350	0.344	0.340	0.332
ethoxide/EtOH site pair (MX*)				
O_{T2}-C_α	1.46	1.45	1.44	1.44
O_E-O_B	2.93	2.91	2.89	2.86
O_E-H_E	0.98	0.98	0.98	0.98
O_B-H_E	1.97	1.95	1.92	1.89
$\angle W_2$-O_{T2}-C_α	149.5°	154.5°	154.5°	154.8°
charge – ethyl ($C_\alpha H_2 CH_3$)	0.365	0.360	0.354	0.346
charge – EtOH	–0.013	–0.019	–0.010	–0.032
charge – ethyl+EtOH	0.352	0.341	0.344	0.314

[a] Atomic and structural labels correspond to diagrams in Figure 3.
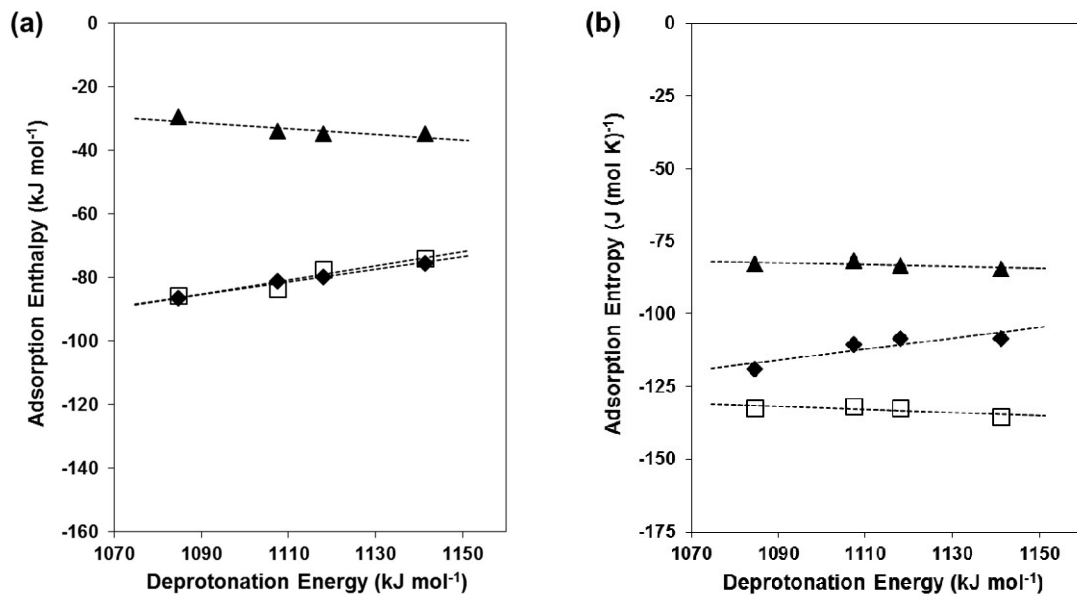
Figure 4. Calculated (a) adsorption enthalpies and (b) adsorption entropies as functions of DPE for monomers (M* in Figure 3, ◆) relative to a bare cluster and EtOH(g), protonated dimers (D* in Figure 3, □) relative to an EtOH monomer and EtOH(g), and for ethoxide/EtOH site pairs (MX* in Figure 3, ▲) relative to an ethoxide (X* in Figure 3) and EtOH(g) for $H_{8-n}X^{n+}W_{12}O_{40}$ ($X^{n+} = P^{5+}$, Si^{4+}, Al^{3+}, and Co^{2+}). Dashed lines are linear best fits of the calculated values to changes in DPE.

3.3.2.2. Ethylene formation via syn-E2-type elimination steps from EtOH monomers, EtOH dimers, ethoxides, and EtOH/ethoxide pairs

All four routes leading to EY in Scheme 1 (Steps 4, 6, 9, 10) involve a concerted syn-E2-type elimination, in which a C_α–O_L bond cleaves with the concerted abstraction of a β-hydrogen atom by a basic O-atom (O_R). When EY forms directly from EtOH monomers or dimers, this β-hydrogen (H_β) is abstracted by a POM O-atom and C_α–O_L cleavage either releases a H_2O(g) molecule (direct monomolecular EY formation; TS4; Figure 5) or forms a H_2O that interacts via H-bonding with the vicinal EtOH (direct bimolecular EY formation; TS6 in Figure 5). Sequential EY formation routes involve the prior evolution of water and the subsequent formation of an ethoxide; these steps cleave the C_α–O_L bond between the ethoxide and the terminal O-atom while a β-hydrogen atom is abstracted by either a bridging O-atom in the POM (sequential monomolecular EY formation; TS9 in Figure 5) or an O-atom in a co-adsorbed EtOH (sequential bimolecular EY formation; TS10 in Figure 5). The β-hydrogen (H_β) and the O-atom at the α-carbon (O_L) in all the elimination TS structures (TS4, TS6, TS9, and TS10) are nearly syn-coplanar on all POM clusters; their H_β–C_β–C_α–O_L dihedral angles range from 0.4° to 13.0° (Table 3), consistent with those expected for syn eliminations (<20°).[63] In all elimination TS structures, the C_α–O_L bonds are more elongated (relative to those in ethoxides) than the C_β–H_β bonds (44–61% for C_α–O_L; 14–31% for C_β–H_β bonds; Table 3); the $C_\alpha H_2$ fragments have positive partial charges (0.271–0.350; Table 3), while the $C_\beta H_2$ fragments are slightly negative (0.071–0.126; Table 3), indicating that C_α–O_L bond cleavage is farther along the reaction coordinate for C_α–O_L bonds than C_β–H_β bonds at the TS. The simultaneous proton transfer,

105

double bond formation, and expulsion of the leaving group at these TS is consistent with those for syn-E2-type eliminations.[63–65] E2-type elimination TS structures can vary from being "E1$_{cb}$-like" when C–H cleavage is more advanced than C–O cleavage, to being "E1-like" in the other extreme (when C–O cleavage is more advanced than C–H cleavage).[64] Thus, the elimination TS structures for direct and sequential routes are more precisely characterized as syn-E2-type TS with some "E1-like" character.

The POM conjugate anions are more negatively charged for sequential bimolecular EY formation (0.667–0.701; TS10) and direct monomolecular EY formation (0.607–0.668; TS4) transition states than for sequential monomolecular EY formation (0.530–0.570; TS9). This is consistent with favorable ion-dipole interactions between the additional H_2O and EtOH fragments in TS4 and TS10 and the POM O-atoms, which cause the transfer of more charge from the POM conjugate anions to the cationic moieties at the TS. Weaker acids give smaller charges at the conjugate anion in TS4, TS9, and TS10 than stronger acids because the charge at the conjugate anion is less stable. Proton transfer has occurred to a much greater extent in TS6 than in TS4 or TS10 as evidenced by their shorter O_R–H_β bonds (1.22-1.30 Å; TS6, 1.32-1.44 Å; TS4 and TS10) and smaller charges on $C_\alpha H_2$ (0.275-0.289; TS6, 0.287-0.350; TS4 and TS10). Also, TS6 exhibits less negative conjugate anions (0.565–0.577; TS6) than TS4 and TS10 (0.607–0.668; TS4, 0.667–0.701; TS10), in spite of its additional EtOH or H_2O fragments, suggesting that ion-dipole interactions between the H_2O and EtOH fragments and the POM O-atoms are less favorable in TS6 than in TS4 or TS10.

Figure 6a shows enthalpies for all elimination TS structures (TS4, TS6, TS9, and TS10) referenced to a bare proton and two EtOH(g) as a function of DPE for $H_{8-n}X^{n+}W_{12}O_{40}$ clusters with different central atoms (X^{n+} = P^{5+}, Si^{4+}, Al^{3+}, and Co^{2+}). These enthalpic barriers are larger for TS moieties with fewer molecular fragments (ethyl, EtOH, or H_2O). For instance, the TS for sequential monomolecular EY formation (TS9; Figure 5), with a single ethyl fragment, has the highest barriers (Figure 6a), while the TS for direct bimolecular EY formation (TS6; Figure 5), with ethyl, EtOH, and H_2O fragments, shows the lowest barriers (Figure 6a) among elementary steps that lead to EY on all POM acids. These trends reflect the larger number of H-bonds and ion-dipole interactions at TS structures containing additional EtOH or H_2O molecules. This enthalpic stabilization, conferred by the presence of several fragments (Figure 9), is attenuated by concomitant entropy losses upon formation of the larger and more complex TS structures (Figure 4b). Weaker acids (larger DPE values) give larger enthalpy barriers for all EY formation routes than stronger acids (Figure 4a), because the formation of all TS structures requires charge transfer into the POM clusters to form the cationic organic moiety at the TS (0.530–0.701; Table 3). The enthalpy and entropy barriers in Figure 4 are used in Section 3.3.2.4, together with those for the formation of DEE and alkoxides (Section 3.3.2.3) to determine the relative contributions of these elimination steps (Steps 4, 6, 9 10) to EY formation.
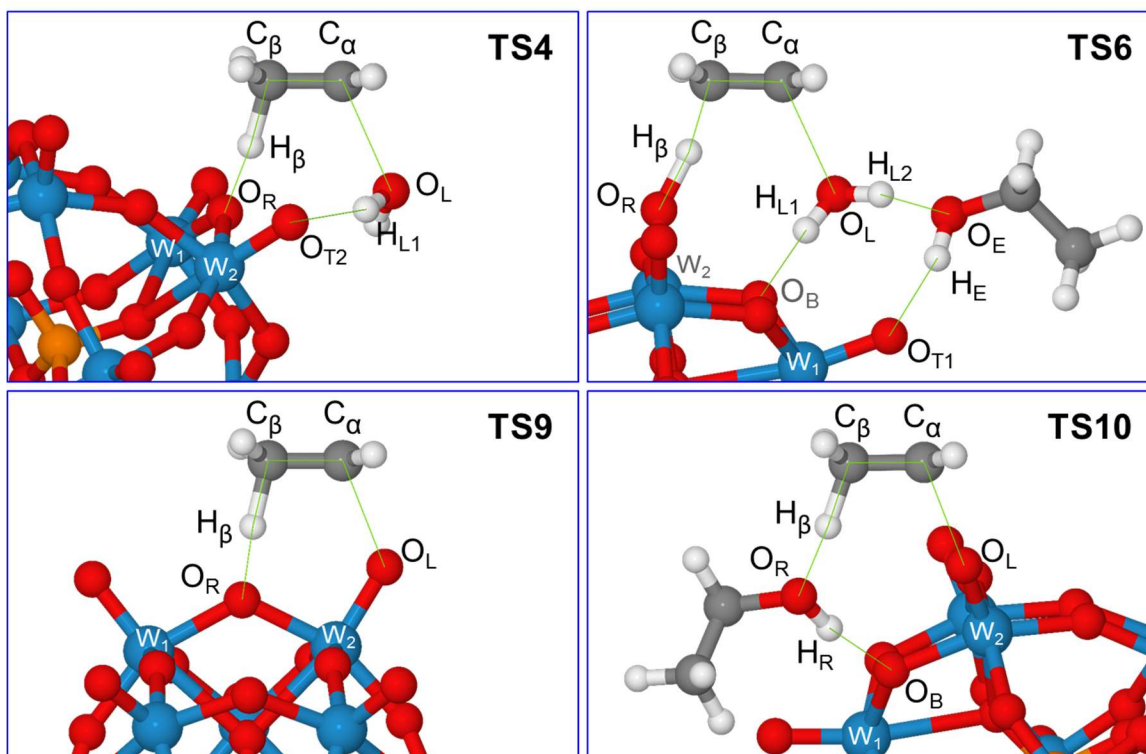
Figure 5. Structures of transition states that mediate elementary steps in Scheme 1 for direct monomolecular EY formation (Step 4; TS4), direct bimolecular EY formation (Step 6; TS6), sequential monomolecular EY formation (Step 9; TS9), and sequential bimolecular EY formation (Step 10; TS10) on $H_3PW_{12}O_{40}$.

Table 3. Atomic distances (Å), bond and dihedral angles (degrees), and charges (electron charges) for transition states that mediate ethylene formation on Keggin POM clusters.

species[a]	central atom			
	P	Si	Al	Co
direct monomolecular EY formation (TS4)				
O_R-H_β	1.37	1.32	1.34	1.33
C_β-H_β	1.28	1.31	1.30	1.30
C_α-C_β	1.39	1.39	1.39	1.39
C_α-O_L	2.25	2.21	2.18	2.16
H_{L1}-O_{T1}	1.89	1.76	1.75	1.71
$\angle H_\beta$-C_β-C_α-O_L	12.0°	2.8°	1.8°	0.4°
charge – ethyl ($C_\alpha H_2 C_\beta H_2 H_\beta$)	0.550	0.512	0.506	0.486
charge – H_β	0.299	0.304	0.302	0.300
charge – $C_\beta H_2$	−0.075	−0.092	−0.096	−0.101
charge – $C_\alpha H_2$	0.326	0.300	0.299	0.287
charge – Leaving H_2O group	0.118	0.116	0.121	0.121
charge – cationic moiety	0.668	0.628	0.627	0.607
direct bimolecular EY formation (TS6)				
O_R-H_β	1.22	1.22	1.26	1.30
C_β-H_β	1.39	1.40	1.35	1.33
C_α-C_β	1.38	1.38	1.38	1.39
C_α-O_L	2.32	2.30	2.28	2.29
H_{L1}-O_B	1.90	1.87	1.85	1.83

107

H_{L2}-O_E	1.73	1.72	1.76	1.76
H_E-O_{T1}	1.86	1.85	1.87	1.85
∠H_β-C_β-C_α-O_L	5.4°	7.9°	9.8°	12.3°
charge – ethyl ($C_\alpha H_2 C_\beta H_2 H_\beta$)	0.519	0.506	0.512	0.504
charge – H_β	0.340	0.339	0.332	0.327
charge – $C_\beta H_2$	−0.096	−0.103	−0.105	−0.112
charge – $C_\alpha H_2$	0.275	0.271	0.285	0.289
charge – H_2O leaving group	0.018	0.021	0.031	0.039
charge – EtOH	0.039	0.038	0.034	0.032
charge – cationic moiety	0.576	0.565	0.577	0.575
sequential monomolecular EY formation (TS9)				
O_R-H_β	1.40	1.37	1.37	1.38
C_β-H_β	1.26	1.27	1.27	1.25
C_α-C_β	1.40	1.40	1.40	1.40
C_α-O_L	2.14	2.12	2.10	2.08
∠H_β-C_β-C_α-O_L	4.4°	3.2°	3.1°	3.2°
charge – ethyl ($C_\alpha H_2 C_\beta H_2 H_\beta$)	0.570	0.549	0.540	0.530
charge – H_β	0.292	0.295	0.297	0.295
charge – $C_\beta H_2$	−0.071	−0.079	−0.086	−0.098
charge – $C_\alpha H_2$	0.349	0.333	0.329	0.334
charge – cationic moiety	0.570	0.549	0.540	0.530
sequential bimolecular EY formation (TS10)				
O_R-H_β	1.44	1.42	1.43	1.39
H_β-C_β	1.25	1.26	1.26	1.28
C_α-C_β	1.40	1.40	1.40	1.40
C_α-O_L	2.07	2.05	2.09	2.08
H_R-O_B	1.72	1.67	1.65	1.60
∠H_β-C_β-C_α-O_L	0.5°	4.7°	13.0°	12.1°
charge – ethyl ($C_\alpha H_2 C_\beta H_2 H_\beta$)	0.524	0.507	0.515	0.494
charge – H_β	0.290	0.289	0.290	0.293
charge – $C_\beta H_2$	−0.116	−0.122	−0.115	−0.126
charge – $C_\alpha H_2$	0.350	0.340	0.340	0.327
charge – EtOH	0.177	0.180	0.174	0.173
charge – cationic moiety	0.701	0.686	0.688	0.667

[a] Atomic and structural labels correspond to diagrams in Figure 5.

Figure 6. Calculated (a) apparent enthalpy barriers and (b) apparent entropy barriers as functions of DPE for direct monomolecular EY formation (TS4 in Figure 5, □), direct bimolecular EY formation (TS6 in Figure 5, ○), sequential monomolecular EY formation (TS9 in Figure 5, ◆) and sequential bimolecular EY formation (TS10 in Figure 5, ▲) on $H_{8-n}X^{n+}W_{12}O_{40}$ (X^{n+} = P^{5+}, Si^{4+}, Al^{3+}, and Co^{2+}). Barriers are with respect to bare protons and two EtOH(g) molecules.

3.3.2.3. DEE and ethoxide formation via SN2-type pathways

All steps that form ethoxides (Steps 5 and 7; Figure 3) or DEE (Steps 8 and 11; Figure 3) involve S_N2-type reactions that cleave and form O-C bonds at the α-carbon ($C_α$) of an ethyl fragment in a concerted manner (Figure 7). In ethoxide formation, a terminal POM O-atom acts as the nucleophile in displacing either a H_2O molecule (monomolecular ethoxide formation; TS5 in Figure 7) or a H_2O molecule that is H-bonded to a co-adsorbed EtOH (bimolecular ethoxide formation; TS7 in Figure 7) at the $C_α$ of a protonated EtOH monomer, thus forming the new O-$C_α$ bond. In DEE formation, the O-atom in a co-adsorbed EtOH acts as the nucleophile in displacing either a H_2O molecule at the $C_α$ of a protonated EtOH (direct DEE formation; TS8 in Figure 7) or a terminal POM O-atom (sequential DEE formation; TS11 in Figure 7) at the $C_α$ of an ethoxide, thus forming the new O-$C_α$ bond. The $C_α$ atom in the ethyl cationic species ($C_αH_2CH_3$) at the TS structures for all S_N2-type substitution steps is nearly equidistant from the attacking (O_A) and leaving (O_L) O-atoms ($C_α$–O_A = 1.99–2.20 Å; $C_α$–O_L = 2.04–2.15 Å; Table 4); this $C_α$ center is penta-coordinated with a nearly trigonal bipyramidal geometry, consistent with the concerted nature and the required orbital alignment of S_N2-type substitution reactions. Also, the partial charges in $C_αH_2CH_3$ fragments at the TS (0.484–0.553; Table 4) are smaller than unity, consistent with solvation of the sp2 hybridized α-carbon and with the concomitant delocalization of its positive charge by the attacking and leaving groups.

Figure 8a shows the enthalpies of these S_N2-type transition states (referenced to a bare POM proton and two EtOH(g)) as a function of DPE for $H_{8-n}X^{n+}W_{12}O_{40}$ clusters (X^{n+}

109

= P^{5+}, Si^{4+}, Al^{3+}, and Co^{2+}). The enthalpy barriers for bimolecular ethoxide formation (TS7; Figure 7) and direct DEE formation (TS8; Figure 7) are similar to each other on each given POM acid and smaller than those for monomolecular ethoxide formation (TS5; Figure 7) or sequential DEE formation (TS11; Figure 7) (by 64.9–73.4 and 94.5–103.5 kJ mol^{-1}, respectively), consistent with their larger number of H-bonds and ion-dipole interactions. Enthalpy barriers for all of the S_N2-type TS structures were smaller on the stronger POM acids, because of the more stable conjugate anions at these transition states. Entropy losses upon formation of S_N2-type transition states (Figure 8b) are larger for transition states with additional molecular fragments (TS7 and TS8), consistent with the decrease in entropy accompanying the adsorption of EtOH(g) (Figure 4b).

In the next section, sensitivity and coverage analysis protocols are used to assess how each transition state (and its associated precursor steps) and surface intermediate contribute to EY and DEE formation on these solid Brønsted acids. These assessments are based on the DFT-derived enthalpies and entropies shown in Figure 4, 6, and 8 (values also shown in Tables S2-1 and S2-2 in Section 3.6).
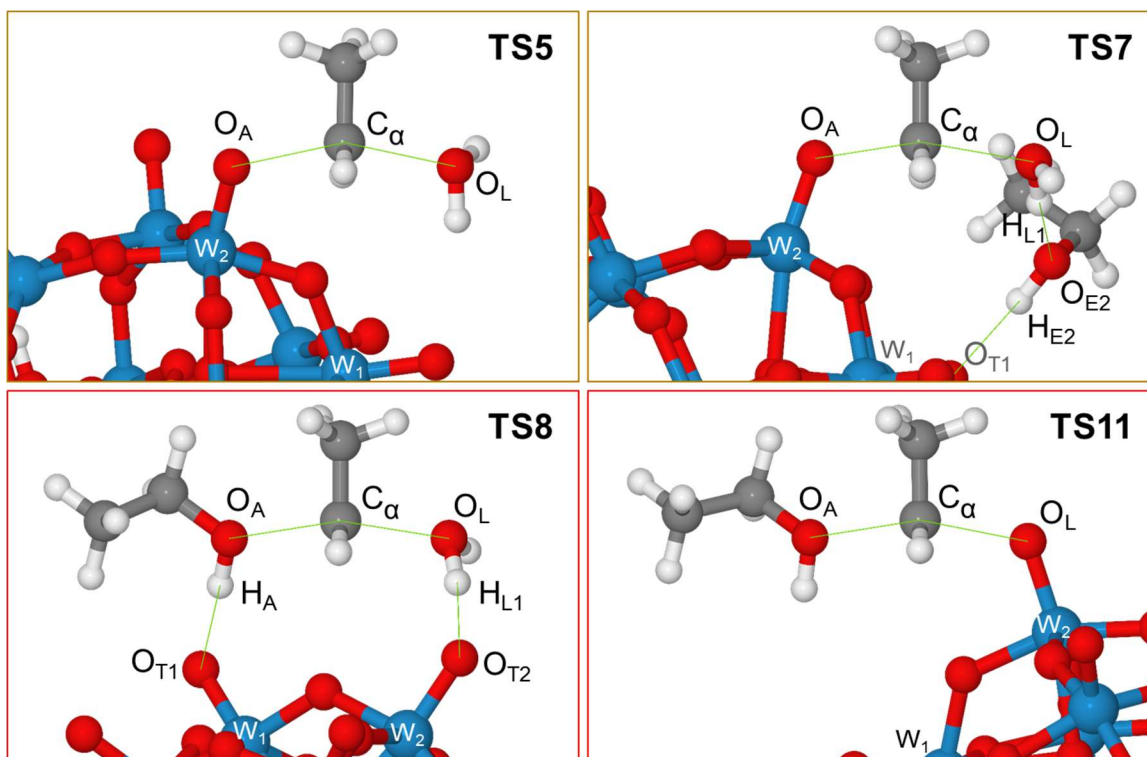
Figure 7. Structures of transition states that mediate elementary steps in Scheme 1 for monomolecular ethoxide formation (Step 5, TS5), bimolecular ethoxide formation (Step 7, TS7), direct DEE formation (Step 8, TS8), and sequential DEE formation (Step 11, TS11) on $H_3PW_{12}O_{40}$.

Table 4. Atomic distances (Å), bond and dihedral angles (degrees), and charges (electron charges) for transition states that mediate ethoxide and diethyl ether formation on Keggin POM clusters.

species[a]	central atom			
	P	Si	Al	Co
monomolecular ethoxide formation (TS5)				
O_A-C_α	2.16	2.17	2.17	2.20
C_α-O_L	2.12	2.11	2.08	2.08
$\angle O_A$-C_α-O_L	155.7°	152.9°	153.2°	146.9°
charge – ethyl ($C_\alpha H_2 CH_3$)	0.553	0.551	0.540	0.545
charge – H_2O leaving group	0.205	0.207	0.222	0.218
charge – cationic moiety	0.759	0.758	0.762	0.762
bimolecular ethoxide formation (TS7)				
O_A-C_α	1.99	2.00	2.01	2.02
C_α-O_L	2.15	2.13	2.15	2.15
H_{L1}-O_{E2}	1.62	1.59	1.61	1.62
H_{E2}-O_{T1}	1.99	1.92	1.86	1.90
$\angle O_A$-C_α-O_L	161.4°	161.8°	159.7°	159.1°
charge – ethyl ($C_\alpha H_2 CH_3$)	0.504	0.494	0.494	0.486
charge – H_2O leaving group	0.091	0.091	0.093	0.092
charge – EtOH	0.086	0.084	0.074	0.075
charge – cationic moiety	0.680	0.669	0.661	0.653
direct DEE formation (TS8)				
O_A-C_α	2.12	2.12	2.11	2.09
C_α-O_L	2.06	2.06	2.06	2.04
H_A-O_{E2}	1.75	1.73	1.72	1.71
H_{L1}-O_{T2}	1.67	1.67	1.67	1.65
$\angle O_A$-C_α-O_L	161.3°	161.1°	160.9°	161.2°
charge – ethyl ($C_\alpha H_2 CH_3$)	0.497	0.496	0.496	0.484
charge – H_2O leaving group	0.157	0.157	0.150	0.154
charge – EtOH	0.155	0.150	0.151	0.148
charge – cationic moiety	0.808	0.802	0.797	0.786
sequential DEE formation (TS11)				
O_A-C_α	2.10	2.07	2.13	2.09
C_α-O_L	2.06	2.08	2.09	2.10
$\angle O_A$-C_α-O_L	159.2°	153.0°	151.2°	150.8°
charge – ethyl ($C_\alpha H_2 CH_3$)	0.522	0.523	0.525	0.518
charge – EtOH	0.227	0.229	0.219	0.229
charge – cationic moiety	0.750	0.753	0.744	0.747

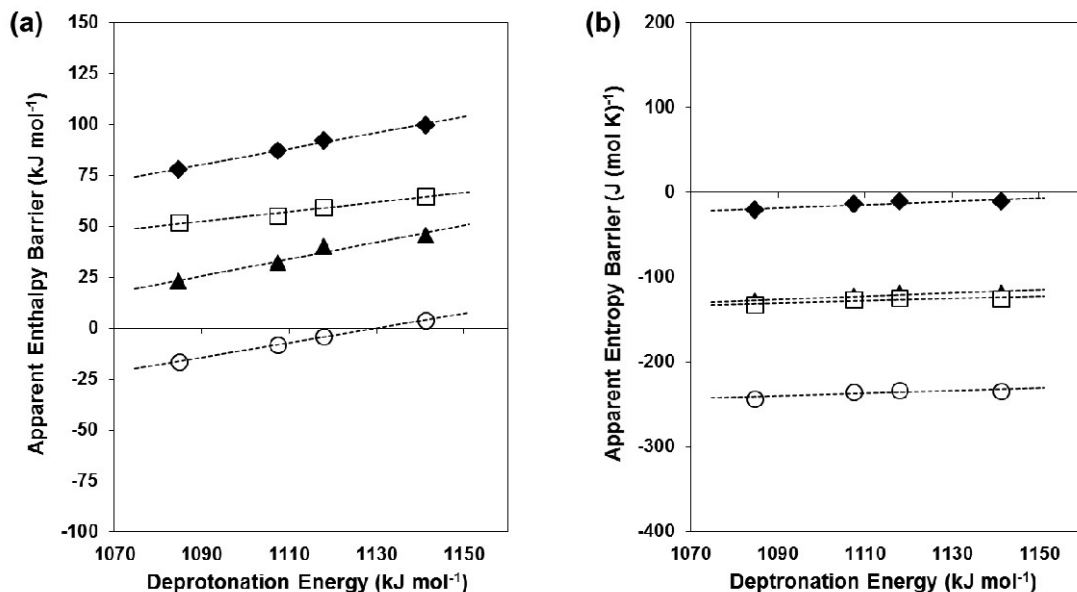[a] Atomic and structural labels correspond to diagrams in Figure 7.
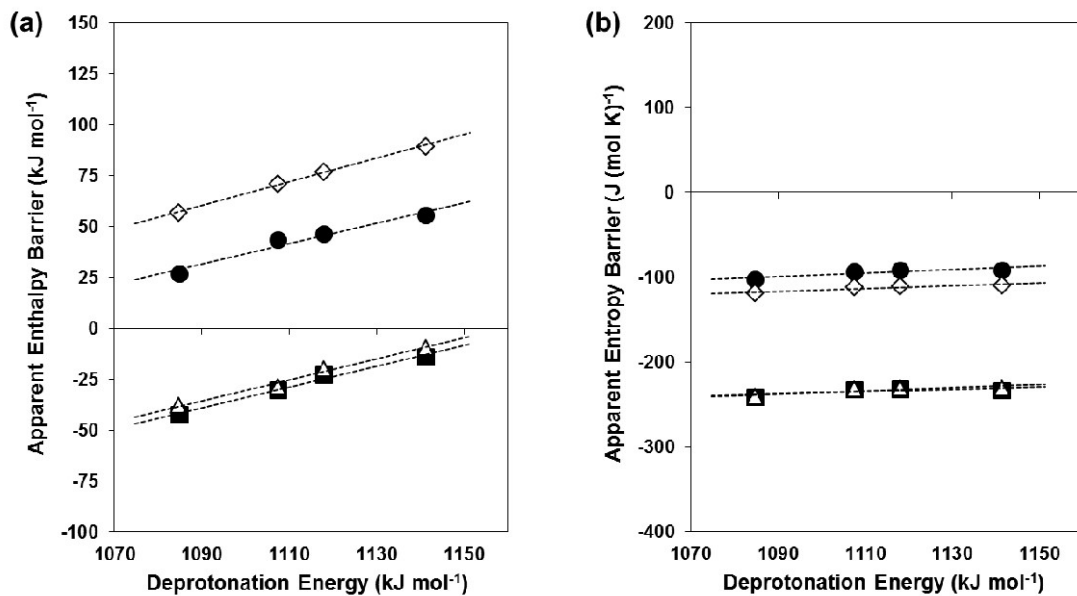
Figure 8. Calculated (a) apparent enthalpy barriers and (b) apparent entropy barriers as functions of DPE for monomolecular ethoxide formation (TS5 in Figure 7, $\diamond$), bimolecular ethoxide formation (TS7 in Figure 7, $\triangle$), direct DEE formation (TS8 in Figure 7, $\blacksquare$), and sequential DEE formation (TS11 in Figure 7, $\bullet$) on $H_{8-n}X^{n+}W_{12}O_{40}$ ($X^{n+} = P^{5+}$, Si^{4+}, Al^{3+}, and Co^{2+}). Barriers are with respect to bare clusters and two EtOH(g) molecules. Dashed lines are linear best fits of the calculated values.

3.3.2.4. Gibbs free energy comparisons among TS and surface intermediates in ethylene and diethyl ether formation routes

Figure 9 shows Gibbs free energies at 409 K for all transition states and surface intermediates in Scheme 1 referenced to a common precursor state (a bare proton and two EtOH(g)) on the strongest ($H_3PW_{12}O_{40}$; solid lines) and the weakest ($H_6CoW_{12}O_{40}$; dashed lines) acids. $H_6CoW_{12}O_{40}$ gives higher Gibbs free energy barriers for all TS structures than $H_3PW_{12}O_{40}$. The direct monomolecular EY formation route (TS4; Figure 5) shows free energy barriers similar to those for the monomolecular ethoxide formation route (TS5; Figure 7) on $H_3PW_{12}O_{40}$. On $H_6CoW_{12}O_{40}$, however, free energy barriers for TS4 are lower than those for TS5. On each acid catalyst, free energy barriers for bimolecular ethoxide formation (TS7; Figure 7) and direct DEE formation (TS8; Figure 7) routes are similar to each other and lower than those for direct bimolecular EY formation (TS6; Figure 5) and monomolecular routes for direct EY or ethoxide formation. The stability of alkoxides (X*; Figure 3) is similar on $H_3PW_{12}O_{40}$ (-32.1 kJ mol^{-1}; Figure 9) and $H_6CoW_{12}O_{40}$ (-34.0 kJ mol^{-1}; Figure 9), consistent with the small charges in such alkoxide species (0.332–0.350; Table 2) and with their largely covalent attachment to terminal O-atoms. Free energy barriers for sequential bimolecular EY formation (TS10; Figure 5) and sequential DEE formation (TS11; Figure 7) were similar on each given catalyst and smaller than those for sequential monomolecular EY formation routes (TS9; Figure 5).

Gibbs free energy differences among the intermediates in Figure 9 reflect their relative concentrations at equilibrium and 1 bar EtOH or H_2O gaseous species:

$$RT \ln\left(\frac{[B]_{eq}}{[A]_{eq}}\left(P_{EtOH}\right)^{\lambda}\left(P_{H_2O}\right)^{\gamma}\right) = G_A - G_B - \lambda \cdot G_{EtOH(g)} - \gamma \cdot G_{H_2O(g)} \quad\quad (10)$$

where $[A]_{eq}$ and $[B]_{eq}$ are the surface concentrations of any two intermediates at equilibrium, G_A and G_B are the free energies of the respective intermediates relative to bare protons and two gaseous EtOH molecules, P_{EtOH} and P_{H_2O} are in units of bars, λ and γ are the differences in the number of EtOH(g) and H$_2$O(g) in the A and B intermediates, and G_{EtOH} and G_{H2O} are the respective free energies of EtOH(g) and H$_2$O(g) molecules. The relative surface concentrations of A and B will depend on P_{EtOH} and P_{H_2O} as prescribed by Equation 10 at equilibrium; away from equilibrium, their free energies cannot be compared directly to assess their relative coverages. The concentration of ethoxides (X*, MX*) relative to those intermediates interacting with bare protons or EtOH(g) (M*, D*) reflect their relative rates of formation (Steps 5 and 7) and consumption (Steps 9-11), according to the pseudo-steady-state-hypothesis (not equilibrium), therefore the relative concentrations of these groups are not given by Equation 10. In Section 3.3.2.5, the fractional coverage of each of the intermediates in Scheme 1 is determined explicitly at all relevant reaction conditions in order to rigorously assess its abundance during EtOH dehydration on these catalysts, thus avoiding the problems associated with direct free energy comparisons.

Gibbs free energy differences among the TS structures in Figure 9 give the relative rates of their associated elementary steps at equilibrium concentrations of their reactive intermediates:

$$RT \ln\left(\frac{r_i}{r_j}\left(P_{EtOH}\right)^{\lambda}\left(P_{H_2O}\right)^{\gamma}\right) = G_j^{\ddagger} - G_i^{\ddagger} - \lambda \cdot G_{EtOH(g)} - \gamma \cdot G_{H_2O(g)} \quad\quad (11)$$

where r_i and r_j are the turnover rates for the two elementary steps, $G_i^{\ddagger}$ and $G_j^{\ddagger}$ are the free energies of their respective transition states (relative to a bare proton and two EtOH(g)), and λ and γ are the differences in the number of EtOH(g) and H$_2$O(g) between their two transition states. If the reactive intermediates for two elementary steps are not at equilibrium, Equation 11 cannot be used to determine their relative rates. According to Scheme 1, ethoxides (X*, MX*) are not in equilibrium with those intermediates interacting with bare protons or EtOH(g) (M*, D*), therefore the relative contributions of the elementary steps in Scheme 1 to EtOH dehydration rates on these catalysts cannot be determined solely from direct comparisons of free energies. Rate sensitivity protocols overcome these limitations and provide a more complete theoretical framework suitable for quantitative comparisons among elementary steps, these are used next to assess the relative contributions of the elementary steps in Scheme 1 to EY and DEE formation rates.
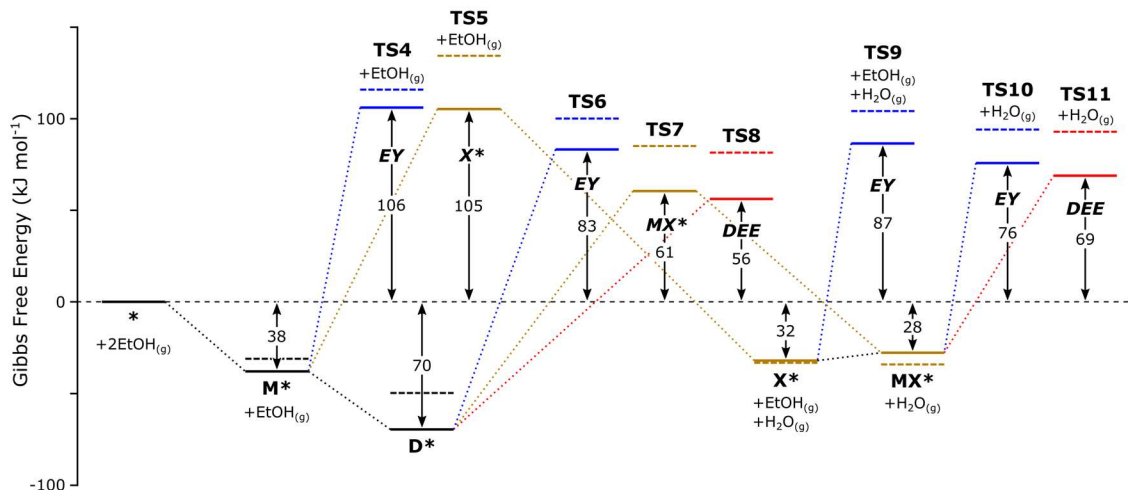
Figure 9. Gibbs free energy diagram for direct EY formation (TS4 and TS6 for monomolecular and bimolecular routes; Figure 5), direct DEE formation (TS8; Figure 7) and ethoxide formation (TS5 and TS7 for monomolecular and bimolecular routes, respectively; Figure 7) from adsorbed ethanol monomers (M*; Figure 3) or protonated EtOH dimers (D*; Figure 3), and sequential EY formation (TS9 and TS10 for monomolecular and bimolecular routes; Figure 5) and sequential DEE formation (TS11; Figure 7) from ethoxides (X*; Figure 3) or EtOH/ethoxide site pairs (MX*; Figure 3) on $H_3PW_{12}O_{40}$ (solid lines) and $H_6CoW_{12}O_{40}$ (dashed lines) at 409 K and standard pressure for all gaseous species.

3.3.2.5. Rate sensitivity and coverage analyses

The previous sections have enumerated plausible sequences of elementary steps for the formation of EY and DEE from EtOH and reported DFT-derived estimates for the enthalpies and entropies of the intermediates and transition states involved. Next, we rigorously compare the contributions of each of these routes and species to EY and DEE formation at relevant reaction conditions on solid acid catalysts with a broad range of acid strength using rate sensitivity and coverage analysis protocols[66,67] instead of the mere visual inspection of reaction coordinate energy diagrams.

The contribution of an elementary step to the rate at which a given product forms (r_i) can be determined for a given condition by evaluating the fractional change in r_i caused by a small fractional change in the magnitude of the DFT-derived rate constant for the elementary step (k_j):

$$F_{ij} = \frac{\partial \ln r_i}{\partial \ln k_j}.$$ (12)

An elementary step is inconsequential for forming all (n) products (and can thus be excluded from a sequence) when its overall rate sensitivity coefficient (V_j):

$$V_j = \left(\sum_{i=1}^{n} F_{ij}^2 \right)^{1/2} \tag{13}$$

is smaller than a specified threshold at all conditions of interest. Here, the contributions to DEE and EY formation rates by each elementary step in Scheme 1 (Steps 4-11) are determined on each POM acid using Equations 12 and 13 at 0.1–10 kPa EtOH, 0 kPa H_2O (valid at differential conversions) and 409 K. DEE and EY formation rates are calculated from Equations 6-9 with kinetic and thermodynamic constants calculated from DFT-derived Gibbs free energies.

Figure 10 shows V_j values for the rate constants for Steps 4-11 in Scheme 1 at each EtOH pressure on $H_{8-n}X^{n+}W_{12}O_{40}$ clusters ($X^{n+} = P^{5+}$, Si^{4+}, Al^{3+}, and Co^{2+}). The rate constants for Steps 4, 5, and 6 in Scheme 1 give V_j values below 0.11 at all pressures (0.1–10 kPa) on all POM acids (Figure 11); the rate constants for Steps 7-11 give V_j values above 0.22 at some or all EtOH pressures (Figure 11), suggesting a value of 0.11 as a reasonable threshold V_j value. Using this V_j value, direct monomolecular EY formation (Step 4; $V_{m,EY}$, TS4), monomolecular ethoxide formation (Step 5; $V_{m,x}$, TS5), and direct bimolecular EY formation (Step 6; $V_{d,EY}$, TS6) would not contribute to EY or DEE formation. Therefore, only Steps 1-3 and 7-11 are retained in describing the rate and selectivity data in Figure 2. Next, estimates of the prevalent coverages of all bound species are used to assess the contributions of the each of the denominator terms in Equations 6 and 7.
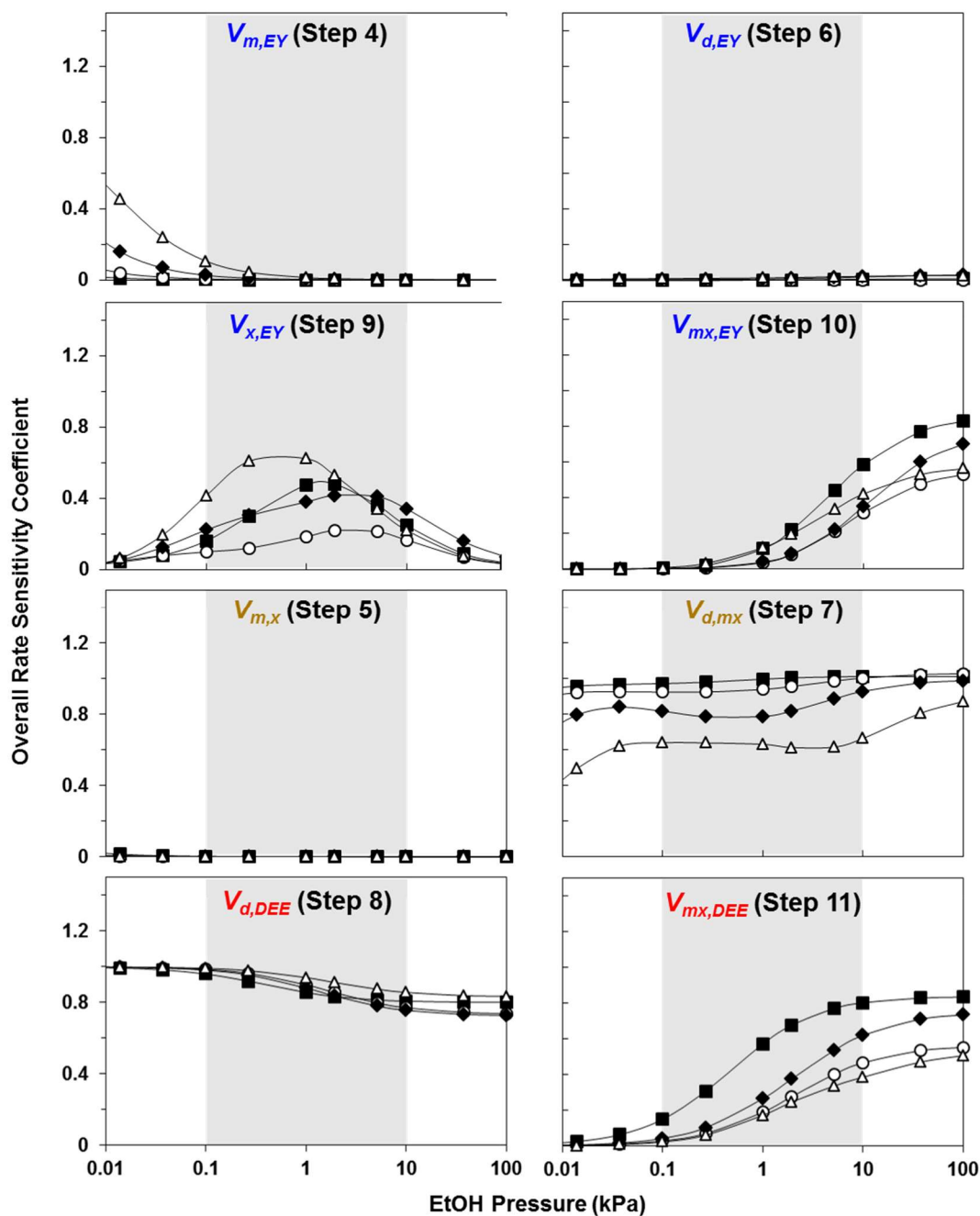
Figure 10. Overall rate sensitivity coefficients (Eq. 13) as a function of EtOH pressure for the irreversible steps in Scheme 1: direct monomolecular EY formation (Step 4; $V_{m,EY}$), direct bimolecular EY formation (Step 6; $V_{d,EY}$), sequential monomolecular EY formation (Step 9; $V_{x,EY}$), sequential bimolecular EY formation (Step 10; $V_{mx,EY}$), monomolecular ethoxide formation (Step 5; $V_{m,x}$), bimolecular ethoxide formation (Step 7; $V_{d,EY}$), direct DEE formation (Step 8; $V_{d,DEE}$), and sequential DEE formation (Step 11; $V_{mx,DEE}$) on $H_3PW_{12}O_{40}$ (■), $H_4SiW_{12}O_{40}$ (○), $H_5AlW_{12}O_{40}$ (◆), and $H_6CoW_{12}O_{40}$ (△) clusters at 409 K. Shaded regions show range of EtOH pressures considered (0.1-10 kPa) during rate sensitivity analysis.
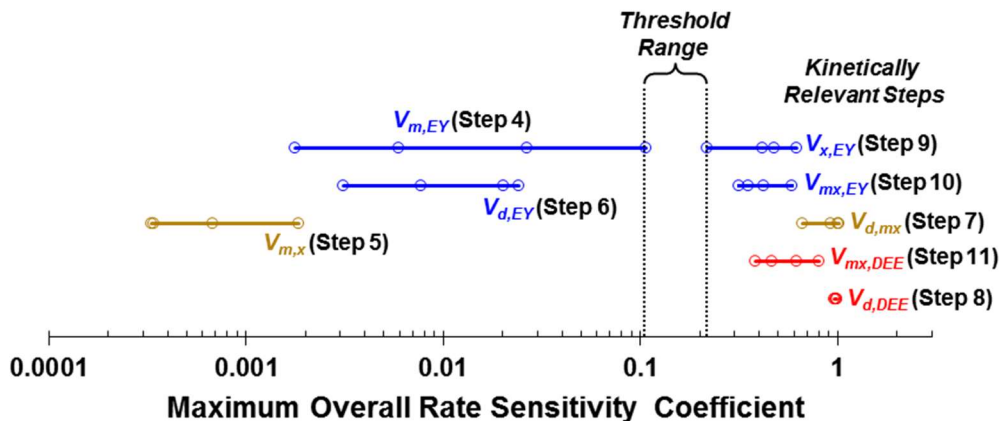
Figure 11. Maximum overall rate sensitivity coefficient for the irreversible steps in Scheme 1 within the considered EtOH pressure range (0.1-10 kPa) on $H_3PW_{12}O_{40}$, $H_4SiW_{12}O_{40}$, $H_5AlW_{12}O_{40}$, and $H_6CoW_{12}O_{40}$ clusters at 409 K.

The fractional coverage of a given bound intermediate j (θ_j) is defined as the number of sites occupied by that intermediate ($[B_j]$) divided by the total number of sites ($[H+]$):

$$\theta_j = \frac{[B_j]}{[H^+]} \tag{14}$$

Values of θ_j much smaller than unity indicate that the denominator term in Equation 6 that accounts for its coverage can be neglected in the rate equation, without any associated implications for the involvement of such intermediates in EY and DEE formation rates. Here, fractional coverages of the surface intermediates in Scheme 1 (bare protons (*), EtOH monomers (M*), protonated EtOH dimers (D*), ethoxides (X*), and EtOH/ethoxide pairs (MX*)) on each of the POM clusters are evaluated at a wide range of EtOH pressures and 409 K.

Values of θ_j from Equation 14, the steps in Scheme 1, and DFT-derived free energies are shown in Figure 12 as a function of EtOH pressure for $H_{8-n}X^{n+}W_{12}O_{40}$ clusters ($X^{n+} = P^{5+}$, Si^{4+}, Al^{3+}, and Co^{2+}). The θ_j values for bare protons and MX* are smaller than 0.06 at all relevant EtOH pressures (0.1–10 kPa) on all POM acids, while X*, M*, and D* give θ_j values larger than 0.07 at most EtOH pressures (0.1–10 kPa) on most POM acids (Figure 13), suggesting a threshold θ_j of 0.06 and leading us to consider only EtOH monomers (M*), protonated EtOH dimers (D*), and ethoxides (X*) as MASI. The steps retained from Scheme 1 by the sensitivity analysis and the MASI identified by the coverage analysis can then be used to simplify the equations for EtOH dehydration rates and (DEE/EY) ratios (r_{DEE}/r_{EY}) and to compare their functional form with that inferred from the rate and selectivity data in Figure 2.

117
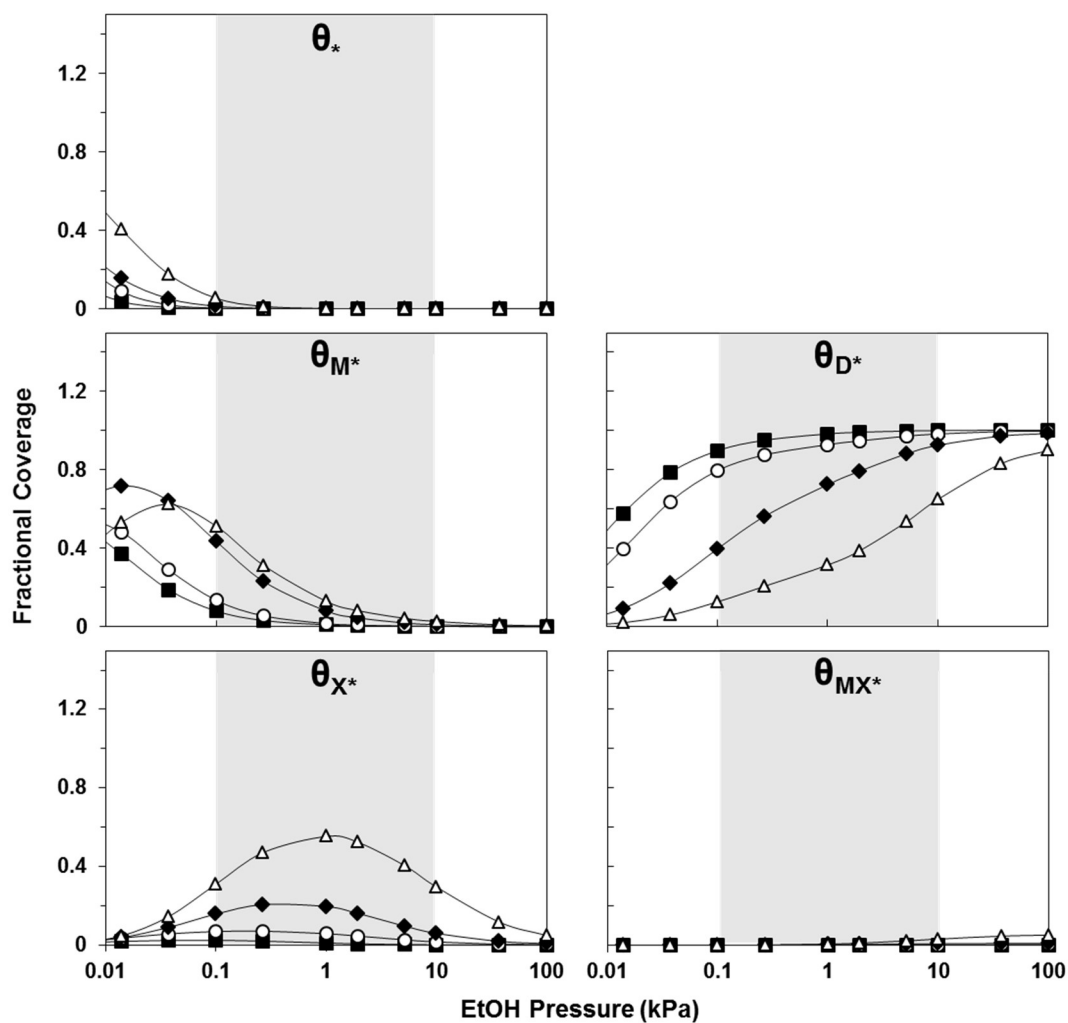
Figure 12. Calculated fractional coverages as functions of EtOH pressure for the surface intermediates considered in the mechanism in Scheme 1: bare protons (θ_*), EtOH monomers (M*; θ_{M*}), protonated EtOH dimers (D*; θ_{D*}), ethoxides (X*; θ_{X*}), and ethoxide/EtOH site pairs (MX*; θ_{MX*}) on $H_3PW_{12}O_{40}$ (■), $H_4SiW_{12}O_{40}$ (○), $H_5AlW_{12}O_{40}$ (◆), and $H_6CoW_{12}O_{40}$ (△) clusters at 409 K. Shaded regions show the range of EtOH pressures considered during coverage analysis.
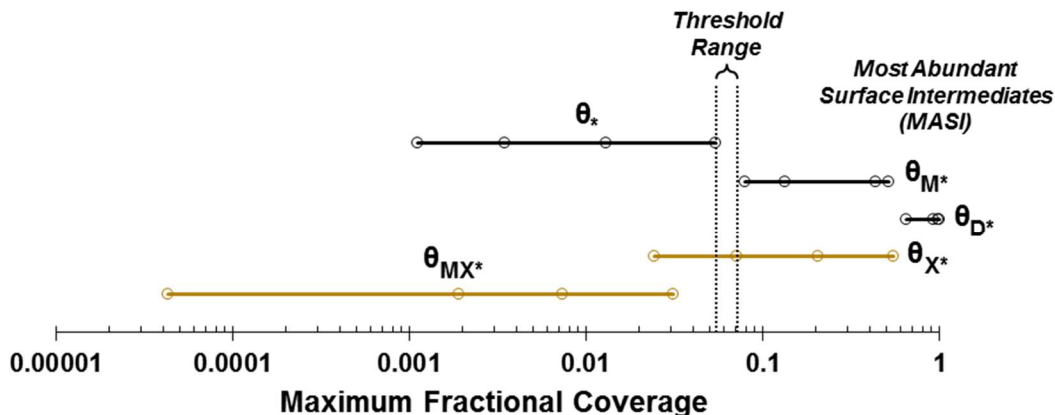
Figure 13. Maximum fractional coverage for the surface intermediates in Scheme 1 within the considered range of EtOH pressure (0.1-10 kPa) on $H_3PW_{12}O_{40}$, $H_4SiW_{12}O_{40}$, $H_5AlW_{12}O_{40}$, and $H_6CoW_{12}O_{40}$ clusters at 409 K.

3.3.2.6. Simplified rate expressions for total ethanol dehydration rates and for the ratio of diethyl ether and ethylene formation rates

The elementary steps depicted in Scheme 1, the results of the rate sensitivity analysis, and the assumptions of quasi-equilibrated EtOH physisorption at H^+ and at O-atoms vicinal to ethoxides or EtOH monomers (Steps 1-3) and irreversible elimination and substitution steps (Steps 7-11) give an expression for the ratio of DEE and EY formation rates (r_{DEE}/r_{EY}):

$$\frac{r_{DEE}}{r_{EY}} = \chi + \frac{(1+\chi)\,\delta\alpha[EtOH]}{1+\alpha[EtOH]}$$

(15)

$$\alpha = \frac{k_{mx,EY}K_{MX}}{k_{x,EY}} \qquad \chi = \frac{k_{d,mx}}{k_{d,DEE}} \qquad \delta = \frac{k_{mx,DEE}}{k_{mx,EY}}$$

These rates depend on three parameters:

(i) α (kPa^{-1}): the ratio of rate constants for sequential bimolecular EY formation with respect to ethoxides (Steps 3 and 10; $k_{mx,EY}K_{MX}$) and sequential monomolecular EY formation (Step 9; $k_{x,EY}$),

(ii) δ: the ratio of rate constants for sequential bimolecular DEE formation (Step 11; $k_{mx,DEE}$) and sequential bimolecular EY formation (Step 10; $k_{mx,EY}$), and

(iii) χ: the ratio of the rate constants for bimolecular ethoxide formation (Step 7; $k_{d,mx}$) to that for direct DEE formation (Step 8; $k_{d,DEE}$).

The similar r_{DEE}/r_{EY} values on H_nXW/SiO_2 of very different acid strength at all EtOH pressures (Figure 2b) reflect α, δ, and χ values that do not depend on POM composition or acid strength. Therefore, one value for each of these three parameters are regressed from

119

the data in Figure 2b using the functional form of Equation 15 (dashed line; Figure 2b); their values are shown in Figure 14 (as dotted lines).

The additional assumptions of pseudo-steady-state for all bound species and of ethoxides, EtOH monomers, and protonated EtOH dimers as MASI give an equation for EtOH dehydration rates:

$$\frac{r_{total}}{[H^+]} = \frac{k_{d,mx}\,(1+\chi)\,K_D[EtOH]}{1+\left(1+\dfrac{\phi}{1+(1+\delta)\,\alpha[EtOH]}\right)K_D[EtOH]}$$

$$\phi = \frac{k_{d,mx}}{k_{x,EY}}$$

(16)

that depends on three additional parameters:

(i) $k_{d,mx}$ (ks^{-1}): the rate constant for bimolecular ethoxide formation (Step 7),

(ii) K_D (kPa^{-1}): the equilibrium constant for protonated EtOH dimer formation from EtOH monomers and EtOH(g) (Step 2), and

(iii) ϕ: the ratio of rate constants for bimolecular ethoxide formation (Step 7; $k_{d,mx}$) and sequential monomolecular EY formation (Step 9; $k_{x,EY}$).

The terms in the denominator of Equation 16 reflect (from left to right) the relative coverages of EtOH monomers (M*), protonated EtOH dimers (D*), and ethoxides (X*) at acid sites. The dashed lines in Figure 2a represent the regression of all rate data to the functional form of Equation 16; using the same values of the three parameters in Equation 15 for all acids (dotted lines; Figure 14) and allowing the three parameters in Equation 16 to differ among the catalysts if so required in the regression. The regressed values of $k_{d,mx}$, K_D, and ϕ are shown in Figure 15a for H_nXW/SiO_2 samples (X = P, Si, Al, and Co).

Next, these parameters, derived from rate and selectivity data, are compared with those derived from DFT estimates of Gibbs free energies. The observed and predicted effects of acid strength on their values are discussed in the context of differences in charge among the different species involved in the steps accounting for the groupings of thermodynamic and kinetic rate constants that define the parameters in Equations 15 and 16.

3.3.3. Comparison of experiment and theory and the consequences of POM composition and acid strength

3.3.3.1. Ratios of rates of DEE and EY formation

Each of the three parameters that determine r_{DEE}/r_{EY} values (Eq. 14) depends on the ratio of constants for routes from a given intermediate (D* for $k_{d,mx}$ and $k_{d,DEE}$, MX* for $k_{mx,DEE}$ and $k_{mx,EY}$, and X* for $k_{mx,EY}K_{MX}$ and $k_{x,EY}$; Scheme 1). As a result, these ratios, and thus selectivities, reflect differences in free energy between the two TS structures that define each ratio and are unaffected by the stability of their common precursor:

$$RT \ln\left(\frac{k_{A \to B}}{k_{A \to C}} (\text{bar}^{-\lambda}) \right) = G^{\ddagger}_{A \to C} - G^{\ddagger}_{A \to B} - \lambda \cdot G_{EtOH(g)} \tag{17}$$

where $k_{A \to B}$ and $k_{A \to C}$ are rate constants for the two competing routes in each ratio, $G^{\ddagger}_{A \to B}$ and $G^{\ddagger}_{A \to C}$ are the free energies of the respective transition states, λ is the difference in the number of EtOH(g) in the two transition states, and $G_{EtOH,g}$ is the free energy of an EtOH(g) molecule.

The value of α reflects the relative free energies of TS9 (Step 9) and TS10 (Step 10) with a λ value of -1 (TS9 has one more EtOH(g) than TS10). The value of α regressed from measurements on POM/SiO$_2$ catalysts (0.22 kPa^{-1}; Figure 14) is within the range of values estimated from DFT (0.10–0.24 kPa^{-1}; Figure 14); thus, Steps 9 and 10 become equal in rate at 4.6 kPa EtOH (experiment) and 4.2–9.7 kPa EtOH (theory, range for different POM) and Step 10 becomes the preferred route at the higher EtOH pressures typical of commercial practice.

The value of δ reflects the relative free energies of TS8 (Step 8) and TS7 (Step 7) with a λ value of zero. It is near unity on all POM/SiO$_2$ acids (0.89; Figure 14), indicative of TS7 and TS8 structures of similar free energies and leading to similar barriers for bimolecular ethoxide formation (Step 7) and direct DEE formation (Step 8). The measured δ value is in reasonable agreement with DFT estimates (0.28–0.64; Figure 14). These two transition states (TS7 and TS8 in Figure 7) contain the same molecular fragments (ethyl, H$_2$O, and EtOH), but in different geometric alignment. In TS7, the displaced H$_2$O is H-bonded to the O-atom in EtOH and a POM terminal O-atom interacts with the α-carbon in the ethyl fragment. In contrast, the displaced H$_2$O in TS8 is H-bonded to a terminal O-atom in the POM and the O-atom in EtOH and interacts with the C$_\alpha$ in the ethyl fragment. The similar free energies of TS7 and TS8 indicate that terminal O-atoms in POM acids and O-atoms in EtOH behave similarly when either interacts with the α-carbon of an ethyl fragment or with an H-atom in H$_2$O.

The χ value reflects the relative free energies of TS10 (Step 10) and TS11 (Step 11) with a λ of zero. Its measured value is 6.5 on H$_n$XW/SiO$_2$ acids (Figure 14). Thus, TS11 has a slightly lower free energy than TS10 and consequently lower barriers for sequential DEE formation (Step 11) than for sequential bimolecular EY formation (Step 10). DFT-derived χ values are 1.3–7.6 (Figure 14), in reasonable agreement with measurements. The variability of χ values among the POM clusters are equivalent to DFT-derived free energy differences that vary by less than 3 kJ mol^{-1} from their average; this range of χ values, as opposed to the single χ value predicted from experiments, is attributed to the inherent inaccuracies of theoretical treatments. These results suggest that O-atoms in EtOH are only slightly better as nucleophiles (for DEE formation; TS11) than as H$^+$ abstractors (for EY formation; TS10) in reactions with ethoxides.

DFT-derived enthalpies for TS7, TS8, TS9, TS10, and TS11 depend similarly on DPE (dH/dDPE = 0.39–0.52; Table 5), consistent with the significant cationic character for the organic moieties at each of these ion-pair transition states (0.530–0.808; Table 3 and Table 4). These TS enthalpies all increase with increasing DPE (Figure 6 and Figure 8) because both protons and ion-pair transition states benefit from the more stable

121

conjugate bases in stronger POM acids. In contrast, r_{DEE}/r_{EY} ratios are not sensitive to DPE because both transition states in each ratio of rate constants benefit to the same extent from more stable conjugate anions. The unexpected r_{DEE}/r_{EY} trends observed experimentally on these POM acids (Figure 2b), which first motivated our re-examination of plausible alcohol dehydration pathways on Brønsted acids, are well described by Equation 15 and give constants in excellent agreement with those obtained from DFT-derived free energies. These findings indicate that that these selectivity trends reflect the contributions of bimolecular routes to ethoxide formation, direct and sequential routes to DEE formation, and sequential monomolecular and bimolecular routes to EY formation.
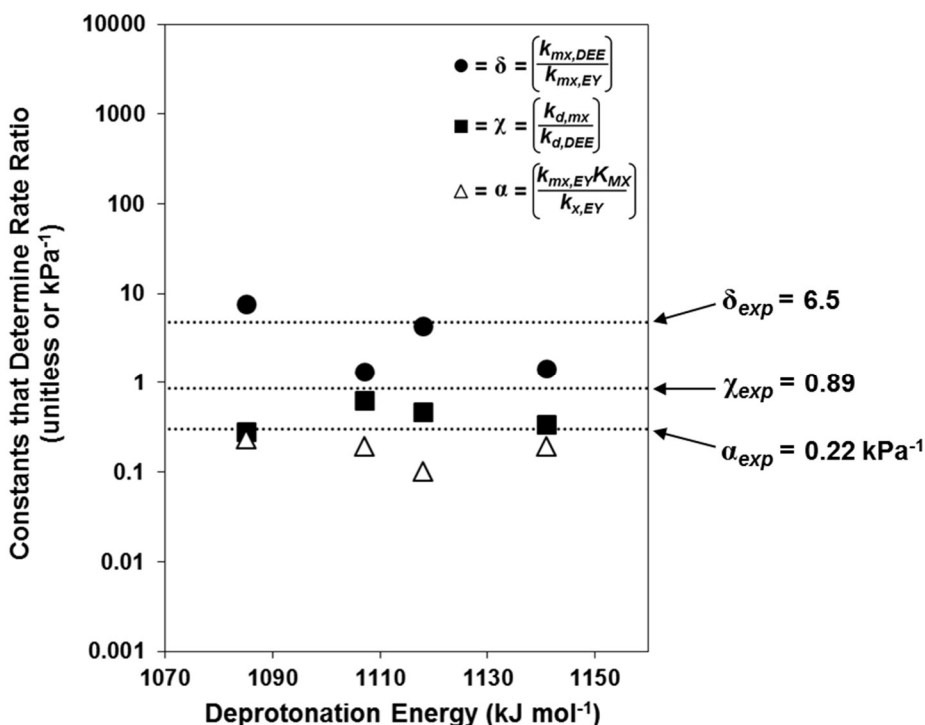
Figure 14. Values of δ (unitless; ●), χ (unitless; ■), and α (kPa^{-1}; △) (for associated steps see the mechanism in Scheme 1) predicted from DFT-derived energies as functions of DPE for $H_{8-n}X^{n+}W_{12}O_{40}$ ($X^{n+} = P^{5+}$, Si^{4+}, Al^{3+}, and Co^{2+}) catalysts at 409 K. Dotted lines are the values of the ratios derived from the regression of experimental data (Figure 2b) to the functional form of Equation 15.

Table 5. Dependences of calculated enthalpies and entropies for surface intermediates and TS relative to bare protons on deprotonation energies (dH/dDPE and dST/dDPE) for $H_{8-n}X^{n+}W_{12}O_{40}$ ($X^{n+} = P^{5+}$, Si^{4+}, Al^{3+}, and Co^{2+}) catalysts at 409 K.

species[a]	dH/dDPE	dST/dDPE
EtOH monomer (M*)	0.20 ± 0.01	0.08 ± 0.04
protonated EtOH dimer (D*)	0.42 ± 0.04	0.06 ± 0.04
ethoxide (X*)	0.03 ± 0.06	0.07 ± 0.04
bimolecular ethoxide formation (TS7)	0.52 ± 0.04	0.07 ± 0.03
direct DEE formation (TS8)	0.51 ± 0.04	0.06 ± 0.04
sequential monomolecular EY formation (TS9)	0.39 ± 0.02	0.08 ± 0.03
sequential bimolecular EY formation (TS10)	0.41 ± 0.06	0.08 ± 0.03
sequential DEE formation (TS11)	0.50 ± 0.07	0.08 ± 0.03

[a] Labels correspond to structures in Figure 3, Figure 5, or Figure 7.

3.3.3.2. Combined EtOH dehydration rates to EY and DEE

Figure 15a shows measured $k_{d,mx}$, K_D, and ϕ values (obtained by regressing the data in Figure 2a to the form of Eq. 16) as a function of the DPE values of H_nXW/SiO_2 with P, Si, Al, and Co central atoms. The $k_{d,mx}$ value reflects the free energy barrier for Step 7 (Scheme 1; free energy difference between TS7, for bimolecular ethoxide formation and D*, a protonated EtOH dimer). Measured $k_{d,mx}$ values (3.3–8.0 ks^{-1}; Figure 15a) are larger than those calculated from DFT-derived free energies (0.05–0.20 ks^{-1}; Figure 15b); these differences corresponds to DFT-derived free energy barriers that are 12.6–14.8 kJ mol^{-1} larger than measured values and appear to reflect approximation methods for calculating entropies of low vibrational modes of weakly-bound intermediates that underestimate TS7 entropies relative to those for protonated EtOH dimers (D*). The $k_{d,mx}$ values decrease exponentially with increasing DPE, but they reflect an increase in activation barriers much smaller than the concomitant changes in DPE; such attenuation effects[20,36] arise from TS7 structures that benefit from a more stable conjugate anion only slightly more than D*, a conclusion consistent with the similar positive charges at the TS7 cation (0.653-0.680; Table 4) and D* (0.701-0.776; Table 2) and with DFT-derived enthalpies of their formation from bare-clusters that depend similarly on DPE (dH/dDPE = 0.42–0.52; Table 5).

The K_D values reflect free energy differences between a protonated EtOH dimer (D*) and an EtOH monomer (M*) and an EtOH(g) molecule (Step 2, Scheme 1). Measured K_D values are larger than unity on POM acids (6.5–156 kPa^{-1}; Figure 15a) and similar to those from DFT-derived free energies (2.4–112 kPa^{-1}; Figure 15b). Measured and DFT-derived K_D values decreased with increasing DPE because protonated EtOH dimers (D*) exhibit larger partial charges than EtOH monomers (0.701–0.776 for D* vs. 0.539–0.568 for M* on POM clusters with different central atoms; Table 2); therefore, they benefit from the more stable conjugate anions on stronger acids more than EtOH monomers.

The value of ϕ reflects differences in free energy barriers between Step 7 (D* to TS7) and Step 9 (X* to TS9). Measured ϕ values (0.3–4.3; Figure 15a) are somewhat larger than estimates from DFT-derived free energies (0.03–2.6; Figure 15b). Measurements and theory give ϕ values that increase with increasing DPE (Figure 15), indicating that activation barriers for Step 7 are less sensitive than those for Step 9 to acid strength. The larger ϕ values on weaker acids reflect protonated EtOH dimers (D*) whose stability depends on DPE more sensitively than for ethoxides (X*), while TS7 and TS9 depend

similarly on acid strength. These trends are consistent with the larger positive charges in D* than ethoxides (0.701–0.776 for D* vs. 0.332–0.350 for X* on POM clusters with different central atoms; Table 2).

Measured rates and (DEE/EY) selectivity ratios are well described by Equations 15 and 16 (dashed lines; Figure 2). The regressed rate and equilibrium constants agree well with those obtained from DFT-derived free energies (Figure 14 and Figure 15) and resolve long standing uncertainties surrounding the mechanism for ethanol dehydration reactions on Brønsted acids. We expect these kinetically relevant routes and MASI to be valid in general for alkanol dehydration reactions on solid Brønsted acid catalysts, with the identity of the alcohol or the Brønsted acid only affecting the relative contributions of the elementary steps or the relative coverages of surface intermediates. With dehydration rates for other alcohols still reflecting alcohol monomers, protonated alcohol dimers, and alkoxides as MASI, a bimolecular route for alkoxide formation, direct and sequential routes for ether formation, and (for C2 alcohols and above) sequential monomolecular and bimolecular routes for alkene formation. The approach described here also demonstrates how the enumeration of plausible steps, DFT-derived estimates of their dynamics and thermodynamics, and sensitivity analysis methods is a more rigorous framework for determining the relevant steps and species in complex mechanisms than their determination via mere visual inspection of reaction coordinate energy diagrams.
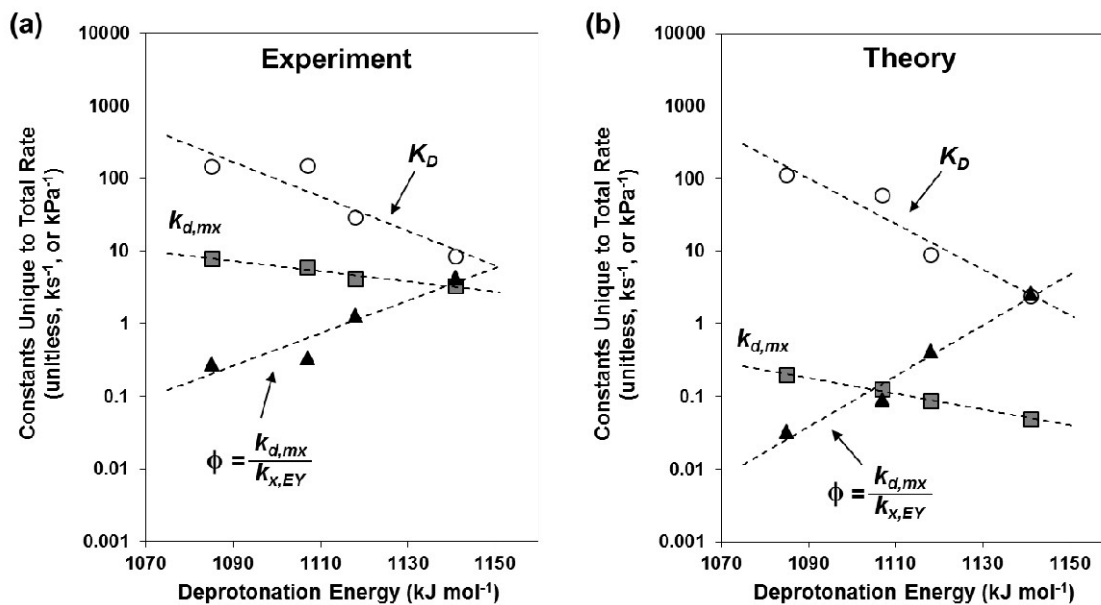
Figure 15. Values of $k_{d,mx}$ (ks^{-1}; ■), K_D (kPa^{-1}; ○), and ϕ (unitless; ▲) derived from (a) the regression of experimental data for H_nXW/SiO_2 catalysts (X = P, Si, Al, and Co; Figure 2a) to the functional form of Equation 16, and from (b) DFT-derived energies for $H_{8-n}X^{n+}W_{12}O_{40}$ clusters ($X^{n+} = P^{5+}$, Si^{4+}, Al^{3+}, and Co^{2+}) clusters as functions of DPE at 409 K. Dashed lines are best fits of the calculated values.

3.4. Conclusions

In this study, the elementary steps for alkanol dehydration reactions to alkenes and ethers on solid Brønsted acid catalysts were identified through theoretical investigations of EtOH dehydration reactions on several Brønsted acids of known structure and a broad range of acid strength. The elementary steps in all plausible dehydration routes were enumerated and evaluated based on their respective contributions to product formation rates (predicted from DFT-derived free energies) using protocols based on sensitivity and rate of production analyses that allow quantitative comparisons among routes. The full mechanism was modified to retain only those steps and surface intermediates that are consequential for product formation at conditions relevant to the practice of catalytic dehydration. Experimental rate and rate-ratio data were well described by the simplified mechanism and gave rate and equilibrium constants in good agreement with those obtained from DFT-derived free energies, demonstrating the usefulness of the systematic protocols used for identifying relevant elementary steps and prevalent bound intermediates, and validating the proposed simplified mechanism.

H-bonded monomers, protonated alkanol dimers, and alkoxides are the prevalent bound intermediates at conditions relevant to the practice of dehydration catalysis. Direct and sequential routes contribute to ether formation via S_N2-type reactions, with the O-atoms in alkanols acting as nucleophiles in attacking the α-carbon in either protonated monomers (direct routes) or alkoxides (sequential routes), displacing a H_2O or a surface O-atom, respectively. Alkenes form preferentially via sequential routes involving syn-E2-type eliminations, with the C-O bond in alkoxides cleaving while its β-hydrogen is abstracted by an O-atom at either the solid acid surface (monomolecular routes) or at a vicinal physisorbed alkanol (bimolecular routes). Alkoxide formation involves S_N2-type substitutions, with O-atoms on surfaces acting as nucleophiles in attacking the α-carbon in protonated monomers and displacing a H_2O molecule, while a second physisorbed alkanol forms hydrogen bonds with the leaving H_2O and a surface O-atom. Favorable bimolecular routes for alkene and alkoxide formation demonstrate the profound effects spectator molecules can have on transition state stability, when their presence leads to the formation of strong H-bonds between cationic moieties and negatively charged surface O-atoms.

Total dehydration rates increase with increasing acid strength on POM clusters (H_nXW/SiO_2) with different central atoms (X = P, Si, Al, and Co) because the ion-pair transition states that mediate kinetically relevant dehydration steps benefit more than their relevant precursors from the more stable conjugate anions in stronger acids (with lower DPE). Dehydration selectivities, however, are independent of POM composition because the elementary steps that contribute to EY and DEE formation from EtOH are all mediated by ion-pair transition states that exhibit a similar amount and distribution of charge.

3.5. Supporting Information
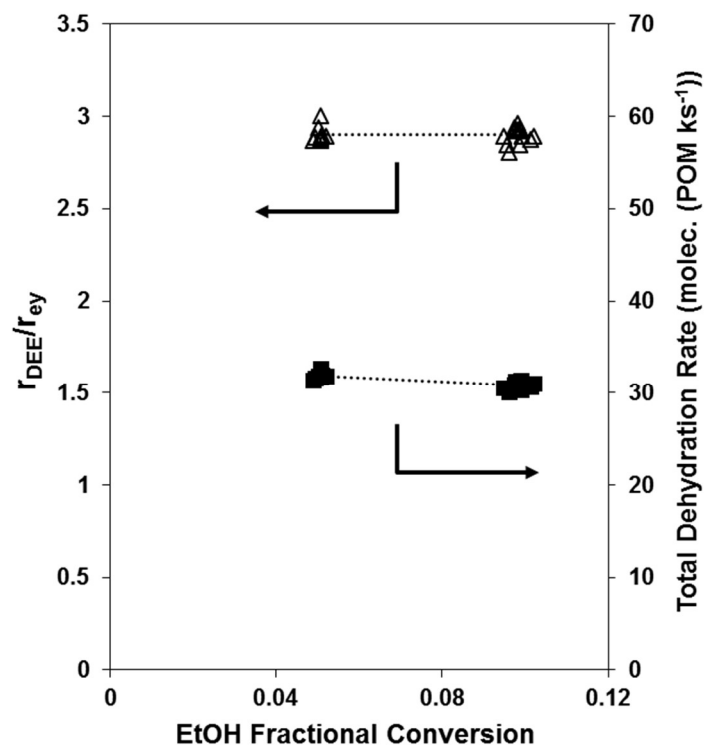
3.5.1. Space velocity effects on rate ratios and total rates

Figure S1-1. Measured total EtOH dehydration rates (■) and ratios of the rate of DEE formation to the rate of EY formation (r_{DEE}/r_{EY}; $\triangle$) as functions EtOH fractional conversion on H_4SiW/SiO_2 (reaction conditions: 409 K, 0.5 kPa EtOH). Dashed lines are linear fits of the data.

3.5.2. Summary of calculated enthalpies and entropies for TS and intermediates

Table S2-1. Calculated **enthalpies** for surface intermediates and TS relative to bare clusters ([*]) and two gaseous EtOH molecules for Keggin polyoxometalates ($H_{8-n}X^{n+}W_{12}O_{40}$) clusters with different central atoms ($X^{n+} = P^{5+}$, Si^{4+}, Al^{3+}, and Co^{2+}) at 409K. Energies have units of kJ/mol.

species[a]	central atom			
	P	Si	Al	Co
EtOH monomer (M*)	-86.7	-81.2	-79.9	-75.5
protonated EtOH dimer (D*)	-172.6	-164.6	-157.2	-149.5
ethoxide (X*)	-30.1	-25.1	-26.7	-28.0
EtOH/ethoxide site pair (MX*)	-59.8	-59.2	-61.5	-62.8
direct monomolecular EY formation (TS4)	51.9	55.3	59.2	64.6
direct bimolecular EY formation (TS6)	-16.4	-8.2	-4.1	3.9
sequential monomolecular EY formation (TS9)	77.8	87.0	92.3	99.8
sequential bimolecular EY formation (TS10)	22.8	32.4	40.1	45.6
monomolecular ethoxide formation (TS5)	56.7	71.2	77.0	89.7
bimolecular ethoxide formation (TS7)	-37.8	-28.4	-19.6	-9.1
direct DEE formation (TS8)	-42.3	-30.0	-22.5	-13.8
sequential DEE formation (TS11)	27.2	43.4	46.6	55.8

Table S2-2. Calculated **entropies** for surface intermediates and TS relative to bare clusters ([*]) and two gaseous EtOH molecules for Keggin polyoxometalates ($H_{8-n}X^{n+}W_{12}O_{40}$) clusters with different central atoms ($X^{n+} = P^{5+}$, Si^{4+}, Al^{3+}, and Co^{2+}) at 409K. Entropies have units of J/mol/K.

species[a]	central atom			
	P	Si	Al	Co
EtOH monomer (M*)	-119.0	-110.6	-108.6	-108.4
protonated EtOH dimer (D*)	-251.5	-242.5	-241.1	-243.8
ethoxide (X*)	4.8	14.7	16.2	14.7
EtOH/ethoxide site pair (MX*)	-78.3	-67.1	-67.2	-69.9
direct monomolecular EY formation (TS4)	-132.6	-127.0	-125.0	-125.4
direct bimolecular EY formation (TS6)	-243.8	-235.3	-234.0	-234.8
sequential monomolecular EY formation (TS9)	-21.4	-13.2	-10.7	-10.8
sequential bimolecular EY formation (TS10)	-129.5	-122.3	-119.0	-118.8
monomolecular ethoxide formation (TS5)	-118.7	-111.2	-110.2	-109.2
bimolecular ethoxide formation (TS7)	-240.3	-231.6	-230.0	-230.3
direct DEE formation (TS8)	-240.8	-231.7	-230.8	-233.0
sequential DEE formation (TS11)	-102.0	-92.9	-90.9	-90.7

3.6. References

[1] J. Sun, Y. Wang, *ACS Catal.* 4 (2014) 1078–1090. doi:10.1021/cs4011343

[2] S. Kaplan, "Monthly Energy Review October 2015," 2015.

[3] C.B. Phillips, R. Datta, *Ind. Eng. Chem. Res.* 36 (1997) 4466–4475. doi:10.1021/ie9702542

[4] D. Varisli, T. Dogu, G. Dogu, *Chem. Eng. Sci.* 62 (2007) 5349–5352. doi:10.1016/j.ces.2007.01.017

[5] D. Fan, D.J. Dai, H.S. Wu, *Materials (Basel).* 6 (2013) 101–115. doi:10.3390/ma6010101

[6] A. Corma, *Chem. Rev.* 95 (1995) 559–614.

[7] I. Takahara, M. Saito, M. Inaba, K. Murata, *Catal. Letters*. 105 (2005) 249–252. doi:10.1007/s10562-005-8698-1

[8] F. Roca, L. De Mourgues, Y. Trambouze, *J. Catal.* 14 (1969) 107–113. doi:10.1016/0021-9517(69)90414-X

[9] Y. Saito, H. Niiyama, *J. Catal.* 106 (1987) 329–336.

[10] F. Figueras, Y. Trambouze, L.D.E. Mourgues, 113 (1969) 107–113.

[11] H. Chiang, A. Bhan, *J. Catal.* 271 (2010) 251–261. doi:10.1016/j.jcat.2010.01.021

[12] T.T. Ali, S. a. Al-Thabaiti, a. O. Alyoubi, M. Mokhtar, *J. Alloys Compd.* 496 (2010) 553–559. doi:10.1016/j.jallcom.2010.02.100

[13] T. Okuhara, T. Arai, T. Ichiki, K. Lee, *J. Mol. Catal.* 55 (1989) 293–301.

[14] C. de las Pozas, R. Lopez-Cordero, J.A. Gonzalez-Morales, N. Travieso, R. Roque-Malherbe, *J. Mol. Catal.* 83 (1993) 145–156. doi:10.1016/0304-5102(93)87015-Z

[15] B.P. Gracey, B.P. Gracey, Process for preparing ethene, US 8,822,748 B2, 2014.

[16] C. Bailey, L.W. Bolton, B.P. Gracey, M.K. Lee, S.R. Partington, Process for producing olefins, US8440873, 2013.

[17] S.R. Partington, A process for the dehydration of ethanol to produce ethene, US20120165589 A1, 2012.

[18]   J. Macht, M.J. Janik, M. Neurock, E. Iglesia, *J. Am. Chem. Soc.* 130 (2008) 10369–79. doi:10.1021/ja803114r

[19]   J. Macht, M.J. Janik, M. Neurock, E. Iglesia, *Angew. Chem. Int. Ed.* 46 (2007) 7864–8. doi:10.1002/anie.200701292

[20]   M.J. Janik, J. Macht, E. Iglesia, M. Neurock, *J. Phys. Chem. C.* 113 (2009) 1872–1885. doi:10.1021/jp8078748

[21]   J. Macht, R.T. Carr, E. Iglesia, *J. Am. Chem. Soc.* 131 (2009) 6554–6565.

[22]   A.J. Jones, R.T. Carr, S.I. Zones, E. Iglesia, *J. Catal.* 312 (2014) 58–68. doi:10.1016/j.jcat.2014.01.007

[23]   W. Knaeble, R.T. Carr, E. Iglesia, *J. Catal.* 319 (2014) 283–296. doi:10.1016/j.jcat.2014.09.005

[24]   J. Cowan, C.L. Hill, R. Reiner, I. Weinstock, *Inorg. Synth.* 33 (2002) 18–26.

[25]   L. Baker, B. Loev, T. McCutcheon, *J. Am. Chem. Soc.* 72 (1950) 2374–2377.

[26]   L. Baker, T. McCutcheon, *J. Am. Chem. Soc.* 78 (1956) 4503–4510.

[27]   C. Baertsch, *J. Catal.* 205 (2002) 44–57. doi:10.1006/jcat.2001.3426

[28]   G. Kresse, J. Furthmüller, *Phys. Rev. B.* 54 (1996) 11169–11186.

[29]   G. Kresse, J. Hafner, *Phys. Rev. B.* 47 (1993) 558–561.

[30]   G. Kresse, J. Hafner, *Phys. Rev. B.* 49 (1994) 14251–14269. doi:10.1103/PhysRevB.49.14251

[31]   G. Kresse, J. Furthmüller, *Comput. Mater. Sci.* 6 (1996) 15–50. doi:10.1016/0927-0256(96)00008-0

[32]   P.E. Blöchl, *Phys. Rev. B.* 50 (1994) 17953–17979. doi:10.1103/PhysRevB.50.17953

[33]   G. Kresse, *Phys. Rev. B.* 59 (1999) 1758–1775. doi:10.1103/PhysRevB.59.1758

[34]   J. Perdew, J. Chevary, S. Vosko, *Phys. Rev. B.* 46 (1992) 6671–6687.

[35]   H.J. Monkhorst, J.D. Pack, *Phys. Rev. B.* 13 (1976) 5188–5192. doi:10.1103/PhysRevB.13.5188

[36] R.T. Carr, M. Neurock, E. Iglesia, *J. Catal.* 278 (2011) 78–93. doi:10.1016/j.jcat.2010.11.017

[37] P. Deshlahra, R.T. Carr, S.-H. Chai, E. Iglesia, *ACS Catal.* 5 (2015) 666–682. doi:10.1021/cs501599y

[38] G. Makov, M. Payne, *Phys. Rev. B*. 51 (1995) 4014–4022. doi:10.1103/PhysRevB.51.4014

[39] P.-O. Löwdin, *J. Chem. Phys.* 18 (1950) 365. doi:10.1063/1.1747632

[40] P.-O. Löwdin, On the Nonorthogonality Problem, in: Adv. Quantum Chem., 1970: pp. 185–199. doi:10.1016/S0065-3276(08)60339-1

[41] W.C. Lu, C.Z. Wang, M.W. Schmidt, L. Bytautas, K.M. Ho, K. Ruedenberg, *J. Chem. Phys.* 120 (2004) 2629. doi:10.1063/1.1638731

[42] W.C. Lu, C.Z. Wang, T.L. Chan, K. Ruedenberg, K.M. Ho, *Phys. Rev. B*. 70 (2004) 041101. doi:10.1103/PhysRevB.70.041101

[43] T.-L. Chan, Y.X. Yao, C.Z. Wang, W.C. Lu, J. Li, X.F. Qian, et al., *Phys. Rev. B*. 76 (2007) 205119. doi:10.1103/PhysRevB.76.205119

[44] X. Qian, J. Li, L. Qi, C.-Z. Wang, T.-L. Chan, Y.-X. Yao, et al., *Phys. Rev. B*. 78 (2008) 245112. doi:10.1103/PhysRevB.78.245112

[45] G. Henkelman, B.P. Uberuaga, H. Jónsson, *J. Chem. Phys.* 113 (2000) 9901–9904. doi:10.1063/1.1329672

[46] G. Henkelman, H. Jónsson, *J. Chem. Phys.* 111 (1999) 7010. doi:10.1063/1.480097

[47] D.D. Hibbitts, R. Jiménez, M. Yoshimura, B. Weiss, E. Iglesia, *J. Catal.* 319 (2014) 95–109. doi:10.1016/j.jcat.2014.07.012

[48] C.T. Campbell, J.R. V Sellers, *Chem. Rev.* 113 (2013) 4106–35. doi:10.1021/cr300329s

[49] H. Eyring, *J. Chem. Phys.* 3 (1935) 107–115. doi:10.1063/1.1749604

[50] M.G. Evans, M. Polanyi, *Trans. Faraday Soc.* 31 (1935) 875. doi:10.1039/tf9353100875

[51] B.B. Bardin, R.J. Davis, *Appl. Catal. A-Gen.* 200 (2000) 219–231.

[52] M.J. Janik, B.B. Bardin, R.J. Davis, M. Neurock, *J. Phys. Chem. B*. 110 (2006)

4170–8. doi:10.1021/jp0553176

[53]   X. Rozanska, P. Sautet, F. Delbecq, F. Lefebvre, S. Borshch, H. Chermette, et al., *Phys. Chem. Chem. Phys.* 13 (2011) 15955–9. doi:10.1039/c1cp21171d

[54]   W. Alharbi, E. Brown, E.F. Kozhevnikova, I. V. Kozhevnikov, *J. Catal.* 319 (2014) 174–181. doi:10.1016/j.jcat.2014.09.003

[55]   J. Sun, Y. Wang, *ACS Catal.* 4 (2014) 1078–1090. doi:10.1021/cs4011343

[56]   K.Y. Lee, T. Arai, S. Nakata, S. Asaoka, T. Okuhara, M. Misono, *J. Am. Chem. Soc.* 114 (1992) 2836–2842. doi:10.1021/ja00034a013

[57]   S. Kim, D.J. Robichaud, G.T. Beckham, R.S. Paton, M.R. Nimlos, *J. Phys. Chem. A.* 119 (2015) 3604–3614. doi:10.1021/jp513024z

[58]   T. Maihom, P. Khongpracha, J. Sirijaraensre, J. Limtrakul, *ChemPhysChem.* 14 (2013) 101–107. doi:10.1002/cphc.201200786

[59]   M. John, K. Alexopoulos, M.-F. Reyniers, G.B. Marin, *J. Catal.* 330 (2015) 28–45. doi:10.1016/j.jcat.2015.07.005

[60]   G.C. Pimentel, A.L. McClellan, *Annu. Rev. Phys. Chem.* 22 (1971) 347–385. doi:10.1146/annurev.pc.22.100171.002023

[61]   C.L. Perrin, J.B. Nielson, *Annu. Rev. Phys. Chem.* 48 (1997) 511–544. doi:10.1146/annurev.physchem.48.1.511

[62]   L. Pauling, "The Nature of the Chemical Bond, An Introduction to Modern Structural Chemistry," 3rd ed., Cornell University Press, Ithaca, United States, 1960.

[63]   S. Gronert, *J. Am. Chem. Soc.* 113 (1991) 6041–6048. doi:10.1021/ja00016a017

[64]   J.F. Bunnett, *Angew. Chemie Int. Ed. English.* 1 (1962) 225–235. doi:10.1002/anie.196202251

[65]   R.D. Bach, R.C. Badger, T.J. Lang, *J. Am. Chem. Soc.* 101 (1979) 2845–2848. doi:10.1021/ja00505a007

[66]   a. S. Tomlin, M.J. Pilling, T. Turanyi, J.H. Merkin, J. Brindley, *Combust. Flame.* 91 (1992) 107–130. doi:10.1016/0010-2180(92)90094-6

[67]   G. Zeng, M.J. Pilling, S.M. Saunders, *J. Chem. Soc. Faraday Trans.* 93 (1997) 2937–2946. doi:10.1039/a701584d